Andrew J W Morris

Laboratory Studies of Hypervelocity Impacts on Solar System Analogues

A thesis submitted in requirement for the degree of Doctor of Philosophy in Astrophysics and Planetary Science in the Faculty of Physical Sciences at the University of Kent in Canterbury

2014/15

Total word count – 50 425

Contents

Thesis References

Annex C – Orthogonally Averaged Crater Profiles

Annex D – KDM Method Code

Annex E – KDM Method Results

Acknowledgements

I would like to thank and dedicate my work to all of those who helped me make my dream come true.

My main supervisor Prof. Mark Burchell for giving me the chance to fulfil my dream and his never ending continued help and support which has meant so much.

My secondary supervisor Dr Stephen Lowry for his help concerning asteroids and having a good chat about Guinness on more than one occasion!

Mr Mike Cole the ever dependable scientific officer in the hypervelocity impact lab at Kent University who was always there with his extensive knowledge and rapier-like wit!

Sophie Godfrey for continually chasing me to keep me up to date with the wider university side of things!

Tim Kinnear and Jacob Deller for their computational expertise on the KDM method.

I would also like to thank Dr Mark Price and Dr Adrian Jones for accepting the task of examining my work.

My family and friends (would need many more pages to state names – you know who you are!!!) for their continued support when times were good and tough.

Armand my old best friend who I miss so much.

And finally la mia bella dea Stefania per essere entrata nella mia vita ed avermi dato cosi tanto – Ti Amo

List of Figures

Figure 6.21 A and B: As Q gets closer to catastrophic disruption, the sections pointed out earlier are easily distinguishable. A) Static shot Q = 861 Jkg^{-1} B) Rotational shot Q = 815 Jkg^{-1}.

Figure 6.22 A and B: Both plots are greater than Q* for each case. The level of change from cratering to disruption can be seen. A) Static shot Q = 1654 Jkg^{-1} B) Rotational shot Q = 1666 Jkg^{-1}.

Figures 6.23 A, B and C: The power law β (middle branch) values for both static and rotation (A and B) and (C) a comparison between the two data sets.

Figure 6.24: A screen dump of a model using Autodyn.

Figure 6.25: The effects arising from the SPH concentric packing boundaries (top image), the fragmentation split along the boundaries every time (bottom image).

Figure 6.26: Packing the targets with rectangular packed SPH particles (top image) helped to reduce the level of fragmentation being affected by packing anomalies (bottom image).

Figure 6.27: Shows the static remnant mass data (laboratory results in black) with the simulation points added (green data points).

Figure 6.28: Rotational simulation data on the remnant mass graph. The laboratory results are in green with the experimental results in black.

Figure 6.29 A and B: For the purposes of comparison, static impact hydrocode simulations were run in order to check the validity of the code with experimentation for both static and rotation. A) shows that the target did not disrupt. B) Once again the level of disruption between experimental and theoretical was not in good agreement but the rest of the distribution was fair.

Figure 6.30 A and B: Experimental and simulation fragment distributions show at least an order of magnitude size difference in A but the size difference in greatly reduced in B. The simulation was changed from concentric packing in A to rectangular in B.

Figure 7.11: Crater comparisons are made by taking the average profile data and error for each full data set as in figure 7.10 and compiling the trends with respect to temperature.

Figure 7.12: A screen-grab from the MeX software; the measurement of crater diameter was very accurate due to the ability of picture zooming.

Figure 7.13: Constructing DEMs of the craters allowed easy selection of crater profiles. This DEM shows a sandstone crater.

Figure 7.14: The profile of the sandstone crater shown in figure 7.13, changes in morphology are shown along a chosen profile slice.

Figure 7.15: The cutting plane crater volume method used a planar reference position as a maximum position for in filling of the crater voids.

Figure 7.16: A sandstone target heated up to 1003 K being impacted by an STST 420 0.8 mm projectile.

Figure 7.17: Three profiles obtained from MeX showing differences in crater floors for cold (top), room temperature (middle) and hot (bottom) basalt impacts.

Figure 7.18: Median profiles for three different temperature impacts are shown using the KDM method.

Figures 7.19 A, B, C, D and E: Series of graphs showing volume, diameter, depth, d/D ratio and cratering efficiency with respect to temperature respectively for Basalt impacts.

Figures 7.20 A, B, C, D and E: Series of graphs showing volume, diameter, depth, d/D ratio and cratering efficiency with respect to temperature respectively for Limestone impacts.

Figures 7.21 A, B, C, D and E: Series of graphs showing volume, diameter, depth, d/D ratio and cratering efficiency with respect to temperature respectively for sandstone impacts.

Figures 7.22 A, B, C, D and E: Series of graphs showing volume, diameter, depth, d/D ratio and cratering efficiency with respect to temperature respectively for Ancaster Hard White limestone impacts.

Figures 7.23 A, B, C, D and E: Series of graphs showing volume, diameter, depth, d/D ratio and cratering efficiency with respect to temperature respectively for Beestone Red sandstone impacts

Figure 7.24 A and B: The coldest temperature impacts for limestone. Photo A shows a cold target impact from the Ancaster Hard White limestone whereas photo B shows the older unknown stock limestone.

Figure 7.25 A, B, C, D, E and F: Photos A, B and C are room temperature impacts into the known Ancaster Hard White Limestone and D, E and F represent spallation zones associated with old stock limestone.

Figure 7.26 A and B: Both figures A and B are from the older stock limestone.

Figure 7.27 A and B: The two photos show the hottest Ancaster Limestone impacts where A and B are 773 and 923 K respectively.

Figure 7.28 A, B, C and D: Photos A and B show Beestone Red sandstone and photos C and D are craters from the stock sandstone. All craters were impacted in the cold region.

Figure 7.29 A, B, C and D: Photos A, B and C show room temperature stock sandstone and photoD shows a crater from the Beestone Red sandstone. All craters were impacted in the cold region.

Figure 7.30 A and B show hot impacts into Beestone Red sandstone at the hottest regions during the impact tests.

Figure 7.31 A and B: These photos detail very cold impacts into basalt. The asterisks denote sheer faces interrupting the crater walls from incomplete spallation.

Figure 7.32 A and B Room temperature basalt impacts with interrupted spallation as mark by the arrows in both cases.

List of Tables

Abstract

Impact cratering and asteroid collisions are major processes throughout the Solar System. Although previous collision-related impact investigations exist (Flynn et al. 2015, Holsapple et al. 2002 and Burchell et al. 1998 are good examples), in the works covering this broad range of investigation, the targets are non-rotating (for the purposes of catastrophic disruption) and different temperature conditions are not considered (for impact cratering). Accordingly, I present experimental processes and data, regarding hypervelocity impact experiments into analogues of (1) rotating asteroids and (2) temperature dependant terrestrial planetary rock.

During the course of this work, it was necessary to develop new apparatus and new experimental techniques such as three separate target holders to aid in both catastrophic disruption and heated impact projects, a 3-dimensional model analysis of craters and a completely new, statistically robust, technique to determine a complete crater profile called the KDM method where KDM is Kinnear-Deller-Morris.

The main result from this work showed that during an asteroid impact collision where the asteroid is not rotating, the impact energy density for catastrophic disruption is $Q*_{static} = 1442 \pm 90$ J kg^{-1}. However, when the target asteroid was rotating, the condition $Q*_{rotation} = 1097 \pm 296$ J kg^{-1}. The mean value of $Q*$ had thus reduced, but the spread in the data on individual experiments was larger. This leads to two conclusions. The mean value for $Q*$, based on measurements of many impacts, falls, due to the internal forces acting in the body which are associated with the rotation. This energy term reduction means that the amount of energy to instigate catastrophic disruption is lower and that a rotating asteroid is effectively weaker upon impact than a stationary asteroid. However, the spread in the results indicates that this is not a uniform process, and an individual result for $Q*$ for a rotating or spinning target may be spread over a large range. For the temperature related impacts, as the targets were heated to approximately 1000 K, the target rocks showed an impact dependence more similar to a plastic phase-state than to solidus, due to being held close to temperatures associated with semi-plastic phases. Basalt impact craters displayed this relationship greatest with crater sizes becoming smaller at the higher temperature ranges but larger in the colder brittle solidus temperatures, partly explained in experiments by increased spallation.

Chapter I: Introduction

From the majestic swirl of galaxies to the discovery of exosolar worlds, the evolution of scientific thought has never been so prevalent, when compared to the unravelling of secrets behind the history and future of the section of the universe in which we occupy; the solar system.

Many theories and models have been generated in order to explain the beginnings of the solar system with many failing in answering such issues as the rotational momentary inertia problem or the similarity of chondritic samples found from meteorites on the Earth. The first Chapter of this thesis is concerned with detailing an historical review of the scientific studies and theories that attempted to explain the origins, mechanics and future of the Solar System. The review will cover from ancient Greek times to present covering such theoretical approaches from Decartes and Kant. By covering the historical aspects of the scientific evolution of the Solar System, the review pinpoints towards the two questions which are covered and answered by this thesis; catastrophic disruption and variable temperature impacts (these are discussed in Chapter 2).

1.1   An Historical Review

To begin the task of detailing the historical facts about the solar system, the ancient Greeks, Hicetas, Plutarch, Philolaus the Pythagorean and Aristarchos of Samos proposed the first forms of the heliocentric solar system models in the timeframe 400 B.C. to 120 A.D., with the motion of the Earth around the central fire or Sun. These models of the solar system took approximately 1800 years to progress into 'usable' and provable forms.

As time progressed and in Europe, the influence of the Roman Catholic Church extended to matters concerning science, questions were being raised due to the lack of explanation on the 'constant length of the seasonal year'. Also, mathematicians were unable to successfully explain the motions of the known five planets with respect to the Earth. From attempting to answer these types of questions, the heliocentric model with the Sun at the centre of the universe and the motion of the Earth around it became deducible from the scientific study of the night sky and positions and durations of motion of the planets and Sun (Copernicus 1543).

However, attempts to organise the thinking behind the motion of the solar system, the works of Copernicus still alluded to the actual initial formation of the solar system. Rene Descartes, reaffirmed the notion of the heliocentric model in his publication "The World" or "Treatise on Light" in 1629 but also included a theory on the formation of the solar system. Descartes' work provided a solar system model with the constituents of the solar system forming from a much larger collection of matter through mutual attraction and collisions thereby forming a solar centre (Descartes [1629]). This work may have been the precursor to the nebula theory which was used by Kants and then Laplace in the mid 17th century.

However, during the late 17th century working away from the nebula framework of solar system formation, Georges-Louis Leclerc Comte de Buffon proposed the first catastrophic theoretical model on the formation of the solar system. Whilst the solar system was in its infancy, the Sun was impacted by a comet on a trajectory through the early solar system. As the comet collided obliquely with the Sun, it had enough speed, density (112 000 times greater than solar density), mass (1/650 solar mass) and energy to remove vast quantities of the solar matter and distributed it throughout the local vicinity. The matter 'river' emanating from the Sun then coalesced into the planets with a density gradient; denser planets are the terrestrials and less dense being the gas giants (Buffon [1778]).

Although there have been a number of different solar system models, the theory of localised solar system accretion coupled with an advancement from Descartes' ideas have given rise to the nebula theory of accreting matter forming the solar system which is relatively close to the theories accepted today.

The theoretical approach from Descartes' solar system nebula origin and the driving vortices moving the celestial objects around, were shown to be insufficient in explaining the different motions of the planets, Sun and comets. It was noted that the vortices did not account for the difference in orbital periods and trajectories. (Swedenborg 1734).

However, in this period of time, Emanuel Swedenborg noted the letter from Sir Isaac Newton to Bentley, in Whewell's Bridgewater Treatise on Astronomy and General Physics (p. 172), as an attempt to incorporate his theories on gravitational attraction and to link them with a model of solar system formation; "In his first letter to

Bentley, he allows that matter might form itself into masses by the force of attraction.

'And thus' says he, 'might the Sun and fixed stars be formed, supposing the matter were of a lucid nature. But how the matter should divide itself into two sorts; and that part of it which is fit to compose a shining body should fall down into one mass and make a Sun; and the rest, which is fit to compose an opaque body, should coalesce, not into one great body, like the shining matter, but into many little ones; or if the Sun at first were an opaque like the planet, or the planets lucid bodies like the Sun, how he should be changed into a shining body whilst all they opaque, or whilst all they be changed into opaque ones, while he remains unchanged: I do not think explicable by mere natural causes, but am forced to ascribe it to counsel and contrivance of a voluntary agent'" (Newton 1756). The aspects of Newton's letter to Bentley allowed for the accretion of matter under gravitational attraction in the solar system nebula to be considered in more detail. Swedenborg took Newton's suppositions further into the generally accepted form of a 'modern' theory of nebula accretion of the solar system.

Seven general hypotheses were made by Swedenborg in order to lay the foundations of the nebula theory of solar system accretion:-

1. That by reason of the same causes, the second elementary particles are most highly compressed near the solar active space.
2. The second hypothesis deals with the nomenclature of accreting matter in terms of finites and other order elementary particles.
3. Continued matter accretion where the cementing of matter around the solar active position grows in immense volume and around the Sun.
4. As matter continues to accrete around the Sun, it starts to rotate in a 'certain gyre' and a crust of forth finites begins to form near the Sun.
5. As rotation continues, it begins to clear the space surrounding the Sun.
6. This hypothesis shows that the higher order matter continues to accrete and planets begin to form. Due to the rotation already in place, the forming planets also move around the Sun. The Sun starts to reduce in size.
7. The final hypothesis formulates the final stages of the nebula and explains why planets have different sizes and orbits around the Sun.

(Swedenborg 1734)

Leading on from this theoretical approach, Immanuel Kant and Pierre Simon Marquis de Laplace towards the end of the 1700s adapted the nebula theory of solar system formation. This theory uses the large nebula gas as the starting point of the formation process. The gas initially is hot, begins to cool, coalesce, rotate and flatten. With the reduction of the nebula, gas rings are left behind which then form the planets as accretion continues. The vast majority of accreted matter makes the Sun at the centre of the nebula. (Laplace 1796)

This theory stood the test of time for at least one hundred years until it was pointed out that serious flaws were present. Issues of solar rotation speed and solar system rotational momentum meant that the Laplacian theory of nebula accretion was not adequate in explaining solar system formation, but it did provide a very useful foundation for the nebula theory which is widely accepted today; Victor Safronov's Solar Nebula Disc Model or SNDM (Woolfson 1991).

Although time has passed since the Kant/Laplace formulation of the nebula theory, the main concepts are still used as a foundation to the SNDM model. With the latest observations into exoplanetary systems and star formation nebulae, such as the Orion Nebula being made continuously, the current largely accepted view on the formation of the solar system is as follows:

Due to the ages obtained from radionuclide dating of primitive chondritic meteorite samples, the age of the solar system is found to be 4.57 ± 0.17 Gyr (Bouvier and Wadhwa 2010). The initial instigating factor which started the collapse is still a topic for debate, with some theoretical models attributing the collapse due to gravitational instabilities and attraction (Shi and Chiang 2013 and references therein).

However, the presence of short lived radioisotopes such as ^{26}Al (Lee et al. 1976 and Amelin et al. 2002) and ^{60}Fe (Tachibana and Huss 2003) found in chrondritic samples do not originate from gravitational collapse alone. Several theories have been proposed on the external enrichment of the solar system's nebula cloud from asymptotic branch stars (Wesserburg et al. 1995) or Wolf-Rayet star envelopes (Arnould et al. 1997 and Taticheff et al. 2010). But these models have been disputed

due to the precise and complex chain of events needed for asymptotic branch stars to enrich the nebula cloud, and that Wolf-Rayet stars have yet to be found in star forming regions of space.

One theoretical approach which hopes to answer the problem of the short lived radionuclides is the supernova explosion hypothesis. A supernova exploding at an optimum distance of approximately 5 pc from the solar system nebula is a two-fold answer; the short lived radionuclides are known to be found in ejected supernova matter and the resulting shockwave from the supernova would help to initiate nebula collapse (Clayton 1977, Cameron and Truron 1977, Gritschneder et al. 2012 and Boss and Keiser 2010 and 2012).

Regardless of the cause or instigation of the nebula collapse, the solar system nebula fulfilled the Jeans instability criterion with an imbalance between the gravitational forces acting towards the centre of the nebula mass and the radiative forces acting in the opposite direction.

As bodies began to attract one another inside the solar system nebula, the dependency on mass and locality introduced factors which governed the accretion process. Body mass and size with surface density of planetesimals and relative velocities have since been attributed as the main dynamical properties to affect the accretion outcome Parisi and Brunini (1999).

One common model to help explain the process of accretion attraction is the two-body approximation;

$$\frac{dM_e}{dt} \cong \pi R_e^2 \Omega m N \frac{v}{v_z}\left(1 + \frac{2GM_e}{R_e v^2}\right)$$

where m is the average planetesimal mass, M_e is the accreting body (embryonic) mass in kg, R_e is the accreting body radius in km, N is the surface number density of planetesimals and v_z is the average planetesimal velocity in kms[-1]. The bracketed factor dictates the strength of the gravitational focusing of the accreting body. If this term is considered to be a two-body term reduces to;

$$\frac{1}{M_e}\frac{dM_e}{dt} \propto M_e^{1/3}$$

which shows that if the rate of accretion increases due to the factors already discussed, then the mass of the accreting body increases rapidly (Wetherill and Stewart (1989)).

As a body increases in size its overall effect on the accretion environment also increases. It has also been found that if the velocity distributions of matter are small enough in the locality of the accreting body, the mass effective dependence of the collisional rate increases and therefore increases the likelihood of accelerated accretion Lissauer (1993).

With more matter being accreted, the governing factor, $\frac{v}{v_z}$, increases in strength and therefore accretion increases linearly. With the accretion of the body increasing by an accelerating rate, the body is deemed to be in runaway accretion and therefore will grow quickly with respect to the continual matter feeding it.

However as the body continues to increase in size the main governing factor which first controlled and initiated the runaway accretion, then acts to help halt the runaway accretion. As the size of the body tends towards protoplanetary status, the gravitational effect it has on the local area acts to perturb and increase the relative velocities of possible accretion constituents; this situation is also aided by the fact that there are more than likely other large bodies and protoplanets in the vicinity of the body in question which also perturb the solar system medium. The actions of the different sources of gravitational attraction act to slow down the runaway accretion Parisi and Brunini (1999) and Rafikov (2003). The actual accretion of the planets however, might not have been completely at the same time, with the Earth and the Moon being late (Touboul et al. 2015).

It is also believed that runaway accretion was not only confined to the terrestrial planets but was also present in the forming of the gas giants. Work by Pollack et al. (1996) concluded the statement on the formation of gas giants probably started with isolated embryos experiencing runaway accretion until large enough to accrete the gaseous envelopes.

The continual feeding of matter towards the solar nebula meant that the solar active region had enough continual feed of gravitational energy to initiate the forming of the sun. During the formation stages, the sun went through a particular stage known

as the T-Tauri phase of formation, which resulted in violent activity from the proto-sun envelope shedding mass into the solar nebula. The timing of the T-Tauri phase helps to pinpoint the accretion of the gas giants, due to large amounts of ejected gaseous material needed to form the gas giants counteracting the forming grains of the nebula. Although the gas giants would have accreted enough material to produce large cores, the gaseous ejections were needed to continue the level of accretion needed to form the gas giants.

The continual formation of the solar system meant that angular momentum needed to be conserved in the form of increased oblateness, whereby the nebula became a rotating solar system disc. However there are still issues arising from the solar system models concerning the angular momentum of the solar system disc and solar rotation. Attempts have been made to explain why the sun isn't spinning as fast as it should with the results obtained from the Solar System Nebula Model (Woolfson 1984, Alfvèn and Arrhenius 1976, Lyden-Bell and Pringle 1974, McCrea 1960, 1978 and Woolfson 1979). Also an attempt to explain the rotation of the solar system disc being slower than hypothesised through grain dragging with respect to turbulence (Jones 2007), one major issue that arose from the accepted accretion model, was the attempt to explain the results from the era of Heavy Bombardment.

1.2   Late Heavy Bombardment (LHB)

Approximately 3.9 billion years ago (Beatty et al. 1999) or 700 Myrs years after planetary accretion (Hartmann et al. 2000), the inner solar system was subjected to an intense level of planetary bombardment, where the record of this period has been preserved on planetary bodies such as Mercury and the Moon (Fernandes et al. 2013 and Marchi et al. 2012).

The era of late heavy bombardment has been hypothesised to have lasted for approximately 1.4 Myr (Chapman et al. 2007), but opponents to the theoretical nature of the era of late heavy bombardment have devised theoretical models to try and explain this epoch. Highly-inclined solar nebula leftovers impacting the terrestrial planets during the LHB time (Morbidelli et al. 2001) and the perturbations induced through the formation of Uranus and Neptune (Levison et al. 2001) amongst others. However each model has not been set within a "self-consistent framework of

Solar System evolution" which lead onto the now generally accepted Nice model (Gomes et al. 2005).

As the planetary bodies formed in the solar system, large amounts of planetesimals were present. The Nice model also stipulates the presence of ice giants of the edge of a planetesimal ring as shown in Figure 1.1.
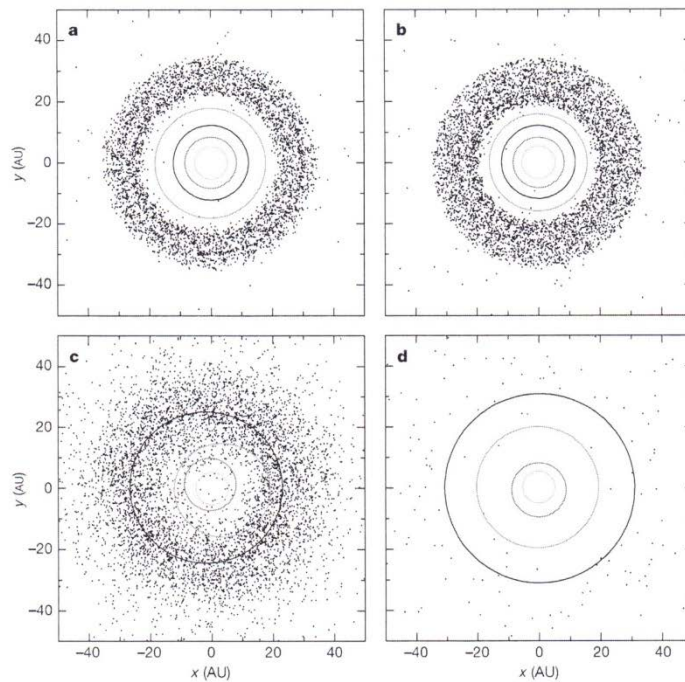
Figure 1.1: This Figure (from Gomes et al. 2005) shows the computational set up used in the Nice model with respect to the boundary of planetesimals and ice giants. As can be seen, the continued orbital resonance between Jupiter and Saturn increases until the resonance ratio of 1:2 MMR is reached and the two planets move into eccentric orbits and in doing so, catastrophically disrupt the planetesimal ring, thereby starting the era of heavy bombardment.

The terrestrial and gas giant planets formed in close proximity to the sun and were held in a quasi-static state by the ring of planetesimals. As the ring lost mass into the inter-stellar medium, the constraining effect of the ring on Jupiter and Saturn weakened. Once their relative orbits reached a 1:2 mean motion resonance, the gravitational instability generated by the resonance coupled with the loss of planetesimal mass resulted in the orbit perturbation of the ice giants. The ice giants

interacted with the planetesimal ring and dispersed the ring into a cascading shower of projectiles in the inner solar system.

The catastrophic disruption of the planetesimal ring greatly increased the impactor flux of the inner solar system which initiated the Era of Heavy Bombardment or EHB (Gomes et al. 2005, Tsiganis et al. 2005 and Morbidelli et al. 2005).

The EHB helped shape the solar system as it is known today, but two intrinsically-linked EHB remnants are of great importance to the scope of the work detailed in this thesis; planetary impacts and their outcomes, and the asteroid belt and its evolution.

Another view point on the aspect of heavy bombardment during solar system formation is theoretical work carried out by Batygin and Laughlin to help explain why the inner solar system appears to be different in formation to the discoveries being made via the Doppler velocity surveys. The results obtained from exo-solar systems show that the inner solar system might have formed due to Jupiter's migration towards the Sun and then back out to a distance of 1.2 AUs (Batygin and Laughlin 2014). The accretion of Jupiter using debris from the inner solar system meant that the inner terrestrial planets lacked the amount of matter to accrete to the sizes of the 'super-Earths' being found today. However, the motion of such a body such as Jupiter in the vicinity of the Sun, would create a catastrophic impact event in the history of the solar system; this in itself leads onto the eras of bombardment.

With respect to asteroids during the LHB, it is believed that asteroids located from the main belt were the main constituents of the LHB (Strom et. al. 2015). Crater population and size surveys indicated that these impacts along with subsequent impacts afterwards hypothesised to originate from Near Earth Objects (NEOs), were ejected in a size-independent manner.

1.3   The Main Asteroid Belt and its Evolution

Regardless of which theoretical model best describes the origin or future of the asteroid belt, it remains that the asteroids are prehistoric signatures of the early solar system (Bottke et al. 2002a, Steinberg and Sari 2015). They have been hypothesised as EHB remnants: collections of non-accreted material (Carry 2012). It was once thought that the Main-Belt asteroids could have originally been a planet in orbit

around the Sun in between the orbits of Mars and Jupiter. However, this model resulted in the planet being catastrophically disrupted via impact and therefore initiated the birth of the main-belt asteroids. This model has long since been disproved through inadequacies in the collective mass of the main belt asteroids in comparison to a planet of similar size to that of Mars.

Although the main-belt asteroids are still viewed as pre-historical signatures, the main-belt and other asteroid locations such as the Trojans and Kuiper Belt, are areas in the solar system which are constantly undergoing evolution.

The space-weathered asteroids of the solar system are found to fall into several forms of body; monolithic/shock annealed objects or fragmented, rubble pile objects (Benavidez et al. 2012). Monolithic asteroids, as the name suggests, are singular bodies with some associated porosity. It is a body which could be large enough to have initiated particulate differentiation internally, such as the largest known bodies, Ceres and Vesta. Being monolithic does not exclude the body from having a purely singular chemical make-up. Monolithic asteroids have been found to contain a variety of chemical constituents such as H and L condrites and basalts (Asphaug et al. 2002), which would show levels of catastrophically-originated accretion or shock-annealed asteroid mergers. If asteroids are close enough to mutually attract, and if the level of impact energy is low enough, the asteroids will merge together forming a monolithic body.

Fragmented and rubble-pile asteroids are bodies which have been subjected to a catastrophic event and have coalesced in a certain amount of time, back into an asteroid form with varying degrees of internal macroporosity (Asphaug et al. 2002).

When an asteroid is impacted by a projectile such as an asteroid fragment, the result of the collision will depend on several factors; the physical properties of target and projectile, the impact velocity, local gravitational effects and the impact energy associated with the impact. If the impact energy is large enough to catastrophically disrupt the asteroid, the fragments will either obtain enough energy to overcome the action of the largest remnant fragment's gravitational field strength, and therefore disperse into the local environment, or the disrupted fragments will become gravitationally attracted to the largest remnant asteroid fragment and therefore accrete back onto the 'parent' fragment.

The level of damage to the parent body will dictate the nature of the rubble-pile, such as causing the larger or smaller fragments to accrete, or whether the largest remnant mass is considerably larger than the family fragments etc.

A fragmented asteroid seen after the event will not have accreted the material back into a monolithic sense, but could be in the process of merging the fragments after the collision. Rubble-piles are further along the accretion evolutionary stages than fragmented asteroids and therefore have coalesced into a singular body.

Work from Chapman et al. (1975) and then Tholen (1984) has allowed for the material characteristics of asteroids to be classified into specific groups, depending on spectra observed from asteroid observations. Asteroids are put into groups denoted by a letter, the main groups are classified as C-type for dark carbonaceous, S-type for silicaceous or stoney and X-type for varying levels of surface albedo originating from metallic asteroids.

As previously stated, the asteroid belts and regions are not only filled with prehistoric signatures of the accretion processes during the solar system's very early history, but are regions which undergo constant evolution.

One of the main factors in the evolutionary processes of the asteroid belt is the results of asteroid collisions. The sizes of asteroids range from very small diameters 5 – 10 m 1991 BA (NASA JPL 1991) to the third largest 107 – 113 km Vesta, (Russell et al. 2012) and when considered that such sizes of asteroids are constrained in orbit by influences of the Sun and Jupiter, the cross sectional flux would mean that asteroid-asteroid interactions are very common with respect to time-frames and location.

Asteroids are constantly weathered from dust and small grains present in the main belt, but if they are impacted by an increasing size of projectile, the outcomes could range from very minor to massively catastrophic.

When considering small impactors or low energy impacts, the evolutionary process is constrained to the actual asteroid rather than the asteroid environment as a whole; although impact ejecta will increase the level of potential impactors in the vicinity of the original impacted asteroid. The ejecta could then always impact other asteroids and possibly other planets (Lauretta et al. 2015)

However when the projectile increases in diameter or impact velocity, the characteristics of the impact increases in severity, and so, the nature of the impact outcome will have a greater impact on the local environment of the asteroid. These highly energetic impacts feed the continual evolution of the main belt and help to produce asteroid families.

1.4   Asteroid Families and Detection

When asteroids are catastrophically disrupted, as previously stated, the outcomes are dependent on the impact characteristics. If the impact energy was sufficient enough to catastrophically disrupt the parent asteroid and prevent re-accumulation, but not enough to disperse the daughter fragments too far, then the situation is known as asteroid family production (Hirayama 1918).

Asteroid families are known throughout the main belt; such as Eos, Koronis (Hirayama 1918) and Hygeia families (discovered by Gasparis in 1849, Leuschner 1922), and are characterised from the asteroid family fragment properties originating from the parent body, meaning that all of the fragments will share the same taxonomic class and will display very similar positional characteristics (Hirayama 1918).

Since the original work of Hirayama, detection methods have progressed to hierarchical clustering method, Zappalá et al. (1995). Used extensively in data analysis, the hierarchical clustering method produces dendograms though agglomerated algorithmic data. The distance data concerning a possible asteroid family is measured and the two closest family members are grouped together. Using a predefined or relative distance, the agglomerated pair is measured in distance with respect to the gravity well escape velocity of the main family body to the next closest suspected family member until there are no more asteroid pairs within the set distance.
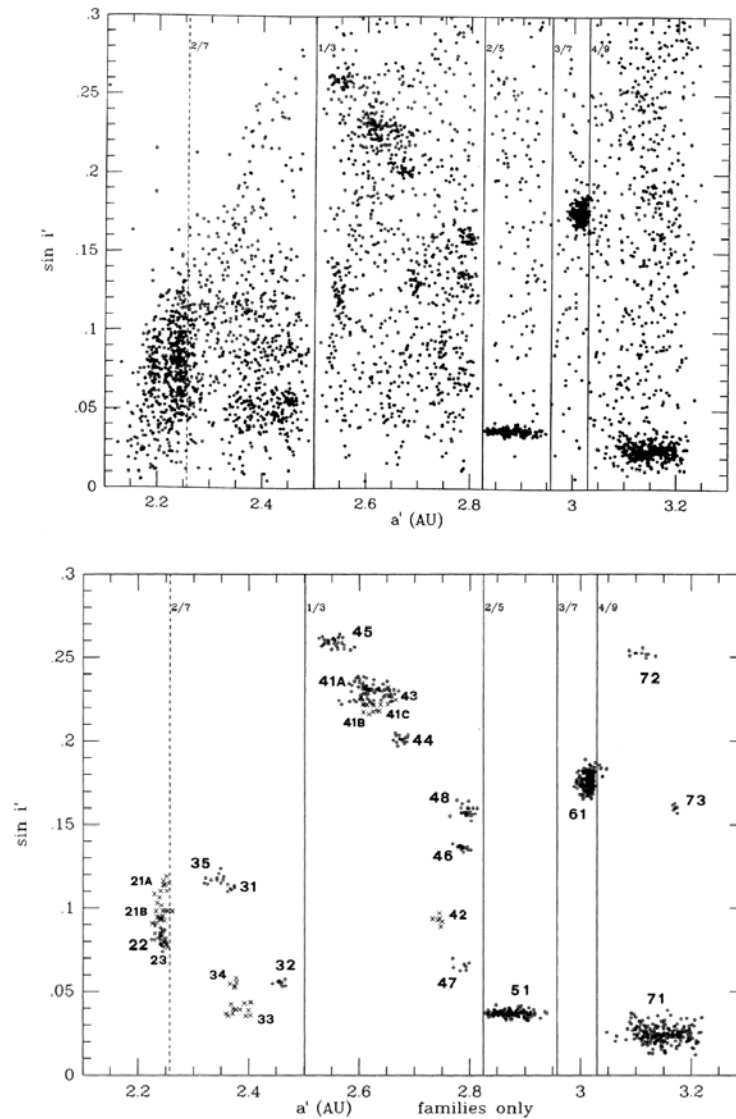
Figure 1.2: Two diagrams taken from Zappalá et al. (1995) which shows raw data and then the results from the Hierarchical Clustering Method. The axes show sine angle of inclination against accentricity with the vertical axis markers showing the rotational resonance ratios.

Therefore, using the hierarchical clustering method (HCM), asteroid detection is able to reduce background asteroids and possible interlopers from asteroid families, helping the family members to stand out clearly in dendograms as shown in Figure 1.2. As more asteroid orbits are measured, these methods can be applied to find ever smaller members of the families (Leliwa-Kopystynski 2009).

Wavelet Analysis Method (WAM) is another preferred tool for asteroid family detection (Bendjoya 1993) and (Zappalla et al. 1995). Asteroids are modelled in N-dimensional space at varying scales and are superimposed on a grid. Each node of

the grid has a wavelet coefficient, computed with respect to a zero weighted wavelet function. The wavelet function is dependent on the level of density of points in each node, therefore, the higher the value calculated for the coefficient more dense the population in that particular node. As the coefficient tends towards lower values, the density of the node shows a uniform distribution of the data points in the node.

This method does require the use of pseudorandom distributions to act as 'calibration distributions' but this in turn allows for the calculation of level of detection with respect to significance of chance Bendjoya and Zappalá (2002).

Another evolutionary process present in the main belt which is linked to asteroid families as well as singular bodies is rotation; both asteroid axial spin and orbital motion. Work into the Yarkovsky-O'Keefe-Radzievskii-Paddack or YORP effect has shown that photonic momentum has a great level of influence on asteroid rotation with consequences on asteroid families and their orbits Lowry et al. (2007), Taylor et al. (2007) and Kryszczyńsky (2013).

As the photons of light strike the Sun facing side of the asteroid, the opposite side emits photons from the dark side of the asteroid into the solar system and in doing so, creates a momentum related moment of inertia. The change of photonic momentum results in causing the asteroid to change its prograde or retrograde motion until the rotating asteroid is 'locked' into a spin-axis. Once the asteroid is locked in the spin-axis position, the gravitational effects from the environment can cause asteroids to drift into gravitational resonances and once in resonance, gravitational effects from planets such as Jupiter or Saturn can perturb the orbit of the asteroid which leads onto the Yarkovsky effect and could result in asteroid ejection from the main belt, Farinella et al. 1997, Chelsey et al (2003) and Nugent et al. (2012).

Also linked with the changes in orbital motion of the asteroids through Yarkovsky driven by YORP, and depending on the locality of the asteroid and the neighbouring asteroids, asteroid – asteroid interactions can occur thereby resulting in further collisions (Vokrouhlicky et. al. 2006, Strom et. al. 2015).

The consequences of these ejections do have an effect on the main belt by reason of removing asteroid material from the main belt. It could be hypothesised that

asteroid-asteroid impacts would decrease if the space in-between the asteroids were to clear through Yarkovsky ejections, but would massively increase the element of risk to the Earth and other planets.

1.5   Summary

The collection of knowledge on the solar system from ancient Greek times to present day modern techniques, still shows that the Solar System is a system which continually undergoes evolution. The dynamic nature of the Solar System still begs questions, some of which need to be answered as a matter of urgency such as the risks originating from asteroids in near earth orbits colliding with earth. The consequent chapters of this work provides an attempt to answer two questions regarding asteroid and planetary impacts which could impact our current understanding on some of the processes of evolution in the Solar System today.

Chapter II: Questions to be addressed

2.1   Catastrophic Disruption

As shown in the previous Chapter, the remnants of formation of the solar system from incomplete accretion processes are a system still very much undergoing change and evolution.   There are many reasons to increase the level of work in catastrophic disruption research, with one end of the regime being that of scientific curiosity, and the other considerations such as the need to protect life on Earth with threat analysis of the risk from asteroids being ejected from the main belt and closer regions. Therefore, this Chapter details some of the research conducted into both catastrophic disruption and more generally, impact cratering. The following works considered, cover a wide range of investigation, but the interested reader is encouraged to research further into the two areas of research. To be able to include all work covered on catastrophic disruption and impact cratering, is beyond the scope of this thesis. Interested readers are encouraged towards following works involving catastrophic disruption as a good starting point to understand current activity in the field: Jutzi 2015 (incorporating friction and shear strength into modelling), Michel et al. 2015 (when rubble piles reassemble after an impact which bits go where?), Durda et al. 2015 (fragment shape after disruption), Hirabayashi and Scheeres 2015 (how rapidly rotating bodies fail),   Ballouz et al. 2014 (rotation rate dependence of failure of aggregates), Morris et al. 2013 (the large crater on asteroid Steins or is Steins really a fragment from a larger disrupted body?), and van der Helm and Jeffers 2012 (how comets evolve under impacts). Whilst for impact cratering the range of current studies is indicated by, for example, Kaur et al. 2015 (the nature of dark halo craters in Mare Nectaris), Schedl 2015 (searching for impact ejecta), Neish et al. 2015 (spectral properties of craters on Titan), Weihs et al. 2015 (reporting the presence of polygonal craters on Mercury), Abed et al. 2015 (is a structure in Jordan really an impact crater?), Burr and Howard 2015 (impact craters as geomorphological structures), Hossain and Kruhl 2015 (rock fragmentation around impact craters), Zellner and Delano 2015 (ages of lunar impact glasses), Siegler et al. 2015 (cometary impacts and lunar polar ices), Fedo et al. 2015 (impact generated grains on the Martian surface), and Bart et 2014(who has revived the discussion of measuring lunar regolith depth via study of small, shallow impact craters). As can be seen from such a list in just the last year or

two, there are many current activities in the field. This chapter continues with a focus a discussion of catastrophic disruption and impact cratering. The Chapter then finishes with a general discussion shockwaves in hypervelocity impacts, which helps the reader understand some of the phenomena to be discussed later in the thesis.

Catastrophic disruption is the collisional break-up of bodies, having been impacted with a variety of impactors ranging in diameter and type. The target bodies can htemsleves have a range of properties, ranging from monolithic, (Jutzi et al. 2010), to highly porous bodies, (Giblin et al. 2004), from CO_2 ices, (Burchell et al. 1997) to basalt (Durda et al. 2007) For further reading on the examples of catastrophic experimental set-ups, the reader is referred to Holsapple et al. (2002), a chapter on laboratory experiments and scaling laws in the Univ. of Arizona book Asteroids III.

When a body is impacted, the impact characteristics play an important governing factor on the overall outcome of the interaction. If the body is impacted very weakly (i.e. with relatively little energy) or the impacted body is very large in comparison to the impactor, the outcome will show a crater formed at the surface of the body at the point of impact. This introduces the concept of impact energy density (the energy of the impactor divided by the mass of the target) as being important in determining the outomce of an impact.

If the result of the impact is a crater, then the dimensions of the crater are affected by the collisional mechanisms of the impact, with crater depths and diameters increasing in the host body, as the impact parameters such as velocity or impactor diameter increase. . As stated however, when considering disruption, we need to consider the whole target body and this is achieved through the impact energy density, or Q value.

$$Q = \frac{m_p v_p^2}{2\, M_T} \tag{2.1}$$

Given in two common units, J kg^{-1} or erg g^{-1}, Q is an energy density function associated with the parameters of an impact. Equation 2.1 details the impact energy density or Q as the projectile's kinetic energy divided by the mass of the target, with m_P in kg being the mass of the projectile, v_p in kms^{-1} being the impact velocity of the projectile and M_T in kg is the mass of the target being impacted. Strictly speaking, the

denominator should be the total mass of the combined system, but the mass of the impactor is usually considered negligible compared to the mass of the target, resulting in the expression for Q we see in eqn. 2.1.

This Q parameter is used extensively throughout the field of catastrophic disruption research, although a new approach to the form of Q in terms of reduced mass was proposed by Stewart and Leinhardt (2009) for planetesimal formation considerations. Their adaptation of the energy density equation was to allow for the level of momentum transfer between the target body being impact, and the projectile being comparable in size to the target.

Using equation 2.1, Q helps to characterise the impact outcomes and allows for comparison of certain impact characteristics with respect to an impact outcome. So, as a projectile mass or impact velocity increases, and the collision is with a body constant in mass, the increasing severity of the impact is shown through the level of damage and the subsequent crater dimensions as showing in Figure 2.1.
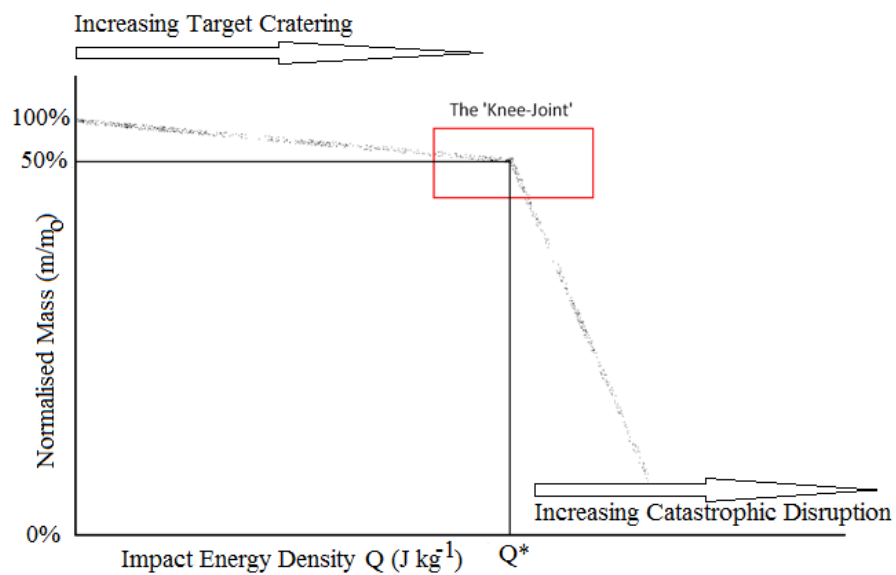
Figure 2.1: This Figure shows a simplistic view of the normalised largest remnant mass data obtained in catastrophic disruption.

The cratering regime of hypervelocity impacts onto targets increases from zero energy density Q, towards a point where 50% of the remaining mass from the target body is intact in a single fragment after the impact. At very low values of Q, the craters produced will be slight indentations and will morphologically evolve in size and shape

with increasing spallation as the cratering regime tends towards the 50% remnant mass energy. At this point, the level of damage to the target body is said to be at the upper cratering limit and simultaneously lowest limit for the catastrophic disruption regime. At this point in remnant mass and impact energy, the Q value is known as Q* and is used as a defining reference for all impacts.

Using Q* allows for quantitative definitions of particular collisional system outcomes. By defining the Q* value of a certain system, such as main belt asteroid collisional evolution, the numerical value obtained in the work or observations, could lead to an enhancement of current theoretical models or possibly new avenues of research.

Depending on the physical characteristics of the body, when at the lower region (nearest the Q* position) of the catastrophic disruption regime, the largest remnant mass decreases in mass percentage as the trend goes from Q* to highly catastrophic disruption. The level of spallation and ejecta increases in quantity but decreases in particulate size as increasing energy pulverises the target body. The fragments also have increasing energy and therefore disperse with higher speeds.

Theoretically the transition from the cratering regime to the catastrophic regime is smoothly linear with the amount of mass being lost from the parent impacted body. On the graph shown in Figure 2.1, the regime cross-over is detailed in the red box labelled as the "knee joint".

Within the framework of catastrophic disruption the regimes of cratering and disruption are very evident when considering small level impacts in the form of laboratory experiments. As the size increases for the target body, so does the influence of gravitational forces. When considering the outcomes and governing attributes in the laboratory, the strength of the target is the overriding factor with respect to the experimental outcomes. However, when considering the diameters associated with bodies such as asteroids, the strength of the asteroid does influence the impact in the initial stages, although it is relatively small in comparison to the gravitational effects attributed to bodies tens of km in size.

There are thus two target size regimes important in catastrophic disruption e.g. small sizes which are strength dominated and large sizes which are gravity dominated. At the larger sizes, a disrupted body is one which has not only broken up but which also

does not reassemble under its self-gravity. Durda et al. (1998) formulated a plot which showed the effect of the strength to gravity crossover from various models (Figure 2.2).

It was found that as target radius increased from laboratory scale impacts (mm < scale < m) to approximately $x10^4$ cm, the effect of material strength weakens due to the size of the body increasing and the overall strength of the body decreasing with respect to impact energy density.
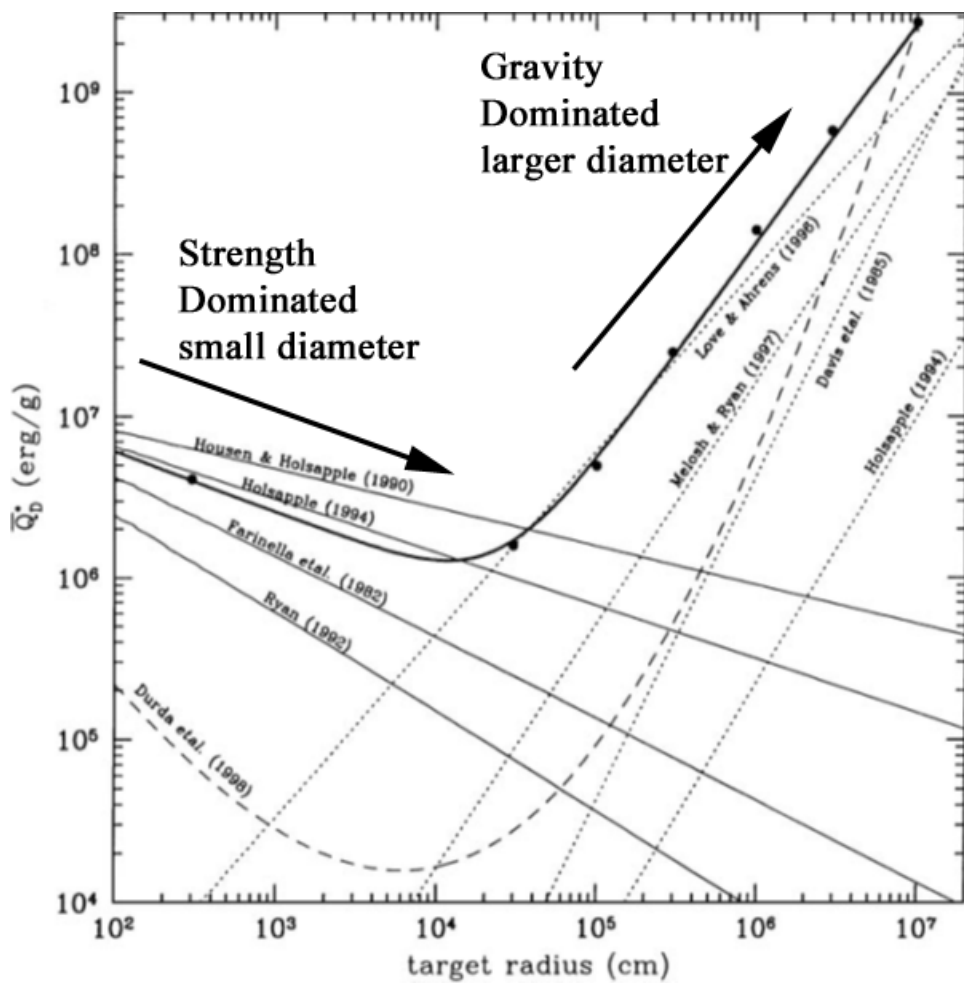
Figure 2.2: The collected data from experimentation and modelling of catastrophic disruption spanning laboratory and computer based investigations from various researchers, complied by Durda et al. (1998).

The gravitational regime begins to influence the impact processes from the saddle point in the data approximately at the $x10^4$ cm size and has a great level of influence as the target body gets much larger ($x10^7$ cm in Figure 2.2) in radius.

For this reason, it is desirable when taking into account the whole range of catastrophic disruption impacts from laboratory to astronomical scales, to define Q* in terms which associate themselves with their respective frames of reference; Q_S^* for Q* associated with shattering a body at laboratory scales and Q_D^* for dispersion of fragments given enough energy through the impact to overcome the self-gravitation of the body at astronomical scales.

2.1.1   Current work into catastrophic disruption events

Here we consider in some more detail, some of the current work relating to catastrophic disruptions.

One effect of disruption is to produce fragments, which may go on to impact other bodies. A proposal linking two separate bodies; the Chelyabinsk meteoroid and the Near Earth Object (NEO) asteroid 86039 1999 NC43 was made by Borovicka et. al. (Borovicka, et al. 2013). However, this was found to be incorrect through computational modelling by Reddy et. al. (Reddy et al. 2015). It was concluded that results of spectral surveys of Chelyabinsk fragments and asteroid 1999 NC43 demonstrated they were not the same and that any close link between the two was very unlikely.

Since many asteroids are considered porous, especially the smaller ones, it is necessary to consider how this will influence breakup. A theoretical modelling approach for catastrophic disruption of astronomically smaller porous bodies ($\leq$ 1000 km) was concluded by Jutzi (Jutzi 2015). Using a newly adapted Smooth Hydrodynamics Particles (SPH) model to include friction, they found that collision break-up thresholds are significantly lower when friction was taken into consideration as opposed to cases without friction.

On a related theme regarding porosity, Nakamura et al. performed a series of low velocity impacts into gypsum targets to investigate the size dependence of the

disruption threshold Q* in porous targets (Nakamura et al. 2015). They found that the gypsum targets had a weaker volume dependence on static tensile strength than that of rock samples. The disruption threshold was shown to be dependent upon impact velocity.

Meanwhile, experimental hypervelocity impacts into porous sintered glass targets (80%, 87% and 94% levels of porosity) found that maximum diameter, entrance-hole diameter and crater depth increased with characteristic length. It was concluded from this that the maximum diameter depends on projectile deformation or disruption. Also it was noted that Q* did not have any dependence upon porosity (Okamoto et al. 2015)

Further studies into porous impacts have been made by Flynn et al. who impacted targets of terrestrial pumice at hypervelocity speeds of 3 to 5 km s^{-1} (Flynn et al. 2015). The craters produced were steep-walled cylindrical in shape and not the common simple forms found in rock impacts. The results indicated that the porosity of the targets attenuated the impact shock waves thereby increase the survivability of the targets with respect to catastrophic disruption. A further experiment into multiple impacts (impact sites close to each other on the same target) reaffirmed the notion that the shock wave energy is not confined to the region of impact but dispersed throughout the target.

However with the wealth of experimental and computational work into catastrophic disruption (the reader is referred to read Asteroid Impacts: Laboratory Experiments and Scaling Laws (Holsapple et al. 2002) and the references therein), one major aspect has remained unanswered; what if the target is rotating? All previous work has had the target stationary in the first instance and when considering the fact that most observed asteroids in the main belt are rotating with varying levels of rotational period and the recent work on the YORP (French et al. 2015 and Sevecek et al. 2015) and Yarkovsky effects (Vokrouhlicky et al. 2015 and Cuk et al. 2015), investigation into the effects of rotation are very much needed.

Knowing the effects that rotation has on catastrophic disruption will help to further the knowledge in the field. The ability to refine theoretical and computational models on catastrophic disruption is of great importance and therefore being able to make models as close to observations is key. The possibility of answering further questions is also important. Should Q* lower with rotational rate? If Q* lowers, does this mean

it is easier to catastrophically disrupt asteroids in the main belt? If it is easier to disrupt asteroids, will this have any knock-on effect on the collisional evolution of the main belt? Can the evolutionary outlook for 'weaker', or easier to disrupt, bodies tell us anything about the early Solar System formation processes?

2.2   Variable Temperature Impacts

Impact cratering is one of the most extensively researched topics in solar system studies due to the abundance of craters which can be examined; such examples include (Martellato et al. 2007) who analysed the craters on the Mercurian surface and the analysis of Venusian craters (Cochrane et al. 2006).

Table 2.1 outlines some of the research associated with craters and cratering experiments and includes a mixture of lab experiments and modelling.

Table 2.1: A series of citations on various aspects of cratering research. A typical example work is given for each topic.

Work on Cratering	Citation
Flux	Kirchoff et al. (2013)
Distribution	Herrick and Phillips (1994)
Size	Fendyke et al. (2013)
Impact Characteristics	Neukum et al. (2001)
Rock	Marchi et al. (2011)
Water	Dypvik et al. (2003)
Ice	Dypvik et al. (2003)
Porosity	Poelchau et al. (2012)
Morphological Transition	Schon et al. (2011)
Shock waves	Melosh (1989)
Influence of Environmental Factors	Aittola et al. (2007)

As is shown in Table 2.1, the level of investigation is extensive and although one citation in each case has been included in the Table, the amount of work contributing to each area of cratering research is much greater than can be included here.

Taking the topics one at a time shows:

The investigation of 36 randomised lunar impact craters by Kirchoff et al. (2013) showed that the impact flux in the Moon's history spiked with the onset of the late heavy bombardment approximately 3Ga ago and then again at ~1.8Ga ago suggesting a varying impact lunar flux with lulls and spikes in the 3-1Ga age period.

Distribution and crater sizes are two very extensively investigated properties in impact crater research. Herrick and Phillips (1994) worked on the distribution of Venusian craters, and found that the distribution of craters on the Venusian surface was randomly impacted. However they included the idea that the geologically active surface of Venus could affect the distribution of craters on the surface.

With global crater investigations, the main crater characteristics which are studied are distribution and the actual crater dimensions. One problem is knowing if laboratory experimental results can be reproduced by successful modelling and then used at different size scales. To investigate this, impact validation programmes of laboratory scale impacts have been carried out. For example, Pierazzo et al. (2008) considered strengthless and metal targets (simulations were good to 10 – 20% of the experimental crater dimensions. Whilst Fendyke et al. (2013) used iSALE2 hydrocode simulations to replicate cratering in a brittle material (ice) and found that the hydrocode simulations were successful in replicating the individual crater depths and diameters to within 5% and 6% respectively.

Observing craters is also a good way to study a planet. For example, Neukum et al. (2001) concluded a comprehensive analysis of the Mercurian surface with the percentage of recorded surface images available at that time. The study looked at many cratering related characteristics such as impact flux, crater basins, tectonism, geological effects, Mercury/Moon comparisons and stratigraphy and chronology. The authors outlined the existence of an increased level of impact history common to the epoch associated with the LHB. This work also included open questions still (at the time of print) to be answered and Neukum et al. stated 34 considerations to be addressed by the two missions Messenger and Bepi-Colombo.

Clealry, if the crater histories of the inner rocky terrestrial planets and moons, are found, then research into factors which affect the craters which are studied is very important.

Target characteristics play one of the most important factors for cratering histories and investigations. Environmental factors can help to determine the size and distribution, such as varying density and strength with respect to layered target depth (Marchi et al. 2011), and the presence of tectonic features which affect the overall shape of crater rims (Aittola et al. 2007).

Another target characteristic is one of continual environmental renewal of an impacted surface. Oceanic impacts are accounted for a very small minority of the Earth's cratering record. But as pointed out by Dypvik et al. (2003), the Earth's surface is 70% water where, results from analysis of impact distribution, many more impacts would have resulted in oceanic collisions than those preserved on land masses. However, due to the nature of the Earth's oceans, it is very difficult to examine the oceanic impacts and to draw any conclusions from them. Dypvik et al. (2003) outline various issues raised in their review chapter entitled Marine Impacts – Future Research.

Associated with impacts into water, and one considered to be very significant in the study of the solar system, are impacts into ice. Kraus et al. (2011) performed a series of hydrocode experiments investigating impacts into ice. They found the target temperature affected the level of vaporisation and melt produced due to the level of entropy. Kraus et al. (2011) noted that the shock Hugoniot for vertical impacts into non-porous water ice, display consistencies with phase changes similar for water ice Hugoniots. Also the impact Hugoniots showed a much steeper exponent shock delay than is found for all other non-porous materials. It was concluded that the complexity of H_2O arises from its exceptional polymorphism.

As stated already, one characteristic which is commonly neglected through an 'idealisation' of a system is porosity. Pore space and porosity are major factors in cratering, morphology and efficiency. Poelchau et al. (2012) conducted an impact project to investigate the effects of water saturation on cratering in sandstone. Their work on porosity found that when considered as a singular target characteristic, porosity greatly reduces crater size and volume as opposed to non-porous materials. But, saturating pore space counteracts this trend and returns the saturated porous target

back to non-porous target strength and cratering mechanisms. Earlier work on this topic was also carried out by Baldwin et al.,(2007).

When craters are formed, they display different properties in shape and size depending upon the nature of the impact parameters and location. Melosh (1989) covered the differences of craters in Chapter 2 in his book: Impact Cratering A Geological Process. The work examines the outcomes from different aspects such as impact variables and the materials in which the craters are formed. Melosh covers each type of crater, from micro craters from very small collisions, to multi ring basins on Mercury. However, one concept which was not covered during this section on craters was the aspect of environmental influence on crater formation. Aittola et al. (2007) identified strange Polygonal Impact Craters (PICs) on Venus. These craters show the common circular perimeter associated with normal craters but areas of the crater rims show straight line segments in the circular perimeter. The conclusion for this was the influence of tectonic lines and geological valleys producing constraints onto the crater rims.

Finally Melosh (1989) covered extensively the main process inherent in cratering processed; shock wave analysis. He used the conservative Hugoniot equations of mass, energy and pressure, to derive the Planar Impact Approximation (PIA). The PIA is used to find shock wave properties such as particle velocities, shock wave speed and shock wave peak pressure with respect to three material constants; density, C which is normally associated to the bulk speed characteristic of the material and the Grüneisen parameter S. The work on Hugoniot shocks helps to understand the main cratering mechanisms at work with cratering. However, while the sheer wealth of work into cratering has only been summarised in this chapter, one major issue is still missing; the effect of variable target temperature on cratering mechanisms and morphology.

2.2.1 Current work in cratering physics

Although the surfaces of the inner terrestrial planets have been mapped extensively, it is still found that some of the geological features are unexplained. For example, Williams et al. looked into possibilities of some craters on Mars being made via an explosive excavation (Williams et al. 2015). With previous work concluding the nature of rimmed craters (see references therein for further details), Williams et al. concluded that smaller rimmed pits on the surface of Mars might have originated from

volatile release during the impact melt stage of the cratering process. Using data obtained from spatial correlations between coarse material correlated with warm material grains, it was found that specific small rimmed pits, helped to explain the explosive excavations of the pits.

Experiments into granular targets in order to investigate crater rays closely associated with crater rays seen on the surface of the Moon (craters Glushko and Kepler) were conducted by Kadono et al. This project combined both experimental and simulation data to ascertain whether ray-specific properties such as ray length and angle, could be associated with the target material. It was found that the overriding factor in the creation of the rays was due to inelastic collisions between the target particles (Kadono et al. 2015).

In order to investigate the effect of regolith in the cratering process, Burchell et al. 2015 conducted a series of SMART-1 simulation hypervelocity impact experiments into shallow lunar regolith. Impact angels were kept at 5 and 10° to the horizontal and the impact speed was approximately 2 kms^{-1}. The resulting impact craters were found to be 20 times the projectile size (rim to rim) and the craters displayed a flat-floor appearance due to subsurface rock (Burchell et al. 2015).

Of particular interest for the work in this thesis is the influence of target temperature on cratering. Throughout the whole solar system, temperatures vary on each of the planets. Mercury, displays a temperature range of 723K at the Sun baked surface to 103K in the deepest shadows. The Earth, with an average temperature of 291K, also has a range globally of 146 K and the Martian surface has been found to average 218K and a range of 73 K. Due to a runaway greenhouse effect, the Venusian surface has been recorded to have an average temperature of 735K (Williams 2005) thereby making it the hottest planet in the solar system. With each of the four inner terrestrial planets showing temperature ranges (even the Venusian temperature does vary slightly), the question to be addressed within this respect is: 'does target temperature have any effect on cratering'?

Will the level of cratering efficiency differ with internal temperature? Will the level of internal energy in a rock target held at a temperature comparable to Venus' temperature make it easier to crater than a target held at almost liquid nitrogen temperature or the shadow sections of Mercury? Will rock targets show greater levels

of plasticity at higher temperature and greater levels of brittle nature at lower temperatures? What will the crater spallation zones look like as craters are made through a range of temperatures?

2.3 Shock Waves

Since the advent of multi-stage light gas guns, it has been possible for researchers to study the effects of hypervelocity impacts through various situations such as porous, water ice and metallic impacts. One such effect which is attributed to a hypervelocity impact is the material shock wave associated with a hypervelocity impact. Shock wave analysis is an important area of research by itself because of the resultant consequences left after a shockwave progresses through a material. These leftover shockwave signatures are used extensively in the study of impacts into geological systems (French and Koeberl 2010).

The concept of a shock wave passing through a material was first investigated by William Rankine (Rankine 1870) and Pierre Hugoniot (Hugoniot 1887). The conditions of the shock wave are described by the Rankine-Hugoniot equations of state for the shock wave, and explain a mathematical jump function in terms of conservation laws for mass, momentum and energy with respect to the material just before the actual shock wave and just after it.

The Rankine-Hugoniot equations are:

$$\rho_1 u_s = \rho_2 (u_s - u_2) \qquad \text{Equation (2.2)}$$

Equation (2.2) details the conservation of mass where ρ_1 and ρ_2 are the mass densities of the material from behind and in front of the shock wave in kg m^{-3}, u_s and u_2 are the particle velocities of the shock wave and particles in the shock respectively in ms^{-1}.

$$p_2 - p_1 = \rho_2 u_2 (u_s - u_2) = \rho_1 u_s u_2 \qquad \text{Equation (2.3)}$$

The conservation of momentum associated with the shock wave is given by equation (2.3). The variables of p_1 and p_2 are the pressures before and after the shock wave in Pa with the other terms as detailed previously.

$$p_2 u_2 = \rho_1 u_s \left(\frac{1}{2} u_2^2 + E_2 - E_1 \right) \qquad \text{Equation (2.4)}$$

The final equation (2.4) is conservation of energy. All terms are covered by equations (2.2 and 2.3) except for E_2 and E_1 which are the internal energies per unit mass in the shock wave regions in J kg^{-1}.

Upon impact a projectile's kinetic energy is transformed almost instantaneously into a high-pressure shockwave which originates from the point of impact and moves out into the material in (ideal case) hemispherical shells of decreasing shock pressure (Kieffer and Simonds 1980, Melosh 1989 and French and Koeberl 2010). When considering waves which propagate and lose intensity, one thinks of a $\frac{1}{r^2}$ situation such as light traversing space. In the case of material shockwaves, the intensity drop of the shockwave is material dependant and ranges from $\frac{1}{r^{1.5}}$ to $\frac{1}{r^3}$ (Melosh 1989). When dealing with planetary impacts, the distances covered are much greater than in the laboratory and the drop in the shockwave intensity is such that at distances from the crater rim, the shockwave intensity drops to an approximate value of 1 GPa as the shockwave changes into elastic seismic waves.

As shockwaves originate from the initial point of impact outwards to the boundary of the surface, the material is set into an upwards and outwards motion thereby excavating a crater. However, the extent of shock related metamorphism and shockwave pressure varies from the point of initial impact to the edge of the excavated crater. Table 2.2 presents the shockwave related metamorphism of rocky impacts undergoing hypervelocity impacts. Each effect is related to the associated shock pressure initiating the metamorphosis.

Table 2.2: Data collected by French 1998 from Stoffler 1984, Melosh 1989 and Stoffler and Langenhorst 1994 detailing the effects of shock metamorphism with respect to shock pressure.

Approximate Shock Pressure (GPa)	Estimated Postshock Temperature (°C)*	Effects
2–6	<100	Rock fracturing; breccia formation
		Shatter cones
5–7	100	Mineral fracturing: (0001) and {10$\bar{1}$1} in quartz
8–10	100	Basal Brazil twins (0001)
10 ———	100*	———
		Quartz with PDFs {10$\bar{1}$3}
12–15	150	Quartz → stishovite
13	150	Graphite → cubic diamond
20 ———	170*	———
		Quartz with PDFs {10$\bar{1}$2}, etc.
		Quartz, feldspar with reduced refractive indexes, lowered birefringence
>30	275	Quartz → coesite
35 ———	300	———
		Diaplectic quartz, feldspar glasses
45	900	Normal (melted) feldspar glass (vesiculated)
60	>1500	Rock glasses, crystallized melt rocks (quenched from liquids)
80–100	>2500	Rock glasses (condensed from vapor)

* For dense nonporous rocks. For porous rocks (e.g., sandstones), postshock temperatures = 700°C (P = 10 GPa) and 1560°C (P = 20 GPa). Data from *Stöffler* (1984), Table 3; *Melosh* (1989), Table 3.2; *Stöffler and Langenhorst* (1994), Table 8, p. 175.

Using the data from Table 2.2, the peak shock pressure at the initial impact region of crater excavation which is considered the point at which most kinetic energy is translated into the shockwave, is at least 100 GPa and can sometimes exceed 100 GPa. The associated temperatures at this pressure is greater than 2500 ºC which in turn results in vaporisation and melting of the rock material and the impactor. As the shockwave propagates outwards from the initial region, the shock pressure lowers which results in different effects on the rocks. Rock glasses and crystallised melt are quenched at pressures of 60 GPa. As the shockwave continues to pass through the material and lose more intensity, shock-related melt effects change into rock metamorphosis with diaplectic glass phases, high-pressure mineral metamorphosis

and planar deformation features (PDFs) occurring at 30-45 GPa, 12-30 GPa and 10-25 GPa respectively. Finally the associated shockwave pressures at lower values such as 2-5 GPa, shatter cones and rock fracturing geological effects occur.

2.4 Gruneisen Parameter

The Gruneisen parameter is a material constant which describes the effect on a lattice's vibrational properties when volume, pressure or thermodynamics of the lattice is not constant. Named after Eduard Gruneisen, the parameter has both micro and macroscopic definitions (Gruneisen 1912). The microscopic definition is concerned with the vibrational modes of atoms in solids, whereas the macroscopic definitions are linked with the thermodynamic properties of the solid, but are considered very difficult to obtain experimentally (Vocadlo and Price 1993, Hofmeister and Mao 2002). Another factor which inhibits the determination of the parameter is the need to determine the phonon frequency dispersion (or dispersions of vibrational modes including superpositions of the lattice) in the Brillouin zone which is incredibly difficult to obtain without the use of a dynamical crystal lattice model or high-pressure inelastic neutron scattering through the lattice concerned.

Due to the nature of the parameter, there are several different examples of the Gruneisen parameter, but for the purposes of this work, the thermal Gruneisen parameter for both macroscopic and microscopic are as follows:

$$\gamma_{TH} = \frac{\alpha V K_T}{C_v} \qquad \text{(macroscopic parameter)}$$

$$\gamma_i(\boldsymbol{q}) = -\frac{\partial \ln \omega(\boldsymbol{q})_i}{\partial \ln V} \qquad \text{(microscopic parameter)}$$

For the macroscopic case, α is the thermal expansion of the lattice in K^{-1}, V is the volume in m^3, K_T is the isothermal bulk modulus in Pa and finally C_v is the lattice heat capacity at constant volume in $J\ K^{-1}$. The microscopic equation was determined by Gruneisen as the vibrational frequencies of the individual atoms in a solid varying with volume, where $\omega(\boldsymbol{q})_i$ is the frequency ith mode vibration of the wavevector function $(\boldsymbol{q})$ and V is the volume.

2.5   Summary

This chapter has attempted to define the science and works behind impact physics and associated experiments. Both experimental and computational approaches have been considered, but only a small amount has been included here due to the sheer volume of work in this area of astrophysics.

The topic considered in this section are in the same order as will be seen in this work, namely catastrophic disruption first and then variable temperature impacts afterwards.

Catastrophic disruption is a prevalent and important area of research in astrophysics but with one major question outstanding – what if the target is rotating? Here the question is asked in the light of the previous work discussed. Following on from this, was a small investigation into research covered in impact cratering experiments. Various impact situations were covered in the latter part of this chapter, but, once again another question was asked – what if the targets are impacted at different temperatures?

The final addition to this chapter, is a discussion on the processes which contributes to both catastrophic disruption and impact cratering; impact shock waves.

The aims of this thesis is to answer these two questions. The following sections of this work contain information on the experimental approaches as well as the apparatus used; both experimental and computational approaches are used in order to answer the two questions addressed in this chapter.

Chapter III: Experimental Methodology I: The Light Gas Gun

Trigger "And that's what I've done. Maintained it for 20 years. This old broom's had 17 new heads and 14 new handles in its time".

Sid "How the hell can it be the same bloody broom then?"

Trigger "There's the picture. What more proof do you need?"

An appropriate quote from BBC's Only Fools and Horses: Heroes and Villains (1996) regarding the view of the two-stage light gas gun at Kent University.
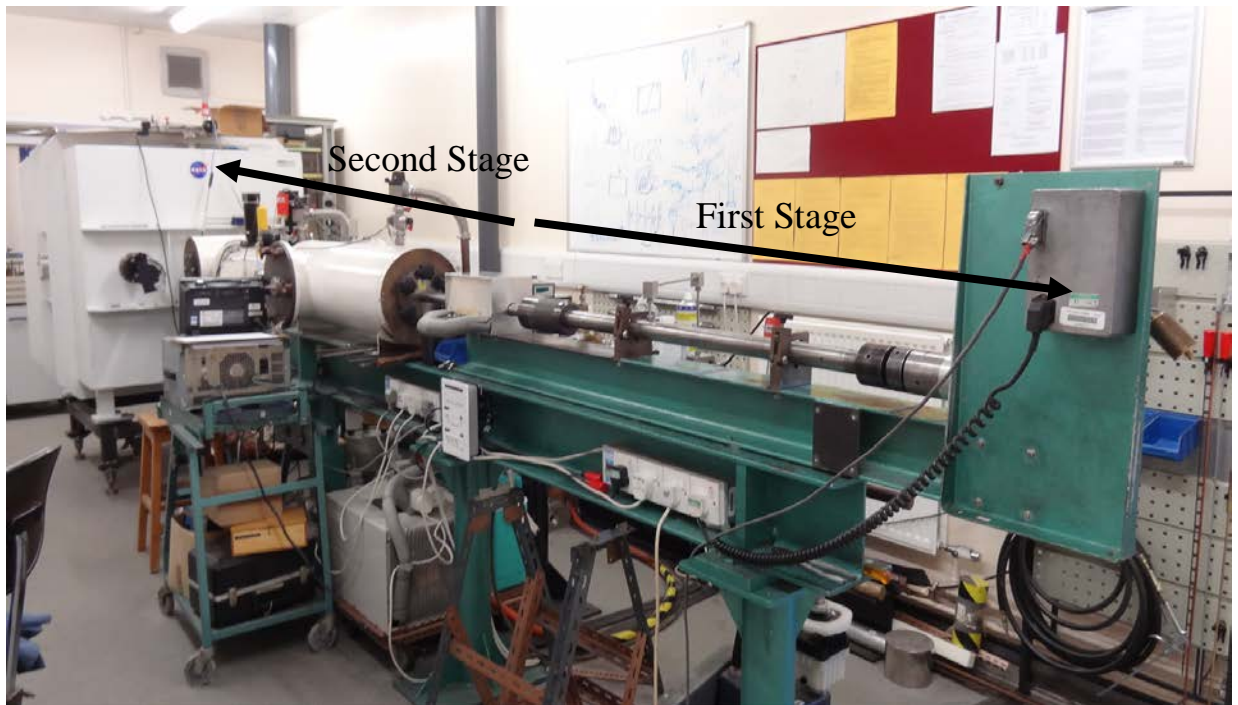
Figure 3.0: The two-stage light gas gun at Kent University with the two-stages marked with arrows. The central breech (section 3.4) divides the two stages of the light gas gun.

Introduction

The previous two Chapters reviewed the current understanding of material in Solar System sciences with respect to asteroids and planetary impacts. With this grounding

established, this Chapter will look to introduce the specialised laboratory equipment need to help answer the questions from Chapter 2.

The light gas gun is a specialised piece of ballistic laboratory equipment designed to propel impactors at hypervelocity (speeds considered hypervelocity above 2000 kms^{-1}). The use of hypervelocity gas guns is extensive throughout research of surface cratering and catastrophic disruption. Due to the nature of projectile speeds in space (commonly given as an average velocity of 5 kms^{-1}), the energy from a light gas expansion acting upon a light projectile is needed to recreate these velocities in the laboratory. The first light gas gun was able to achieve impact velocities approximately 7 kms^{-1} for projectiles 0.01 g in mass (Crozier and Hume 1957). Since then light gas guns are used for impact studies internationally with various configurations to include differing impact velocities ranging from ms^{-1} to kms^{-1} due to reduction of propellant accelerating gas or being a single stage light gas gun, whereas some light gas guns are multi-staged which uses more than one element of acceleration. Some light gas guns being used are able to elevate the launch tube in order to investigate impact angle where stationary light gas guns require angled investigations to be made through varying the impact location on targets. This Chapter details each section of the gun, in the direction of the projectile from trigger to target as well as the use of each part the two stage light gas gun at University of Kent.

The two-stage light gas gun at University of Kent comprises at least 20 sections, each fully removable and serviceable. The gun sections can therefore be replaced or upgraded when needed and the gun as a whole can be adapted per shot with requirements such as low and high temperatures or slow or fast impact velocities etc. The initial gun used at Kent University's hypervelocity impact laboratory, as detailed by Burchell et al., (1999), has since had some changes made, such as a new 1.8 m^3 target chamber and increased upper impact velocity.

3.0.1 The First Stage of the Light Gas Gun

The first stage (Figure 3.0) of the light gas gun encompasses the compression of a light gas as a result of the explosive energy of a pre-adapted shotgun cartridge driving a

piston. As the pressure increases and ruptures the burst disc (covered in Section 3.5) the gas delivers kinetic energy to the projectile through gaseous expansion. The underlying concept behind is stated in equation 3.1:

$$v_{ex} \propto \left(\sqrt{\langle m \rangle} \right)^{-1}$$ 3.1

where v_{ex} is the expansion velocity in kms^{-1} and m is the molecular mass of the gas used. The expansion velocity of the gas molecules is proportional to the inverse of the square-root of the gaseous molecular mass. Therefore the lighter the gas used, the faster the expansion velocity of the gas, which in turn relates to faster projectile velocity.

3.0.2 The Second Stage

Once the compressed light gas has achieved the required amount of pressure, the burst disc will rupture and the expansion of the gas will translate kinetic energy to the projectile.

Each section of the light gas gun, and its uses, is detailed as follows.

3.1 Firing Mechanism
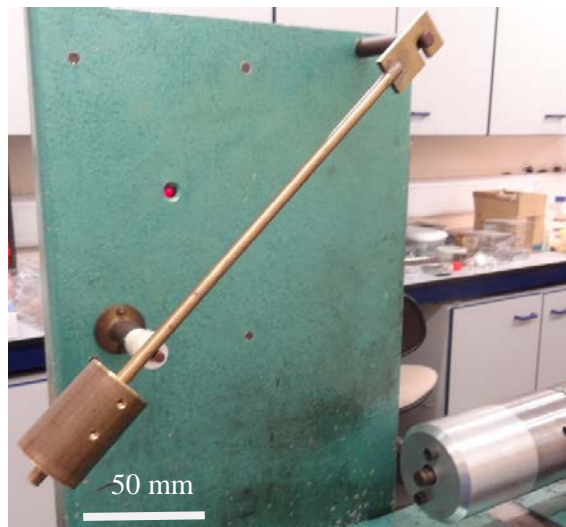
Figure 3.1: The pendulum, held in place by a remotely controlled electromagnetic trigger, falls through an angle of 50° to the striker rod. This in turn initiates the firing process.

The remotely controlled triggering mechanism (Figure 3.1) drops a pendulum mass of 656 g (pendulum mass and pivot rod) through an angle of 50° to the striker rod (Figure 3.2), causing it to strike the firing pin holder and then the primer of the cartridge.

Figure 3.2: The striker rod is placed into the striker rod guide and initiates the cartridge firing through the firing pin.

The mild steel striker rod is positioned in the striker rod guide at the trigger end of the striker rod support.

The firing pin assembly (Figure 3.3) houses the firing pin held by the firing pin holder which is 40.9 mm in length and 9.4 mm in width (along the main channel of the holder before the stopping brace). The pin measures 25.4 and 2.39 mm in length and width, respectively and the primer striking end has a radius of curvature of 1.19 mm.
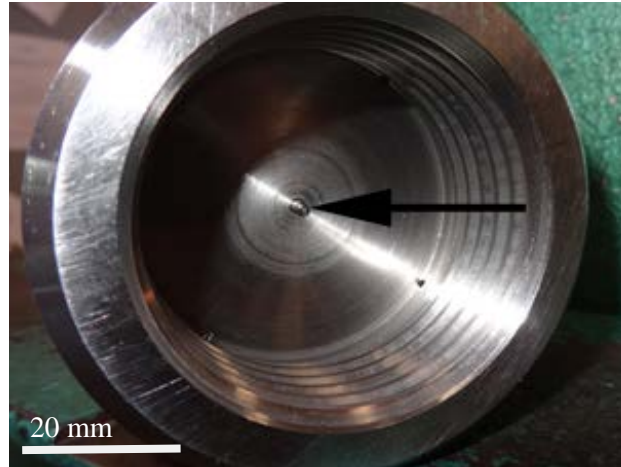
Fig: 3.3: The firing pin (shown arrowed) held by the firing pin holder and initiates the first stage of the light gas gun.

3.2 Powder Chamber Coupler

Figure 3.4: The powder chamber coupler connects the firing pin assembly with the cartridge used to initiate the firing sequence.

The powder chamber coupler (Figure 3.4) made from Chromoly steel, acts as a breech and housing section in the first stages of the gun's set-up. Adapted shotgun cartridges are inserted into the trigger end of the coupler which has an inner diameter of 20.45 mm, just before the firing pin. The cartridge needs to be in very close proximity to the firing

pin in order to ensure good contact and prevent misfires. The secondary purpose of this section of the gun is to attach the firing pin assembly, via the powder chamber coupler, to the pump tube, which houses the pressurised gas and piston.

All breeches and contact points are made air-tight by the use of 'o' rings and secured by the use of threaded components to prevent gas loss, gas introduction into evacuated areas or serious failure points due to pressures achieved in the gun during first or second stage initiation.

3.3 Pump Tube

Figure 3.5: The pump tube forms the first part of the two-stages in the two-stage light gas gun and contains the light gases for compression.

Figure 3.5 shows the steel-chromium alloy tube, which contains the gas used to determine the shot speed, and is fed from the gas regulation assembly via a gas port into the top of the tube. The length of the tube depends on the specific requirements needed for a particular shot and allows for variation of pistons and volumes of gas. The adaptability of the gun is essential because of the variability of shots required. The length used for the purposes of these projects was 700 mm (Figure 3.5). The internal diameter was measured as 12.7 mm which accommodates the nylon pistons with o-rings (Figure 3.6) used for the compression of the gas, a proper seal is formed with the o-rings thereby eliminating any compressed gas escape. The pistons are inserted at the trigger end (upstream) closest to the chamber coupler.

When the cartridge fires, the release of the chemical energy from the powder charge (Reloader 19 and 22 propellants were used for this project) accelerates the piston

downstream (in the direction of the target chamber) in the pump tube therefore compressing the gas housed in the tube to very high pressures, approximately 2 kBar. The compressed gas then starts the second stage of the gun's operation once the barrier (burst disc) between the two stages fails.
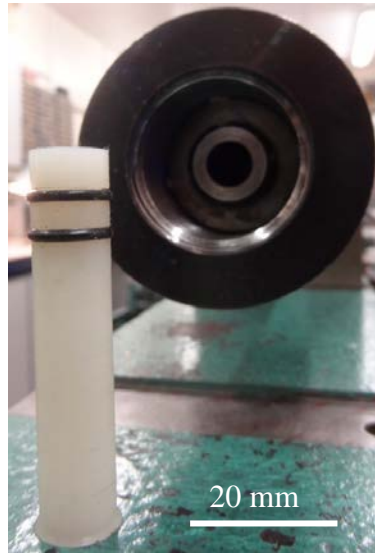
Figure 3.6: The nylon piston used to initiate the first stage of the light gas gun must be airtight to allow complete gas compression. The piston is inserted into the pump tube at the trigger end of the light gas gun.

3.4 Central Breech
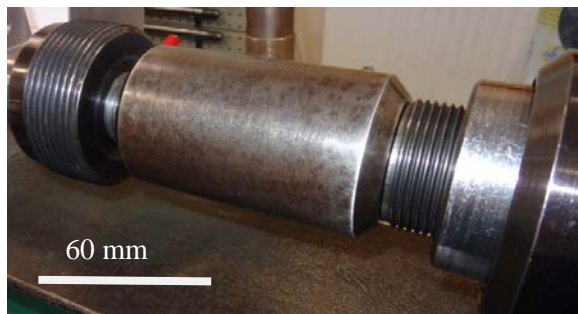
Figure 3.7: The central breech inner collar has two main uses; the first is to channel the highly compressed gas from the pump tube down to the entry of the launch tube and the second is to act as a failsafe section for gas back pressure and the propelled piston impact.

90 mm

Figure 3.8: The central breech outer collar is the main binding piece between the pump and launch tubes. The outer collar also serves to prevent damage, or injury, resulting from failure of the breech.

The central breech has one inner and one outer collar (Figures 3.7 and 3.8 respectively). The two collars are used to attach the first stage to the second stage of the light gas gun. The outer collar binds the pump tube to the launch tube (Figure 3.8), and has the central breech component fitted in the middle of both tubes. The central breech component acts to funnel the highly compressed gas from the pump tube to the diameter of the launch tube.

Another function of the inner and outer breech collars is that of safety. The inner collar helps to contain failures resulting from back pressures produced by the compressed gas interacting with the burst disc or piston impact. If the burst disc failed to break open, (possible manufacturing problems etc.) the compressed gas channelled from the pump tube would be confined into a very small volume, consisting of the internal volume of the inner breech collar minus the volume taken up by the piston inserting into the inner channel. Therefore should any failure occur, the inner central breech component would fail under the pressures generated and be contained inside the outer breech collar, preventing injury or damage to the surrounding area.

For efficient energy transfer from the piston to the gas, the piston is slowed considerably by compressing the gas. If this is misjudged or a premature failure of the burst disc

occurs, the central breech must stop the piston which may be travelling at approximately 1 kms^{-1}.

3.5 Launch Tube

Figure 3.9: The launch tube is a rifled tube used to house the sabot and marks the second stage of the light gas gun's two stages

Figure 3.10: Here is shown a picture of two burst discs used as a boundary in between the two stages of the light gas gun, right shows the burst disc pre-shot and left shows a burst disc post-shot.

The launch tube (Figure 3.9) measures 698.5 mm in length with an inner diameter of 4.3 mm. Although some of the launch tubes are designed to accommodate larger sabots, for the majority of this project this size was used. To allow for the best possible flight of the projectile and removal of the in-flight sabot pieces, the barrel is rifled one turn in 0.76 m.

The accumulated pressure generated from the first stage of the light gas gun is halted at the start of the launch tube; this constitutes the beginning of the second stage. The diaphragm in-between the two stages of the gun is called the burst disc and measures 0.6 mm width and 12.88 mm diameter and is made of 7075 grade aluminium. It is held into position by the use of double sided tape at the breech end of the launch tube, in between the inner central breech collar and the launch tube, thereby creating a plug. Each burst disc is scored as shown on the right hand side of Figure 3.10 using a cross-shaped press

which is stamped at a force of 7 kN. When the gas compression is sufficient to exploit the weaknesses made from the score lines, the burst disc ruptures (Figure 3.10).

The sabot is a four-piece serrated isoplast cylinder, designed specifically to hold the required projectile for that particular experiment in place before, and at the beginning, of the shot. The design of the sabot allows the projectile to be held in place at the trigger end of the launch tube.
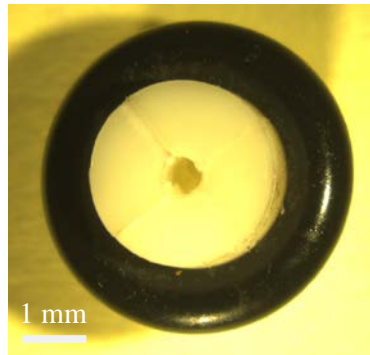
Figure 3.11: Top view of a sabot prior to shot. The sabots are pre-drilled to aid in perfectly aligning the projectile in the middle of the four sections. The pre-drilled hole normally requires further drilling to accommodate the projectile.

Figure 3.11 shows a sabot being held together by a small rubber ring. The use of a rubber ring is needed in order to keep the four sections of the sabot and the projectile in place until the sabot is placed into the launch tube.
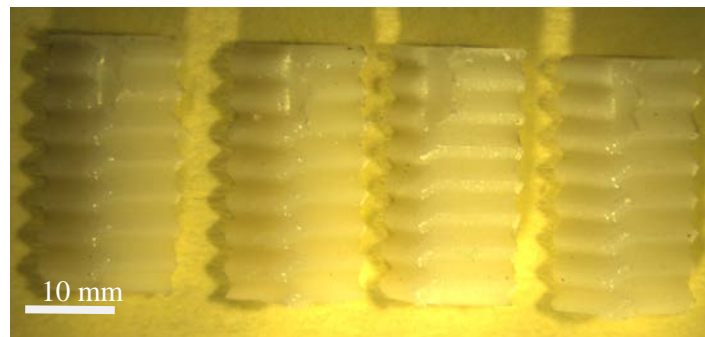
Figure 3.12: The four sections of the isoplast sabot are arranged such that a visual inspection is made for excess nylon flashing. All excess nylon is removed with a scalpel.

At first, a visual inspection of the sabot is needed to ascertain if any preparation is needed. The segments of the sabot are arranged as in Figure 3.12 and inspected for cleanliness of edges and any other foreign matter which might affect the action of the sabot during flight. Excess isoplast material, or flashing, is cut away by the use of scalpel until clean edges are obtained.

1 mm
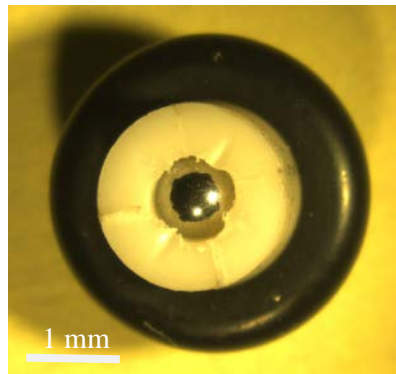
Figure 3.13: The final stage of inspection for the sabot with the projectile in position. This step checks that the sabot sections fit perfectly together and that the projectile is correctly positioned. At the top of each section small grooves are made in order to produce lips which help to retain the projectile inside the sabot when in place in the gun.

A final inspection of the sabot is then completed in order to make sure that all edges are clean and then the sections are fitted back together and the rubber ring is used to hold them in place ready for projectile insertion.

Once the projectile has been placed into the sabot, the final stage of preparation is to depress the four inner-circumference edges to make four notches as shown in Figure 3.13. These notches add further retention to the projectile making sure that the projectile is held in place and will not fall out in the launch tube. Once this has been done, the sabot is then inserted into the beginning stage of the launch tube – just behind (downstream) of the burst disc.

With the sabot in position, the burst disc is attached and the two stages of the light gas gun are brought together and secured through the inner and out breech collars.
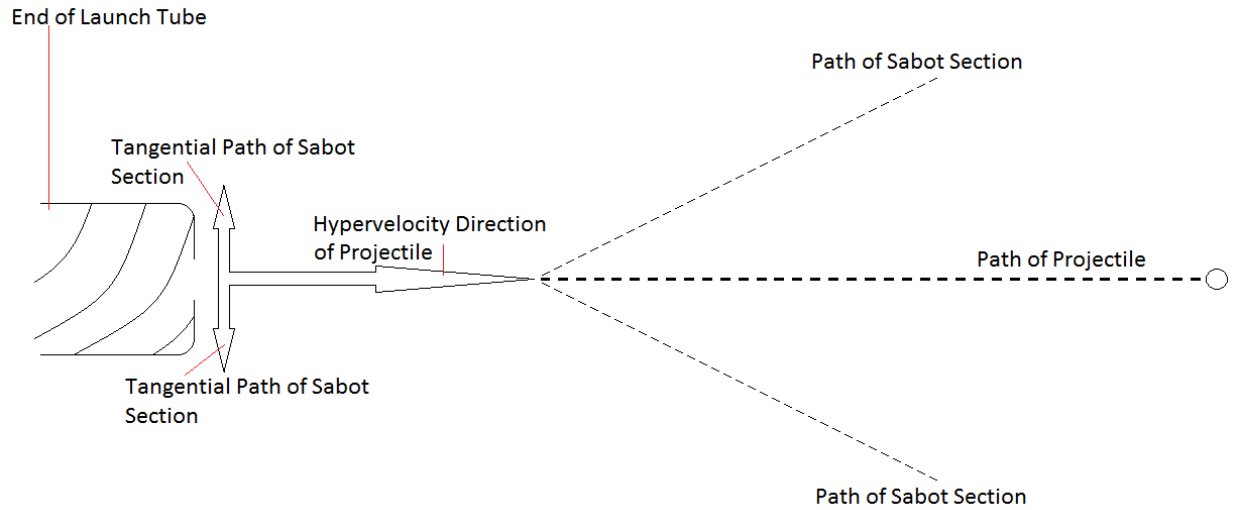
Figure 3.14: A diagram showing the action of the rifling on the sabot and the motion of the projectile and sabot during shot. The sabot pieces move 21° from the central projectile path.

Upon firing the gun, the sabot travels down the launch tube and is rotated by the rifling constant in the launch tube. The four isoplast sections of the sabot are ejected with a component perpendicular to the motion of the projectile. The perpendicular aspect of the motion allows the sabot sections to fall away tangentially leaving the projectile to continue along its path towards the target chamber (Figure 3.14).

3.6 Blast Tank
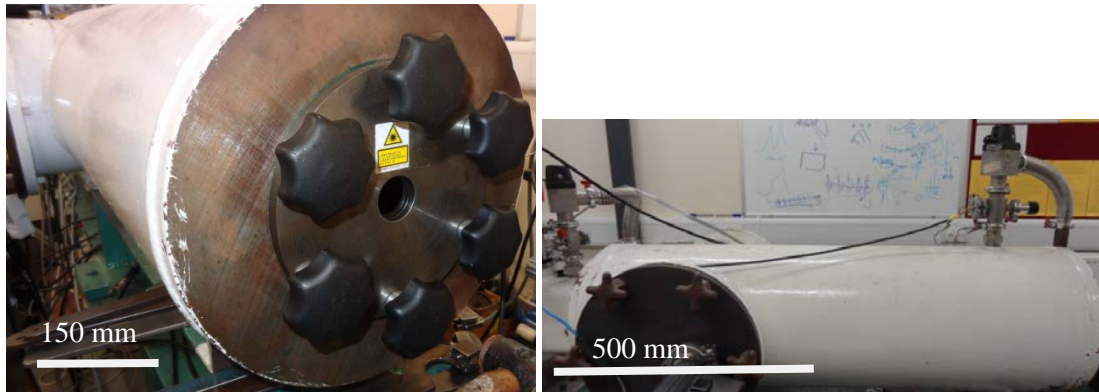
Figure 3.15: The blast tank is used to allow the exhaust gases (pressurised first stage gas mixed with the burnt cartridge powder) from the two stages to dissipate so that they do not interact with the target in the target chamber.

The blast tank contains the gas and sabot ejection site in the gun and is positioned before the target chamber (Figure 3.15). Once the projectile has been fired out of the launch tube, the rifling introduced from the launch tube will allow the four segments of the isoplast sabot to fall away from the axis of projectile trajectory. Allowing for dispersion of shot debris is of vital importance, as any impacts coming from shot debris, such as sabot segments or burst disc petals will greatly affect the impact of the target and produce an erroneous impact.

The gas from the first stage of the gun is mixed with the Reloader 19/22 powder gas from the cartridge, and must be allowed to disperse during the shot but before reaching the target area.
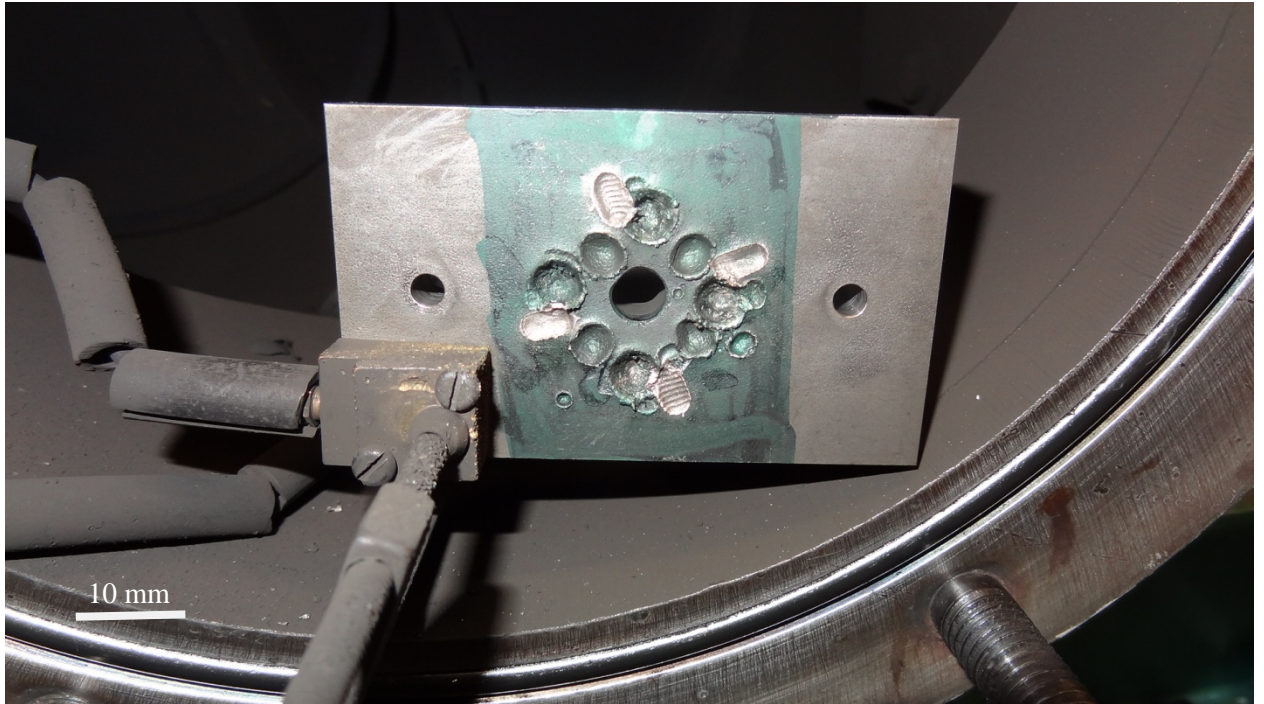
Figure 3.16: The blast tank aperture stop plate is positioned at the target chamber end in the blast tank. Its main purpose is to prevent any sections of sabot from damaging the internal sections of the gun.

If the gas mixture was allowed to hit the target in any appreciable amount, the target could be impacted by grains in the gas mixture or moved by the interaction with the gas as it produced a 'wind blowing' effect on the target (targets which are not held into position will be most susceptible).

The blast tank (Figure 3.15) measures 0.97m in length and 0.33m in diameter, allowing the majority of the gas to be dispersed, which in turn results in only a small percentage interacting with the target.

The blast tank also holds a removable metal plate called the blast tank aperture (Figure 3.16). The stop plate is a rectangular piece of mild steel with an impact sensor clamped onto it. When the stop plate is impacted by the sabot sections, the impact sensor registers the impacts providing a timing signal and external trigger. Figure 3.16 shows the level of impact damage and cratering by the sabot pieces when they are stopped by

the stop plate. New impacts are always distinguishable from older impacts, as all impacts are coloured with permanent marker at the gun preparation stage. The newer impacts, having cratered the metal, show up as non-coloured impacts making identification easy. Colouring the metal pre-shot allows for identification of two characteristics with respect to the dispersion of the sabot segments from the projectile trajectory:

- Placement of the sabot impacts – This is important in ascertaining the effectiveness of the rifling in the inner diameter of the launch tube. If the rifling grooves were becoming worn or inefficient, the sabot pieces would strike the plate closer to the exit hole, showing that the pieces of sabot are not being diverted away from the main direction of travel.
- Number of impacts – With each impact showing up on the plate as newly bared metal, four impacts should be present after each shot. If a piece of sabot had deviated too far to impact the stop plate, the data from the sensor could show that it had either gone down into the target chamber or impacted inside the blast tank. Fewer than four impacts could point to various problems, such as obstruction of the sabot or insufficient rifling.

Due to the level of sabot impacts into the stop plate and consequently the level of damage as a result of the impacts, this plate is changed frequently, prolonging the life span of the blast tank.

3.7 Vacuum Pump Valves and Vacuum Displays

Edwards vacuum valves are used to determine the level of evacuation of the light gas gun. Prior to use, the range of the gun was evacuated to approximately 0.5 mBar +/- 0.1 mBar in all shots here. This is to prevent deceleration of the projectile in flight.

The internal environmental evacuation during the pre-shot phase of gun preparation is achieved through vacuum pumps attached to the two vacuum ports on the light gas gun,

both situated in the target chamber, and return the light gas gun to atmospheric pressure once a successful shot has been completed.
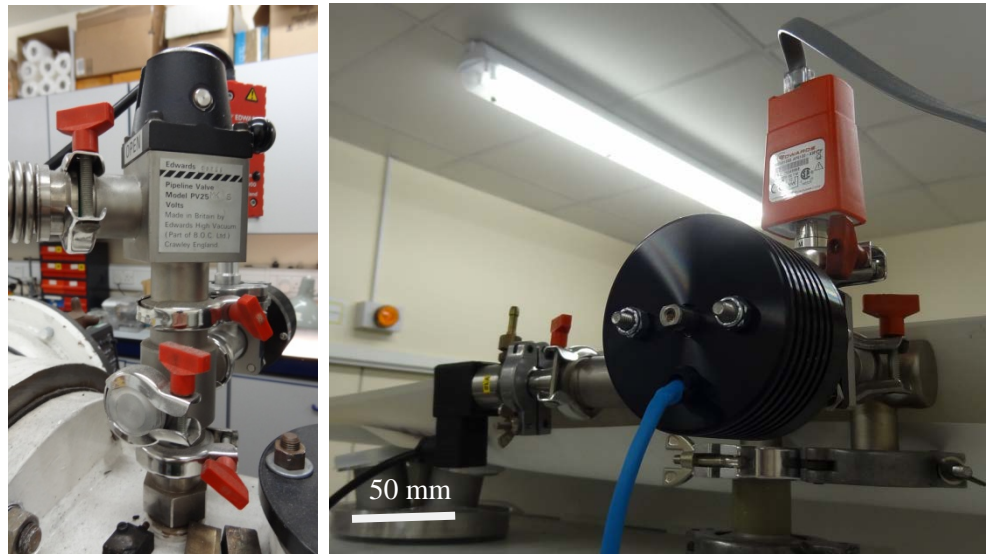
Figure 3.17: The evacuation and return to normal pressure of the light gun gas is made possible by the vacuum pump valves, which are attached to vacuum pumps.

The vacuum pump valves are attached to two Pirani vacuum displays, where they measure the internal gun and target chamber pressures. The average pump-down time for the gun is approximately 30-40 minutes, depending on the moisture level of the targets to be fired into. If excess moisture is still retained in the cement spheres (used as targets for the catastrophic disruption project, covered in Chapter 4), the moisture will leak out of the pores in the cement and be evacuated due to the vacuum. This is registered by the length of time taken to obtain the required level of vacuum.

During evacuation of the light gas gun, a noticeable vacuum gradient is shown. From Figure 3.17 the two vacuum valves are positioned in the time of flight (left) and target chamber (right). As pressure is reduced inside the gun the vacuum displays show two different values of pressure due to the length of the gun from the central breech to the target chamber (the second stage). The gradient in the vacuum levels out to a final

pressure reading (close to the target vacuum) thereby showing that a constant vacuum pressure is being maintained.

3.8 Oscilloscope Displays

The LeCroy Wavejet 324A oscilloscope shown in Figure 3.20 (right hand side) is used to determine the rotational data from the target housed in the rotating target holder. The four channels are:

Channel 1 – Blast Tank exit aperture sensor. This gives information on the impacts from the four sections of the sabot as the sabot and projectile exit the launch tube. This is required to ascertain whether all sections of the sabot have been stopped mid-flight and the only projectile has travelled towards the target.

Channel 2 – Records encoder phase B signal.

Channel 3 – Details information from encoder phase A signal.

Channel 4 – Allows for the rotational rate of the target holder to be obtained and measured. This channel records 200000 samples s^{-1} with 500 encoder marks per revolution (encoder marks detailed in section 5.1). With the rotational rate being set to that of 4 Vesta (Russell, C. T. *et al.* [2012]) which equates to 3.44 revolutions s^{-1}, each encoder mark records 116 samples.

Figure 3.18: The 2 LeCroy oscilloscope displays LeCroy 9304 AM (left) and LeCroy Wavejet 324A (right) are used to obtain the impact data from the time of flight section of the gun, and the rotation data from the target holder.

A LeCroy 9304 AM oscilloscope from Figure 3.18 (left) is associated with the time of flight section (following Section) and records, the impact velocity from the projectile in mid-flight. The channels are as follows:

Channel 1 –Impact sensor on the blast tank aperture as detailed from channel 1 LeCroy 324A.

Channel 2 – This channel is attached to laser curtain 1 (shown in Figure 3.21 [next section] as the right hand laser nearest to the pump valve) and initiates the timing procedure of the time of flight section.

Channel 3 – This is the display from laser curtain 2 which stops the timing procedure of the time of flight. With the two timings known and the distance in-between the timings, the projectile velocity is found.

3.9 Time of Flight Section
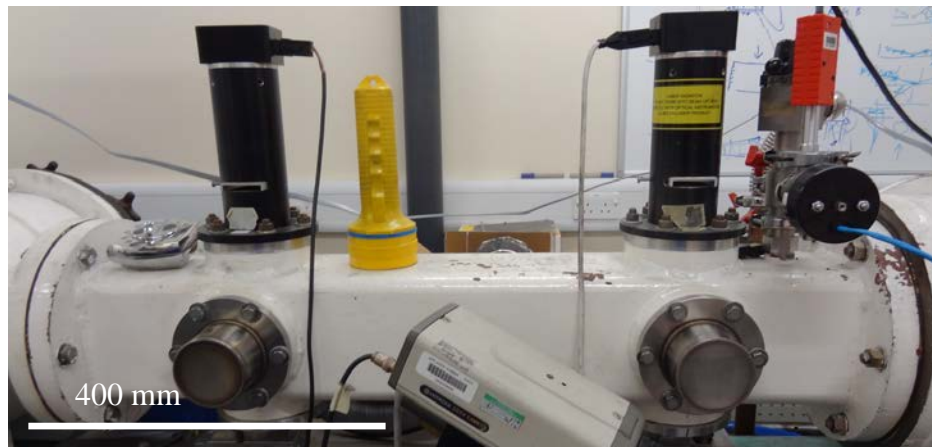
Figure 3.19: The time of flight section comprises a rectangular section of the gun used to determine the velocity of the projectile (or existence of burst disc/blast tank debris). Two line generating laser diodes at a separation of 0.499 cm record the velocity.

As the name suggests, this section, measuring 915 mm, is concerned with recording the flight path and time of the projectile just before it enters the target chamber. The time of flight section has two laser curtains separated by a distance of 499 mm, both of which are connected to the main oscilloscope. As a projectile breaks one beam then the other, the velocity is recorded as the distance travelled and the time taken to cover that

distance is known. The measurement of the velocity has an accuracy of 1 mm in the distance measurements obtained through the interruption of the laser beams and 0.0025 μs in the timing obtained from the lasers. As shown in Figure 3.19, two side hatches are bolted onto the side of the time of flight section. These covers are removed to aid with cleaning the laser optics, due to the amount of in-flight debris, such as cartridge waste, traversing through this particular section.

The time of flight section also serves a secondary purpose; it will detect whether anything else is fired towards the target chamber, such as pieces of burst disc or sabot. This is invaluable in determining whether the target has been struck purely by the projectile or not.

3.10   Safety Check Camera

Figure 3.20: Due to working with highly pressurised sections in the gun and explosives, safety is of paramount importance to the light gas gun operators. The gun is fired remotely outside the main gun room in the laboratory, so visual feeds from the gun are needed to finalise the shooting procedure.

The Hitachi safety check camera in Figure 3.20 forms the final safety precautionary check before the gun is fired. The camera which is positioned alongside the time of flight section is directed towards the main oscilloscope display. The status of the oscilloscope display is viewed from a monitor situated at the firing console. Once this check is complete, the gun is fired.

3.11   Small Target Chamber (STC)
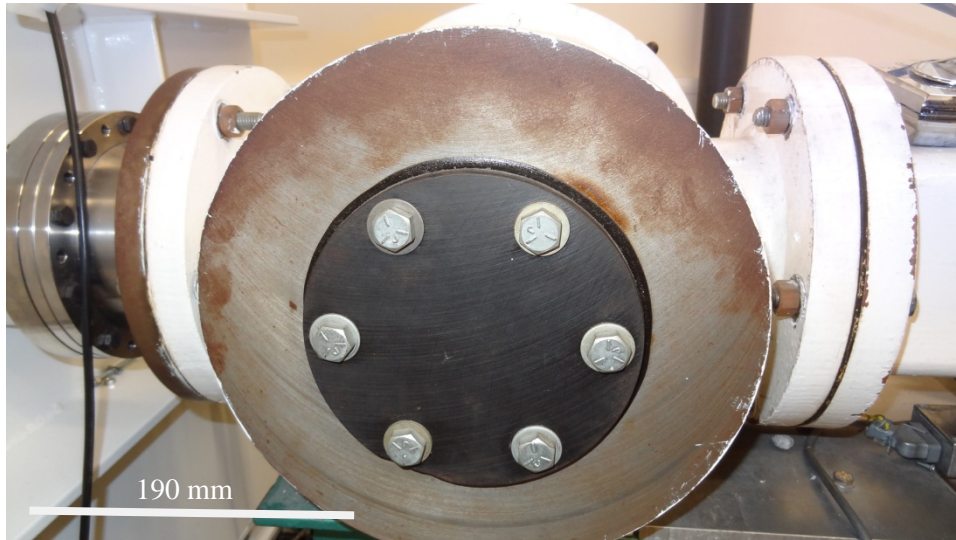
Figure 3.21: The Small Target Chamber (STC) is the second to last section of the gun. It served no purpose for the characteristics involved in this project but it can be used to extend the adaptability of the gun in general by using this section for small targets only.

The Small Target Chamber (STC) is used when the amount of target chamber space would be wasted because the target under investigation is small. Measuring 310 mm in diameter and 370 mm long, this target chamber has an access panel to the side as detailed by the bolted cover in Figure 3.21 for ease of access. When not in use as a target chamber, the projectile fired from the launch tube will pass through this section into the main target chamber.

3.12   Target Chamber

The target chamber houses the targets under investigation and forms the final section of the light gas gun. Figure 3.22 shows the recent addition of the 1.8 m^3 chamber from LACO Technologies, Utah. This target chamber is one of three which can be used with the light gas gun; the small target chamber (gun section 11) which is constantly in position in the gun, and the older version (Figure 3.23) which was previously attached to the gun. The older chamber did not have an evacuation port and the access point was at

the rear through a clamped door. Four portholes were drilled into the side of the chamber to allow electronic feeds or viewing glass.
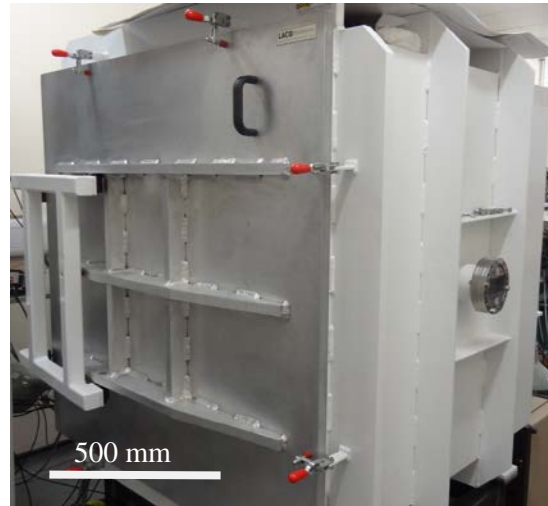
Figure 3.22: The main Target Chamber (TC) measures approximately 1.8 m^3 which allows for a very wide range of targets to be tested. It has side ports built in to allow for electrical interfaces to be fed through to targets housed inside such as temperature probes, oscilloscope data cables and power couplings.

Figure 3.23: The impact project detailed in this thesis had started shot runs before the new target chamber was acquired. As shown here, the older target chamber was a much smaller cylindrical version of a target chamber with only two side ports for feeds and viewing

On commencement of the projects detailed in this thesis, the original target chamber was much smaller. Measuring internally 0.4 m diameter and 1.06 m long, the original target chamber as can be seen in Figure 3.25 was cylindrical in shape and had a much smaller internal volume. The size of the original target chamber imposed a target size constraint, whereas the newer, larger target chamber will accommodate a very wide range of targets, with an upper size limit of around $1m^3$. The addition of the larger target chamber allowed the use of internal lighting to help illuminate the targets undergoing investigation. With the positioning of the viewing portholes in the side and front of the larger target chamber, cameras, camcorders and high frame-rate video equipment is able to be used to ascertain as much information from the impacts.

On the evacuation of the internal atmosphere and pressure of the gun, the original target chamber would pump down in approximately 30 minutes to a shot pressure of 0.5 mBar. However, the pump down time with the newer target chamber has been measured at approximately 40 minutes, due to the positioning of a second evacuation valve located at the top of the target chamber (right hand side photo Figure 3.17). This allows for two vacuum pumps to be used to reduce the internal atmosphere of the gun, but due to the size of the new target chamber, it gives a slight complication of the internal pressure gradient as detailed in section 3.7.

3.13   Firing Console

Figure 3.24: The Lasermet firing console is the remote firing mechanism for the light gas gun. This console allows for the safe use of the light gas gun by monitoring the access doors into the main gun room of the laboratory via magnetic sensors on each door

The final section to the gun is the Lasermet firing console (Figure 3.24). Once the gun has been prepared and safety checks have been made, the final safety checks are made with the firing console. Door lock sensors on each door in the gun laboratory act as a safety system in conjunction with the firing console; therefore if one or more of the doors are open, the system overrides the firing protocol and the electromagnetic trigger cannot be used. Once the doors are shut, the system is primed by use of a firing key, the console is reset to finally check all door sensors are working and the gun is fired.

3.14   Summary

The light gas gun used in this work has been described in this chapter. The velocity obtained in any shot can be controlled by varying: the amount of gun powder and the type of pre-measured gas in the pump tube. This is determined on past experience with the actual velocity obtained being measured in each shot.

Each section of the gun is fully maintainable and adaptable which allows for a range of firing set-ups to be designed and conducted. The addition of the larger target chamber has increased the viewing potential of the targets during impact which in turn means that further information such as video obtained information can be gathered. The new target chamber portholes at present are covered with thick glass which can be changed to full spectrum glass thereby allowing target temperature measurements to be conducted through the use of infra-red cameras.

Chapter IV: Experimental Methodology II: Cement Target Manufacture

As seen in the previous Chapter the two stage light gas gun is the main piece of laboratory equipment required to investigate whether rotation has any effect on catastrophic disruption of asteroids. However, a suitable target is required to represent asteroids modelled such as 4Vesta.

It was decided that targets made from hardened Portland cement paste would best fulfil the criteria of asteroid analogues. Cement paste is a network of hydrated $3CaO.2SiO_2.3H_2O$ needles and plates with capillary pores in-between (Powers T.C. 1958). As will be discussed further in this Chapter, the mechanical properties of cement paste are testable in the laboratory, such as, strength or hardening of the cement paste with respect to curing time or optimum hydration ratios. Two further reasons for the use of cement are based on how readily available cement is so that supply would not be an issue, and the cost of cement due to the need of making many targets.

Figure 4.1: Cement targets typical of those used in this work.

In order to make this experiment successful and reproducible an easy method for making the catastrophic disruption test targets was needed. The sizes of the targets were constrained to the range of 8 cm to 12 cm diameter. The target holder was designed specifically to test the effect of rotation of targets in a small range of target diameters.

It was decided that two hemispherical moulds would be the best method for target manufacture so long as the moulds were made of a material strong enough to withstand normal laboratory wear and tear. Two Christmas tree baubles were found to give the best target size of approximately 10 cm diameter, with examples shown in Figure 4.1. The baubles were cut in half to form the moulds which were then attached together through the use of packing tape and final sealing with a heat treated cling film wrap.

Figure 4.2: Vacuum formed moulds were to enable mass production of spheres.

However one major disadvantage arose with only having two sets of bauble moulds; if something should happen to one of the sets, the manufacturing output would be halved and therefore slow down the project. To remedy this issue, several moulds were produced by vacuum forming new moulds around existing targets obtained from the baubles. This had two main advantages; 1. The plastic used in the vacuum forming of these moulds was thicker than the bauble plastic and therefore would withstand greater amounts of stress from manufacturing the targets when compared to the thin plastic of the baubles and 2. Any number of moulds could be produced, thereby increasing the amount of targets being produced. They were made by placing two hemispherical cement target halves into a vacuum forming machine. In each case a 1cm rod was cut in half and attached to the halves of the cement sphere, these channels were made in order to aid in filling, the moulds as can be seen in Figure 4.2.

When set, the moulds were cut down to size (Figure 4.2) and had holes drilled into each mould such that the moulds could be attached to each other via M8 nuts and bolts.

The cement used for the experiments was LaFarge Portland Cement (bag identification numbers; PKD 05.10.10 13:21 and PKD 12.05.11 04:34). Cement was used because it provided a good model for stone, where the levels of porosity and strengths etc. could be obtained through investigation.

In order to fabricate asteroid analogues, investigations were needed to ascertain a good sound method for making the cement targets. The variables associated with cement work such as curing time, age-related strengthening, porosity and particle differentiation were tested prior to the onset of the shot programme and are detailed below.

4.1   Ratio Tests on Cement

In order to ascertain the optimum manufacturing conditions for the cement sphere targets, a series of tests were completed within the first few weeks of the project. The tests were to find the optimum values of water-to-cement ratio, curing time and porosity. Below (Table 4.1) is an account of the ratio tests. The type of cement used for the experiments was LaFarge hydraulic cement which does not need to be kept dry in order to cure to a hard body. However being hydraulic does require the cement to be mixed with a certain amount of water to initiate the chemical reactions needed to crystallise the cement mortar and therefore harden and strengthen. The data in Table 4.1 are as follows: "Tube Number" details the assigned number to the ratio test (two samples were tested to aid with statistical robustness). The cement to water ratio was the main parameter of the tests. These ratios varied from adding very little water added to the cement powder, to greater amounts of water with respect to the amount of cement powder. The "Fill Height" gives data on the measured height of the cement paste mixture in each tube; this was important because the tubes varied in height. "Differentiation" is related to the reduction in height of the test sample when hydration and setting had occurred, the differentiation is also given in terms of percentage height reduction. The final two columns give the strength data of each test sample, with the numerical values in Pa and the tensometer test. Each sample was cured for four days.

4.1.1 Experimental Outline

A series of 10 plastic cylinders measuring (average values for both) 68.78 ± 0.89 mm in height and 31.99 ± 0.27 mm in diameter were used to encase the cement mixtures with rubber bungs stopping one end in order to close the tube.

The best method of calculating the ratios was to use mass instead of volume. Although liquids and solids both have volumes, the experimental accuracy was found to be insufficient if the cement was measured in volume due to the settling of the powder in the glass beaker and the packing fraction affecting the overall volume.

Ratios ranged from 3:7 cement to water through to 10:3 cement to water in order to test a suitable range. It was found that the optimum ratio mixture was 7:3 cement to water which was in agreement with the ratio work by Brandt (1998). The results of the tests are detailed in Table 4.1.

Table 4.1: Data Set for the Ratio Tests

Tube Number	Cement:Water Ratio	Fill Height (mm)	Differentiation (mm)	Differentiation (%)	Strength (Pa)	Strength Test
1	3:7	61.52	17.42	28.32	N/A	N/A
2	3:7	59.19	19.47	32.89	N/A	N/A
1	3:5	54.64	20.00	36.60	N/A	N/A
2	3:5	63.61	26.53	41.71	N/A	N/A
1	1:1	62.26	49.90	80.15	2.06E+07	Compression
2	1:1	61.89	51.10	82.57	3.36E+05	Brazilian
1	5:3	58.5	48.22	82.43	5.18E+07	Compression
2	5:3	50.5	41.47	82.12	7.33E+05	Brazilian
1	7:3	70.46	62.37	88.52	1.92E+08	Compression
2	7:3	67.9	53.12	78.23	1.20E+06	Brazilian

Figure 4.3: Showing the powdery residues for the cement test for ratio 3:7 cement-to-water. As expected, the level of particulate differentiation was increased largely due to the amount of fluid allowing the cement particles to sink to the bottom of the test cylinder by gravity.

The results show that for larger amounts of water in the mixture, such as 3:7 and 3:5 ratios, the particles of cement settle under gravity due to the viscosity of the mixture being very close to water and not water-cement mixed. As the samples cured over a period of four days, a large amount of excess water was still present in the water dominant ratios, which had to be siphoned off, and more time was needed in order to dry the samples. Once dry due to the allotted curing time given, the cement blocks were heavily differentiated and very powdery as seen in Figure: 4.3. Strength testing on these samples was ineffectual due to the very soft nature of the residue left.

As the mix ratios increased from highly saturated to optimum, the data in Table 4.1 shows that the mix ratio of 7:3 agrees with Brandt (1998). It is also noted that the data shows an order of magnitude increase from the 1:1 ratios for both compression and tension (Brazilian) strength tests and the least particle differentiation.

Also noted was the effect of too much cement in the mixture. Having too much cement meant that the water was only able to hydrate a small percentage of the cement powder and therefore the mixture.

4.1.2 Optimum strength

One aspect of cement which makes it an ideal material for engineering is the fact that the strength (under normal conditions) of cement increases as time passes. On the Lafarge properties sheet for the Mastercrete series of cement products, the

compressive strength of the cement increased from 16-26 N mm^{-2} at two days curing age to 37-47 N mm^{-2} at 28 days curing age (LaFarge 2009). However the values obtained from the LaFarge data sheet are obtained from cement-ballast mixtures and not pure cement mortars.

Therefore, considering the dynamical nature of the strength properties associated with the cement, it was concluded that a series of tensile – compression strength tests would be needed to ascertain the best time frame in which to shoot at the cement spheres, thereby ensuring the highest level possible of accuracy and reliability in the results.

The apparatus used for the strength testing was a 20 kN tensometer which uses two plates to apply forces along a single axis load in the direction of two screw threads. The cement mixture (using the same ratio for the best mix case) was cast into cylinders and placed into an oven set at an externally monitored temperature of 21.8^{o}C for one day to ensure no fluctuation in temperature, then to be removed and placed into a room environment with the ambient temperature of 19.2^{o}C to cure over a range of days.

Once the specimens reached a certain amount of curing time, they could then be strength tested. The type of test was compressive see Figure 4.4. These were conducted in the 20 kN tensometer in Figure 4.5 where samples were compressed to find the strength-curing age relationship.
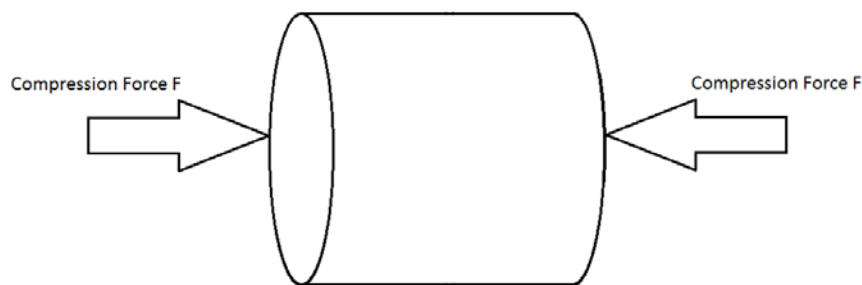
Figure 4.4: A free body force diagram representing a test cylinder under compressive tension. As force is applied to the two faces of the test cylinder, the sides of the test cylinder would be under tension due to the perpendicular translation of the force.

Figure 4.5: The tensometer with a test cylinder in place. The crank handle is used to turn the principal driving mechanism which controls the central thread attached to the right hand side of the compression assembly.
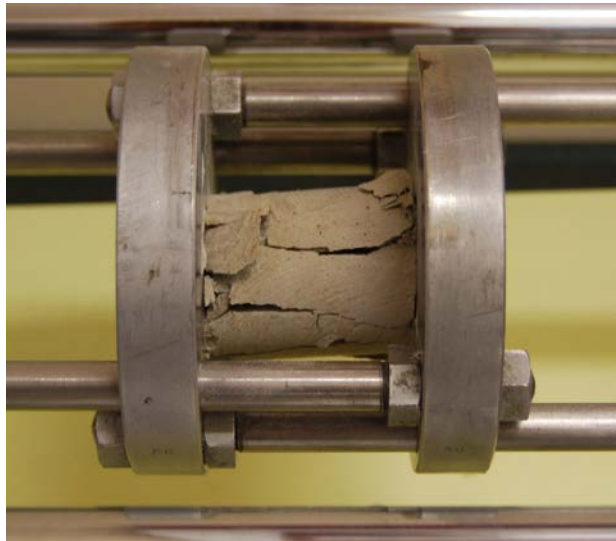
Figure 4.6: Here a test cylinder which has failed under the compression. Note the latitudinal cracks of the failure along the sides of the cylinder.
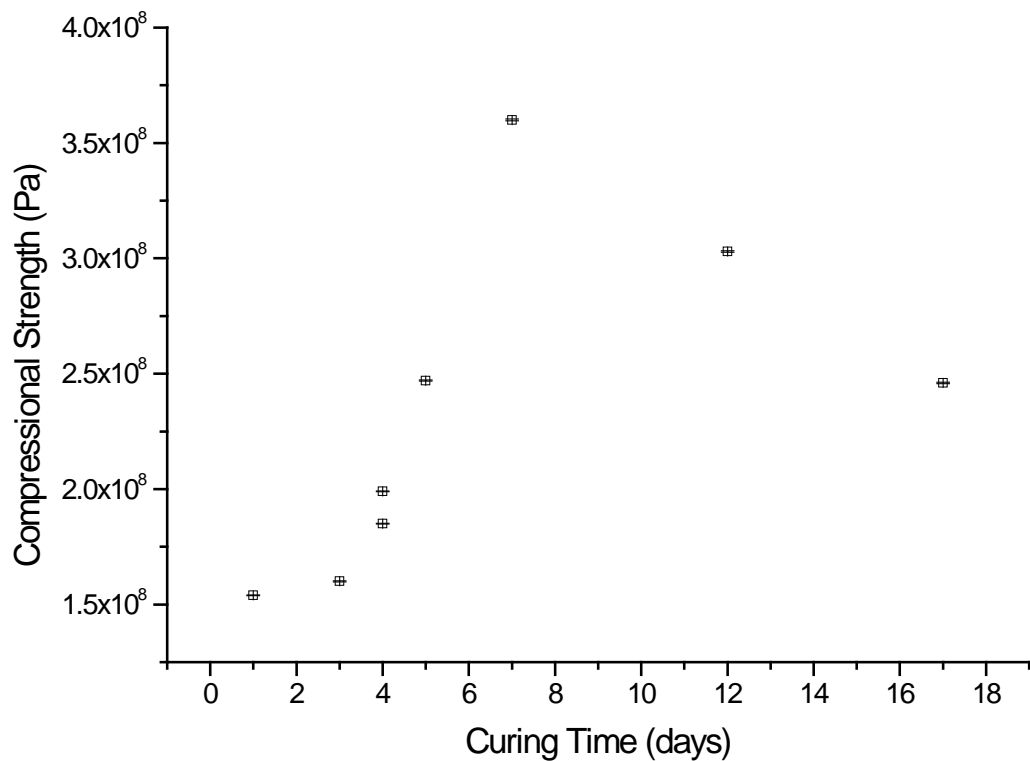
Figure 4.7: The data obtained from the curing time-strength relationship of the LaFarge Portland cement test cylinders. The data shown in the graph are the average of three values of strength with respect to curing time in days. Error bars are given in the plot but are small due to the range of data.

Force was applied to the specimens by turning the crank handle at one end of the tensometer at intervals of four complete turns as depicted by the tensometer set-up in Figure 4.5. Once the turns were completed, the force was recorded from the digital force meter and the compression lengths were measured using digital vernier callipers. Figure 4.6 shows the material fail outcome where the amount of pressure had increased beyond the strength limits of the test cylinder, at this point the tensometer would register a 'slump' in strength. The tests were conducted for a range of curing times from one days to 17 days. The results are shown in Figure 4.7.

The results show that the optimum curing age for the Mastercrete being used to make the spheres is seven days with an increase of strength before this time and a decline in strength appearing afterwards. This result did appear to contradict the data

obtained from the Mastercrete physical properties sheet but, as stated, the LaFarge Company did not conduct their tests using a pure cement mortar. Although the seven day test did yield the strongest value of test cylinder, the timing constraints of the project meant that waiting for seven days to cure the targets was too long. In fact, the optimum curing time was determined to be the four day period allowing a one week turnaround from manufacture to shot and data acquisition.

4.1.3 Brazilian Strength Testing

Whilst it is easier to measure compressive strength, it is harder to measure in the lab, tensile strength. Tensile strength is important because it can have a different value to compressive strength and can lead to failure of shocked samples. In order to more readily measure tensile strength of samples, a common approach is to use the so-called Brazilian strength method (Fairhurst 1964). This assumes isotropic behaviour of a cylindrical sample.

This test involves a different surface area being put under compression and allowing the compressive forces to dissipate through the sides of the cement cylinder. This is very similar to the previous compression tests, but the direction of force and the failure points are different.

This form of tensile testing requires the test cylinder to be compressed along the sides of the cylinder as can be seen in Figures 4.8 and 4.9. Failure of the test cylinders normally occurs with a central crack through the middle of the test subject as in Figure 4.9 and often the material failure would lead to three cracks through the middle of the test piece; this was due to an excess of moisture remaining inside the cement matrix showing the possibility of not fully hydrated sections of the test cylinder being stressed.

Figure 4.8: The experimental set up for the Brazilian tensile strength test differs from the normal compression test used when testing Hooke's Law and Young's modulus. Instead of the ends of the cylinder being compressed, the sides are compressed for the Brazilian strength test.
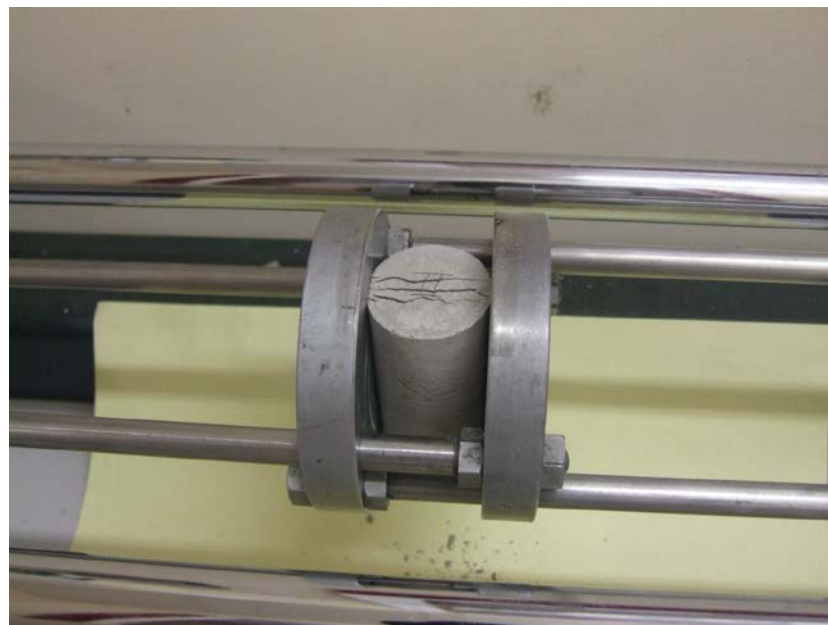
Figure 4.9: A cement cylinder which has failed under the applied force. Note the cracks through the middle. The three cracks might be due to excess moisture was still inside the cement cylinder as opposed to the normal single fault line expected.

The equation concerning Brazilian strength testing is:

$$\sigma_t = \frac{2\,P}{\pi\,D\,L} \hspace{4cm} [4.1]$$

Or with radius substituted:

$$\sigma_t = \frac{P}{\pi\, r\, L} \qquad\qquad [4.2]$$

Where P is the load in N, D is the diameter in mm and L is the sample length in mm.

Instead of the conventional methods adopted with normal compression strength testing, such as measuring load force and strain percentage, with the Brazilian test, either time and load or maximum load at the point of failure are used. In these tests, the use of maximum load was used as the upper strength of the cement was needed, and not the intermediate stages of compression.

However an issue regarding data acquisition arose; the electronic readout from the tensometer would show the current load on the system and when the cylinder failed, the load would reduce in strength as the cement under stress would relax and therefore the readout would show a lower value of the actual upper tensile strength than the actual value.

To overcome this issue, digital video capture was used to obtain the upper yield values. A Panasonic HX-WA20 HD camera was mounted onto a tripod and focused onto the tensometer readout. The camera was set to record and then the subject was tested until failure. The video was then downloaded onto a Dell Inspiron 560 computer and the video was watched through the test and in particular, the failure point.

Technological advances in photography and video capture has resulted in better microphones in digital camcorders and the model used had an internal microphone which made recognising the failure point very accurate. As the cement fails, a loud cracking sound could be heard which acted as a point of reference to pause the frame at that precise moment, shown in Figure 4.10, and to record the upper tensile strength. With the data collected, the values were evaluated and the Brazilian Test strength of the cement cylinders were found.

Figure 4.10; The digital display attached to the tensometer shows the actual force in kN being applied in real time. Due to the need for the upper tensile strength of each test cylinder, the tests were recorded with the use of a digital camcorder therefore allowing the point of failure to be read just as it happened.

4.1.4 Brazilian Test Results

Eight cylinders where tested for the optimum day-curing strengths as with the compression tests outlined previously. Average cylinder measurements were taken and equations [4.1] [4.2] were used to calculate the values of cylinder strengths. The results from the Brazilian tests are shown in Figure 4.11 with very small error bars calculated using the Pythagorean error method in equation [4.3].

The values of error in the readings were found by the following equation:

$$\frac{\delta \sigma_t}{\sigma_t} = \sqrt{\left(\frac{\delta D}{D}\right)^2 + \left(\frac{\delta L}{L}\right)^2 + \left(\frac{\delta P}{P}\right)^2} \qquad [4.3]$$
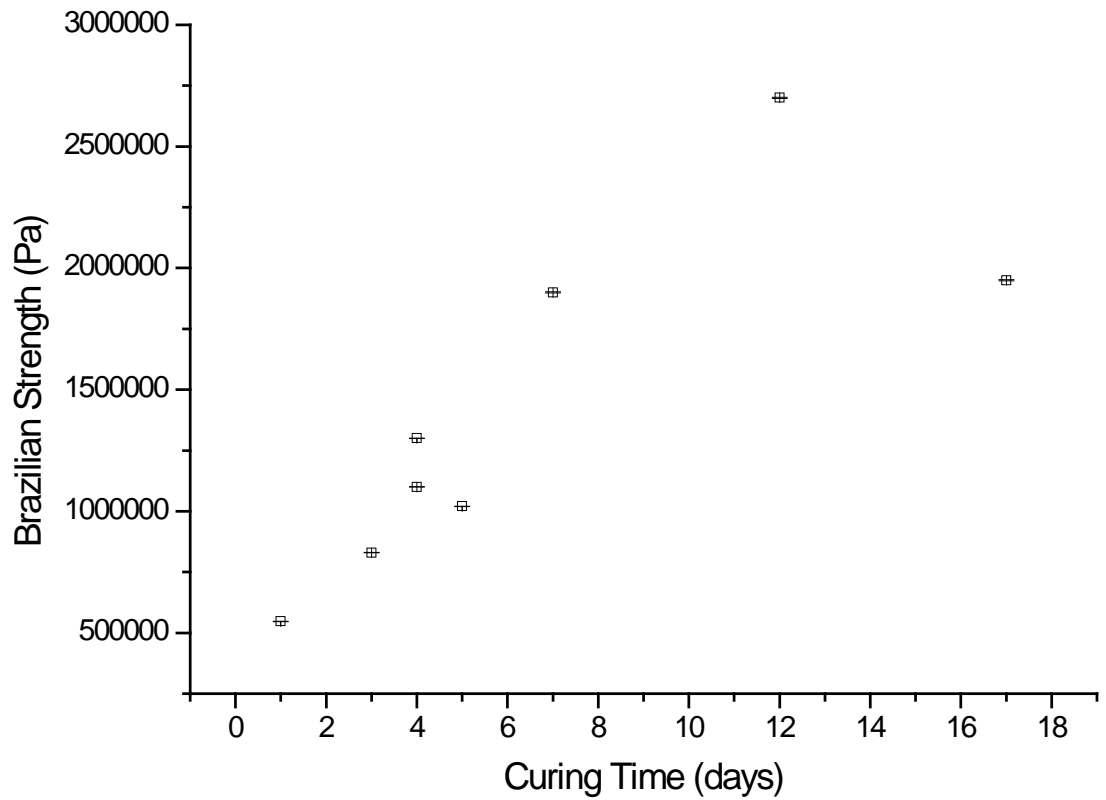
Figure 4.11: The data for the Brazilian tests obtained from the curing time-strength relationship of the LaFarge Portland cement test cylinders. The data shows a similar increasing trend as in Figure 4.7 although with lower yield strengths.

The systematic errors were found to be:

δD and $\delta L = \pm 0.03$ mm (from the Vernier Caliper manufacturers)

$\delta P = \pm 0.0005$ kN $= 0.5$ N (from the Tensometer instruction booklet)

4.2   Curing Related Weakness

Figure 4.12: The results of cement shrinkage during curing show signs of surface cracks of varying length. For the purposes of the crack influence test, the cracks were marked with a permanent marker to see whether the body break-up would follow the cracks already present on the surface of the sphere.

A series of experiments were designed in order to find whether the curing time of the cement bodies had any effect on surface cracks. This was an important aspect to cover as the cracks in the cement bodies would undoubtedly affect the strength both internally and on the surface by making lines of weakness.

One explanation relating the curing of cement and crack lines forming is known as 'drying shrinkage' PCA (2012). This is when the cement has been made with more water than the optimum ratio for the cement saturation and as it evaporates, the cement then shrinks during the curing process and forms cracks. The loss of mass through vapour release during curing of the cement spheres is on average 11% of the total mass.

Two cement targets, shown in Figure 4.12, lost moisture rapidly and therefore resulted in shrinkage were tested in order to see how much of an effect the surface cracks would have on the result of an impact. The cracks on the surface were highlighted so that any influence on the disruption of the bodies could be found (depending on the amount of disruption). The spheres in Figure 4.12 were cured for 4 days on removal and shot at on the 9th February 2011.

Figure 4.13 The results after the crack influence test show that the surface cracks (marked with blue lines) did have an effect on the fragmentation outcome and therefore would show that surface cracking from shrinkage would bias any outcome.

The level of influence can be seen in Figure 4.13. The fault lines on the surface of the cement sphere 090211.1, did have an effect on the collisional break-up of the body due to the edges of each fragment having been previously identified by the marker.

With respect to each of these tests, it should be stated that comets and asteroids within the solar system are not perfectly spherical and will have some element of physical weakness associated with them.

4.3   Porosity Testing

In order to devise manufacturing processes for the cement sphere targets, several tests were needed in order to investigate the factors affecting the targets during the manufacturing phases. One of the tests was to deduce, and reduce, the level of porosity in the targets.

The targets are made through the method of cement hydration and mould filling. This method, though very reproducible and dependable, did have one problem; the

introduction of air bubbles throughout the cement mortar mix. One experimental shot in the multi-shot programme did have a large void or pore space at that centre of the target which weakened the target and therefore affected the outcome.

Upon researching for viable methods of pore reduction, one method used in the silicone mould making industry is called the "bombs away" method (tapplastics.com). This uses gravity to pull a viscous material over a large distance relative to the amount of material. In doing so, the stream of material is reduced in thickness from the spout to the objective thereby 'popping' the air bubbles which are too large for the area occupied by the thin stream of liquid.

This method was considered and given an initial testing but it was concluded that this method was not suitable for the cement target manufacture. This was due to cement mortar flow properties being relatively variable with no steady stream of mortar and the size of the entry hole of the hemispherical sphere moulds being too small for the thickness of the cement flowing stream. Therefore in order to reduce the level of pores in the cement mix, four finishing tests were completed and are outlined below.

4.3.1 The Test

In order to examine the porosity of the cement targets, the cement mortar was made by the same method adopted throughout the project, but with various finalising elements. The moulds used for these tests were cylindrical nylon tubes measuring on average; 68.78 ± 0.89 mm in height and 31.99 ± 0.27 mm in diameter.

Finalising element 1:

This was the 'standard' for the purposes of the test. The cement mortar was filled into the moulds and left to cure naturally without introducing any method to reduce porosity. This would show the level of pores present in the sample if filled and left.

Finalising element 2:

Excess pores were removed through excitation of the cement samples via the use of a laboratory test tube shaker. The shaker oscillates at 50 Hz which caused the air bubbles in the cement mix to flow up to the top.

Finalising element 3 (a) and (b):

The final method used vacuum degassing as the technique of air extraction. Test (a) samples were placed into the target chamber of the light gas gun and the chamber was then closed and evacuated of air. A vacuum of 50 mBar was maintained for approximately 30 minutes until no further gas release from the test cylinders was noted.

Test 3(b) used a larger cement container to be de-gassed and then which was used to fill the nylon tubes with the mixture of de-gassed cement mortar.

4.3.2 Results from Tests

Finalising Element 1

As noted, this technique does not utilise any method of bubble removal from the cement mix. The basic method of pouring in the cement and leaving it to cure over the four day period, traps excessive levels of bubbles into the material matrix and therefore results in high levels of porosity. As indicated by Figure 4.14 below, a significant number of pores ranging in diameter sizes between 0.02 mm to 0.85 mm were present throughout the mixture as expected.

With the presence of larger pores in the material matrix, the susceptibility of failure increases and therefore results in weakened targets. The random nature of pore distribution throughout the material results in a large variance of material strength. This variability means that finalising method number one is insufficient in reproducing targets within a reproducible material strength.
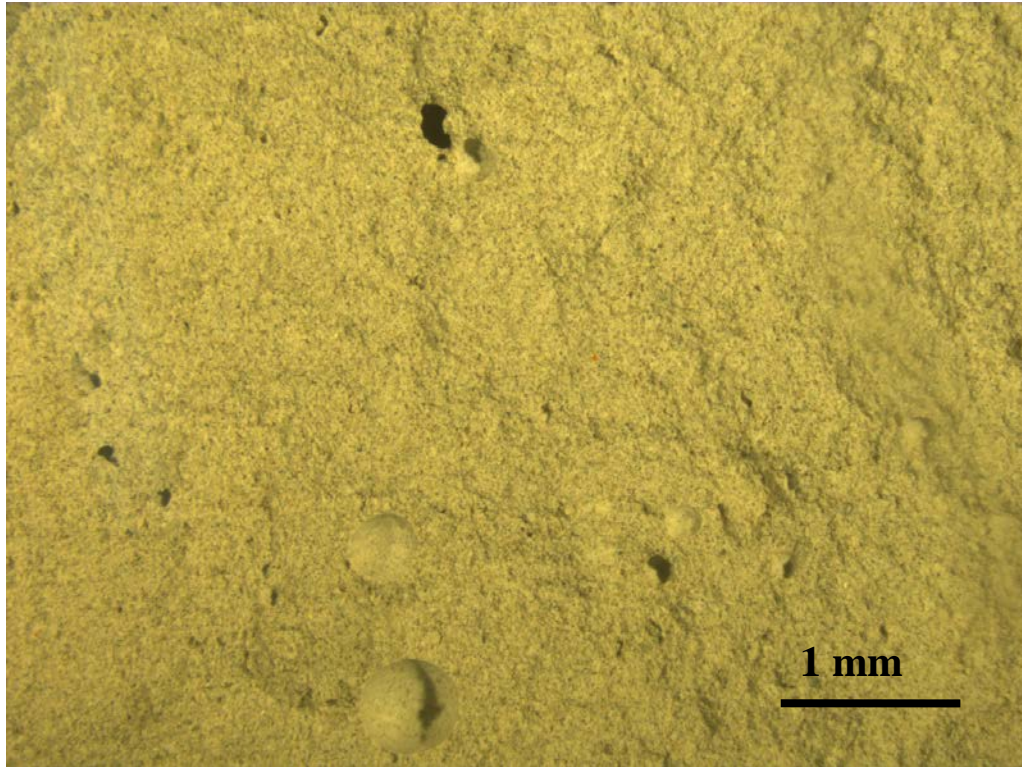
Fig 4.14: Variable sized pores were found to be present throughout the material of the cement resulting in finalising element number one. The distribution of the pores did not follow any kind of pattern and therefore must be considered to be relatively anisotropic. The pores ranged in diameter 0.02 mm – 0.85 mm.

Finishing Element 2

This method utilised the action of shaking the test piece in order to displace the air bubbles trapped throughout the material. One aspect which arose from this finalising method was that this could not be done by hand due to the introduction of variability. In order to obtain reasonable results from this method, a laboratory test tube shaker was used; this allowed for a known oscillating frequency to be used each time.
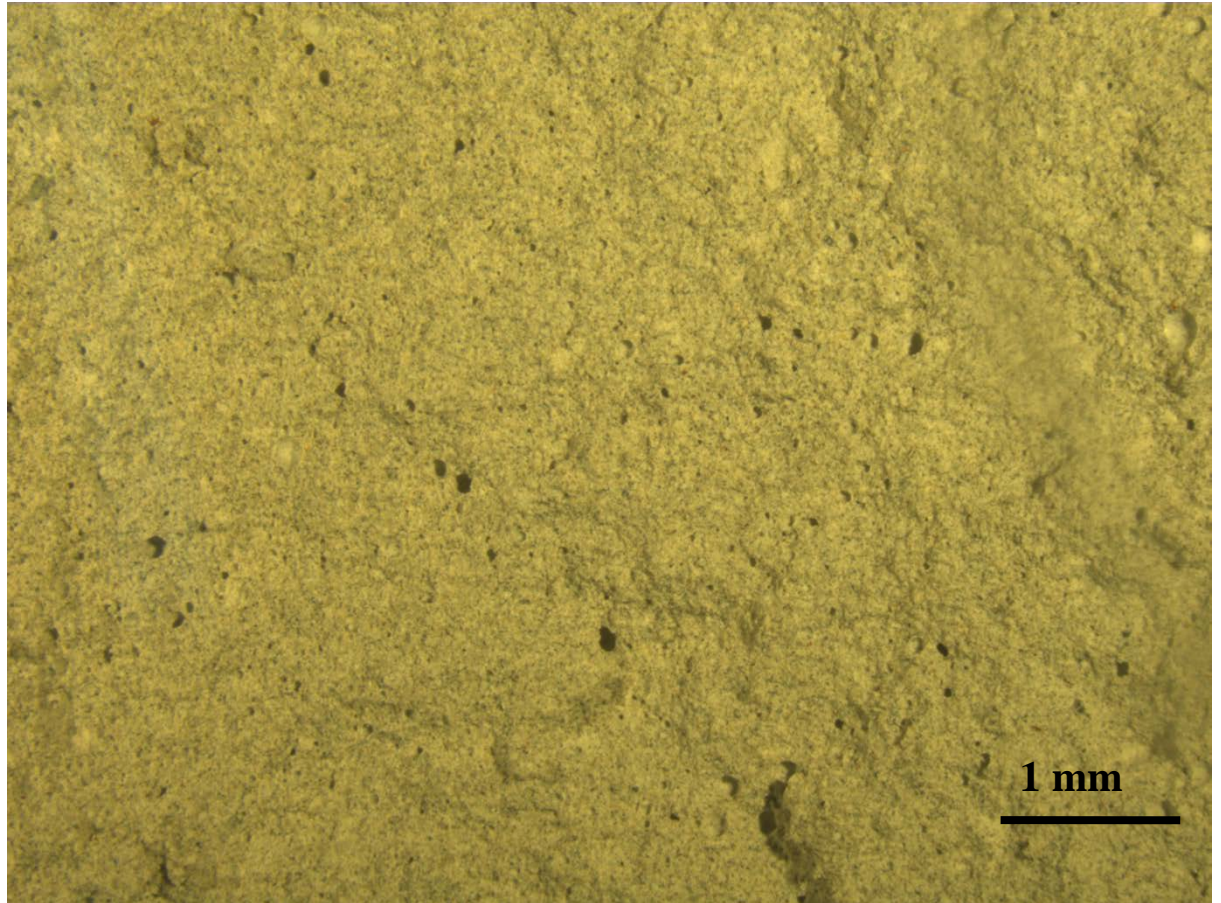
Fig 4.15: This image was taken from the test piece for finalising element 2. Smaller but numerous pores are seen but large pores were not present. Whereas the level of smaller pores would reduce the strength of the material, without larger pores being present means that there are no areas of greater susceptibility.

Once the nylon cement tubes were filled, the end was placed into the test tube cup of the shaker and then vibrated at 50 Hz for 2 minutes. During the vibration of the cement material, air pockets were noted to rise to the surface of the mortar thereby showing definite movement of trapped air from inside the mix. However, to ensure fairness with this method the tubes were rotated 360° about the central axis of the test tube cup, so that any air pockets being removed from the mix would not settle on the sides of the nylon tube.

One consequence associated with the use of this method was that the pores which remained inside the material matrix upon setting, were small in comparison (less than 0.02 mm) to finalising elements 1 and 3 (b) pore size.

As detailed in Figure 4.15 the level of porosity, although still not reduced to zero, does show that a larger proportion of the matrix space is hydrated cement mortar. A shock wave propagating through the matrix would lose energy in the shock front when encountering the smaller pores but the loss would be much smaller when compared to larger pore crushing.

Finishing Element 3 (a) and (b)

This method used the vacuum produced in the light gas gun target chamber to test for pore space in three directly degassed samples. The final three tubes were filled from a container of cement at the rear of the three direct de-gassed tubes in Figure 4.16 and was labelled 're-filled de-gassed'. This was decided upon due to the level of possible material loss through the de-gassing process.

One result of vacuum de-gassing was the overflowing of cement causing (Figure 4.16) spillage over the sides of the test tubes. This was due to air bubbles trapped in the mixture being drawn out by the vacuum increasing the sample volume. This did illustrate the level of trapped air in the material matrix. The large container at the back left of the set-up was approximately three quarters filled with the cement mixture but due to the relative volume occupied by the cement, the material did not flow out and therefore there was no loss in material.

Figure 4.16: The pump-down of the test subjects in the target chamber. The larger container of cement at the rear of the Figure was used to re-fill three test cylinders. Material spilled over the sides during the de-gassing and therefore resulted in large amounts of material loss.

During de-gassing it was noted that vapour was being released from the material at the start of air bubble extraction as the material started to bubble and rise. This was found to be water content from the material due to the target chamber pressure being very close to the partial pressure of the water (24.877 mBar at room temperature) D. R. Lide et al. (1995).

Table 4.2 Data from the Vacuum De-Gassing Tests

Vacuum Form	Test Subject Height (mm)	Strength Test	Strength (Pa)
Direct De-Gassed	29.30	Compressive	1.91×10^7
Refilled De-Gassed	55.18	Compressive	1.12×10^7
Refilled De-Gassed	63.00	Tensile	4.70×10^5

Table 4.3 Data showing four day curing strength test for comparison (data from figs. 4.7 and 4.11)

Curing Time (days)	Strength Test	Strength (Pa)
4	Compressive	1.99×10^8
4	Compressive	1.85×10^8
4	Tensile	1.1×10^6

The reduction of water from the cement mixture due to external vacuum pressures has been previously tested in this project by placing test samples made from the same cement used for a particular catastrophic disruption shot in the target chamber. During the pump down and maintained vacuum of the target chamber, the targets are further reduced in mass through moisture loss. This was found to be 5% pre-shot mass for four day-cured targets.

With this in mind, it is therefore expected moisture to be lost during vacuum de-gassing. However, the level of moisture loss did have a reduction in overall strength of the test subjects when compared to previous four day-cured strength tests (Compression and Tensile) as shown above in Tables 4.2 and 4.3. As can be seen, the de-gassed samples displayed an order of magnitude reduction in strength tests when compared to the 'standard' curing time of four days results.

On testing both parts for porosity, the refilled cylinders showed a large level of pores present in the material matrix. Figure 4.18 reveals the level of porosity in the refilled tubes and when compared to Figure 4.17 (the direct de-gassed test). The level of porosity from the refilled tube was comparable to the case considered in finalising element number one.
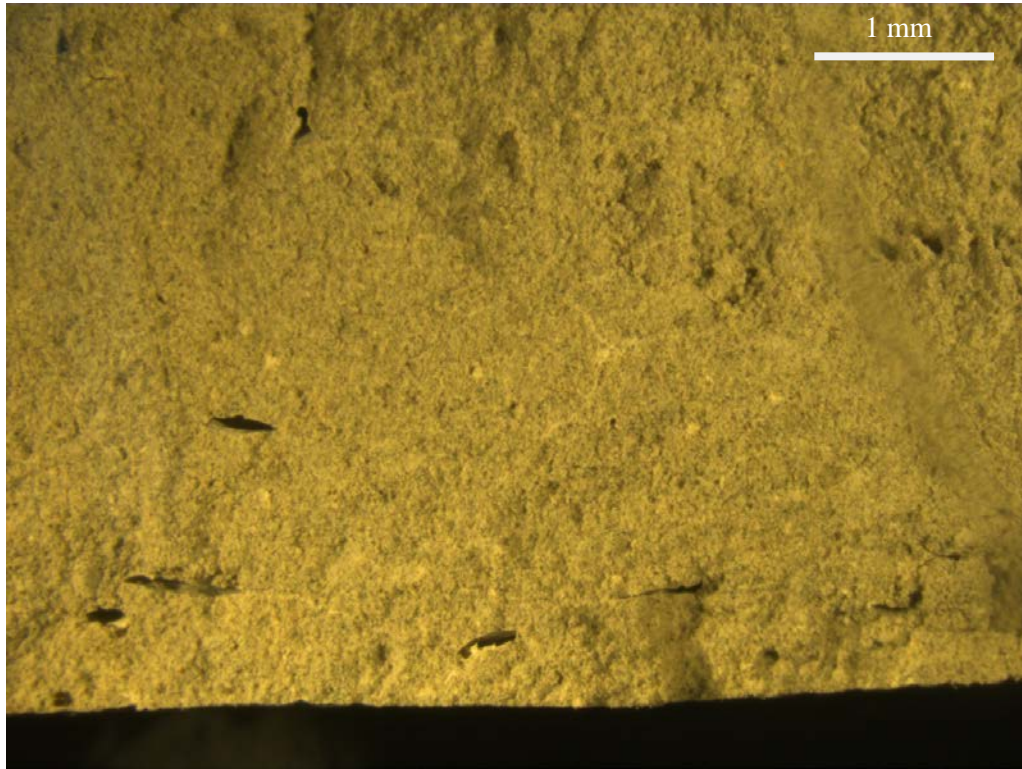
Figure 4.17: A photo of the direct de-gassed sample after testing. Note the pores at the bottom of the sample show elongation which was considered to be an effect from the material slumping back down into the tube after the vacuum pressure was released.

The direct de-gassed samples showed a few pores were present at the bottom of the cylinder and elongated in shape as shown in Figure 4.17. The positioning of the pores was due to the vacuum not having enough time to extract the air pockets out of the mixture. The shape of the pores was assumed to be material slumping after the vacuum pressure was released. The target chamber was brought up to atmospheric pressure over a period of 20 minutes and therefore the material would have been held in its quasi-perturbed state by any air pockets the vacuum was extracting and slowly relaxed thereby 'squashing' the air pockets as the material rested under gravity.
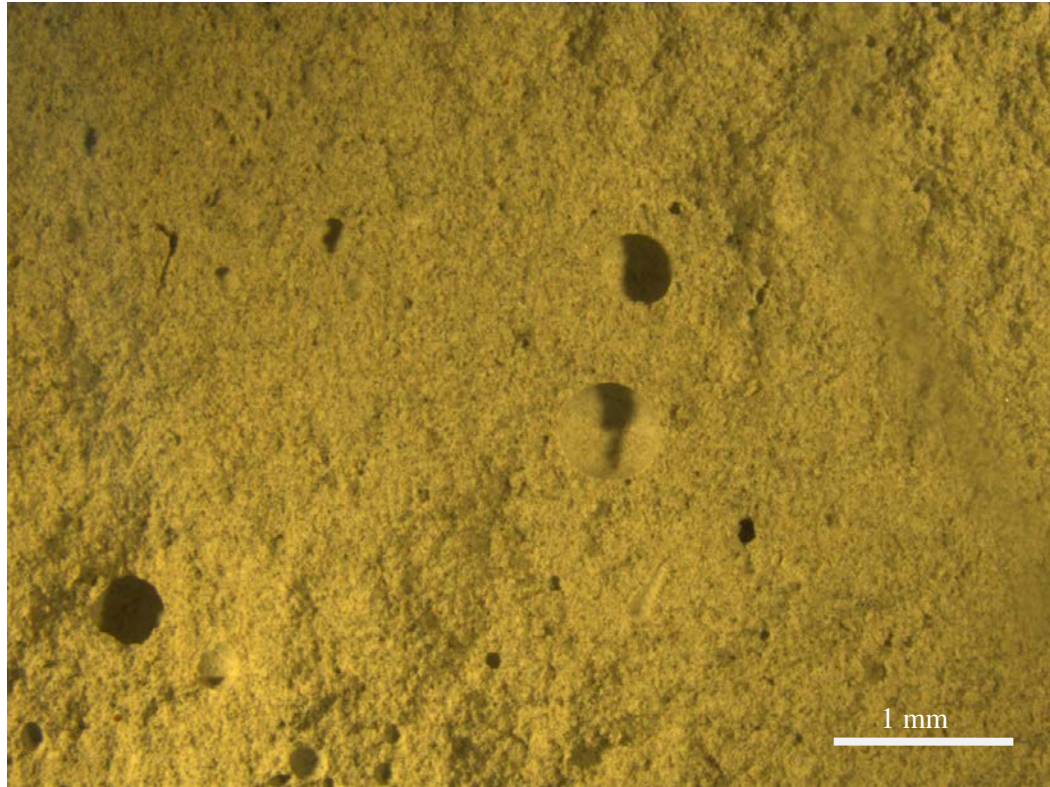
Figure 4.18: The cement in this finalising test was extracted from the large de-gassed container and poured carefully into the tubes. The level of porosity shown is very similar to finalising element number one detailed in Figure 4.14.

Table 4.4: Percentage levels of porosity

Method	Theoretical Mass[*] g	Measured Mass g	Porosity Level %
Finalising Element 1	119.41	68.90	42.30
Finalising Element 2	119.41	82.15	31.20
Finalising Element 3 (a)	119.41	109.86	8.40
Finalising Element 3 (b)	119.41	72.96	38.90

The overall level of porosity of each finalising method was determined through a density calculation. Cement mortar is given the density of 2.16 g cm^{-3} (Aqua-Calc 2012) and so with the cylinder test subject measurements, the mass will change as a result of porosity because the theoretical mass was calculated using the density value of 2.16 g cm^{-3} assuming zero porosity and the volumes of the samples were directly measured.

The calculated values of mass change from the theoretical mass are given in Table 4.4 as a simple porosity percentage value.

As noted in Table 4.4, the simple percentage values of the porosity from the mass change shows only one value which is low; finalising element 3(a) which was the direct de-gassing of the cement mixture. A certain level of caution is needed for this result as it shows a very low value, but as already noted; the mixture lost a lot of water moisture during the de-gassing which, in turn, affected the strength of the test piece.

Also noted are the porosity levels from finalising element 1 (poured and settled method) and finalising element 3 (b) (de-gassed refill method). Here it is seen that the percentages are very close (within 10%) once again showing that the larger pores were taking up more space in the cement matrix.

Finalising element 2 (the vibration method) shows approximately 31% of pore space within the material matrix. This method of pore reduction was considered to be the best at reproducing targets with lower values of pores (in comparison to just pouring the mixture and leaving it). The use of the test tube vibrator also meant that the production of the cement targets was less time consuming when considering the time taken to pump down the target chamber for de-gassing.

4.4 Summary

The method of making spherical cement targets has been described. The method chosen for the use in the thesis was to reduce the level of porosity via agitation through the test tube shaker and to allow the targets to cure for four days.

The targets used for the purposes of this work had corresponding average characteristics of 30% porosity and 1.8×10^8 Pa material strength. Work was not conducted to find how the strength of the cement paste changed as a function of porosity. The porosity was to be kept as low as possible and as constant as possible with respect to the manufacturing processes described in this Chapter. As an element of future work, an investigation of the relationship between porosity and material strength is suggested.

Chapter V: Experimental Methodology III: The Target Holders

The nature of the work contained in this thesis required the need to design, and build, specific apparatus in order to achieve the goals of investigating rotational catastrophic disruption, and the effect of temperature in the cratering process. As will be covered in this Chapter, three target holders were produced to aid in the experiments. Each of the target holders were designed by the impact laboratory experimental officer (Mr Mike Cole) with input for the heated target holder and the MeX stereomount (covered later in this section) from the author of this work and made by the University's workshop.

5.1 The Rotating Target Holder

The catastrophic disruption project required the target to be rotating in order to investigate the level of influence the rotation has on the target during the initial stages of a hypervelocity impact. To achieve this, a rotating target holder was designed and made. The pre-requisites of the target holder were such that the holder needed to work at approximately 0.5 mBar pressure, had variable rotational rates, was resilient enough to withstand the energies from the impacts striking the targets and any secondary or off-trajectory impacts striking the rotating target holder itself.

The rotational rate of the rotating target holder was designed on rotational values to be at least the rotational rates of the largest non-protoplanetary asteroid in the main belt 4Vesta (Russell et al. 2012). This was calculated as follows:

Vesta acceleration due to Gravity $g = 0.25 \, ms^2$ (Hamilton 2014)

Target surface acceleration $= r\omega^2$

$$\therefore r\omega^2 \geq 0.25 \, ms^2$$

$$\omega = \sqrt{\frac{0.25}{0.0375^2}}$$

$$\omega = 2.58 \, rad \, s^{-1} \, or \, 0.41 \, rotations \, s^{-1}$$

Knowing the rotation of 4Vesta gave the lowest rotational value comparable to an actual asteroid. The upper limit of the rotating target holder was rated at 3.44 rad s^{-1} and therefore was noted as a rotational limit to use because any effects seen from rotation would be noticeable at this rate.

However, due to the increase of the rotational rate being close to fast rotating asteroids, a simple calculation was made to see whether the rotational rate of 3.44 rad s^{-1} was negligible enough in comparison to the impact velocities being used in the experiments.

The catastrophic disruption project used a variety of impactor diameters from 1 to 3 mm stainless steel ball bearings and included one shot which used a solid nylon projectile. In order to simplify the calculation, a diameter of 2 mm was used. Also the impact velocities ranged from 1 to 7.2 km s^{-1} but a mid-point velocity of 5 km s^{-1} was used to aid in the calculation.

In terms of projectile-target interaction times, a specific equation is used:

$$\tau = \frac{L}{v_i} \qquad\qquad [5.1]$$

Where τ is the projectile interaction time in seconds, L is the projectile length in m and v_i is the impact velocity.

Using equation 5.1 we find the interaction time to be:

$$\tau = \frac{L}{v_i}$$

$$\tau = \frac{2 \times 10^{-3}}{5000} = 0.4 \; \mu s$$

The rotational rate of the target is equal to:

$$\omega = 3.44 \times 2\pi = 21.61 \; rad \; s^{-1} \equiv 1238.4 \; degrees \; per \; second \qquad [5.2]$$

Using the timing answer from [5.1] and incorporating the rotational rate obtained in [5.2], it is noted that the amount of target rotation during projectile flight is given by:

$$\tau \times \omega = 0.4 \times 10^{-6} \times 1238.4 = 4.95 \times 10^{-4} \; degrees \qquad [5.3]$$

The result obtained from [5.3] shows that during projectile, the rotational velocity is negligible in comparison to the impact velocities being used, and that any effect of projectile-target contact during rotation is very minor but the rotational effects would be attributed to the actual rotation of the target before and after the collision.

The resulting apparatus is shown in Figure 5.1. In position 1 from Figure 5.1, the cement targets are placed into position which is then held by two aluminium alloy (for light mass) restraints; the target base at position 4 and the clamping crown and tines at position 2. The aluminium alloy target base (measuring 39.92 and 33.87 mm outer and inner diameters respectively and 36.50 mm in height), along with the clamping crown (24.99 mm diameter and 33.03 mm length including the tines and 27.00 mm without including the tine lengths), are adjustable to accommodate varying target diameters (from 75mm to 100mm).

If the impact energy is insufficient to catastrophically disrupt the target, the cratered targets must remain in position to avoid falling targets breaking upon impact with the rotating target holder or the target chamber itself. To safeguard against the target falling from the holder after being non-catastrophically cratered after an impact, the tops of the cement targets have the crown tines inserted into the body therefore allowing the targets to remain in place if not disrupted (Figure 5.2).
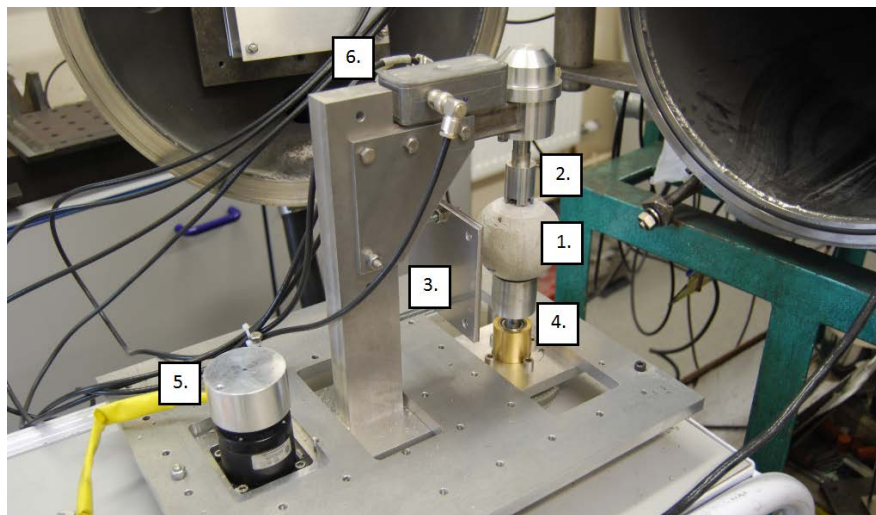
Figure 5.1: The rotating target holder (made from aluminium) was designed (by Mike Cole) specifically to work in the target chamber of the light gas gun. 1- Target position, 2 – Crown, 3 – Central strut shield, 4 – Rotating base holder, 5 – Vacuum motor and 6 – Electrical relays.
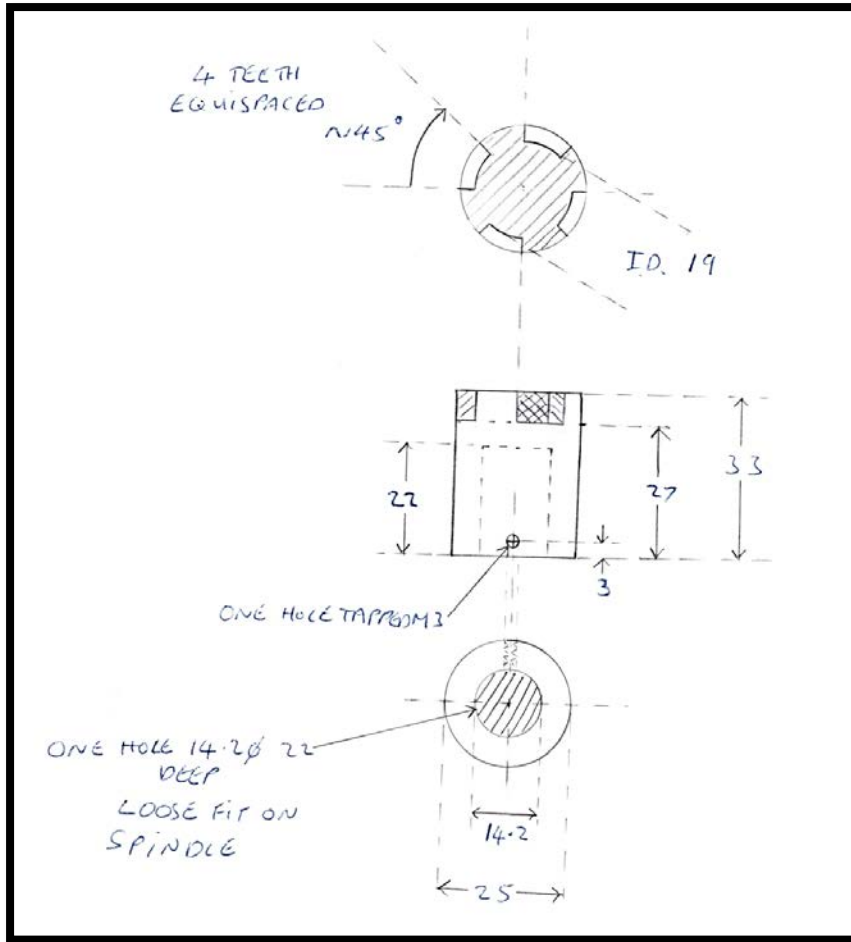
Figure 5.2: The design schematic of the rotating target holder's restraining crown (by Mike Cole).

Table 5.1: Rotating target holder tine test data

Cylinder Number	Test Type	Test Data		
		Cylinder Volume (mm^3)	Crown Tine Volume (mm^3)	Strength (Pa)
1	Youngs Modulus Test	42385 ± 46	22.64	$1.86x10^8 \pm 1640$
2	Corresponding Youngs	43493 ± 49	0	$1.88x10^7 \pm 1120$
3	Brazilian Modulus Test	41392 ± 56	21.43	$1.21x10^6 \pm 118$
4	Corresponding Brazilian	44943 ± 51	0	$1.19x10^6 \pm 143$

The possible introduction of weaknesses into the target from inserting the crown tines into the top section was tested. Table 5.1 shows the results from tests in order to find whether the insertion of the tines did reduce the strengths of the targets. The results showed that the compressive strength test was comparable to the average strengths tested in Chapter 4 results Table 4.3; 1.86 x10^8 Pa.
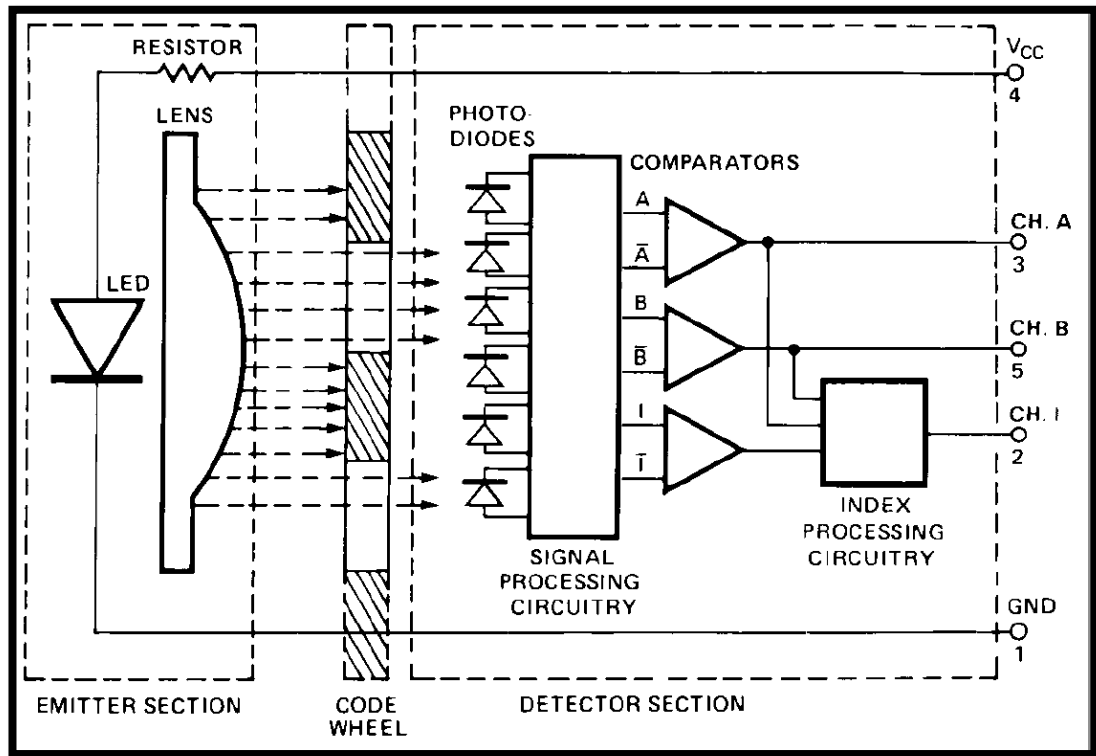
Figure 5.3: A block diagram from Agilent Technologies showing the internal structure of the Series Three Channel Optical Incremental Encoder

The top cross beam of the rotating target holder was designed to house an Agilent AEDB-9140 Series Three Channel Optical Incremental Encoder with Codewheel (Figure 5.3). The incremental encoder used a LED to produce light which was blocked by the attached codewheel. The codewheel was attached to the stainless steel upper spindle which forms the section of the holder above section 2 of Figure 5.1 and used to detail information on the rotation of the targets. The codewheel was also chosen due to containing an index pulse reference marker (encoder mark) (Figure 5.4). This marker was used to define the 'front', or gun facing direction, for the targets and was sometimes used in order to give a point of reference on cratered rotating targets.
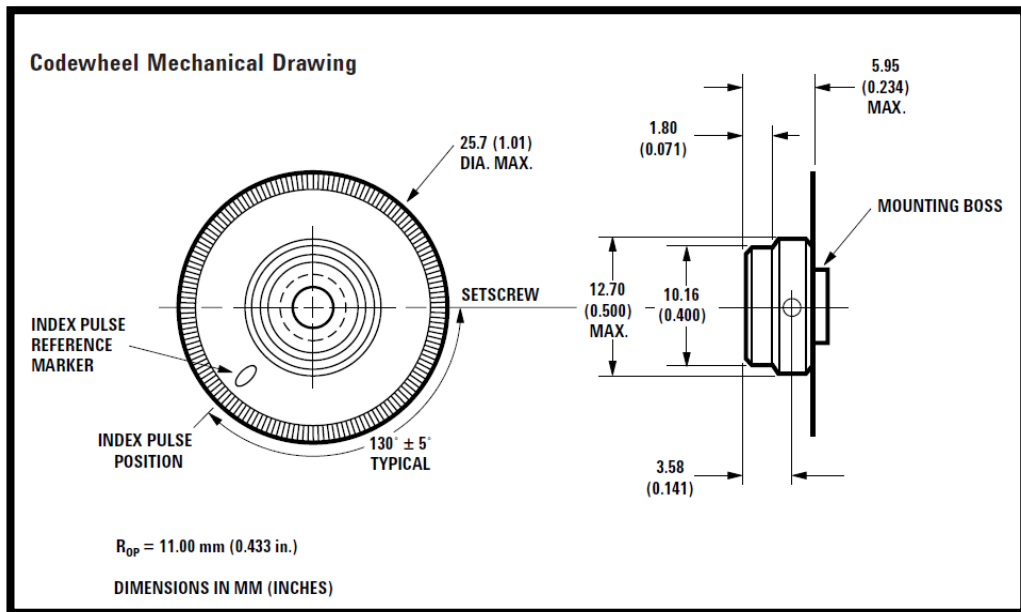
Figure 5.4: The schematic of the codewheel used to determine the rotational data for the target holder, source Agilent Technologies.

Figure 5.1 position 3, shows the necessary shielding in the plane of the impactor trajectory used to protect the central strut. The shielding is necessary to protect the central strut because of impactor spread along the projectile axis being approximately 1 cm^2.
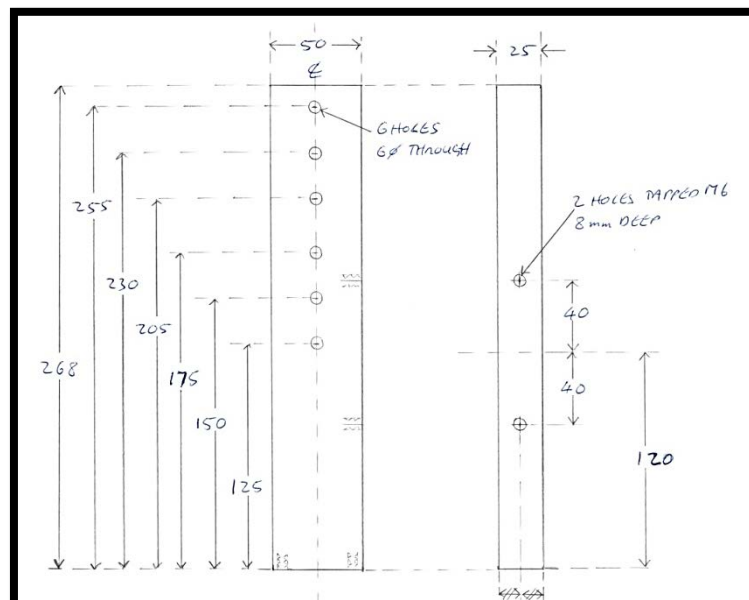
Figure 5.5: The central strut of the rotating target holder was designed to allow for the accommodation of a range of targets (by Mike Cole).

However the projectile is sometimes followed by sabot pieces, or internal gun debris, which has been impacted en route by the projectile which would shorten the working life of the rotating target holder.   The aluminium alloy strut (Figure 5.5) measuring 273 mm in height, 25.27 mm in width and 50.07 mm in depth was designed to accommodate different target sizes.   Several M8 bolt holes were drilled at 25 mm intervals so that the top assembly could be increased to accommodate targets up to a size of 200 mm.

Position 5 (Figure 5.1) shows the stepper motor (Farnell #959-8693). The motor is a 12 volt 4 phase unipolar electromagnetically driven vacuum motor with a working holding torque of 0.539 mNm. It was imperative to use this type of motor for the type of environment it would be subjected to; a vacuum. If an oil or lubricant based motor was used instead, the pressure differential between the target chamber environment and the internal sections of the motor would have resulted in the extraction of the oil, or lubricant, from the motor into the target chamber. This in turn would have resulted in two undesired effects, the pump down of the target chamber pressure would not have been achieved until the flow of the oil/lubricant had ceased and the vacuum pump filters would have been damaged from attempted to extract the oil or lubricant.

The Farnell motor is attached to a Synchroflex 15 teeth timing pulley which drives a rubber belt underneath the metal platform of the target holder. The belt is connected to another Synchroflex pulley with 60 teeth which is attached to the rotating assembly where the target base is situated.

Position 6 (Figure 5.1) three data feeds from the rotating target holder are used to ascertain the position and rotational speed of the targets whilst in the target chamber. One feed is used to determine the fiducial marker of the target whilst rotating. The two remaining data feeds are allocated to the quadrature phases of the motor. When the targets are impacted, the data obtained from the phase lines will show whether the impact was on or off target. If the target was impacted off centre towards the right hand side of the target's central axis with respect to the projectile trajectory, the data obtained from the target holder phase feeds would show an increase of rotation experience by the target itself. Conversely, if the target impact was towards the left hand side, the data would show a retardation of rotation of the target. Also from the

data provided from the position 6 can be used to show the level of projectile axis deviation as increasing distances away from the central rotational axis would show greater amounts of rotational acceleration or deceleration.

5.2   MeX Stereomount

The second phase of the project contained in this work required algorithmic three-dimensional construction of craters resulting from the variable temperature impacts. The constructed Digital Elevation Maps, or DEMs, help to provide crater data such as depth, diameter and volumes without altering the crater morphology by invasive measuring techniques.   The importance of being able to measure crater characteristics without altering or destroying the crater itself is of great importance due to the need of being able to re-measure the crater in its original condition at later times.

The programme used for this non-evasive measurement technique comes from Alicona (http://www.alicona.co.uk/home/products/mex.html, site accessed August 2015). The MeX programme is extensively used in surface analysis industries. In order to construct the DEMs, photos of the craters are taken with a microscope and camera. The samples need to be rotated through small angles around a rotational axis in order to provide the programme with the required field of views to ascertain the correct depths etc.

The MeX Stereomount (Figure 5.6) was designed in order to achieve this aim.
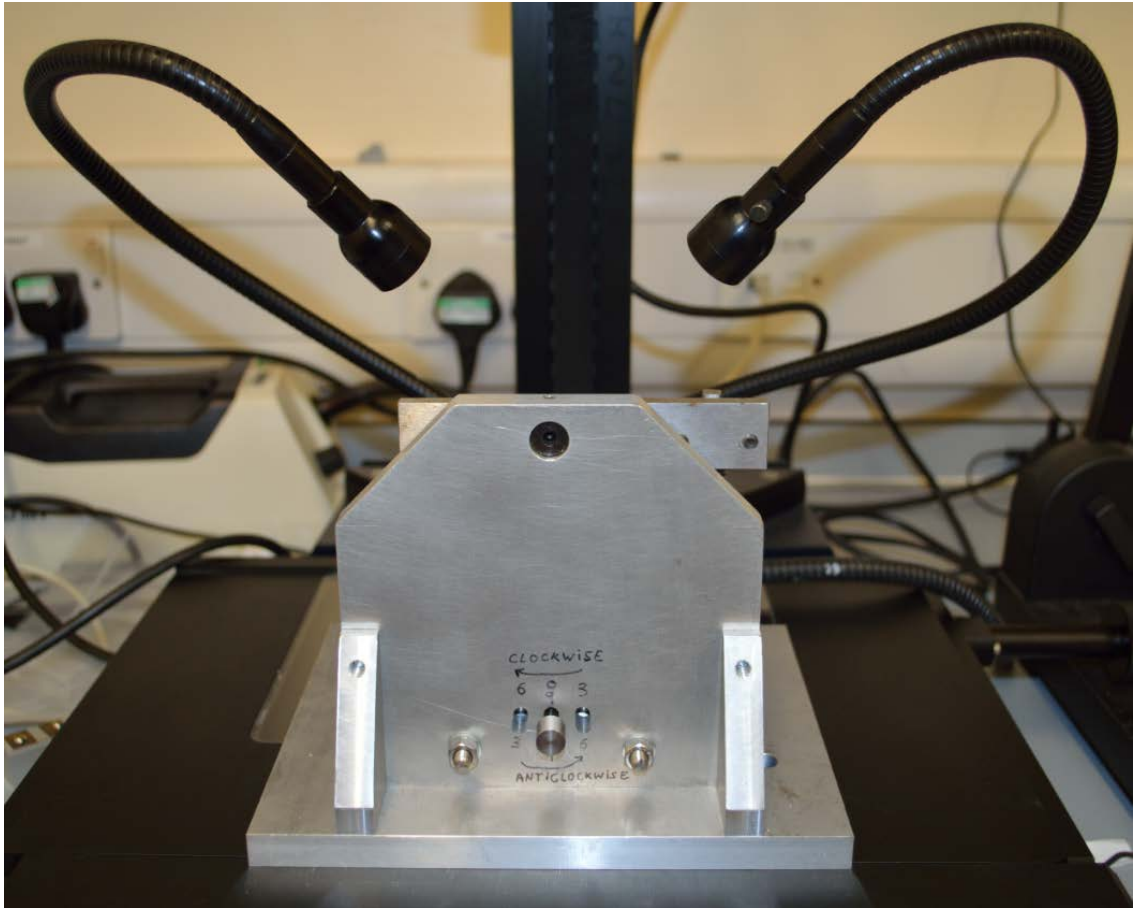
Figure 5.6: The target mount for obtaining the photos for the MeX programme; The MeX Stereomount, two light guides used to illuminate the targets are also shown.
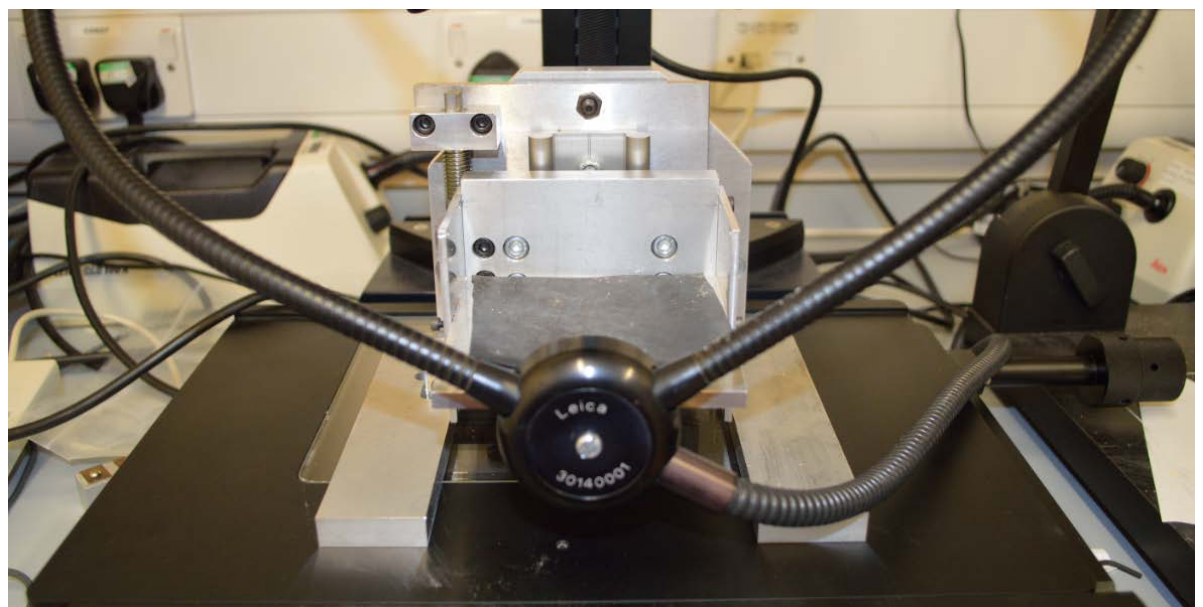
Figure 5.7: The Leica Fibre Optic mount attachment to the base is needed to illuminate targets during image capture.
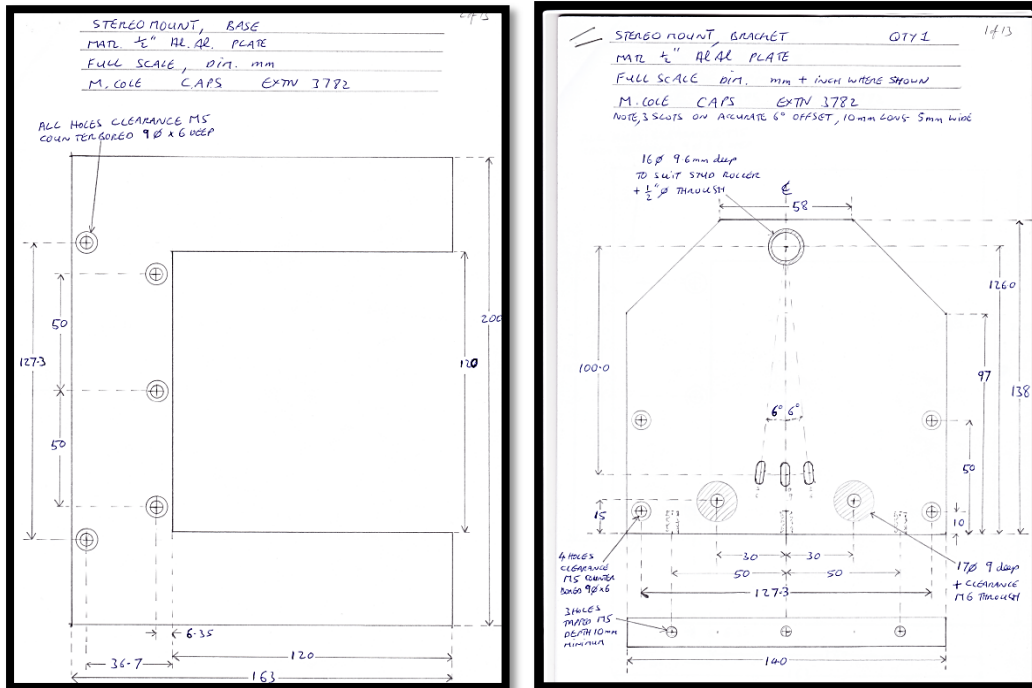
Figure 5.8 (a) (b): Design schematics for the MeX Stereomount base section and the bracket respectively (by Mike Cole).
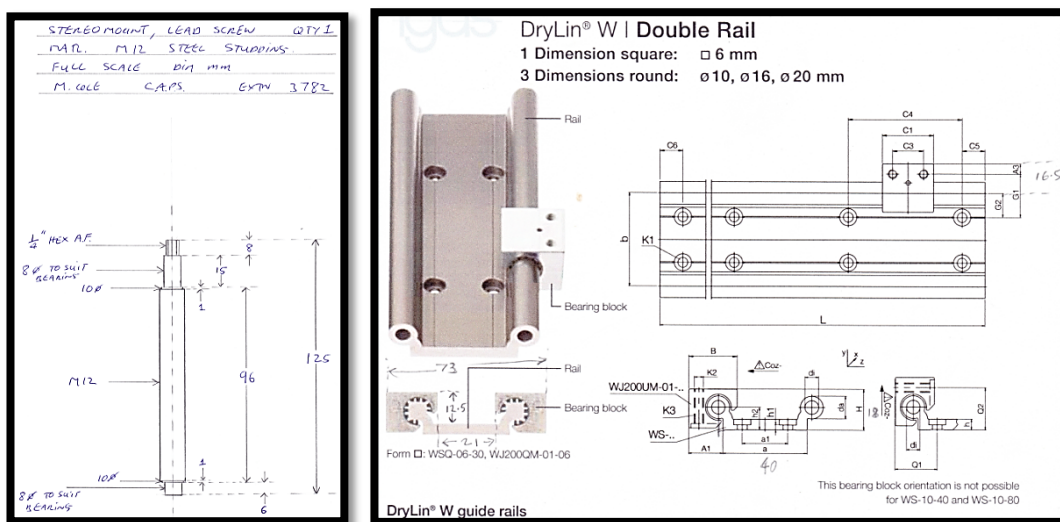
Figure 5.9 (a) (b): Design schematics for the adjusting lead screw (a) (by Mike Cole) and the DryLin double guide rail.

The MeX stereomount is an aluminium metal target holder with an adjustable target base measuring 200 mm at the base of the holder (Figure 5.8 a) and 134 mm in height (Figure 5.8 b). The height adjustment to allow for sufficient image focus is

achieved through rotating a lead screw with a thread approximately 96 mm in height and is positioned at the top. The lead screw thread raises or lowers the adjustable base through a range of 0 to 120 mm along a DryLin double guide rail (Figures 5.9 (a) and (b) respectively).

Attached to the adjustable base is a fibre adaptor light screw attachment needed to illuminate the craters (Figure 5.7). This was an important consideration in the design of the Stereomount because the use of a lighting system external to the mount and not remain constant in the Stereomount's rotational frame of reference would invalidate the construction of the DEMs by introducing non-constant shadows.

The black section of rubber on the adjustable base is required to prevent damage to the targets from the metal base and to aid in keeping the target samples fixed when being tilted.

As can be seen in Figures 5.6 and 5.8 (b), the Stereomount is designed to rotate around the central axis in steps of 0, 3, 6 and 9° in left and right tilts. The MeX software is constrained to stereopairs (images used to construct DEMs) sweeping through small angles; one feature of the programme is to use three images swept through angles greater than 10° left to right for the basis of calibration. Commonly for the purposes of this project, the angles were kept small at 6° total left to right.

5.3   The Variable Temperature Target Holder

The final phase of the project, was designed to ascertain whether any changes in crater morphology resulted from differences in target temperature. The variable temperature crater impact project required rock targets to be impacted through a range of temperatures; 83 to 1273 K with heating of the targets to be continued during the pump-down phase of the light gas gun and to hold the required temperature during a shot.

The variable temperature target holder was designed specifically with the aim to heat rock targets up to 1200 K, whilst being robust enough to survive the shocks produced in the targets during the hypervelocity impacts. Another important factor

in the design was to ensure that the temperature of the target could be read whilst in-situ.
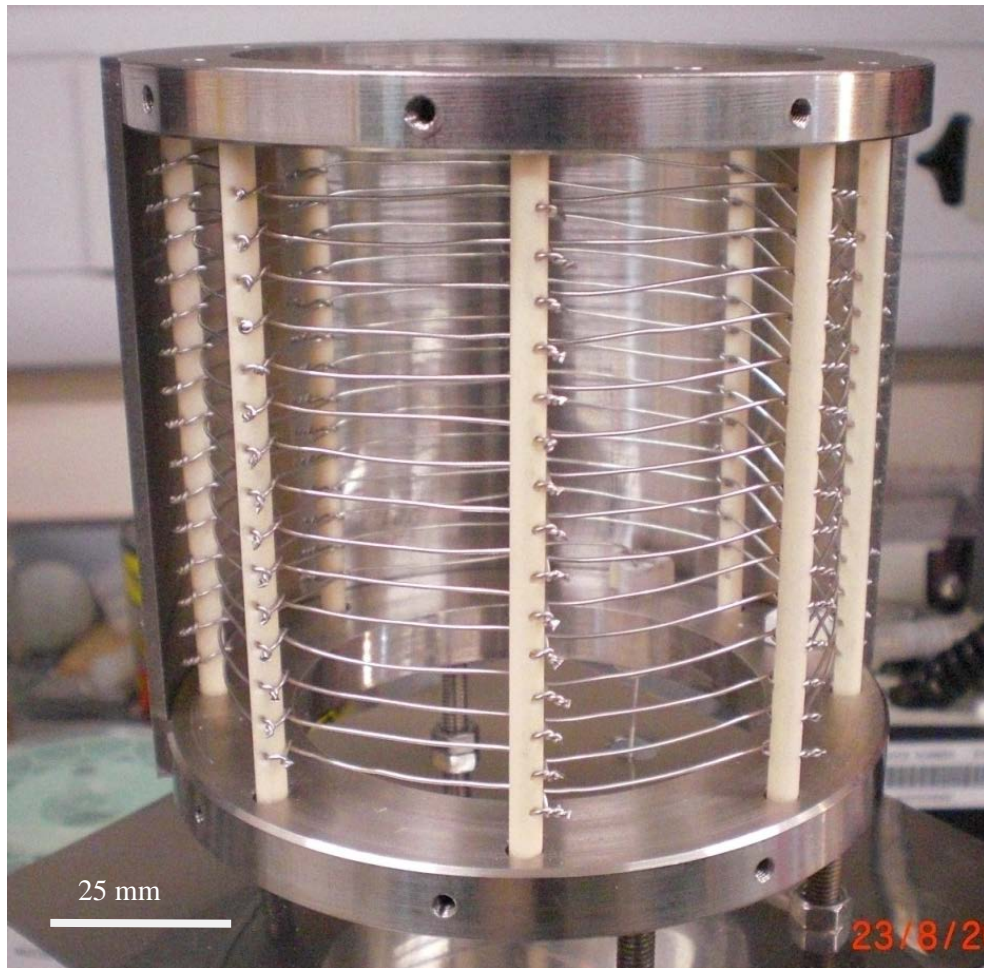
Figure 5.10: The assembly stage of the heating element for the variable temperature target holder. The rock sample is inserted from the top and sits in the centre of the holder.

The top and bottom of the target holder had two rings of 316 grade stainless steel measuring 68.2 and 104 mm inner and outer diameters respectively (Figure 5.10). Each steel ring is separated by alumina rods measuring 100 mm length and 4 mm diameter. The rods act not only to separate the two steel rings and thereby accommodating the rock samples, but also to position the heating element wires as shown in Figure 5.10.
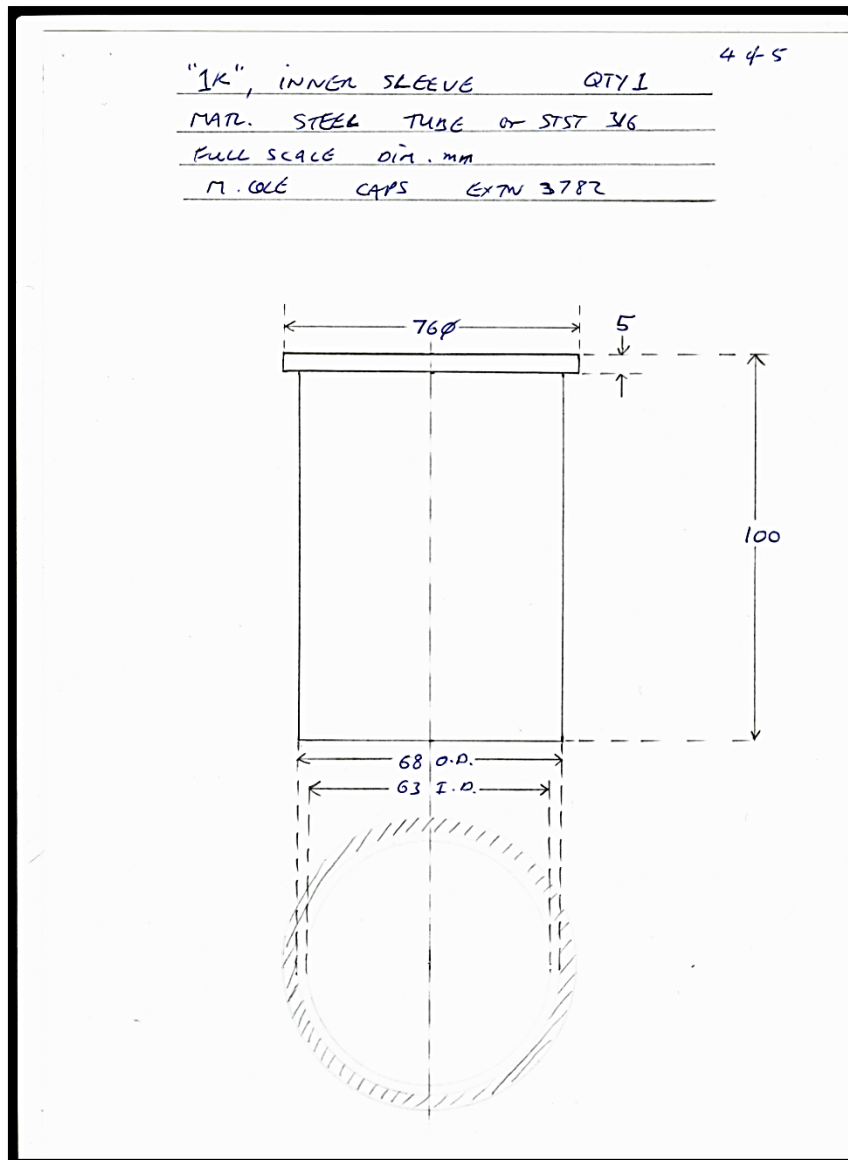
Figure 5.11: A schematic of the inner sleeve used to separate the heating element away from the samples (by Mike Cole).

The heating element wires were chosen due to being capable of maintaining a high electrical current in order to heat the rock samples to temperatures close to 1200 K. In order to protect the samples from directly touching the heating elements, an inner sleeve measuring 100 mm in total length (Figure 5.11) made from mild steel was attached to the assembly. This allowed for a large area of heating of the rock targets to ensure good thermal conductivity to the samples.
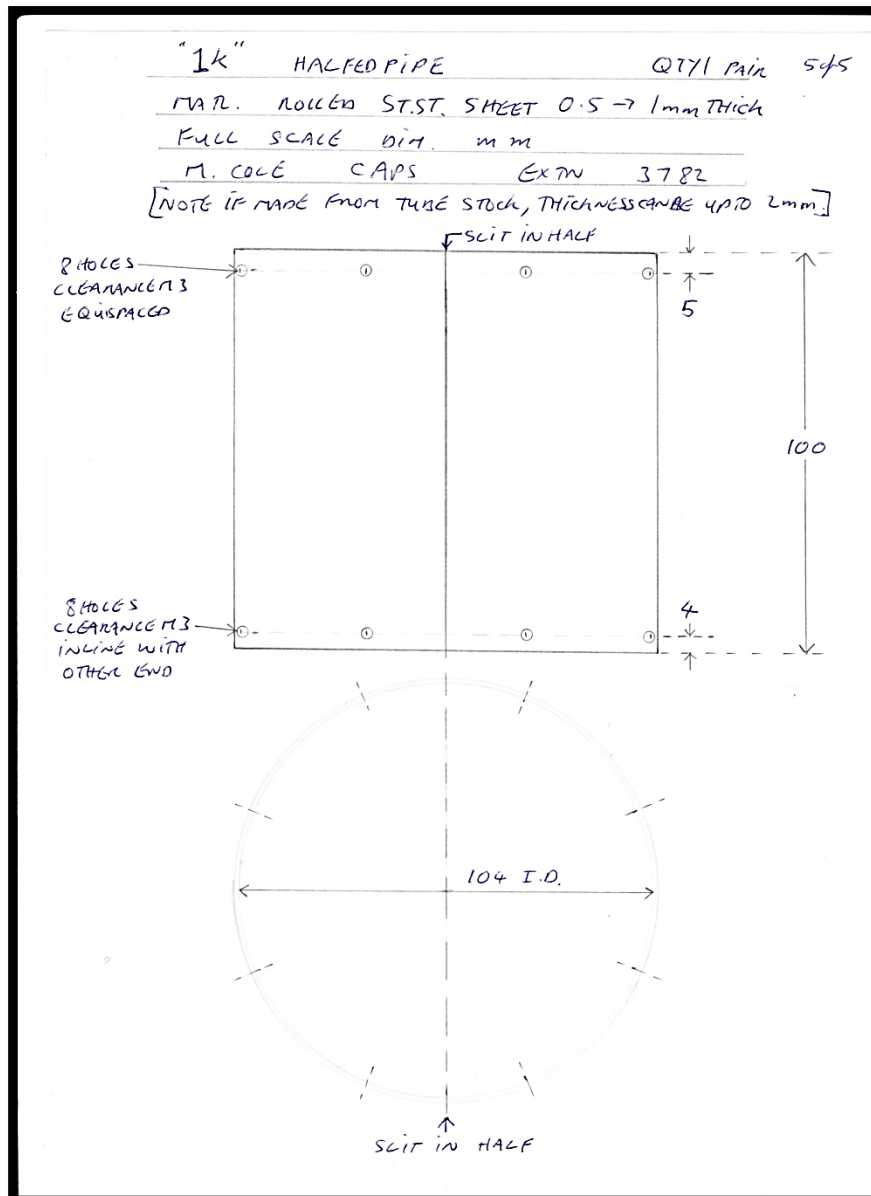
Figure 5.12: Design schematic of the steel halved pipe heat reflector needed to redirect the heat back into the sample (by Mike Cole).

Figure 5.12 shows a secondary stainless steel sleeve called the halved pipe. This sleeve measuring 100 mm in length and 104 mm in diameter was used to close off the heating element so as to protect operators and preserve the life of the heating element, as well as a thermal redirecting shield needed to intensify the thermal energy towards the rock samples. This allows for greater, and more efficient, heating of the samples.

However, it was important to separate the sleeve into two sections, to allow for easy access to the heating element for maintenance and holder inspection; this proved very advantageous as will be discussed in Chapter VII Experimental Processes.
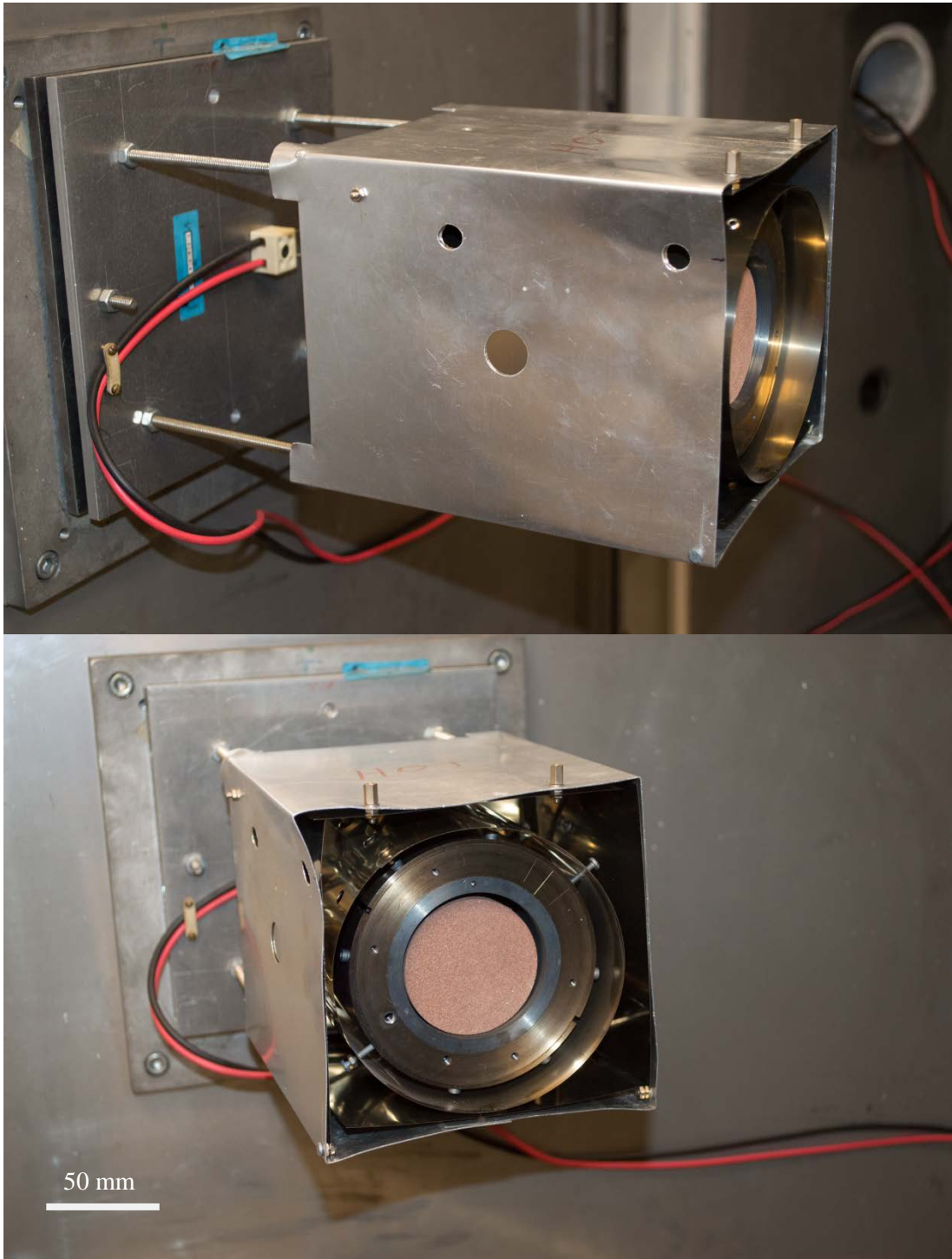
Figure 5.13: The fully assembled variable temperature target holder with enclosure. The protection plate at the front of the holder has been removed to show the complete internal set-up.

Another section of the holder to aid in reflecting the thermal energy towards to the sample, were eight sections of steel plate reflectors positioned around the half-pipe section. Just as with the halved pipe section, the plate reflectors aided in the heating of the samples whilst simultaneously protected the outer aluminium casing of the holder; if the reflector plates were not present, the outer casing would distort rapidly during heating, and would have needed to have been replaced frequently.

In order to mount the heated target holder to the target chamber, an aluminium mount plate measuring 145 mm^2 was designed. The target holder was attached to the plate by the means of four mild steel rods attached and provided a clearance distance of 100 mm (Figure 5.13). Also added to the mount plate was a thermal conductivity strip displaying the surface temperature of the mount plate and therefore the level of heat energy being lost through the target holder into the mount plate and then onto the target chamber door.

Chapter VI Rotational Catastrophic Disruption: The Experiment

Catastrophic disruption experiments have been conducted by many research groups using experimental apparatus and computational modelling. In order to investigate whether rotation has any effect on the outcome of an impact which is fast enough to initiate catastrophic disruption, experiments using the equipment discussed in Chapters 3 and 5 are detailed in this Chapter. The following explains the experimental and theoretical methodologies, as well as methods used to obtain data from impacts into cement paste targets.

6.0 *Mould Preparation*

Figure 6.1: Initial mould preparation stage would start with cleaning and greasing the hemispherical moulds with Carlube LM2 grease. The moulds were then covered in heat sealed cling film to prevent spillage.

The moulds were inspected for cleanliness and cleaned because of the risk with dried or older fragments of cement introducing changes to the strength of the cement targets. The inner walls of the moulds were greased with Carlube multi-purpose LM2 Grease (Figure 6.1) to aid in removal of the targets after the curing time had elapsed.

Once the inner walls were lubricated, the mould hemispheres were attached together with the aid of M8 bolts and nuts. The whole mould was then wrapped in Polyethylene

wrapping film (Figure 6.1) and then heat shrunk onto the mould to prevent cement leakage from small gaps in the mould lips.

Figure 6.2: The cement mixtures were made from 7 parts cement to 3 parts water.

6.0.1 Cement Target Manufacture

Pre-sieved cement powder and water contents were measured out to attain the required ratio of 7 parts cement to 3 parts water and then mixed in a metal bowl as shown in Figure 6.2. Sieving the cement powder was an important step to ensure that only loose, fine, cement was mixed; any large lumps of cement might not have been properly hydrated, therefore creating weak points of pure dry cement inside the targets. The cleanliness of the mixing bowl was of great importance due to the risk of mixing previously made and dried cement into the targets, therefore the mixing bowl was cleaned of loose dried cement prior to target manufacture.
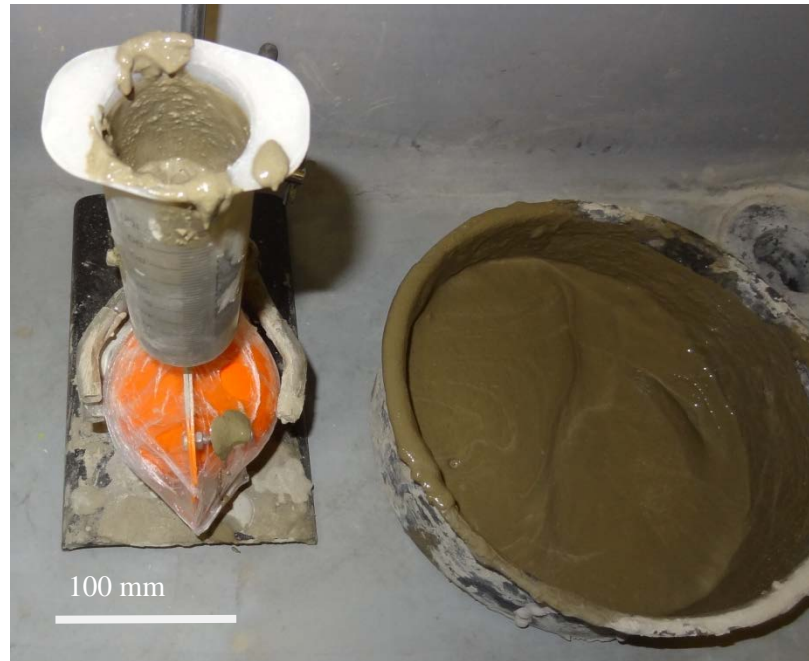
Figure 6.3: Shown here is the filling stage of the cement target manufacture. The apparatus used was a 100 ml Plastipak syringe to fill the moulds with the cement mixture seen on the right.

6.0.2 Setting the Moulds

When the mixing of the cement mortar was finished, the moulds were held in a retort stand and a Plastipak 100 ml syringe was inserted into the channel at the top of the moulds as shown in Figure 6.3. To begin with, the cement mixture was poured into the syringe and the action of gravity-fed the mould with the cement mortar with the syringe acting as a funnel. As the mould filled to approximately 2/3 volume full, the internal pressure inside the mould, and the natural viscosity of the cement balanced the action of gravity and therefore the syringe plunger was needed to inject the final third of the cement. This final step did have the unwanted action of introducing air pockets into the cement mixture and for that reason, it was important not to allow the syringe to fully empty. The final stage of this section of the process required the use of the test tube oscillator shown in Figure 6.4.

The mould was released from the retort stand and the bottom lip was placed into the oscillation cup. The moulds were shaken for one minute to release trapped air inside the mixture and then placed back into the retort stand. The moulds were placed at the

same position in the laboratory throughout the project during curing, so as not to introduce further variables such as excess moisture from the sink area or temperature fluctuations.

Figure 6.4: In order to remove as many air pockets in the cement mortar a test-tube shaker was employed to vibrate the mixture for one minute.

Figure 6.5: The moulds, once filled, needed to be positioned in a constant designated area in order for environmental effects on curing to be negated as can be seen in this Figure. The tubes of cement seen next to the moulds were used to ascertain physical properties for their respective cement targets.
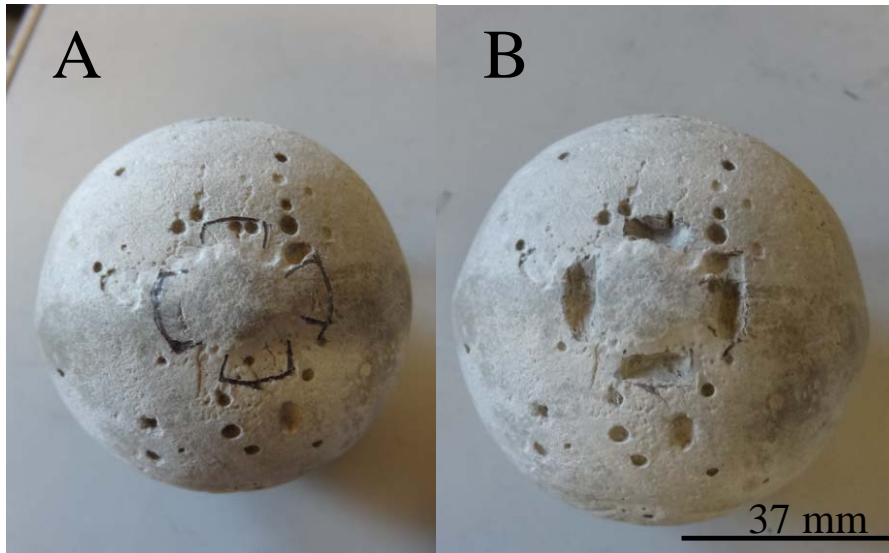
Figure 6.6: Targets after one day curing in the moulds. Still being 'soft' meant that the targets were easily adapted for the holder as shown by the carvings.

6.0.3 Curing

From previous experiments into the effect of curing time and associated weaknesses (detailed in Chapter 4: Cement Target Manufacture), the optimum time for curing the cement targets was calculated to be four days. Even though this time frame did not yield the highest recorded strength of the material, the point lies on the increasing trend of the strength data fit. Also the timing constraints with respect to the light gas gun and the project length in general, meant that waiting for any further time rather than the four day period, would extend the project in completion time considerably and further affect the timetable for the whole PhD project.

Once the moulds were filled, shaken and placed in the designated drying area, as shown in Figure 6.5, they were left to cure for one day. After this the moulds were opened and the targets were removed and dried outside the moulds for three days.

Upon release from the moulds, the targets were weighed in their excess-moisture states and the tops were prepared for restraining crown tines as shown in Figure 6.6 A and B. Cement strengthens as it dries, the removal of the restraining crown tine volumes from the tops of the targets was easier than if the cement was allowed to fully dry and then worked on. Preparing the targets at this stage also meant the cement was softer and easier to manipulate and therefore would not introduce flaws (apart from those already present internally) at the points to be held by the tines.

6.0.4 Installation of the Targets

The installation of the cement targets was carefully done during the set-up procedure of the light gas gun. Once the targets were cured, they were positioned in-between the clamping crown and the cup base as noted in Figure 6.7 of the rotating target holder. After the clamping crown restraining screw was tightened, the sphere was checked for lateral motion perpendicular to the rotational axis. This was done by moving the sphere very gently (so as not to break any cement near the tines) in situ and then rotating it by turning on, and increasing the speed of the rotation vacuum motor slowly to the set maximum speed of 3.44 rev s^{-1}.
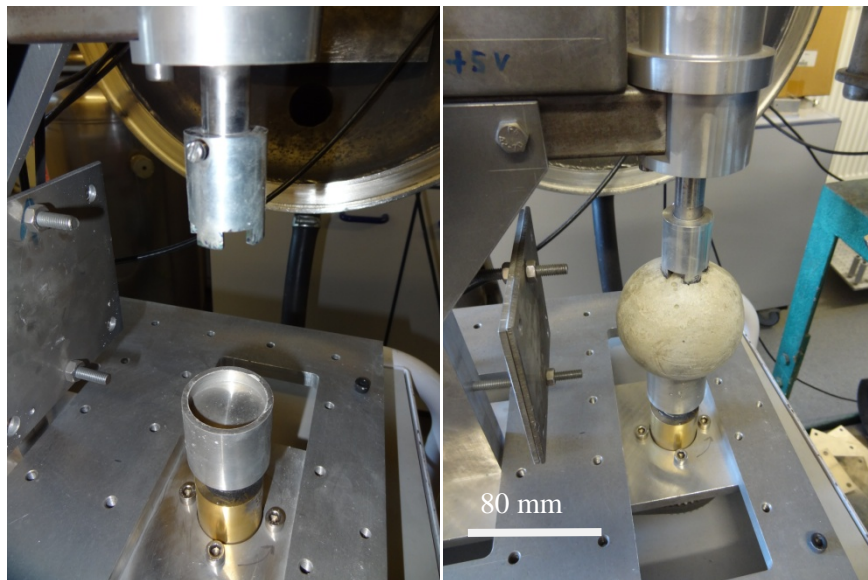
Figure 6.7: The targets once ready are positioned in-between the base cup and the restraining crown.

6.0.5 Removal of Target and Data Acquisition

A cement samples was removed from the target chamber and, depending on the shot characteristics the sample was either cratered or disrupted, as shown by Figures 6.8 and 6.9 respectively. For both cases, individual fragments were collected by hand and placed into a tray for weighing. Further debris and dust were removed from the target chamber by using a paper towel and then placed with the rest of the fragments in the collection tray.

For the case of disrupted material, the fragments were weighed separately and then placed onto one side in order not to mix weighed with non-weighed fragments. The individual fragment measurements were taken until a cut-off mass of 0.03g was achieved.
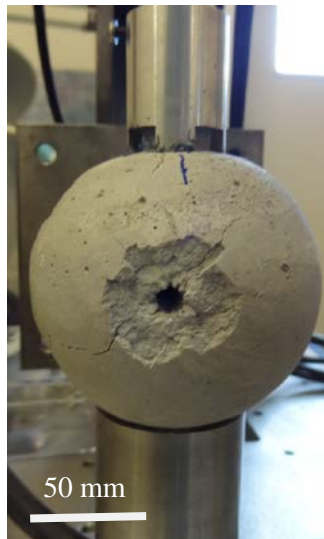
Figure 6.8: Here is shown a cratering outcome where there impact energy removed a small amount of target material but large cracks were present emanating from crater.

The remainder of mass (smallest fragments and dust) collected from the impacts were sieved through a series of Gilson Company USA Standard test sieves with holes of 2.8 mm, 2.0 mm, 1.4 mm, 1.0 mm and 500 μm. The collective mass ejecta were then tabulated into mass-distribution profiles. However it must be noted that the dust

collected during the sieving could also include particulates from the carbonised gas such as soot from the initial stage of the light gas gun firing.

For the case of cratering, the largest remnant piece is the main target body, is still held by the rotating target holder. This fragment was carefully removed from the restraining clamps in order for it not to break apart.

Figure 6.9: As a consequence of the shot characteristics, the experimental outcome will either be cratering (as seen in Figure 6.8) or disrupted as presented here.

Once the main target body had been removed from the target holder, it was placed in a collection tray along with any further debris as stated before. Also, as with the disruption data collection method, the fragments are weighed, or sieved, depending on mass profile and the results were tabulated and analysed.

However a caveat must be included at this point because of the nature of the impact, there is in all likelihood that the ejecta in both cases vaporise in the initial stages of the impact as the projectile interacted with the target. Although mass was lost because of the presence of the craters, mass loss from the targets were tested when pumping

106

down the target chamber. Mass results showed an approximate value up to 5% of mass is lost after the four day curing period when the targets are subjected to the vacuum pressure of the target chamber.

Catastrophic Disruption: Experimental Results

This Chapter outlines the results obtained from the catastrophic disruption experiments. Both experimental runs are covered, the rotational case and the static or (stationary) target case. It was deemed very important to include the static data in order to ascertain whether rotation of the body has any effect on the disruption outcomes. Two types of analysis were carried out, the first to determine Q^* from an impact and the other to find the fragment size distribution.

Section 6.1 *Q^* Determination*

Here we use the same data to determine the Q^* values of the static and rotating cases. As discussed in Chapter 2, the impact energy density value which corresponds to 50% remnant mass after an impact is called Q^*.

Data obtained spanned the two regimes of cratering and disruption; this was achieved by varying impactor diameter and impact speed. The masses for each largest fragment was normalised with respect to the original pre-shot mass. The key data and Q value for each shot are given in Tables 6.1 Static and 6.2 Rotating. Associated errors were found $\pm$ 0.01 m/m_o and 0.25% for Q.

The final column of both Tables gives notes associated with a particular shot, for example, if there were target defects which could affect the impact outcome or if the targets were hit by gun debris as well as projectile. Any shots which showed defects, or damage resulting from debris impacts, were not included in the data analysis. Based on the data shown in Tables 6.1 and 6.2, there were a total of 52 shots; 21 static and 31 rotational, with 6 failed shots, thereby detailing a 90% success overall.

The data for m/mo vs Q are plotted in Figures 6.10 and 6.12 respectively. As can be seen, the cratering and disruption regimes are distinct with a cross-over region between them.

Table 6.1: Catastrophic Disruption Static Data

Shot Code	Projectile Diameter (mm)	Impact Speed (kms^{-1})	m/m_0	Q Value (Jkg^{-1})	Notes
280311.3	1.0	1.124	0.99	7	
280311.4	1.0	3.06	0.99	52	
290311.2	2.0	1.731	0.98	117	
140311.1	1.0	7.5	0.92	280	
210311.3	3.0	1.954	0.97	518	
240511.1	2.0	3.87	0.29	592	
140311.2	2.5	3.05	0.72	701	
30311.2	2.0	4.58	0.72	861	
50711.1	2.0	4.84	0.00	895	Burst Disc impacted
120711.1	2.0	4.83	0.7	930	
100611.1	2.5	3.75	0.17	1107	
310513.2	2.0	5.68	0.55	1428	
70711.1	2.5	4.57	0.58	1655	
300911.1	2.5	4.44	0.11	1660	
30311.1	3.0	3.81	0.17	2144	
200712.3	3.0	3.79	0.19	2337	
210311.2	3.0	4.36	0.04	2609	
240513.1	3.0	4.25	0.04	2613	
150611.1	2.0	5.03	0.00	N/A	Surface cracks present

Table 6.2: Catastrophic Disruption Rotational Data

Shot Code	Projectile Diameter (mm)	Impact Speed (kms⁻¹)	Rot Speed (Hz)	m/m_0	Q Value (Jkg⁻¹)	Notes
90911.1	2.0	3.46	Failed		0	Hit by gun debris
150612.3	2.5	4.65	Failed		0	Hit by gun debris
60712.2	2.5	0	Failed		0	Hit by gun debris
150411.2	1.0	1.187	3.59	0.99	8	
50411.2	1.0	3.07	2.62		47	Forgot Ramp Switch
80411.1	2.0	1.63	3.384	0.99	98	
140211.1	3.0	0.999	3.44	0.96	157	
190111.1	1.0	7.75	3.47	0.94	317	
90211.1	3.0	1.916	3.43	0.44	555	
160511.1	2.0	4.05	3.39	0.73	700	
100511.1	2.0	4	3.44	0.68	734	
150711.1	2.0	4.71	3.45	0.34	815	
260811.1	2.5	3.46	3.46		1004	NHM
90911.2	2.0	3.46	3.46		1061	NHM
140911.5	2.5	4.54	3.44	0.32	1061	
260811.2	2.5	3.85	3.5		1243	NHM
90211.2	3.0	2.93	3.44	0.71	1323	
90312.3	2.0	3.86	3.44	0.71	1392	
20512.2	3.0	2.68	3.43	0.14	1388	
260811.2	2.5	3.85	3.43	0.41	1470	
210111.1	2.0	5.78	3.45	0.41	1479	
220711.1	2.5	4.24	3.51	0.79	1493	
240812.1	2.5	4.16	3.43	0.17	1589	
250211.1	2.5	4.09	3.45	0.47	1666	
150711.2	2.0	4.62	3.95	0.21	1677	
220612.2	2.5	4.61	3.45	0.39	2085	
140211.2	3.0	3.62	3.45	0.14	2114	
200712.2	3.0	3.81	3.46	0.13	2326	
80211.2	3.0	4.16	3.46	0.11	2527	
180211.1	3.0	4.07	3.44	0.08	2538	
90312.1	solid sabot	7.59	3.44	0.16	7114253	Q Value very large

*NHM denotes that the fragments were taken to the Natural History Museum for Cat-
Scan analysis before data analysis of the fragments were performed.
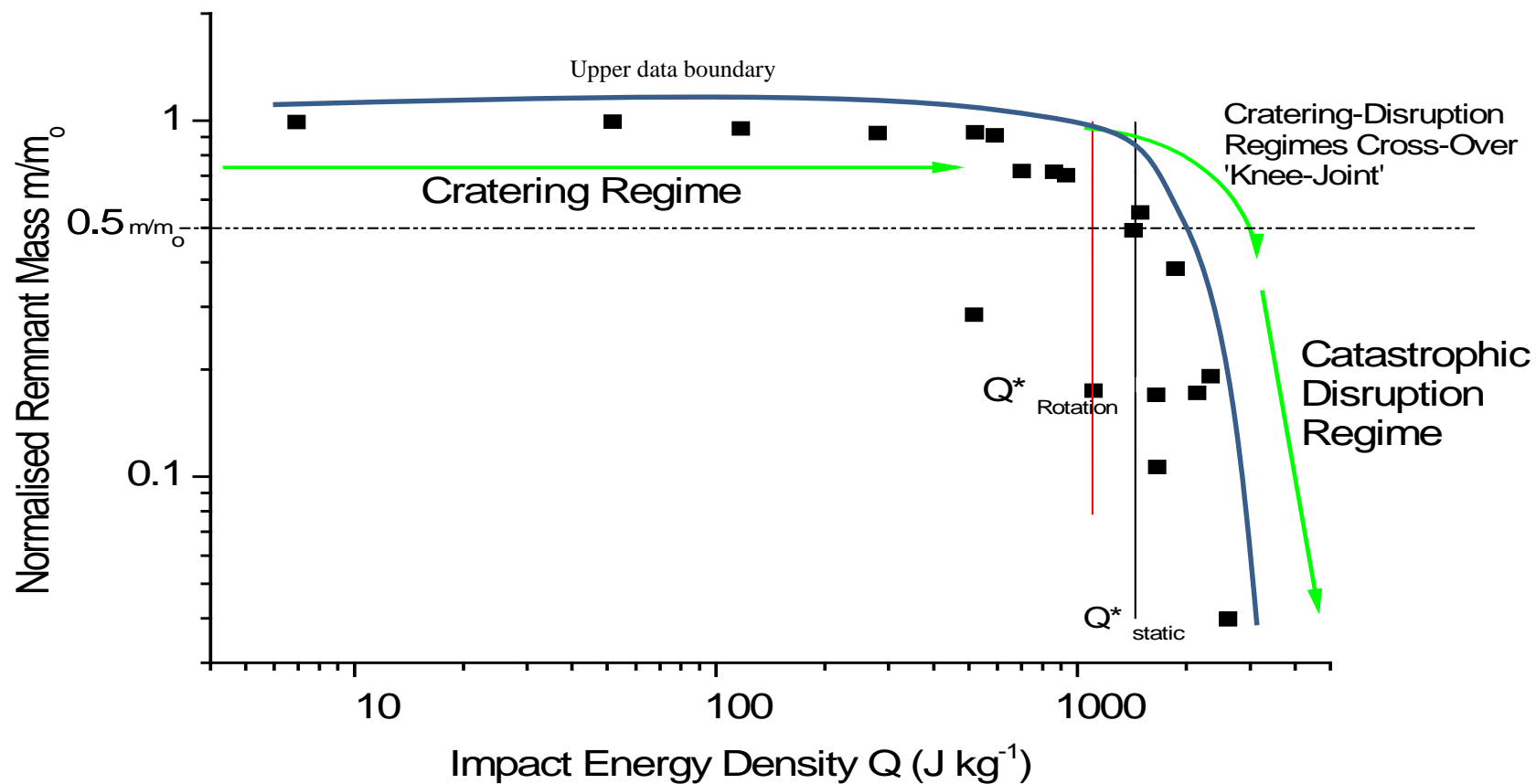
Figure 6.10: The static shot data points with respect to a varying impact energy density. Error bars are not shown because below Q values of 1000 J kg^{-1} the error bars are similar size to the symbol used for the data and above Q of 1000 Jkg^{-1} the error bars are typically only 50% larger than the symbol size.

Section 6.1.1 Static Shots

The data points in Figure 6.10 are the static shots. As can be seen, the static data begins at very low Q (6.92 Jkg^{-1}) for small craters (i.e. m/m_o values close to 1) and trends approximately horizontally towards the cratering-disruption regime cross-over position.

The static data at high Q are for the catastrophic disruption regime. One outlying datum lies at a position on the plot $m/m_o \approx 0.3$ Q ≈ 600 J kg^{-1}, with initially no explanation. The original pre-shot mass for this particular target (210311.3) was 405.7 g.

Once the trend has moved through the regime cross-over position near Q*, the data progresses towards the highly catastrophic disruption section, as noted by the final green arrow from the plot shown in Figure 6.10. Although the static data do show elements of data spread, with the exception of the datum noted earlier, the data follows the expected trend for catastrophic disruption i.e. from the cratering regime, through the Q* regime cross-over region (known in this work as the "knee-joint") and finally towards the catastrophic disruptive regime.

Section 6.1.2 Finding Q*

In order to obtain a value for Q* for both cases, it was found best to plot linear trends for each normalised largest remnant mass with respect to Q, but not to include the cratering regime, as Q* is only concerned with the onset of the catastrophic disruption regime.
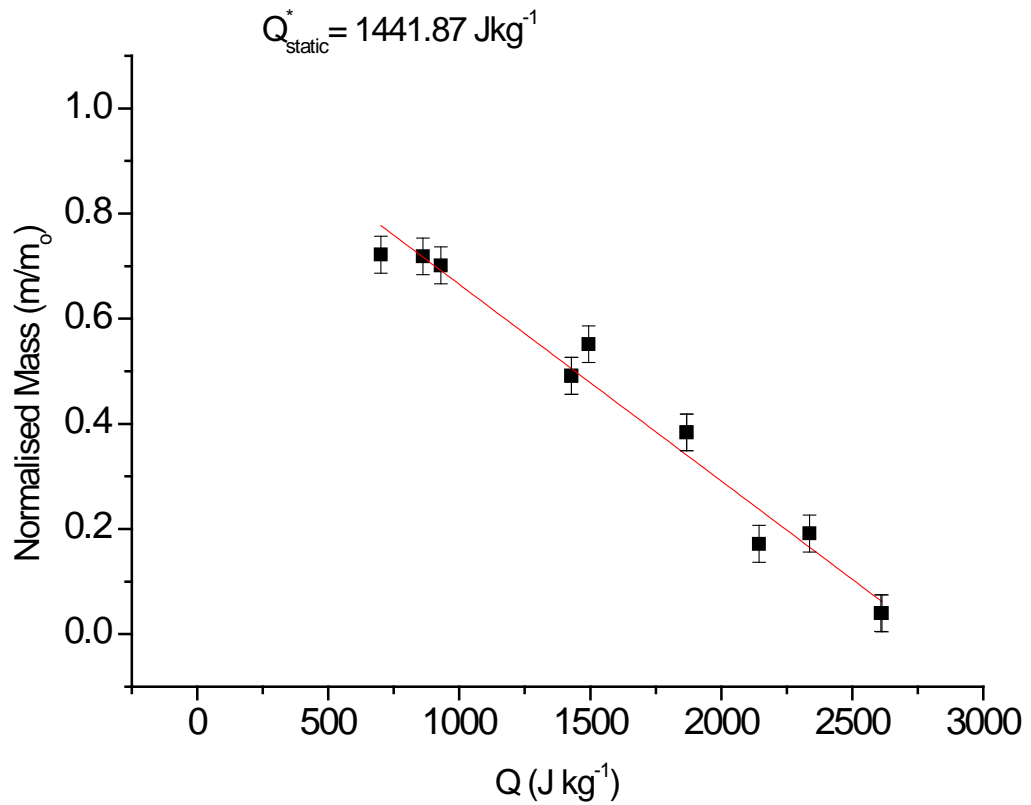
Figure 6.11: Linear plot used for static catastrophic disruption calculation of Q*.

Figure 6.11 displays the linear plot for the static case of catastrophic disruption. The data shows a strong correlation.

$$y = a + bx$$

$$^m/_{m_o} = a + bQ$$

$$\therefore Q = \frac{^m/_{m_o} - a}{b} \qquad \text{Equation 6.1}$$

$$Q^*_{static} = \frac{0.5 - 1.03929}{-3.74021 \times 10^{-4}} = 1442 \, J \, kg^{-1}$$

Error treatment:

The Origin Pro 8 programme (used for this work) fits linear plots through regression fitting. The data set is fitted according to the following equation which is the normal straight line equation with an added residue term ε;

$$y = \beta_0 + \beta_1 x + \epsilon$$

Where the two β terms are associated to the intercept and gradient respectively.

$$res_i = y_i - (\beta_0 + \beta_1 x)$$

The fitting of the line assumes that the residues conform to a Gaussian distribution with a mean value equal to zero and a variance is equal to σ^2. Therefore the errors in both β terms comes from minimising the χ^2 equation:

$$\chi^2 = \sum_{i=1}^{n} \frac{1}{\sigma^2} (y_i - \hat{y}_i)^2$$

Using the numerical values obtained from the regression fitting for the errors associated with the β_o and β_1, the values are then input into a Pythagorean error equation 6.4:

$$\left(\frac{\partial A}{A}\right) = \sqrt{\left(\frac{\partial B}{B}\right)^2 + \left(\frac{\partial C}{C}\right)^2} \qquad \text{Equation 6.2}$$

$$\therefore \delta A = A \left[\sqrt{\left(\frac{\partial B}{B}\right)^2 + \left(\frac{\partial C}{C}\right)^2} \right] \qquad \text{Equation 6.3}$$

For the static case, the error is as follows:

$$\delta Q^* = 1441.87 \left[\sqrt{\left(\frac{0.03523}{1.03929}\right)^2 + \left(\frac{1.95208x10^{-5}}{-3.74021x10^{-4}}\right)^2} \right]$$

$$\delta Q^* = \pm 90 \, J \, kg^{-1}$$

From the above treatment of the static normalised remnant mass with respect to the impact energy density, the Q* value for static is:

$$Q^*_{static} = 1442 \pm 90 \, \text{J kg}^{-1}.$$
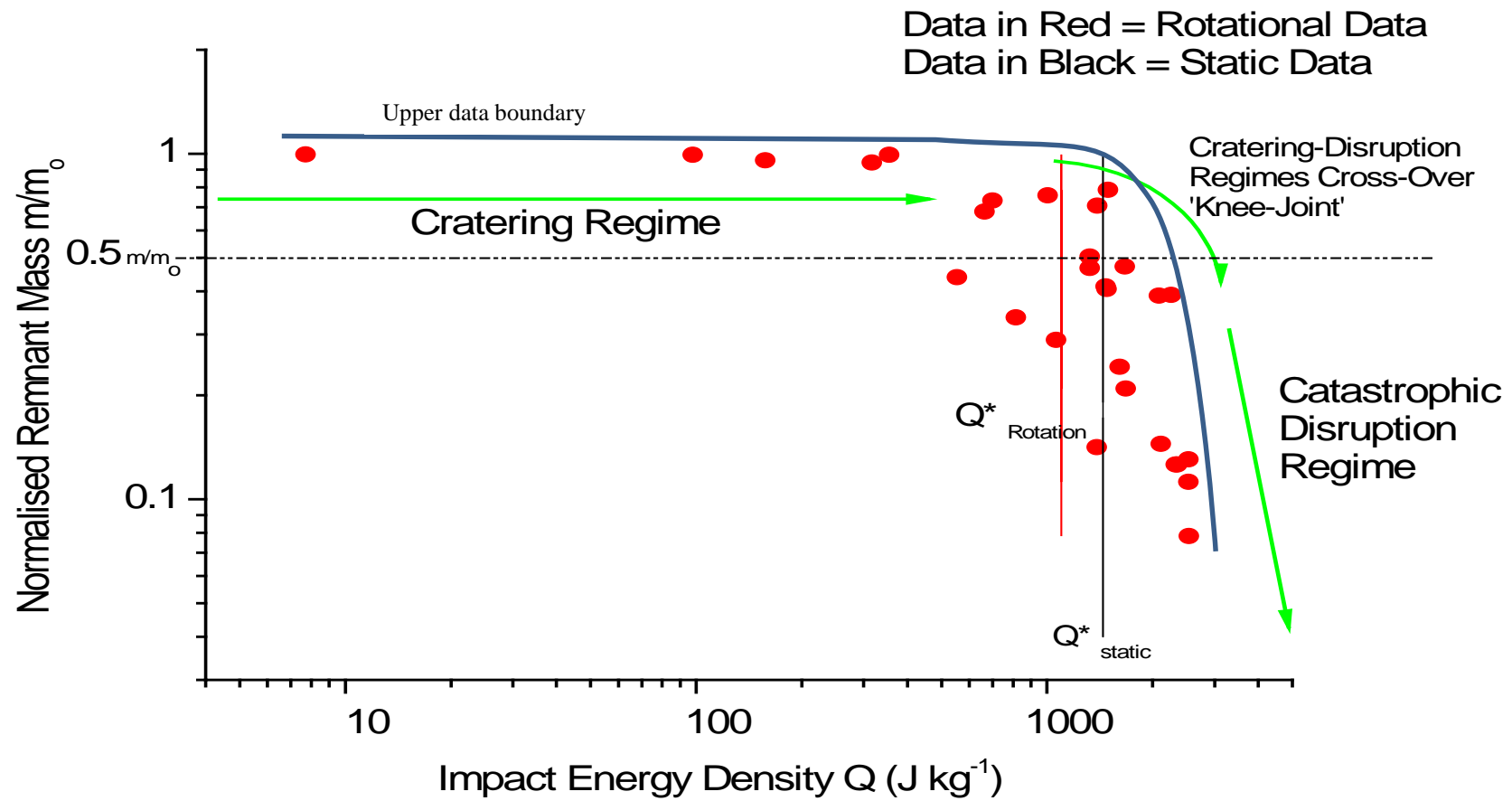
Figure 6.12: m/m$_o$ vs Q for rotation shot data points.

Section 6.1.3 Rotation Shots

The rotationally dependent data are shown in Figure 6.12. Starting from the same position as with the static example, the data trend begins with the very low Q shots giving (8 Jkg^{-1}) very small craters. At the regime cross-over, a considerable spread in the data is present around this position. This is notably worse than for the static case so is considered an effect from the rotation acting on the target.

As Q progresses past the regime crossover, the data enters the catastrophic disruption regime with increasing levels of disruption as the impact energy density increases. Within this region, the energy density associated with the impacts is very large and so the scatter on the data begins to narrow again as Q becomes much larger than Q*.

Section 6.1.4 Cratering-Disruption Regime Cross-Over or 'Knee-Joint'

The knee-joint data spread associated with the rotational case is made from 11 data points (Figure 6.13). This regime was extensively tested due to the spread in the data. As more shots were conducted to fill the regime cross-over region and to check the data spread, new data points added with each shot showed the same level of spread. Therefore this appears to be an important factor arising from target rotation.
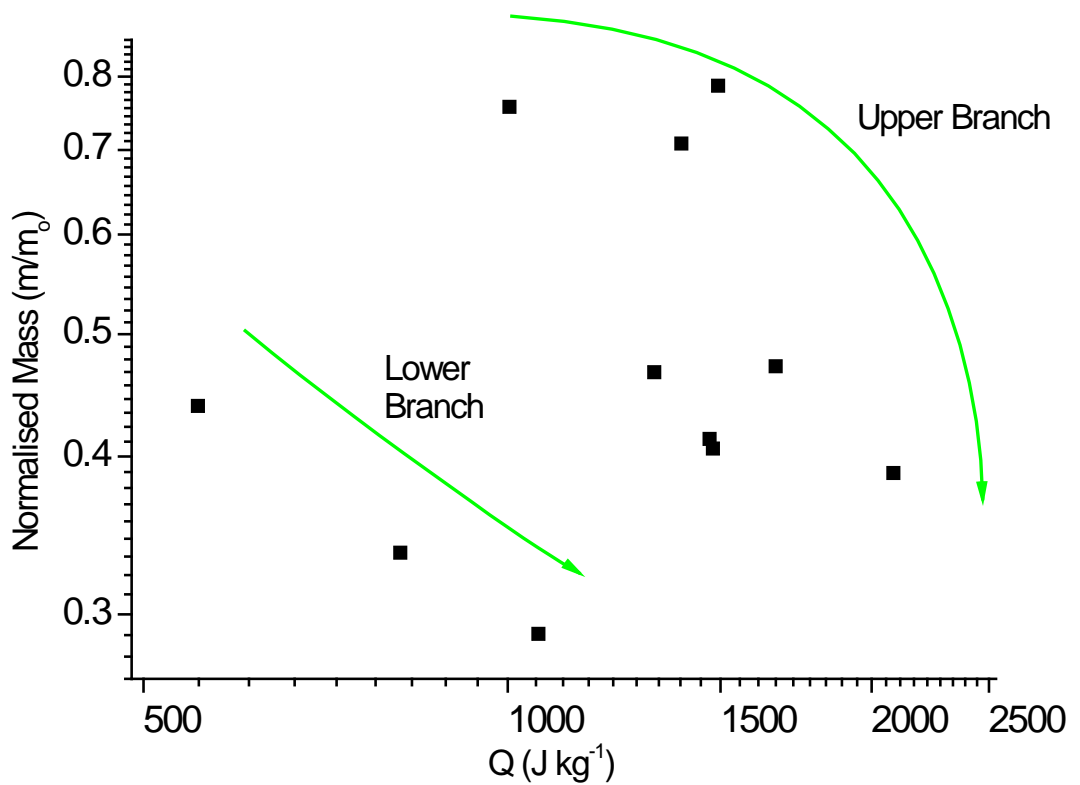
Figure 6.13: The cratering disruption regime cross-over for the rotational case shows considerable spread in the data. There appears to be two trends which surrounds the Q* region labelled "upper" and "lower" branches in this plot. It was necessary to separate the data in this method to analyse possible reasons why the data spread at this particular point.

The spread around the knee-joint position in Figure 6.13 for the rotational case was characterised into two branches; upper and lower. This designation was used in order to find the reasons for the spread. This is discussed further in this chapter.

Table 6.4: Knee Joint Data for static project

Q (J kg^{-1})	Projectile Diameter (mm)	m/m$_o$	Shot Type	Shot Code	Pre-shot mass (g)
517.61	3.0	0.2852	Static	210311.3	405.7
700.84	2.5	0.7218	Static	140311.2	398.2
861.10	2.0	0.7187	Static	30311.2	365.4
929.69	2.0	0.7014	Static	120711.1	376.4
1427.96	2.0	0.4913	Static	310513.2	338.9
1493.16	2.5	0.5515	Static	070613.1	367.2
1867.77	2.5	0.3839	Static	310513.1	353.3
2337.35	3.0	0.1914	Static	200712.3	338.0

Table 6.5: Knee Joint Data for rotation project

Q (J kg^{-1})	Projectile Diameter (mm)	m/m$_o$	Shot Type	Shot Code	Pre-shot mass (g)
554.70	3.0	0.4387	Rotation	90211.1	364.0
815.39	2.0	0.3357	Rotation	150711.1	408.1
1004.05	2.5	0.7568	Rotation	260811.1	357.7
1060.69	2.5	0.2894	Rotation	140211.1	374.6
1322.60	3.0	0.4664	Rotation	90211.2	357.0
1392.49	2.5	0.7081	Rotation	90312.3	321.0
1469.51	2.5	0.4131	Rotation	260811.2	359.0
1478.68	2.0	0.4057	Rotation	210111.1	338.9
1493.16	2.5	0.7868	Rotation	220711.1	361.2
1666.15	2.5	0.4715	Rotation	250211.1	301.2
2084.90	2.5	0.3882	Rotation	220612.2	305.8

Tables 6.4 and 6.5 outline the cratering disruption regime cross-over with projectile diameter from 2 to 3 mm and from the distinct regions associated with cratering and disruption. The static dependant knee-joint has a Q range from 517 to 2337 J kg^{-1} and the rotational example Q range to be 554 to 2258 J kg^{-1}. These ranges are similar in value which shows no apparent shift in the data positions from both static and rotation with respect to the knee-joint area.

Section 6.1.5 Finding Q*
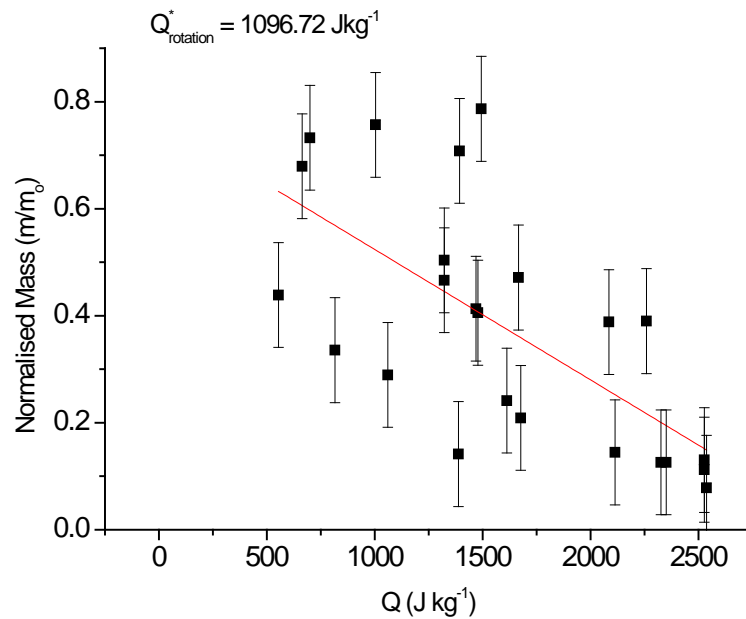
Figure 6.14: Normalised mass vs. Q for rotational data. A linear fit is shown. There is scatter on the data leading to a low r^2 value of 0.67. Q* is the Q value where normalised mass = 0.5 and can be seen to lie around 1100 J kg^{-1}.

The same method was used to calculate the rotational case for Q* as in for the static case. The coefficient data obtained from the plot in Figure 6.14 combined with Equation 6.1 gives the following:

$$Q^*_{Rotation} = \frac{0.5 - 0.7676}{-2.4377 \times 10^{-4}} = 1097\ J\ kg^{-1}$$

Using Equation 6.3 and incorporating the error calculation, the Q* value for the rotational case is:

$$Q^*_{rotation} = 1097 \pm 296\ \text{J kg}^{-1}$$

The data shows, that a relative drop of 24% in the onset of catastrophic disruption is present when the target body is rotating with the rotational velocity associated with 4Vesta.

The considerable level of spread in the data from target rotation also explains the much greater error value. The effect of the rotation is dominant around the knee-joint position of the normalised mass Q plot below.

Section 6.1.6 Analysis of the Data Spread in the Knee-Joint

Figure 6.15 displays the level of spread around the Q* for the rotational case. The plot is sectioned into four quarters labelled cratering, Q* cratering, Sub Q* catastrophic disruption and finally Q* catastrophic disruption.

Two lines were applied to the plot in Figure 6.15 which acts as boundaries symbolising 50% remnant mass and Q*, this divides the plot into four sections shown. The cratering section has three data points and signals the trend entering the regime cross-over position. This is expected. The adjoining section of Q* cratering is one of the two sections which resulted in unexpected data.
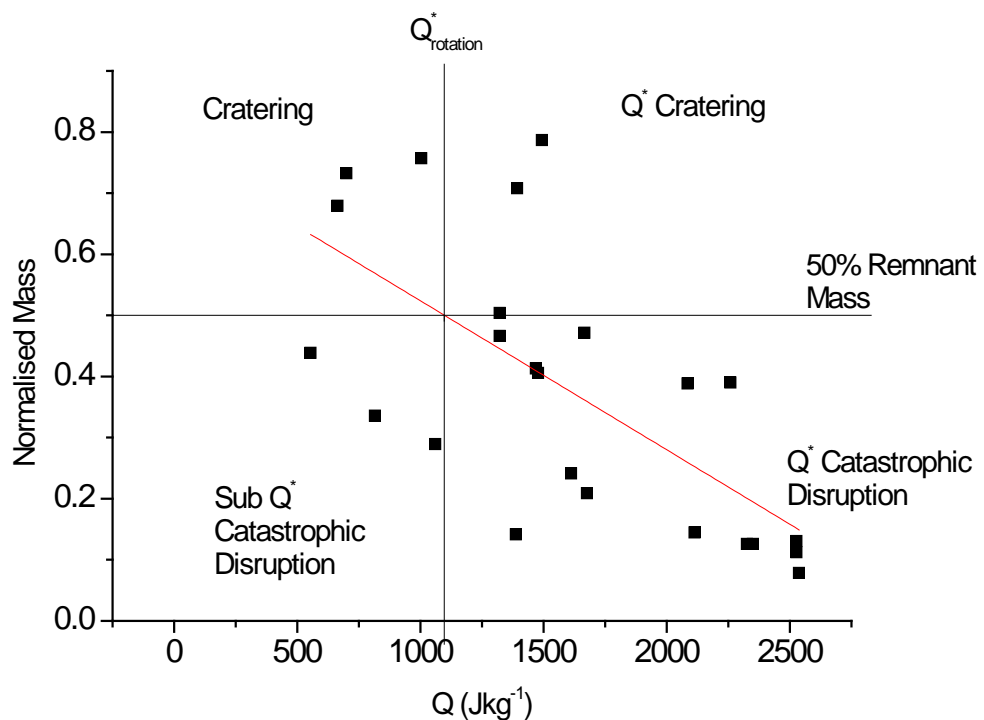
Figure 6.15: Categorisation of data distribution around Q* for the rotational case. This helps in detailing data around the 'knee-joint'.

The three data points which lie in the section labelled Q* cratering should not have cratered, they should have catastrophically disrupted. The targets were subjected to the level of impact energy density to initiate catastrophic disruption but resulted in cratered surfaces. One option considered for the underlying cause of the spread was the densities of the individual targets. Table 6.5 shows the associated pre-shot mass values for the data points around the knee-joint for the rotational case. Using the average target volume size calculated from six different targets (220.89 cm^{-3}), the mean density for the targets was 1.60 ± 0.12 g cm^{-3}.

However, there have been circumstances within the solar system which have provided an element of surprise, such as Mimas the moon orbiting around Saturn. Mimas is a moon which is thought mainly to comprise of mostly water ice with a small amount of rock internally (due to low density of 1.15 gcm^{-3} (Roatsch et al. 2009)) but has one surface feature which is not easily explained, the Herschel crater.

The Herschel crater is approximately 130 km in diameter (one third the diameter of Mimas) and 10 km in depth. The crater is a complex impacted crater with a central peak approximately 6 km in height from the crater floor.

During its history, Mimas experienced an impact large enough to have formed the crater, but it's believed that the body did not catastrophically disrupt during that impact. This would suggest that the impacts noted in the Q* cratering quadrant from Figure 6.15, are to be expected if real life examples such as Mimas have been found. However, another body which is believed to have undergone a similar impact history but could have originated from a catastrophic event is 2867 Steins. The Steins asteroid is diamond shaped (due to YORP migration of matter (Keller et al. 2010)) with a very large crater in the top which should have been enough to catastrophically disrupt the body. During data analysis of this experiment, one impact fragment was noted for its likeness to the Steins asteroid which proposed a different view on the origin of Steins. It could be that the Steins asteroid was never an accreted asteroid in its own right which was then impacted but remained intact. Steins could have originated as an internal impact fragment from a much larger parent body (Morris et al. 2013).
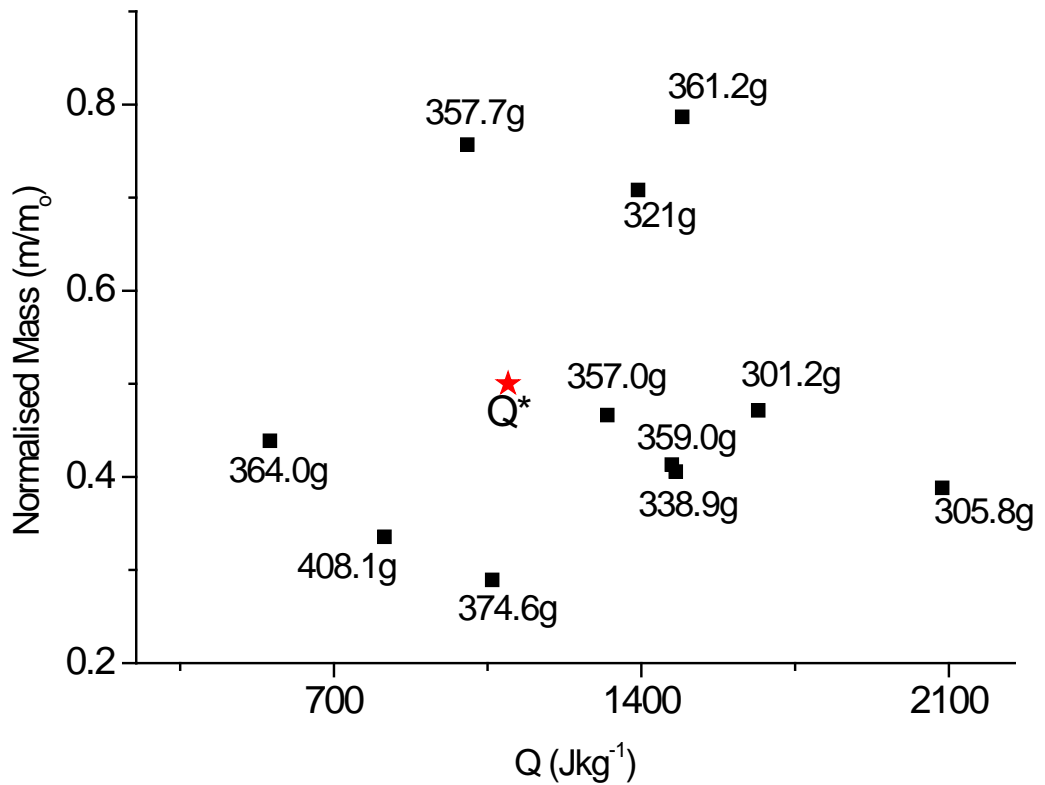
Figure 6.16: Distribution of pre-shot mass around the knee-joint to find whether pre-shot mass contributed towards the 'knee-joint' spread in data.

Linked with the concept of density is the distribution of pre-shot mass with respect to the knee-joint spread. As can be seen in Figure 6.16, the knee-joint data points are shown with their respective pre-shot masses. The upper-most datum point in Figure 6.16 shows the pre-shot mass of 361.2g. This indicates that the target had a much lower porosity in comparison the pre-shot mass target associated with 321.0 g, but with the final Q* cratering point having a mass of 357.0 g. Although the mass is so heavily cratered (almost to the point of Q*), it is comparable to the furthest datum point (from Q*) at 361.2g.

The three points which lay in the sub Q* catastrophic disruption quadrant could have meant that the targets were weaker with respect to Q* and the calculated value of on-set catastrophic disruption. It might be considered that the targets were weaker due to

manufacturing processes and pore creation, but the masses disprove the pore hypothesis and therefore requires more investigation.

One other concept which could explain the spread of the knee-joint branch away from the Q* region is a direct proportional relationship between pre-shot mass and rotational force.

Newton's 3rd Law treatment to the rotational force is the pseudo centrifugal force which acts with the same magnitude but opposite direction.

$$v = \frac{2\pi r}{T} \qquad\qquad \text{Equation 6.4}$$

$$F_{cent} = \frac{mv^2}{r} \qquad\qquad \text{Equation 6.5}$$

The treatment for this investigation requires the use of Equation 6.4 – the tangential velocity of the rotating target where v is the tangential velocity (ms⁻¹), r is target radius (m) and T is rotational period (s⁻¹), and the negative sense of Equation 6.5 to act as the centrifugal force where m is fragment mass (kg), v is tangential velocity (ms⁻¹) and r (m) is target radius, acting on target fragments which are transferring from rotational to tangential motion through catastrophic disruption breakup.

The average rotational rate of the targets is found to be 3.44 Hz.

The time for each period of average rotation is:

$$s = T^{-1} = 3.44^{-1} = 0.29s$$

From equations 6.4 and 6.5:

$$v = \frac{2\pi r}{T} = \frac{2\pi \times 0.0375}{0.29} = 0.812 \; ms^{-1}$$

$$F_{centrifugal} = -\frac{mv^2}{r} = -\frac{0.357 \times 0.812^2}{0.0375} = -6.28 \; N$$

The above result is for a rotating mass of 357g which is the closest point to Q* in Figure 6.7.

$$F_{centrifugal} = -\frac{mv^2}{r} = -\frac{0.4081 \times 0.812^2}{0.0375} = -7.18 \, N$$

Because of the direct nature of mass on rotating bodies given by Equation 6.5, there is a definite increase in the centrifugal force magnitude between the closest point to Q* and the furthest point on the lower knee-joint branch as shown by the increase in force.

Section 6.2 Fragment Size Distribution

As stated in Chapter 2 'Questions to be Addressed', the impact data are represented in the form of normalised mass;

- the mass of the fragment / original pre-shot mass of the target.

Or in mathematical form:

$$m_n = \frac{m}{m_0} \qquad \text{(Equation 6.6)}$$

Where

- m_n is the normalised mass,
- m is the mass of the largest remaining fragment after impact in kg. It is also the individual masses of each post impact fragments when used for complete fragment distributions.
- m_0 is the mass of the target before the shot in kg.

Figure 6.17 shows a 'typical' representation of the data for a distribution in this work. It is useful to plot normalised mass with respect to number of fragments in order to arrange the data as distributions, and then to look at each section of the distribution. The different regions in Figure 6.17 are explained in general below to aid the reader in understanding the data plots.
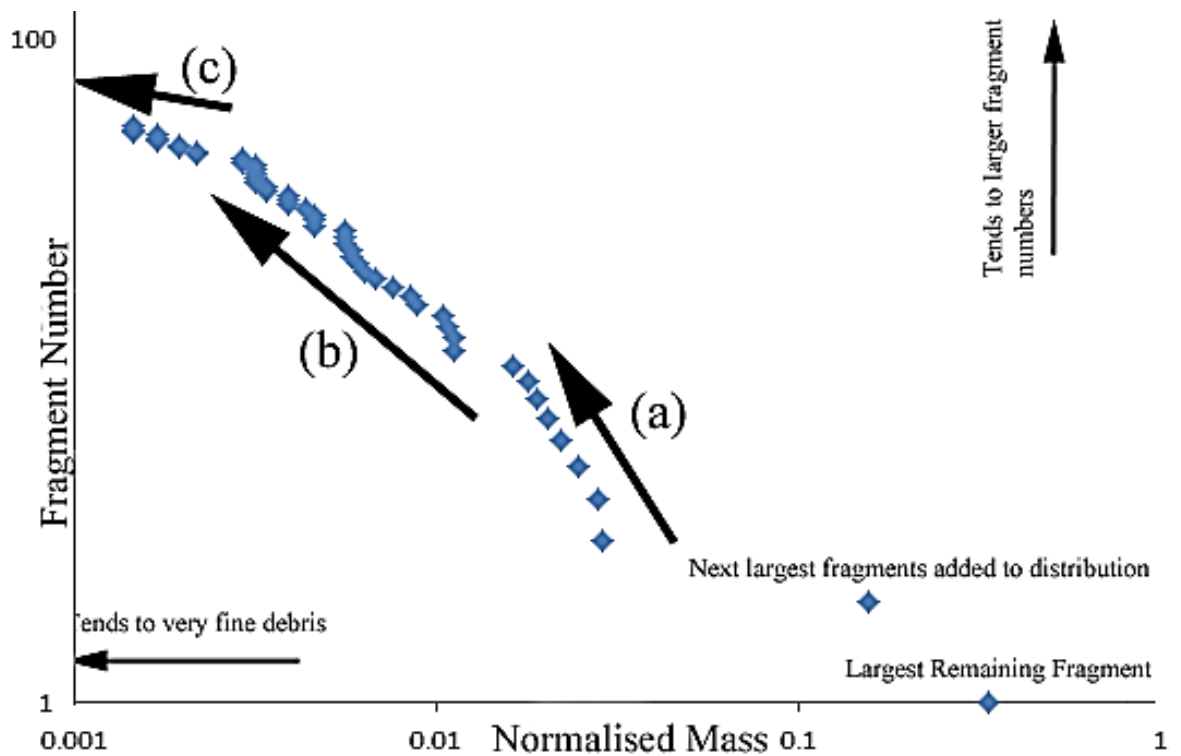
Figure 6.17: The regions and details concerning the distribution graphs in this thesis. This example distribution is an impact very close to Q* with normalised mass ≈ 0.5. Regime (a) is referred to the 'lower branch', (b) the 'mid branch' and (c) is the upper branch.

The log-log distribution plot shows various regions and information contained from the debris, both coarse and fine (dust) fragments retrieved from a typical impact which resulted in a catastrophically disrupted outcome.

The x-axis in Figure 6.17 is the normalised mass obtained from Equation 6.6 and the y-axis is the fragment number per normalised mass. Assigning a fragment number to each weighed piece of debris allows for the plots to be cumulative and shows the relationships between the individual fragments with respect to the impact parameters which have produced the debris. The largest remaining fragment is always placed on the x-axis due to being assigned the first number of the fragment numbers.

As the fragments continue to accumulate, the data shows the reduction in mass and hence debris size. The trend in region (a) is a common aspect to the cumulative plots throughout this project and shows the start of the main trend. Here the fragments are the largest fragments remaining after the impact but, due to their masses being relatively close, they form the start a steeply rising distribution which then leads to section (b) of the curve.

Section (b) contains the majority of the fragments along a trend of lower gradient. From the impact, a shockwave present in the target will eject the larger pieces (dependant on crack propagation) of debris initially as it propagates through the target. This makes section (b) ideal for determining the level of target destruction from the impact.

Section (c) shows the finer fragments in the initial stage of the impact and dust after the impact, and shows the gradient of the trend being approximately horizontal. At this point the fragments are becoming so small that the type of data collection used here lacks the sensitivity to fully collect all fine fragments and be able to measure them individually, so there is a loss of data and the roll-over seen in the distribution need not be a real effect.

The order of fragmentation detailed previously is: (c) represents the initial impact and ejecta, section (b) is associated with the main body being catastrophically disrupted, and finally, section (a) leads to the largest fragments (the singular pieces shown as single datum points closest to the origin of the plot) and represent the body or largest remnant mass, after the collision.

The various regions in Fig. 6.17 can be fit by the function:

$$y = ax^{\beta} \hspace{3cm} \text{(Equation 6.7)}$$

If the trendline is plotted steeply with respect to the coordinates, the amount of energy supplied to the system i.e. energy originating from the impact, is great enough to rapidly fragment the target and the fragments will be smaller in mass and greater in number in comparison to weaker impacts. However, if the impact energy is large enough to initiate large-fragment fragmentation from the target, such as impacts just lower than that Q* regime crossover, the β-value will be much shallower in comparison. This means that the energy contained within the shockwave propagating through the material matrix is large enough to crush pores and interact with internal flaws in the target thereby instigating crack development and transmission, but is not large enough to crush the fragments into smaller pieces.

In the following section, data are shown for normalised mass distributions at five different Q values (7, 300, 700, 800 and 1600 J kg^{-1}), which span the cratering and disruption regimes. In each case there is a static and rotating target experiment. The

data are shown in Figures 6.18 to 6.23, one Figure per Q value. Each shot is labelled with a unique shot number in the format of the date followed by the shot number for that particular day, e.g. 280311.3 was shot in the 28th March 2011 and it was the 3rd shot of the day.

6.2.1 Cratering Distributions

Q << Q: Impacts producing only small craters.*
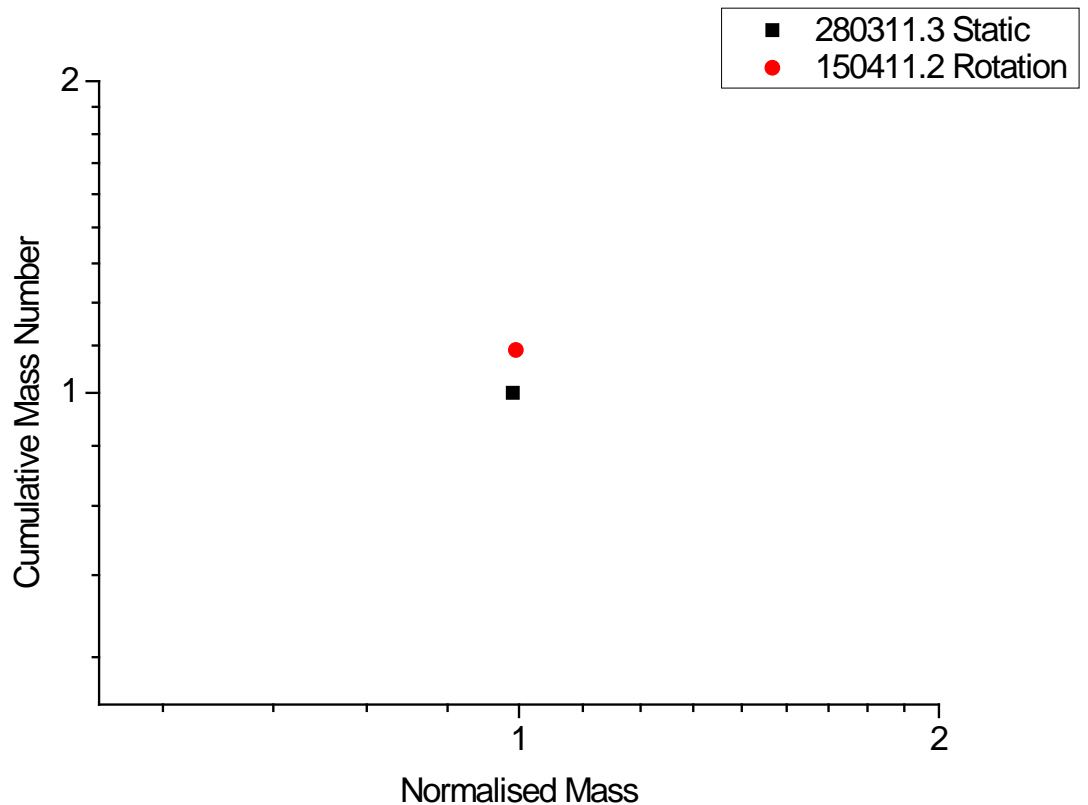
Figure 6.18: A plot showing the largest fragments after very low Q value impacts. (Note: data points actually completely overlap; an offset has been introduced for clarity)

The two data points in Figure 6.2 show very similar remnant masses due to the Q value being very low; static shot = 7 Jkg^{-1} and the rotational shot = 8 Jkg^{-1}. The values for Q being thus low resulted in the impact outcome displaying nothing more than very small craters; the ejecta was lost in the target chamber and so only the main target bodies remained.
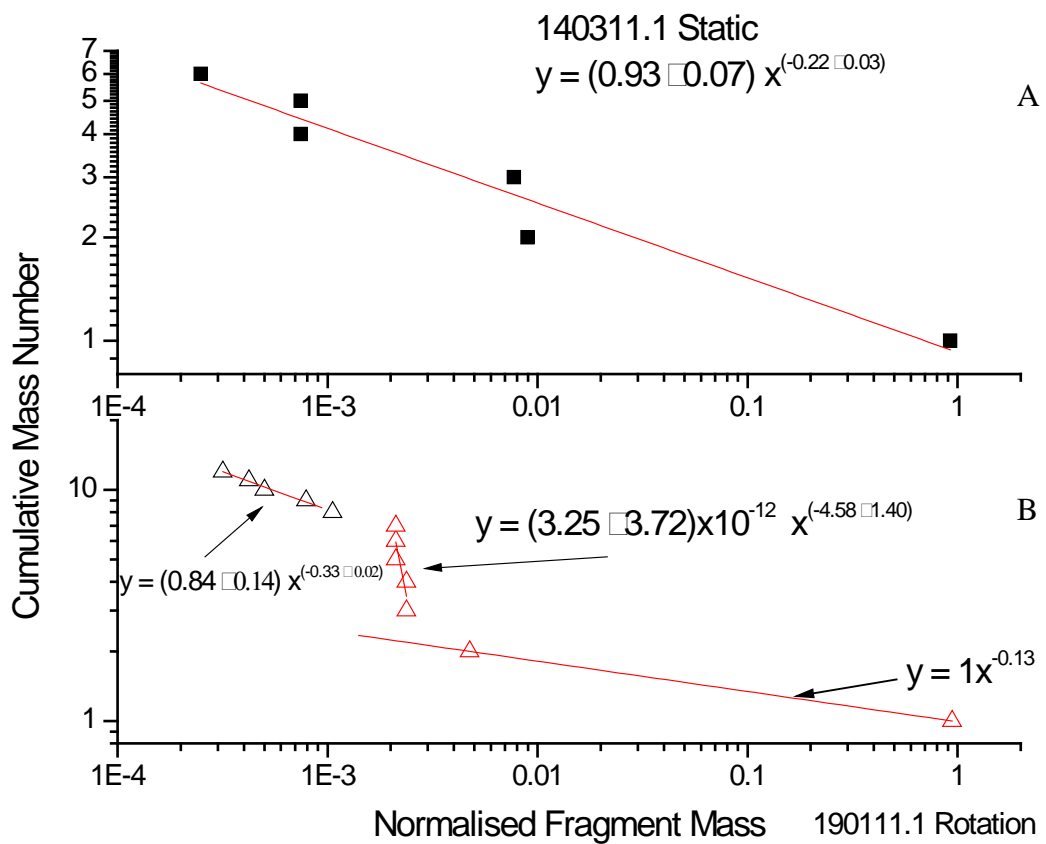
Figure 6.19: Cumulative mass number vs normalised mass at impact energies of 300 J kg^{-1} for (a) Static (shot 140311.1) (b) rotating (shot 190111.1) cases. The rotating target produced twice as many fragments in the same size range.

Static Q = 280 Jkg^{-1} and Rotation Q = 317 Jkg^{-1}

Figure 6.19 A shows a single fit extending throughout the whole range of data available. This analysis shows that the fragmentation from the static impact energy to be a lot lower than the rotational case. Both targets were impacted with 1mm diameter stainless steel ball bearings at velocities of 7.5 kms^{-1} and 7.75 kms^{-1} for static and rotational respectively and pre-shot masses of 401.8g for the static target and 378.6g for the rotational case. Although the rotational case impacted at 200 ms^{-1} faster, the level of difference in shockwave pressure is negligible; from the planar impact

approximation the static case peak pressure was calculated to be 127.00 GPa and the rotational value was 126.81 GPa. The shockwave velocities for static and rotation in the target material were calculated as 13.27 and 13.48 kms^{-1} respectively. With the values showing no more than 1% difference in the planar impact approximation, the conclusions for the difference in fragmentation must either remain with the material matrices for each target or the rotation.

The β values from each power law for each distribution, shows definite differences. The static β value was calculated as -0.22 whereas the rotational case showed β values assigned to three different regions of the distribution.

The β value for the largest fragment distribution was calculated as -0.13, without error calculations due to there only being two data points to fit. The main section of fragmentation, following on from the largest remnant pieces distribution showed the β value of -4.58 which was the steepest part of the distribution. The smallest fragment distribution shows a β value similar to the static case with a value of -0.33.

The presence of the three distributions in the rotational case, shows that the rotational forces acted on the target body fragments during the initial stages of the shockwave propagation and resulted in more fragments being produced than the stationary case.

6.2.2 Q* Region Impacts
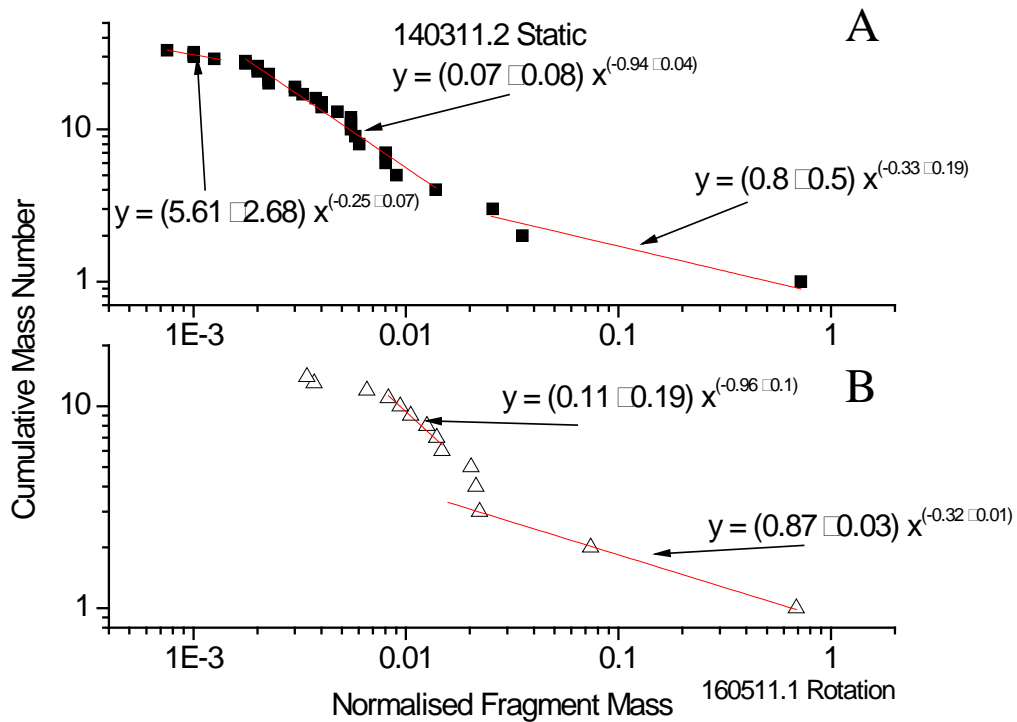
Figure 6.20 A and B: Two plots showing the level of disruption as the impact energy density nears the upper boundary of cratering. A) static shot Q = 701 Jkg⁻¹ and B) rotational shot Q = 700 Jkg⁻¹.

Static Q = 701 Jkg⁻¹ and Rotation Q = 700 Jkg⁻¹

In Figure 6.20, results are shown for Q values very close together. The shot characteristics were – static: 2mm stainless steel projectile impacting at 3.05 kms⁻¹ into a target of mass 398.6g and rotation: 2mm stainless steel impacted at a velocity of 4.05 kms⁻¹ into a target with mass 351.1g.

The main difference in-between the two data sets is the degree of fragmentation. The static case shows a greater number of fragments resulting in three defined regions of distribution, as seen in the previous examples. Whereas the rotational case has fewer fragments and only two notable regions. The β values for both cases do show similarity in values with static and rotation being -0.94, -0.96 for the upper branch respectively and -0.33 and -0.32 for the lowest branch respectively.
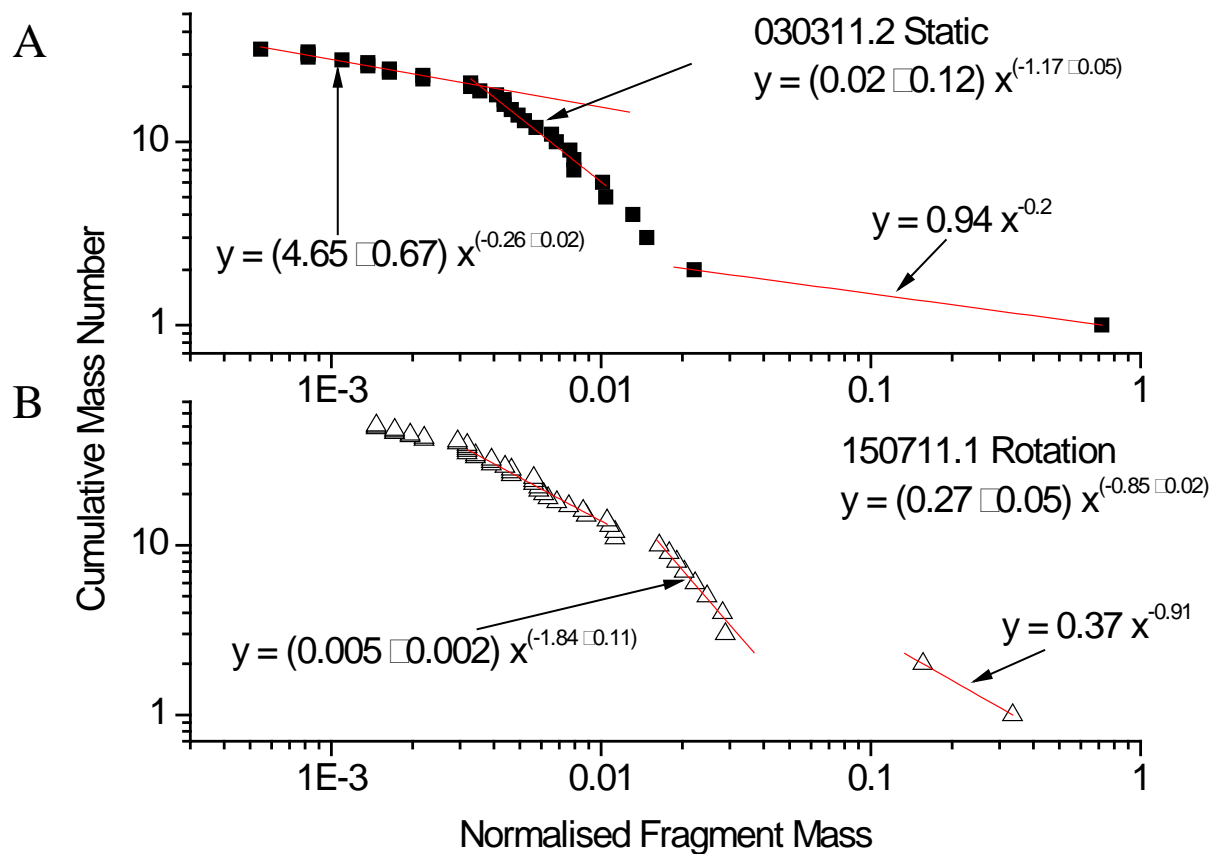
Figure 6.21 A and B: As Q gets closer to catastrophic disruption, the sections pointed out earlier are distinguishable. A) Static shot Q = 861 Jkg^{-1} B) Rotational shot Q = 815 Jkg^{-1}.

Static Q = 861 Jkg^{-1} and Rotation Q = 815 Jkg^{-1}

The comparison for the above Figure (Figure 6.21) show a considerable rate of fragmentation for the static case with the β value for static being -1.17 and rotation = -0.85; a 27% difference. Both shots used 2mm stainless steel projectiles but the impact velocities were slightly different: the static case impact velocity was 4.58 kms^{-1} and rotational was 4.71 kms^{-1}.

6.2.3   *Q > Q*: Catastrophic Disruption Regime*
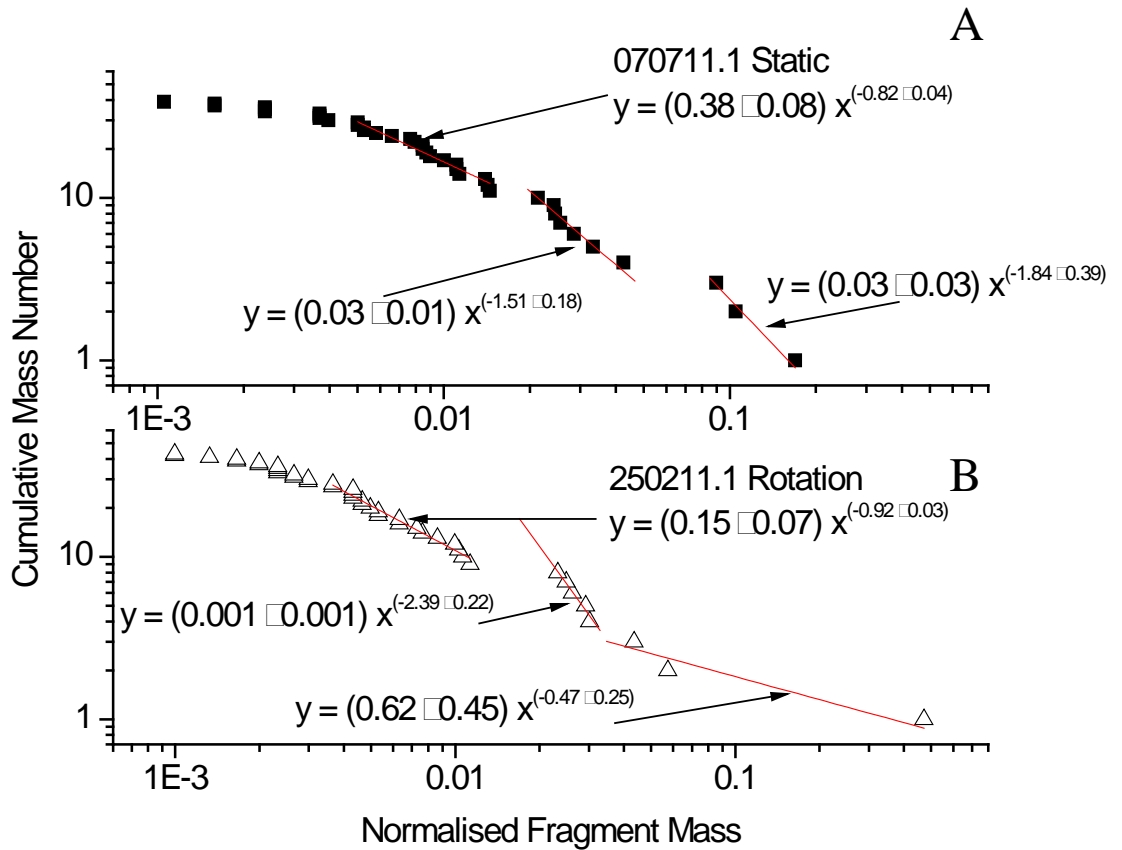
Figure 6.22 A and B: Both plots resulted in Q greater than Q* for each case. The level of change from cratering to disruption can be seen. A) Static shot Q = 1654 Jkg^{-1} B) Rotational shot Q = 1666 Jkg^{-1}.

Static Q = 1654 Jkg^{-1} and Rotation Q = 1666 Jkg^{-1}

The final comparison (Figure 6.22) between the static and rotation shots included in this Section shows two shots at the much disrupted region. The static data was: pre-shot mass = 378.9g, 2.5mm stainless steel projectile shot at a velocity of 4.75 kms^{-1} and rotation target mass = 301.2g, projectile was 2mm stainless steel impacting at 4.09 kms^{-1}. The relative β values for static and rotation were calculated as -0.82 and -0.92 respectively. Less than half the mass was recovered from both cases at this level of disruption. This was due to the level of impact energy being much greater than all previous shots which resulted in more of the target material being crushed into dust

during the shockwave-matrix interaction and consequently settling around the target chamber.

These comparisons show real-life experimental data with larger fragments tending towards 1 on the normalised mass axis, progressing towards much smaller fragments through the range of normalised mass. Three of the five comparisons resulted in β being greater for the rotational cases.

The number of fragments ejected through the impacts, with the exception of the $Q = 700$ Jkg^{-1} comparison, showed that the rotational cases produced more ejected fragments.

Table 6.6: Beta Comparisons from the fragment distributions

Q (Jkg^{-1})	Shot Type	β Values		
		Upper Branch ($\leq$0.01 m)	Mid Branch (0.01$\leq$m$\leq$0.06)	Lower Branch (0.06$\leq$m$\leq$1.0)
280	Static		-0.22 ± 0.01	
317	Rotational	-0.33 ± 0.01	-4.58 ± 0.01	-0.13 ± 0.02
701	Static	-0.25 ± 0.01	-0.94 ± 0.03	-0.33 ± 0.02
700	Rotational		-0.96 ± 0.02	-0.32 ± 0.01
861	Static	-0.26 ± 0.01	-1.17 ± 0.02	-0.2 ± 0.03
815	Rotational	-0.85 ± 0.02	-1.84 ± 0.02	-0.91 ± 0.02
1654	Static	-0.82 ± 0.01	-1.51 ± 0.02	-1.84 ± 0.01
1666	Rotational	-0.92 ± 0.01	-2.39 ± 0.02	-0.47 ± 0.01

A comparison of the beta values with respect to distribution position is shown in Table 6.6, which separates the different distributions shown in Figure 6.17. The entries to the Table show the upper, mid and lower distribution branches where found in the plots. The $Q = 280$ and 700 Jkg^{-1} rotational data sets show only two or one β value.

Tables 6.7 and 6.8 show the data sets for static and rotation impacts (not including the shots which resulted in very small cratering and failed shots such as targets struck by gun debris). Included in these Tables are the values for the regression coefficients.

Table 6.7 : Beta values for static project run

Shot No.	Shot Type	Q (Jkg^{-1})	Power Law β	Regression Coefficient r^2
140311	static	280	0.218	0.9491
130511	static	521.66	1.078	0.9452
140311	static	700.84	0.939	0.959
30311.2	static	861.1	1.170	0.9783
50711.1	static	895.47	0.755	0.9605
120711	static	929.69	0.605	0.9627
120711	static	929.69	0.579	0.9665
100611	static	1107	1.064	0.979
310513	static	1427.96	0.736	0.9646
70711.1	static	1653.59	1.510	0.9684
300911	static	1659.86	0.655	0.99
310513	static	1867.77	0.572	0.9746
30311.1	static	2144.47	0.994	0.9912
210311	static	2609.25	1.025	0.9708
240513	static	2612.93	0.773	0.981

Table 6.8: Beta values for rotation project run

Shot No.	Shot Type	Q (Jkg^{-1})	Power Law β	Regression Coefficient r^2
190111	rotation	317.29	0.288	0.9813
90211.1	rotation	554.7	4.580	0.9766
100511	rotation	663.35	0.655	0.9434
160511	rotation	700.36	0.960	0.9669
150711	rotation	815.39	1.840	0.9882
260811	rotation	1004.05	0.885	0.9887
140211	rotation	1060.69	0.735	0.9857
90211.2	rotation	1322.6	0.810	0.9838
90312.3	rotation	1392.49	0.903	0.9805
260811	rotation	1469.51	0.538	0.9722
210111	rotation	1478.68	0.590	0.7352
220711	rotation	1493.16	0.376	0.9411
240812	rotation	1588.64	1.046	0.936
250211	rotation	1666.15	2.391	0.9746
150711	rotation	1677.14	0.838	0.986
140211	rotation	2113.61	1.064	0.9371
80211.2	rotation	2526.7	0.747	0.9673
80211.1	rotation	2526.7	0.696	0.965
180211	rotation	2537.8	0.896	0.9816
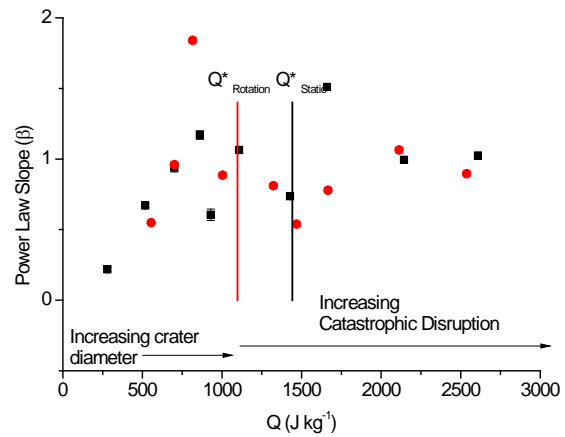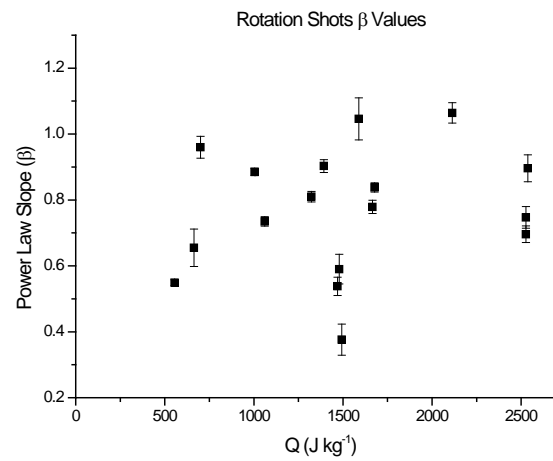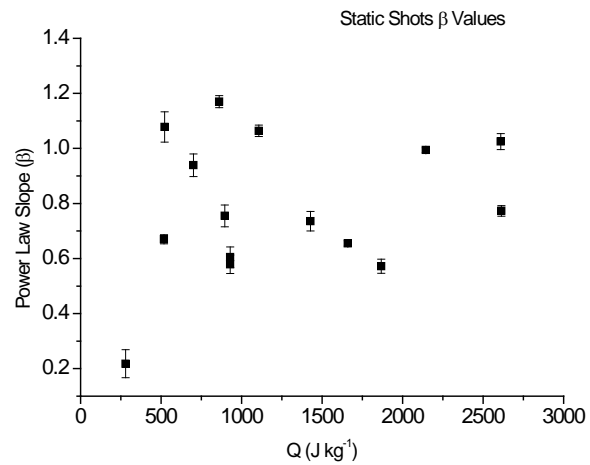
A

B

C

Figures 6.23 A, B and C: The power law β (middle branch) values for both static and rotation (A and B) and (C) a comparison between the two data sets. The data in black are the static β values and rotational data are given in red.

Figures 6.23 A, B and C show the mid-section β values obtained from each impact. The mid-sections were chosen because the mid-points show the damage resulting from the main body interaction with the shockwaves passing through. The upper distributions show the initial impact damage in terms of small debris and dust, while the lower branches outline the largest fragments after the impact.

Considerable scatter of the data is evident, in Figures 6.23 A, B and C, with the static programme data showing the largest amount of scatter with a regression coefficient value of $r^2 = 0.0254$ as opposed to the rotational $r^2 = 0.0995$. These plots indicate that the rate of fragmentation throughout the range of Q values has very little dependency upon the impact energy density. What can be seen with the scatter in both cases is that the rotational case shows some level of relationship between Q and β. From the very low Q values, a trend is noticeable which grows with increasing Q to a turning point approximately positioned at $Q = 750$ Jkg^{-1}.

The comparison of data in Figure 6.23c shows both the static and rotation trends being similar for similar Q values with respect to each case. The data in red details the rotational case and the black data are the static impact β values. Each dataset starts at low values of Q which indicates small craters in the parent body. As the value of Q increases from zero to larger crater sizes, close to the crater-disruption regime cross-over for rotation, the trends increase with Q value and then reduces in β as Q continues to increase. The data trend shown by the rotational case indicates the increase in β value up to the approximate value of Q* for rotation and then the trend flattens in the range β=0.8 – 1.0. Two exceptions to this are noted with the first datum at approximately $Q \sim 1500$ J kg^{-1} having a lower value of 0.5 β and the second point located at $Q \sim 2000$ J kg^{-1} with a β value being larger than 1.0.

6.3   Theoretical Catastrophic Disruption (SPH Hydrocode Models)

It is important to associate what is measured in the laboratory with the real-life situations being investigated. As noted in Chapter 2 'Questions To Be Addressed', there are often magnitudes of size difference between laboratory solar system analogues and actual Solar System bodies. In order to cross the magnitude gap, it is important to have a model which can be run at solar system scales and which are validated by laboratory experiments.

The theoretical section of the catastrophic disruption experiments used the Ansys Autodyn hydrocode v14 modelling computer program. It was decided that the Smoothed Particle Hydrodynamics (SPH) approach was more suitable than to use a grid method, such as Lagrangian or Euler grids, because individual target fragments could be analysed.

6.3.1   Material and Equation of State

The impacts onto concrete were modelled using Ansys Autodyn. Initially the concrete was simulated with the Conc-35MPa Autodyn library model which used the P-α Equation of State (EoS). The P-α EoS includes a total of 17 parameters which affect the outcome of the model. However this proved to be computationally intensive.   Accordingly the model was adapted to include a polynomial EoS and von Mises strength model.

Using the polynomial EoS helps to reduce the total number of material parameters from 17 to 10. Reducing the overcomplicated strength model from RHT Concrete (Bourvall and Riedel 2013) previously used with Conc-35 MPa (Riedel et al. 2009) to von Mises resulted in the models running through an appropriate shorter cycle time with usable results.

The EoS parameter values remained the same for the Conc-35MPa model but the von Mises strength model used only two parameters: Shear Modulus and Yield Stress, both of which could be obtained from testing the cement targets.

As stated previously, the main objective for this project was to start the process of extended laboratory impacts into theoretical models used at solar system sizes. The models generated in this project was to recreate the laboratory experiments therefore validating the material and EoS; if the computer models successfully recreated the

laboratory impacts then further work could be done to the models to extend them to astrophysical analogues.

6.3.2 Setting Up
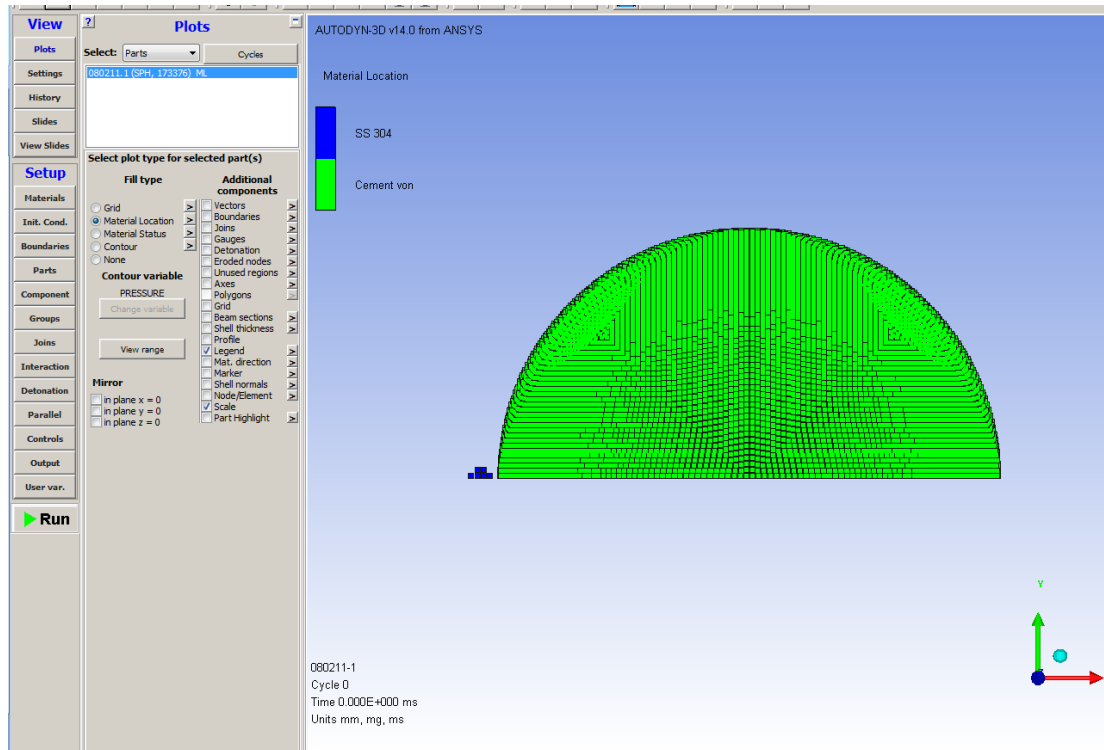
Figure 6.24: A 'screen dump' of a model using Autodyn. Half models were used to help computing time.

When the target and projectile were made, they were filled with SPH particles depending on the projectile size. The projectile acted to limit the maximum SPH cell size and therefore affect the computational power being used.

In order to limit computational cycle time, the SPH cell size was calculated in order to adequately fill the projectile with at least 16 SPH particles in a projectile hemisphere; hemispheres were used to lower the number of SPH particles in the target thereby reducing cycle time further (Figure 6.24). Due to runtime errors produced by impacts bodies with different cell sizes, the projectile was always filled first. By filling the projectile first, the target, being much larger, would fill with a large number of SPH particles; typically in the region of ~ 170 000 SPH particles where a 1 mm projectile

increases the target packing up to approximately 4.7 x10^6 particles. The simulation run times varied, but were commonly one to two weeks in duration.

Initial conditions of impact velocity and rotation were applied the projectile and target respectively. Because these computer simulations were direct representations of the experiments from the laboratory, the impact velocities varied in accordance to the experimental projectile velocities, and the target rotation was a selected initial condition held constant at a tangential speed of the equator of 0.811 mm s^{-1} for targets rotating about the z-axis.

Upon completion of a computer simulation, the fragment data were exported from the program directly into a spreadsheet with the results graphically presented. The first test of simulations was to compare the size distributions of the fragments with those in the equivalent laboratory experiments. The second form of validation was to use the largest remaining fragment data with respect to the impact energy density; this would allow for the modelled data to be checked through the regimes of cratering to disruption.

Even with the EoS and material failure models being changed from the more complicated version to the von Mises model, problems did arise with the SPH packing of the targets.

The standard method adopted to pack the target spheres was to use a concentric packing method of filling the target, but this method produced SPH packing boundaries within the target orthogonally across the target (Figure 6.25). These regions were susceptible to failure during the impact and therefore produced biased fragmentation outcomes for the majority of the simulations. To deal with this issue, the targets were packed using rectangular packing (Figure 6.26) which eliminated the packing boundaries thereby ensuring that the crack propagation within the target was due to the shockwave interaction and not areas of void resulting from the packing algorithm.
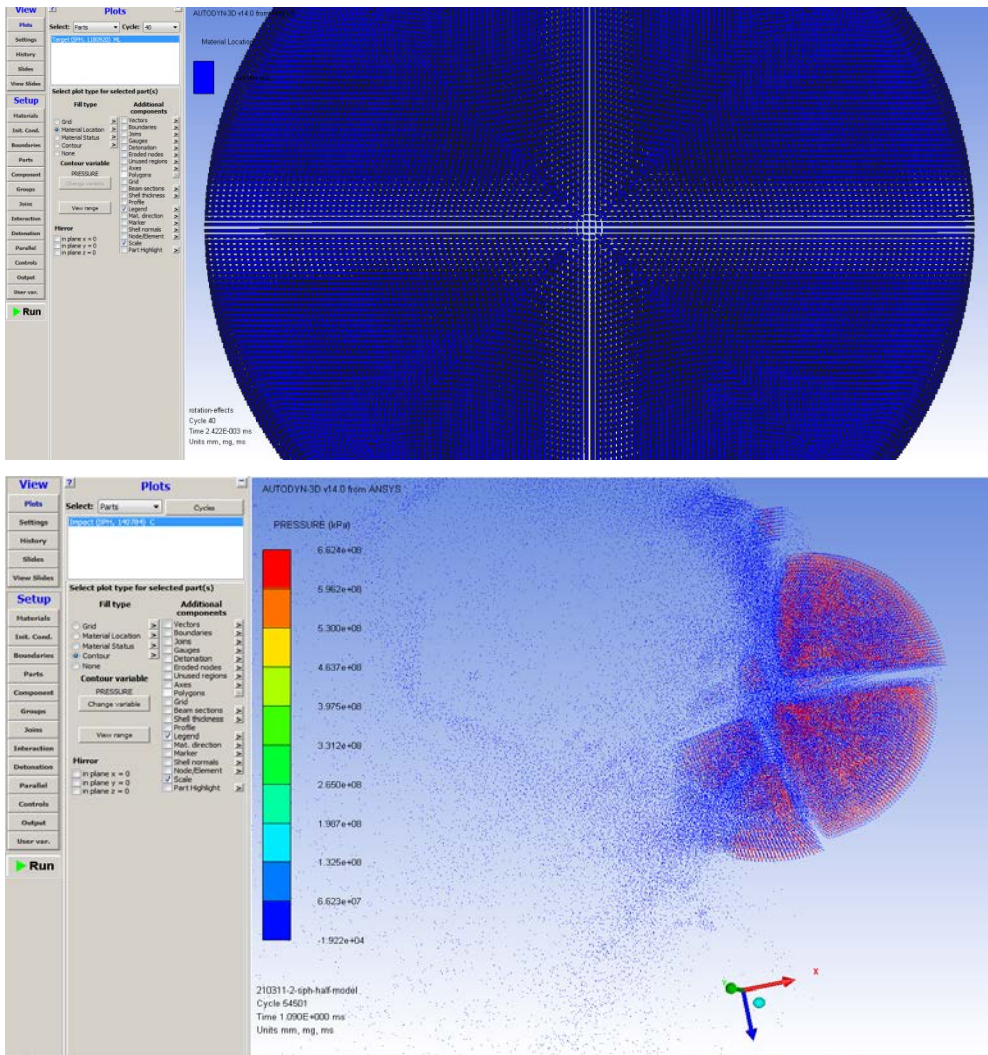
Figure 6.25: Boundary effects arising from the SPH concentric packing boundaries (top image), the fragmentation split along the boundaries every time during simulated impacts (bottom image).
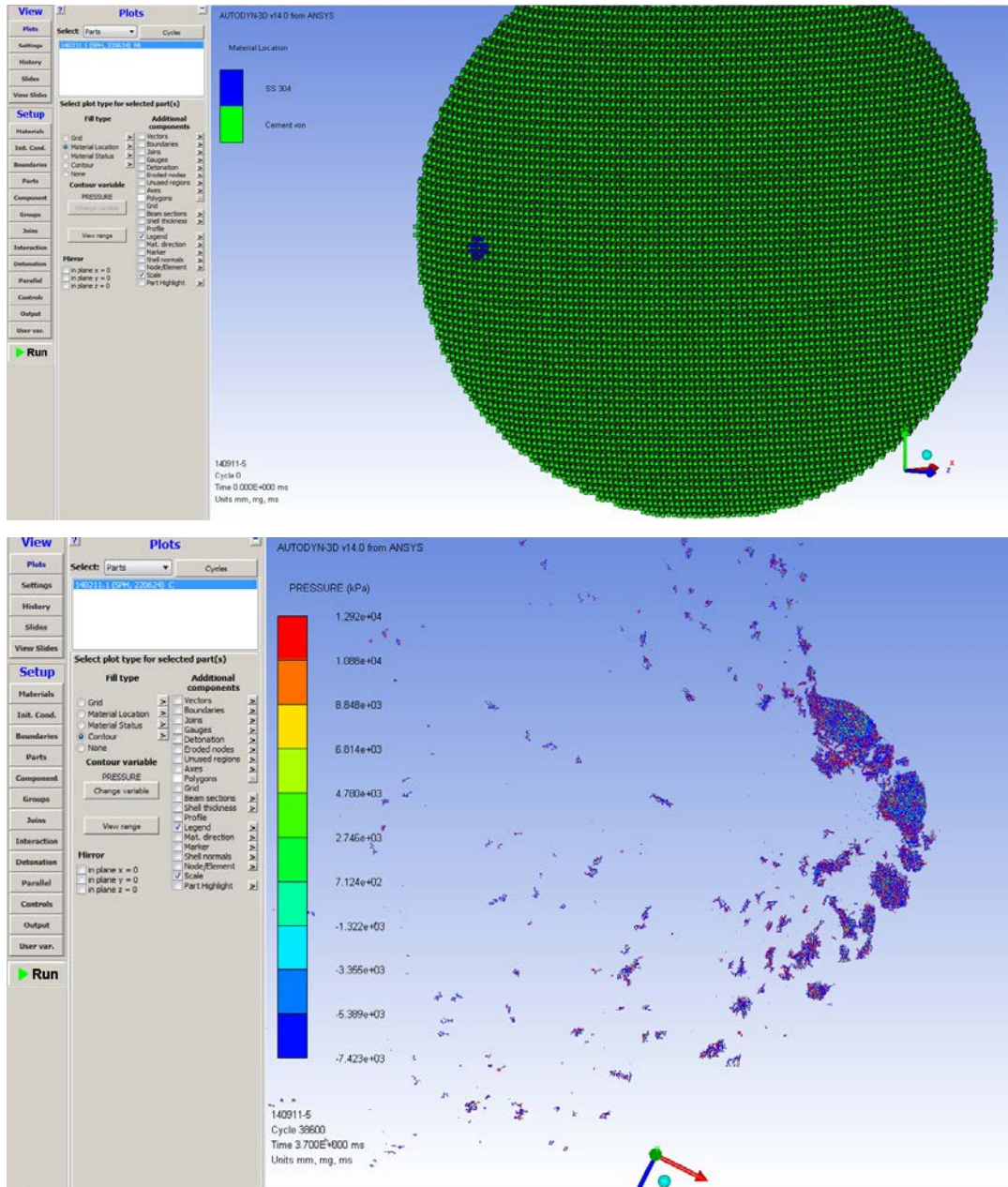
Figure 6.26: Packing the targets with rectangular packed SPH particles (top image) reduced numerical artefacts associated with the cell packing and the models fractured due to the models being used (bottom image).

6.3.3   Results

The results obtained from the simulation data shows the viability of using the von Mises EoS. Although not every laboratory shot was simulated because of time constraints, the data show good agreement with the laboratory data for both the remnant masses with

respect to the impact energy and the individual cumulative fragmentation distributions obtained from the debris.

Static Catastrophic Disruption Simulations
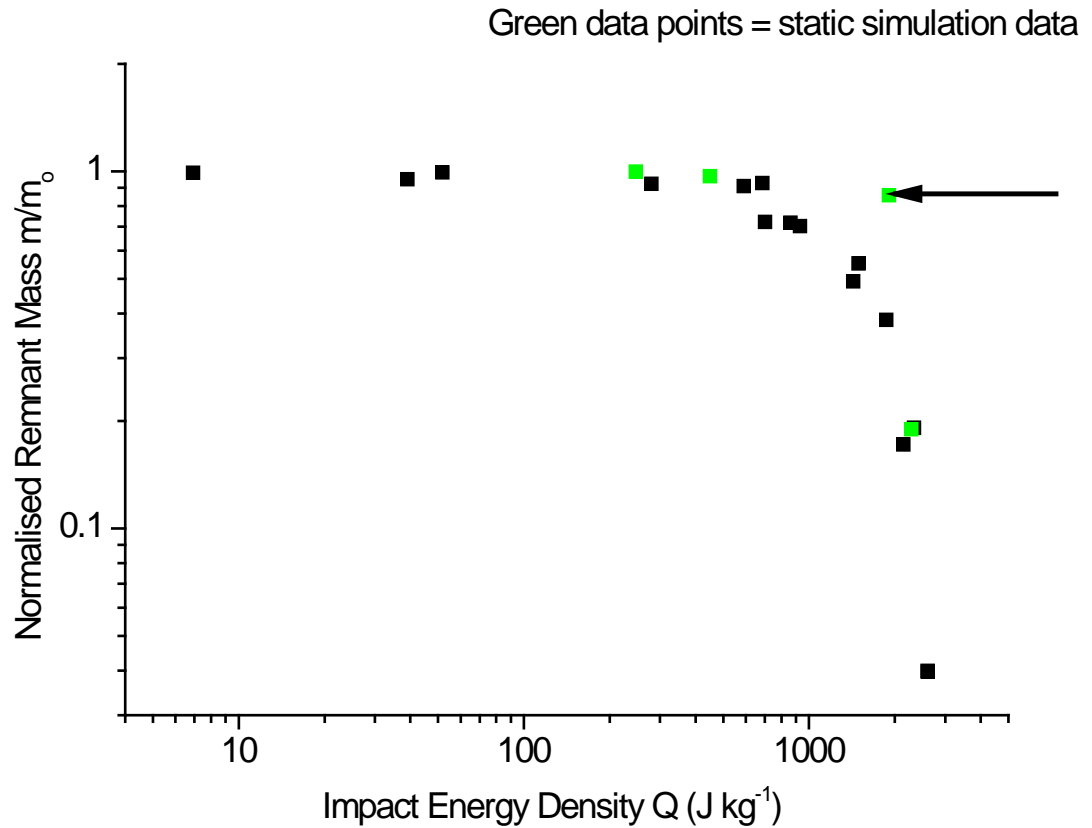
Figure 6.27: Shows the static remnant mass data (laboratory results in black) with the simulation points added (green data points). The arrow shows a datum point which was anomalous to the rest of the points.

Figure 6.27 shows the static data for both the simulations and the experimental data points. The simulation data points in green show good agreement with the experimental data in

the form of the close proximity of the data points to the data trend from the experiments shown in black.

Rotational Catastrophic Disruption Simulations
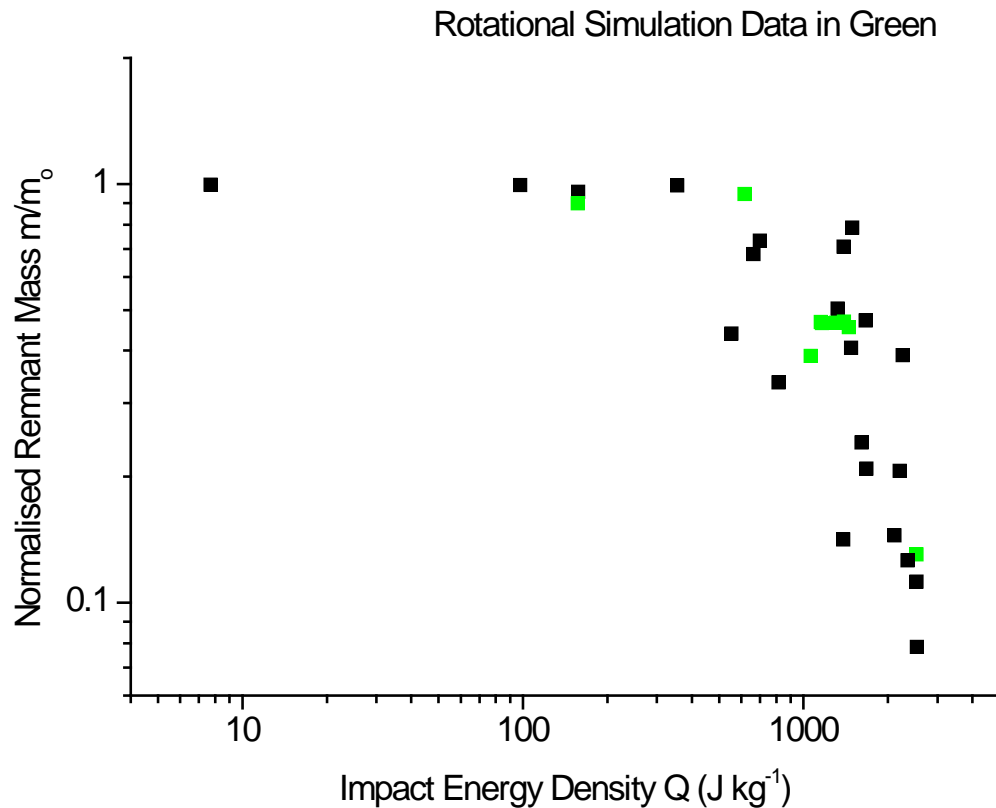
Figure 6.28: Rotational simulation data on the remnant mass graph. The laboratory results are in green with the experimental results in black.

Again the model tracked the laboratory experiments as shown in Figure 6.28. The Q* value was well reproduced. One difference however was in the cratering-disruption transition region where the laboratory data showed a greater degree of scatter than did the simulations. It may be that some slight variations or imperfections in the targets are present in the laboratory experiments but not the simulations, or the target rotation was influencing the laboratory results but not fully reproduced in the physics in the models.
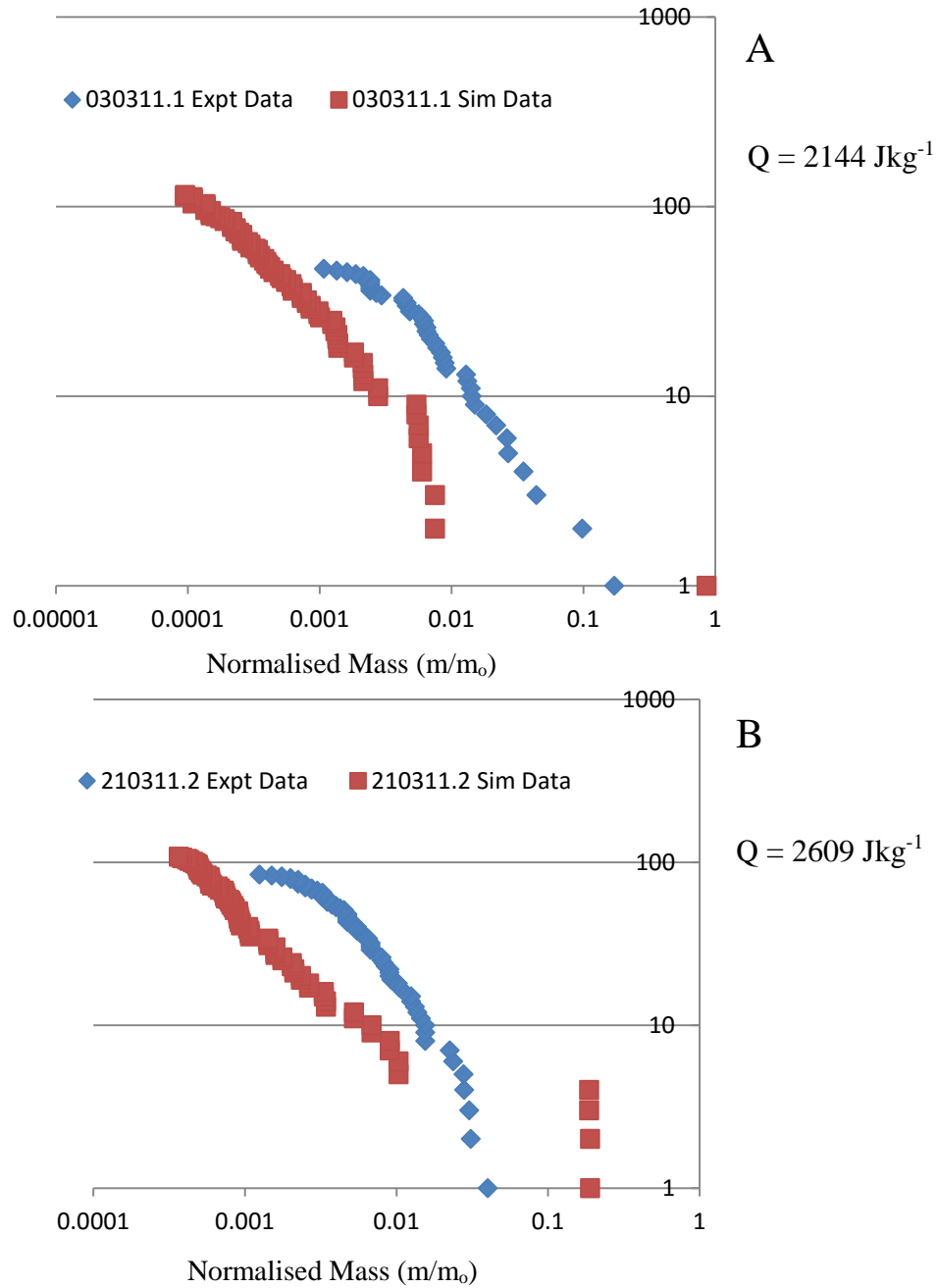
Figure 6.29 A and B: For the purposes of comparison, static impact hydrocode simulations were ran in order to check the validity of the code with experimentation for both static and rotation. A) shows that the target did not disrupt. B) Once again the level of disruption between experimental and theoretical was not in good agreement.
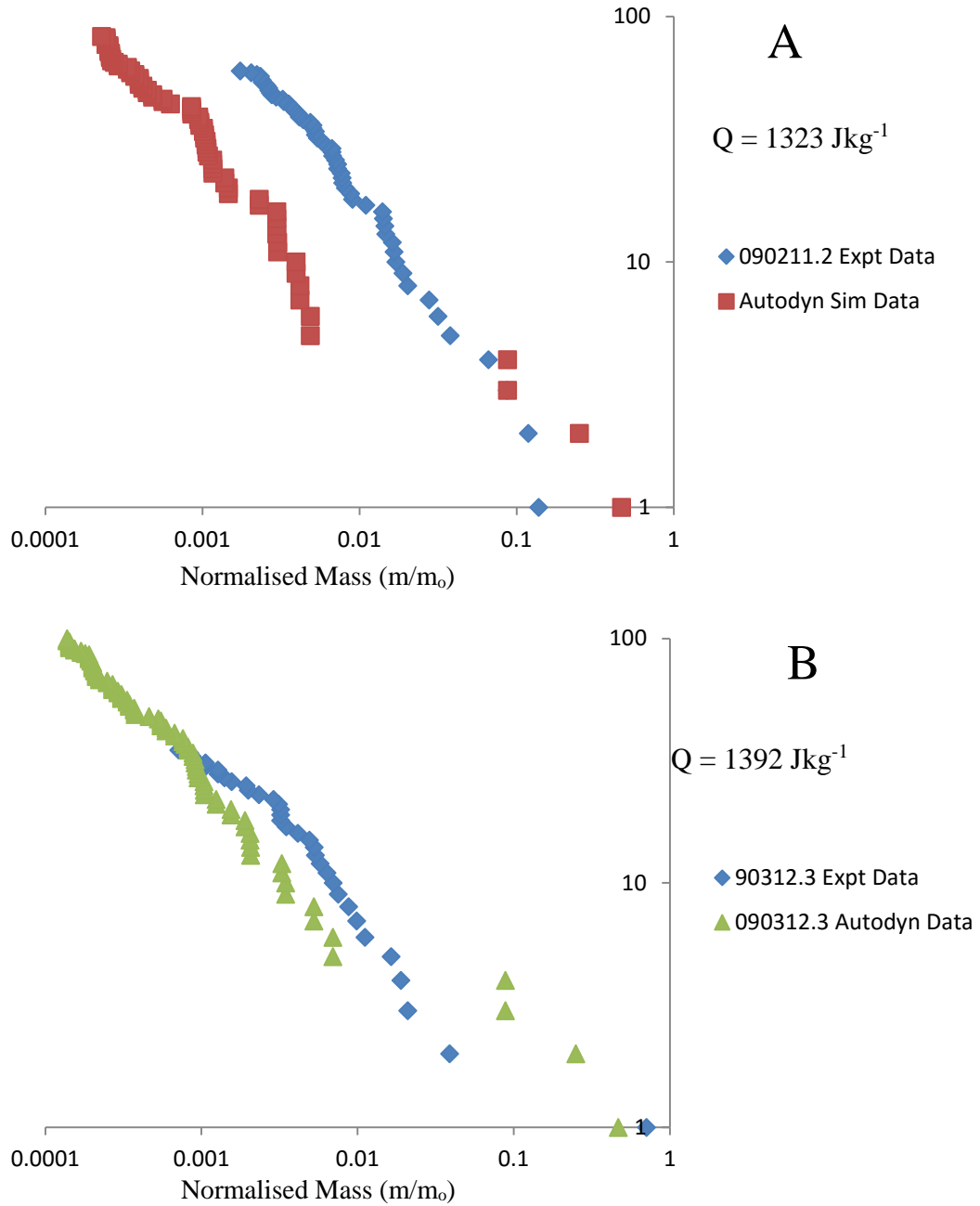
Figure 6.30 A and B: Experimental and simulated fragment distributions show at least an order of magnitude size difference in A but the size difference is greatly reduced in B. The simulation was changed from concentric packing in A to rectangular in B.
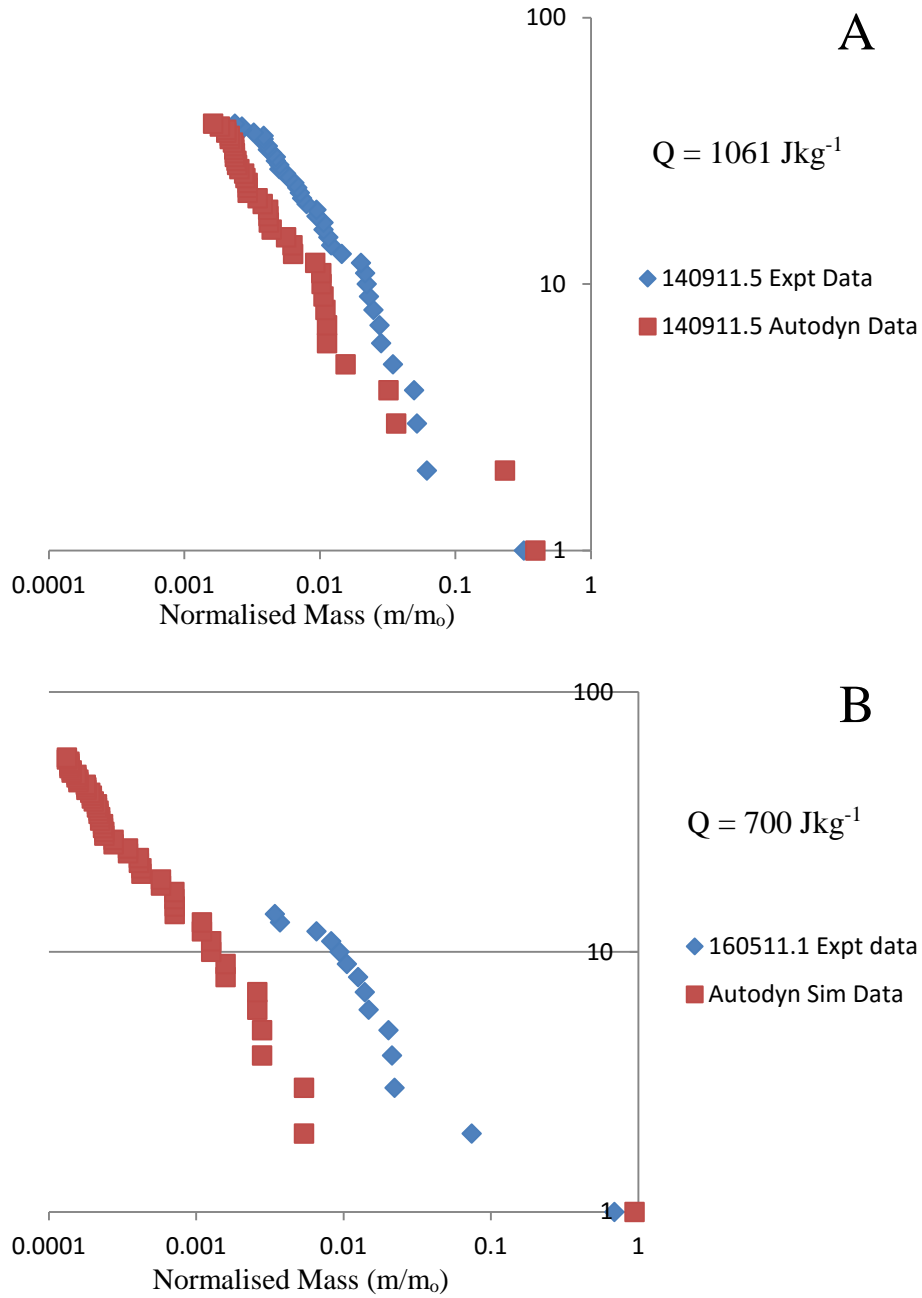
Figure 6.31 A and B: The difference between rectangular (A) and concentric (B) packing shows difference in fragment sizes being generated. In (B) the large size difference between the body and the next largest fragment shows difference in data even though the impacted parent body was very close to the experimental analogue.
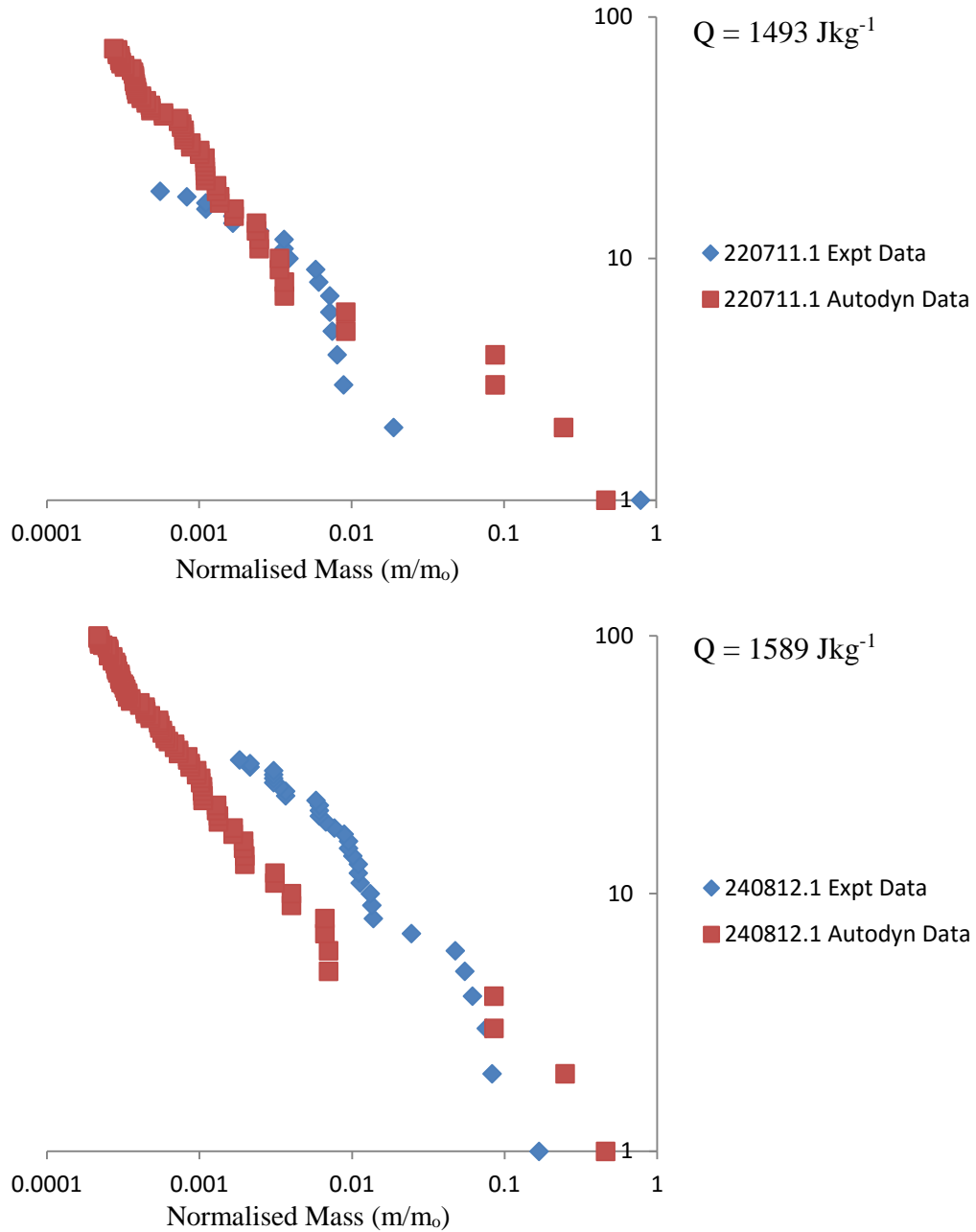
Figure 6.32: Both cases in this Figure used rectangular packing and in both cases the experimental and simulation data are relatively close in data position.

The cumulative fragmentation data shown in Figure 6.32 show that the model still needs fine tuning in order to produce fragment distributions closer to the distributions obtained during the laboratory experiments.

6.4   Summary

The aim set out by this section of the thesis was to provide a viable method into researching possible effects that rotational motion has on collisional break-up during hypervelocity impacts. The choice of test material was an adaptable analogue to stone type asteroids which afforded a level of control on test subject manufacture.

All impacts were conducted with respect to a calculated value of impact energy density Q (J kg^{-1}) which required impactor size and velocity to vary. The rotational velocity was kept constant to resemble 4Vesta's rotation reduced down to the size of the targets used in this project (detailed in Chapter 5).

The data shows that a rotating body undergoing hypervelocity impacts does affect the average Q* with respect to impacting the same target if it was stationary. The Q* values for static and rotation were found to be 1442 ± 90 and 1097 ± 296 J kg^{-1} respectively. These values show a difference of 25% between the two variables.

Another factor affected from rotation was shown in the level of spread in data from stationary to rotational. The spread in data became more apparent around the 'knee-joint' region which corresponds to the cratering-disruption regime cross-over position. A series of extra shots were conducted around the 'knee-joint' in order to test the level of spread, but these proved ineffective in reducing the spread in the 'knee-joint' region which shows that this region is particularly susceptible to the rotational forces supplied to the body during rotation.

Fragment distributions were obtained through individually measuring the mass of the largest debris fragments and then sieving the fragments which were too small for direct measurement. The fragment data were displayed as cumulative log plots in order to obtain the power law exponent related to the rate of fragmentation; β. By finding β, the level of fragmentation regarding material matrix-momentum coupling can be shown, along with fragment size being ejected from the impact.

Table 6.6 showed a series of β calculations for similar Q values with the β values indicating that the largest pieces of debris were associated to the rotational case, and the

rotational forces acting on the parent body meant that crack propagation was effectively influenced by the target pulling itself apart due to the rotation.

The final stage of the catastrophic disruption project was to investigate a suitable theoretical model with the possible outlook to incorporate the model to astronomical sizes. All experiments conducted through hypervelocity impact research are in the laboratory frame and there is a real need to be able to experiment at the astronomical regime. This project used Ansys Autodyn SPH hydrocodes to replicate the laboratory impacts. Once issues of material constants and model packing were solved, a series of 12 theoretical impacts were conducted.

Simulated data for the cumulative fragment size distributions corresponded with experimental data within one order of magnitude for mass in most cases; this indicates that the hydrocode requires further fine tuning. However, when it came to the largest fragment size (as given by m/m_o), the simulations reproduced the laboratory data over the full range of Q studied.

Chapter VII Variable Temperature Impact Cratering: The Experiment

7.0   Introduction

In this Chapter we investigate the effect of target temperature on impact cratering in rocks as an analogue to the rocky terrestrial planets (ignoring the surface effects of regolith or soil, water etc.). Prior work on cratering on rocky planets has included topics such as crater counts (e.g. on Mercury, Neukum et al. 2001) and influence of tectonic environmental effects on cratering (e.g. Aitolla et al. 2007). However, no extensive work has investigated the role of target temperature on impact cratering, but many studies have been undertaken of the behaviour of rocks under quasi-static pressure (e.g. Zhang et al. 1999, Ming et al. 2014, Zou et al. 2014, Hampson and Moatamedi 2007 and Yuan et al. 2015), thermal effects on rocks (e.g. Ghobadi and Babzedeh 2015, Gonzalez-Gomez et al. 2015 and Abdulagatov et al. 2015), and rock-related fracturing mechanics (e.g. Jin et al. 2015, Yang 2013 and Cicero et al. 2015) with a view to understanding geological process on Earth. We can use the results from such studies to give us an insight into how rocks deform under high strain rates, pressures and temperatures induced by impacts that we study in this chapter.

7.1 Experimental Processes

As a feasibility study, samples of rock already present in the University of Kent hypervelocity impact laboratory were used. Unfortunately the sources of these particular rock types could not be verified as they were 'old stock' from previous impact projects.

7.1a The Initial Shots

The samples chosen for the initial temperature related shots were

- Limestone
- Sandstone
- Haematite

The reasons behind the use of the chosen samples were due to the abundance of the rock types, their relative malleability and that they represent a good analogue to the surfaces of the inner solar system planets; with varying levels of composition throughout the inner solar system.

The samples which were to be heated were cylindrical in shape (70 mm in diameter) to fit into the temperature regulated holder (Figure 7.1). The target holder was maintained at a constant temperature by an external power source with inbuilt thermostatic control and fed to the heater through a specially designed connection port.

The samples of rock were pre-heated by the use of a Gallenkamp fan oven set to a maximum temperature of 200°C. The oven temperature was recorded using a CHY 504 RTD thermometer probe.

Once the samples were heated for six hours (to ensure thorough heating throughout the sample), they were transferred into the heated target holder (with a small drop in temperature being recorded during transit) and the light gas gun target chamber was readied for pre-shot pump down.

70 mm
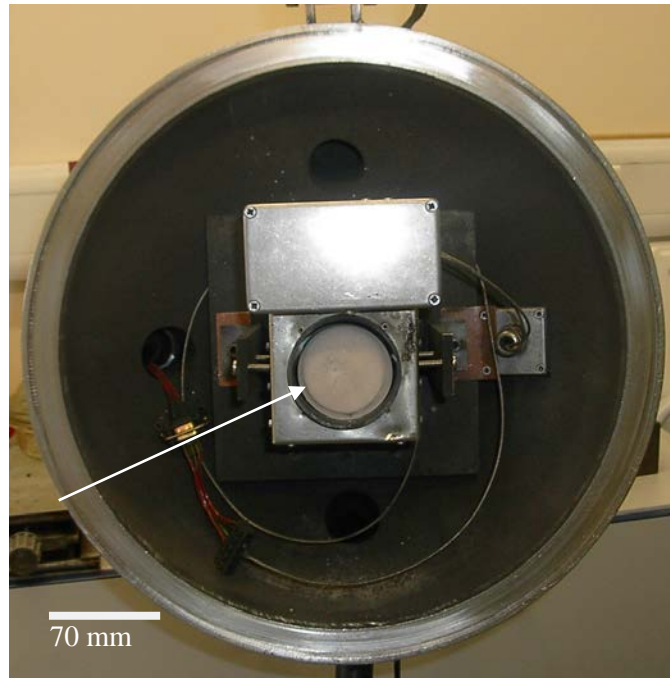
Figure 7.1: A limestone sample (face view) in the heated holder after a hypervelocity shot. The arrow indicates the crater in the rock. The aluminium box above the target masks the power feedthroughs.

Once the required vacuum of approximately 0.1 mbar was achieved, the sample was allowed to sit in the holder for 5 to 10 minutes to allow the sample to reach equilibrium.

420 stainless steel ball bearings measuring 0.8 mm in diameter were used as the projectiles for all of the impacts and they were fired with an impact velocity of 5 kms^{-1} (corresponding to the average impact velocity of bodies in the solar system).

The temperatures of the samples were recorded just before, during and after impact. Once the firing was completed, and the two stage light gas gun was normalised to atmospheric pressure, the samples were removed from the heated holder and given time to cool down to a safe temperature.

For the room temperature shots the rocks were placed into target holders which were dual purpose for cold impacts (covered later in this Chapter) and room temperature shots (Figure 7.12) and positioned onto the retaining assembly of the target chamber. Temperature thermocouples were placed onto the samples with zip-ties in order to record the pre, during and after shot temperatures of the rocks.

The final stage of preliminary testing required cooling the rock samples down to two known temperatures. The first cooled temperature was approximately 253 K which used a Frigidaire upright freezer and the second temperature was 133 K and used on Ultima II low temperature CO_2 chest freezer. Both experimental procedures required care to reduce the amount of heating the rock targets would be subjected to during transit to the light gas gun.

Both sets of targets were placed into evacuated zip-lock plastic bags in order to prevent the samples from forming ice on their surfaces would could lead to externally influenced impacts such as impact dampening from frost acting as a barrier on the rock target. The targets were placed into their respective freezing environments to cool for at least three days prior to impact.

The heated rock experimental procedure required the transfer of the targets to be the final stage before the pump down of the light gas gun; so as to limit rock target heat loss.

7.2   Data Analysis of the Targets
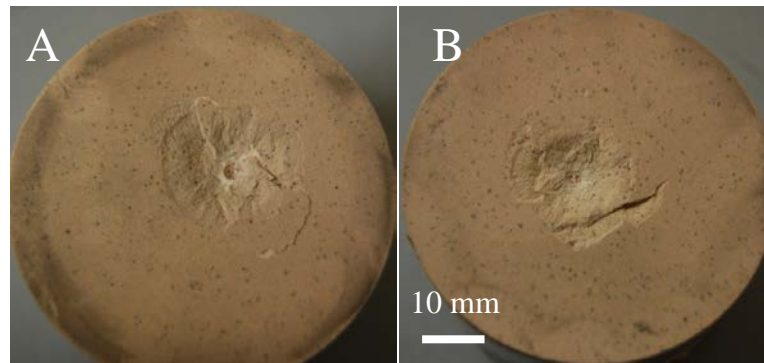
Figure 7.2: Two photographs of heated limestone impacts A and B impacted at 5 kms^{-1}. Impact A shows shallow spallation surrounding the crater central pit and B displays extra spallation at the bottom edge of the shallow spallation zone.

After a shot, before removal of the targets from the gun, a visual inspection was conducted to ascertain whether the impact had produced damage which could be affected by removing the samples from the rock holders. Once removed, a further visual inspection of the targets was concluded and information recorded e.g. photos taken or measurements made (Figure 7.2).

The heated sandstone and haematite samples gave no change to the surface of the stone itself. However on visual inspection of the limestone samples, a definite surface colour change was recorded. The colour of the limestone samples was a light golden yellow before being heated and a pink hue afterwards as shown in Figure 7.3.
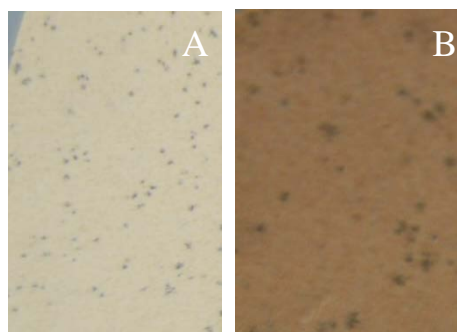
Figure 7.3: Two photographic sections of the same limestone sample, A is a section which has not been heated whilst B was heated to 500 K. A colour change can be clearly seen as a result of heating the limestone.

The reasons for the colour change of the limestone material have not yet been found. Collaboration with several research staff at Royal Holloway (University of London) geology department, has given a possible reason of oxidation of iron in the limestone. However the occurrence of the colour change did raise the question on whether the possible oxidation of the limestone constituents would have affected the cratering properties of the samples.

To obtain data on the rock samples, initially two direct measurement techniques were used to ascertain the crater diameter and depth. Later this was superseded by a modelling technique utilising 3D modelling techniques to provide the same measurements.

7.2a   Crater Diameter

Crater diameter was initially measured by the use of vernier callipers. The initial impact region (commonly the centre of the impact) was used as a point of reference with the callipers being positioned to opposite edges of the crater and an imaginary straight line going through (Figure 7.4). To allow for the statistical treatment of the irregularity of the crater diameter, the callipers were rotated about the initial impact position thereby measuring multiple positions around the crater diameter. Once the data were obtained, the standard deviation was found to give the degree of irregularity of the crater diameter. The diameters throughout the thesis included extra spallation resulting from the impacts.

10 mm
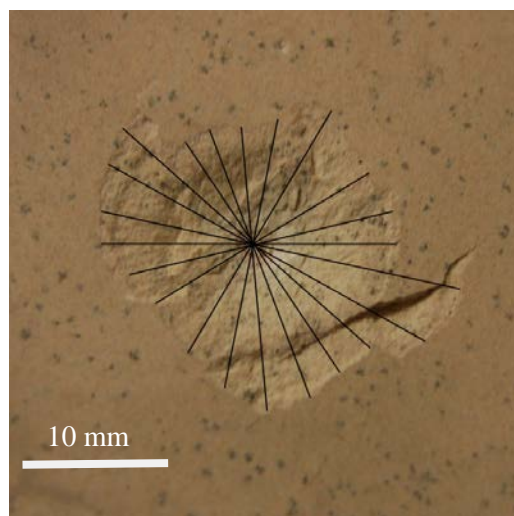
Figure 7.4: Positions for crater diameter measurement are shown by the black lines in the diagram. The measurements were taken with the initial excavation zone as the focus.

7.2b   Crater Depth

The use of a manual depth probe was incorporated to measure the depth and profile of a crater under investigation. The depth probe was a vernier calliper with a metal needle attached to the bottom of the extending calliper slide, and was measured along a graduated stand to give depths and profiles.

This depth profile gives a relatively accurate assessment of the crater but the profile was 'quantised' in appearance (Figure 7.5). The measurement process uses per mm divisions along the profile with depth measurements being taken at every mm. The size of measurement used by this method is not small enough to deal with the problem of the quantisation of crater morphology.
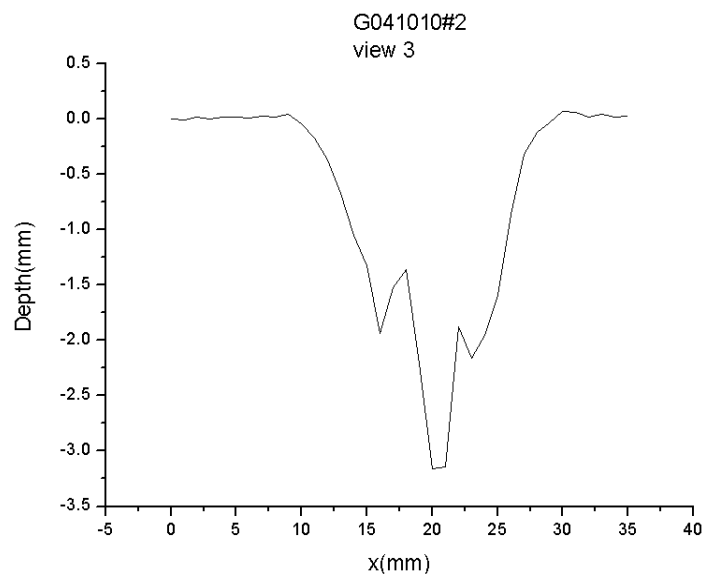
Figure 7.5: A depth profile of a sandstone crater using the manual depth probe. The manual method resulted in a 'unsmooth' plot which did not show the morphological features to better than 1 mm horizontal displacement.

However using the manual techniques of crater profiling did cause some concern with the alteration of the crater surface from the depth probe needle penetrating into the rock surface. Also the unsmoothed profiles gave data not totally accurate crater profiles in general.

7.3c   The Crater Volume

The final measurement to be taken was the crater volumes produced during the impacts. 75 – 90 μm diameter glass beads were sieved using a series of fine sieves to

obtain glass beads of a known size range to fill crater voids but large enough to give a recordable volume measurement in a measuring cylinder.

A mass-volume calibration graph (Figure 7.5) was calculated by measuring the glass beads in 0.2 ml steps in terms of mass. Once the data were obtained, the results were used to make a straight line graph showing the simple linear relationship between the mass and volumes of beads.
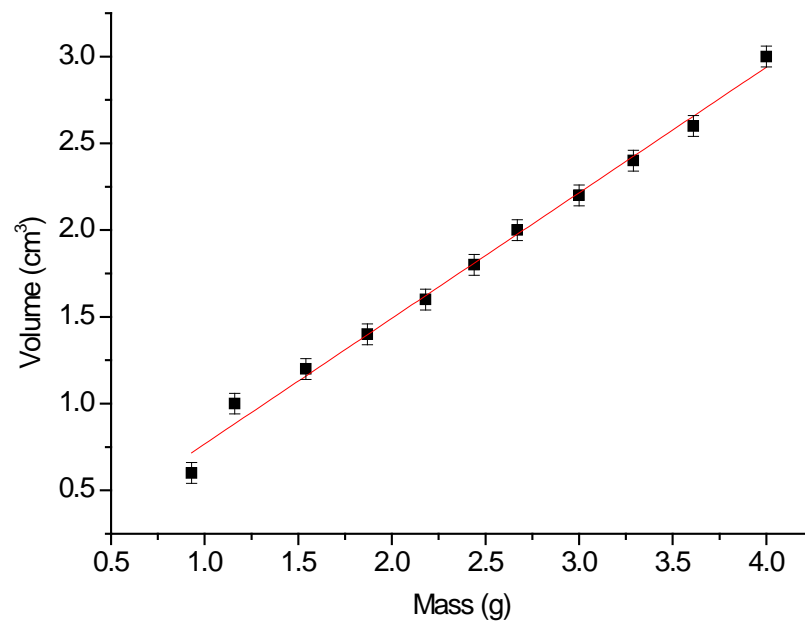
Figure 7.5: The calibration graph of the 75 – 90 mm glass beads to be used for determining the crater volumes – $r^2 = 0.99$

The equation of the line fitted to the data in Figure 7.5, was as follows:

$$y = [0.1349 \pm 0.1494] + (0.69375 \pm 0.1896)x \qquad \text{Equation 7.1}$$

With y = volume of crater in cm^3 and x = mass of beads in g and a regression $r^2 = 0.99$.

However, Equation 7.1 displays a value for the intercept of the fit. The calculated error was greater than the actual value itself; therefore the equation of the line was reduced to only incorporate the slope resulting in:

$$y = (0.69375x) \qquad \text{Equation 7.2}$$

The craters were filled with the glass beads until level with the surface and then the difference in bead mass from the primary container was recorded. The mass difference was then used in Equation 7.2 and the corresponding volume was calculated in terms of cm^3; this was then converted into mm^3.

As will be explained later in this Chapter, the manual methods were superseded with a new measurement technique using the Alicona MeX surface analysis program. However, in certain circumstances, the crater sizes were too big for the Leica microscope used and instead the manual methods for data analysis were used. However, the depth probe was not used due to being too invasive on the samples so a focal plane depth method was used instead.

The non-invasive method of depth analysis used a МБс-10 stereomicroscope to focus from the surface to the bottom of the crater. The microscope used a Mitutoyo measuring probe which was displaced vertically during focusing of the microscope at the two points of reference, thereby registering the depth of the crater.

To obtain a good image in the eye piece, the magnification was increased to 4x magnification to focus on a smaller section of the surface. The probe was zeroed at this position and the deepest section of the crater was brought into focus using the same magnification.

7.3   Variable Temperature Rock Impacts – Phase II

The second phase of the variable temperature impacts project formed the main part of the experiment. Working from the preliminary techniques and results from the first phase, some changes were put into place in order to improve upon the experiment and data acquisition.

The preliminary results were presented at LPSC 2011 (Morris et al. 2011). One suggestion from the audience was the option to increase the temperature range for the heated targets from approximately 500 to 1273 K. This increase in temperature allowed for the investigation of the cratering processes as rock targets approached the plastic region. This change required a new heated target holder which could reach the desired temperature range; the new target holder is detailed in Chapter V – The Impact Target Holders.

It was also decided to cover a greater range of temperature rather than just to increase the maximum temperature. Two further changes were made to the experiment data analysis techniques; the first was to incorporate non-invasive computer modelling and measuring of the craters and the second used computer modelling to produce unique data handling of crater profiles.

7.3a   Rock Types

The three types of rock used were: basalt from Ruddons Point in Fife Scotland, sourced from a collaborator at the National History Museum, Ancaster Hard White limestone from Lincolnshire and Beestone Red sandstone from Cumbria (sourced via www.realstone.co.uk). It was very important to obtain the sources and location of the rock types for information and characteristic purposes.

The petrology of the rock samples are as follows: The Ancaster hard White Limestone is a fine-grained Jurassic limestone which is cream white with pink variations. The density of this particular limestone is 2.3 gcm^{-3} and has a compressive strength of 25 MPa and porosity of 15.30%. The Beestone Red Sandstone is a fine-grained sandstone with some clay holes from the Triassic period. The perpendicular rift compressive strengths for both dry and saturated are 115 and 66 MPa respectively and has an overall porosity of 12.36%.

Basalt was chosen due to being indigenous throughout the solar system where volcanism is prevalent (Thiessen et al. 2014) and provided a very good analogue to impacts which would occur on the terrestrial planets as well as moons such as the Moon. The choice of the limestone sample was made due to being an Earth specific rock type with an associated global abundance of 10% in all sedimentary rocks and would show cratering characteristics on Earth with different temperature profiles. The final source of rock was sandstone; sandstone was used to investigate grain type rocks.

7.3b   Advanced Cooling of the Samples

With new temperature ranges being investigated, new experimental techniques were needed. The rock samples used for the liquid nitrogen rock impacts were cylindrical measuring 60 mm in diameter and 60 mm in length for the heated samples and for the cold and room temperature samples, the square dimensions were 90 by 90 by 50 mm.

The rocks were pre-chilled down to 133 K for three days in the CO_2 chest freezer in order to cool the whole interior of the rocks.

On the day of the shot, the rock samples were transferred to a Thermo Cryomed liquid nitrogen freezer approximately 45 minutes prior to the experiment for further cooling. The Thermo Cryomed LN_2 freezer used two solenoid-valve controlled feeder coils, situated behind an electrical fan system to 'wash' samples inside the freezer with LN_2 liquid and vapour. The system was controlled with a temperature control program named 'Andy1' which cooled the samples as follows:

- Pre-Cycle Cooling Phase – Cool down to 143 K then hold.

This cycle was important to pre-chill the freezer environment prior to transfer of the sample from the CO2 chest freezer. This was done so that the sample would not warm up and produce thermal shocks in the interior of the samples if placed in a warm chamber which then cooled.

- Cooling Cycle – Cool sample down to 93 K then hold.

The main cooling cycle cooled the samples from 143 to 93 K over steps of 10 K min^{-1}. It was important to cool the rocks down quickly to give a longer time at the required temperature to reduce temperature gradients inside the samples, but slow enough to allow the samples to accommodate the drop in temperature. The cooling programme measured the sample directly with a temperature probe.

For the purposes of accuracy, a PT100 temperature sensor (already attached to the rock) also recorded the sample temperature.

- 'Soaking' Cycle – Hold the temperature in the range of 93 to 82 K for 30 minutes.

The final stage of rock cooling was to stabilise the rock core temperature of the samples for at least 30 minutes. Once the allotted time was reached, the rocks were transferred to the light gas gun target chamber for pump down and shot.

Unfortunately, problems of thermal warming of samples during transfer were prevalent in this temperature range. Moving the samples, securing them to the target base and pumping down the gun, resulted in excessive sample warming. During the

limestone and sandstone experiment runs, the targets warmed up by 100 K in both cases, which was undesirable. To remedy this problem, after cooling a basalt sample down in the LN_2 freezer, the samples were placed into a thermally insulated liquid nitrogen bath and transferred from the freezer to the target chamber. The assembled target was removed from the bath at the last possible moment and placed into the target chamber, but once again a considerable temperature increase was recorded with the basalt sample warming from 82 to 196 K.

When the targets were ready to be fixed into position, they were removed from the 82 K environment and clamped onto a sheet of expanded polystyrene insulator with a pair of Irwin Quick Grip Mini hand tighten clamps (Figure 7.6 A); these type of grips were considered the best to use during target assembly because of the timing factors involved.

Once the shot was completed, the targets were removed from the light gas gun after pump-down and allotted sufficient time to thaw properly before removing from the target assembly. This was an important step to guarantee that the resultant crater was from the impact and collisional interaction and not due to stresses caused from thermal effects (Figure 7.6 B).
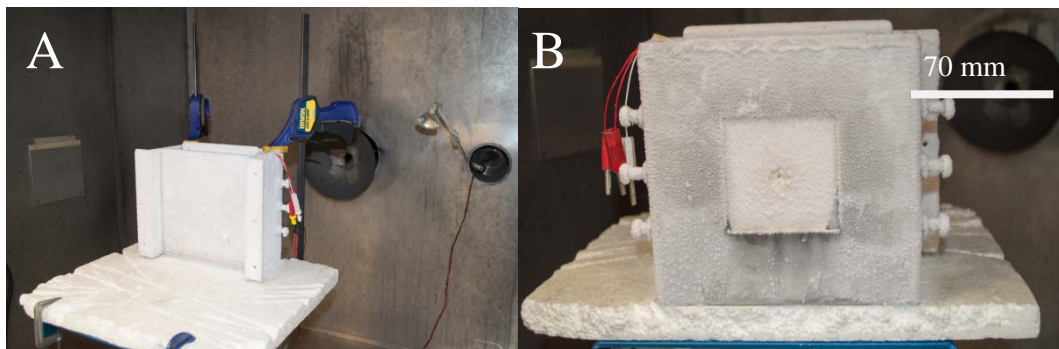
Figure 7.6 A and B: Two photographs showing before and after an impact into very cold limestone. The target is held into a pre-determined position via Irwin Quick Grip Mini clamps and after the impact, the samples were thawed and data collected.

7.3c   Advanced Heating of the Samples

The rock targets were placed into the newly designed holder and the Eurotherm Adiabatic Temperature controller electrical supply was turned on. The current from the supply was thermostatically controlled to provide the heating elements of the

heated target holder with bursts of 9A current until the required temperature was reached.

The first stage of heating was to get the rocks as close to 473 K and to maintain that temperature for 30 minutes, again to allow the samples to reach equilibrium.

At this point of the experimental preparation, the electrical feed into the heating assembly had to be switched off during the target chamber pump-down. This was very important due to the residual breakdown of the internal atmosphere in the target chamber which can induce a breakdown voltage as described by Pachen's law or a Townsend avalanche Discharge. As the vacuum increases inside the chamber, points which are in very close proximity to each other – the live feed and the feedthrough into the chamber, increase the likelihood of electron discharge, but once the internal pressure has dropped enough, the voltage required for electron flow increases due to the lack of a gaseous mediator.

$$V = \frac{apd}{\ln(pd)+b}$$
<div align="right">Equation 7.3</div>

Equation 7.3 shows Pachen's law for electron discharge in voltage where V is the breakdown voltage, p is pressure in atm, d is gap distance in m and a in V (atm m)[-1] and b in (m atm)[-1] are gas constants depending on which gas is being reduced. Using standard air values for the constants, discharge in air is given as 327 V at standard atmospheric pressure being 7.5 mm.

This theoretical consideration gave a good approximation of the reasons when the safety fuse blew previously around the 1 mBar region. But Townsend discharges also play an important factor in this problem.

The Townsend discharge produces an electron cascade through an ionised gas due to a sufficiently large electric field being present. Equation 7.4 shows the Townsend discharge which is dependent on distance as with Paschen's law;

$$\frac{I}{I_o} = e^{\alpha_n d}$$
<div align="right">Equation 7.4</div>

I is the input current (A), I_o is the photoelectric current (A), e is the Euler number, α_n is the Townsend coefficient (m^{-1}) which describes the production of ion pairs in length and d is the distance (m).

It was decided that not only was Paschen's law a possibility, but the level of ionisable gun debris contained in the target chamber such as cartridge powder particles etc. would increase the likelihood of electrons following and subsequently shorting the electrical system when the internal target chamber pressure was reduced.

As soon as the safe level of 0.2 mbar vacuum pressure in the target chamber was reached, the power supply was turned on again and started to heat the rock sample.

One issue which arose from the heating of the targets up to high temperature, and this was more common with the basalt, was the consequence of outgassing from the samples. As the rocks were being heated, they started to give off gas, which was registered on the light gas gun pressures gauges. One result of this was the shorting of the heating assembly and consequent failure of the safety fuse.

To deal with the issue of outgassing, a pre-heating of the basalt rock samples was conducted in a heated furnace. It was decided to allow the samples to outgas at a higher temperature than the proposed shot temperature maximum, thereby driving more gas from the sample than was contained at that holding temperature.

The samples were placed into the high temperature furnace and heated through a heating and cooling cycle which lasted approximately a day. Commonly, on removal, the basalt showed a reduction in the pre-heated mass to the outgassed mass by approximately 33.5 g.

One final issue was the thermal decomposition associated with the limestone samples, as shown in Figure 7.7.

Thermal decomposition of limestone is given by the following reaction;

$$CaCO_3 \rightarrow CaO + CO_2$$
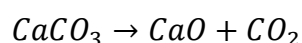
Figure 7.7: A heated limestone target with advanced thermal decomposition after a 923 K impact test. Although decomposition did not occur straight after the shot, the time frames in which to take data were very short (within hours).

The temperature range for thermal decomposition of calcium carbonate is 908 K to 1138 K (Halikia et al. 2001). The final heating temperature of the hottest limestone impact was recorded at 923 K, which was just at the onset of thermal decomposition. A limestone sample which was heated to 773 K showed a considerable amount of colour bleaching from the sample during the heating process. After impact, the target was robust enough to allow data to be obtained from the crater, but rapidly progressed thermal decomposition from heating shortly afterwards as shown by sample breakup.

Considering that Halikia et al. found the decomposition range to be from 908 K, the extra energy supplied to the target during the impact coupled with the internal temperature the target was being held at, may well have supplied enough energy to accelerate thermal decomposition at this temperature.

The second limestone target shot at was in the thermal decomposition range and on upon visual inspection, showed the same level of colour bleaching but this time, a definite accelerated decomposition.
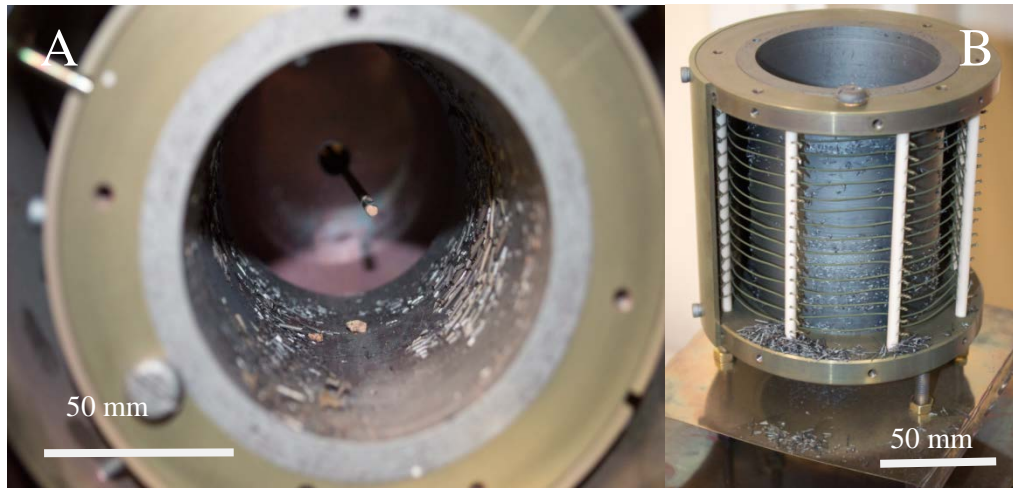
Figure 7.8 A and B: A - Outgassing of the rock samples during heating produced oxidation layers collecting on, and around, the inner sleeve of the target holder. B - The oxidation layer fragments in the target holder produced a problem with electrical shorting due to the oxidation layers collecting around the heating elements.

Two final issues were encountered with the target holder associated with the higher heating of the targets. The first issue arose from the outgassing of the rocks. As the rocks outgassed, layers of oxidation were formed on and around, the heating tube of the target holder (Figures 7.8 A and B). The oxide layer peeled and fell away which produced no effect on the target side of the heating cylinder, but did create electrical shorts in between the element wires which in turn triggered the safety fuse to blow.

Also, the constant heating up and cooling down of the variable target holder led to a problem with annealing of the target holder shields. Although the shields were inspected on a regular basis and could easily be changed, on finding this issue, the target holder was inspected fully in order to check that other regions of the holder were not annealing. The full inspection of the holder showed no adverse effect from the temperatures except for the softness showed by the shields.

7.4   Calculation of Cratering Efficiency

One characteristic which is covered by theoretical approaches to cratering and impacts is the quantity known as cratering efficiency. From the scaling work concluded of Hosapple (1993), cratering efficiency is determined by Equation 7.5 below:

$$\pi_v = \frac{\rho V}{m} = \bar{f}\left[\frac{ga}{U^2}, \frac{Y}{\rho U^2}, \frac{\rho}{\delta}\right] \qquad \text{Equation (7.5)}$$

Where

$$m = \frac{4}{3}\pi\delta a^3.$$

And g is surface gravity in ms-1, a is spherical radius of body in m, U is velocity in ms^{-1}, Y is a strength with stress in Pa and finally δ and ρ are densities in kg m^{-3}.

Cratering efficiency is a term which uses three forms of ratios to determine the scaling of an impact. The first term is the ratio of lithostatic pressure at one projectile radius of the target to the dynamic pressure. The second term is the material strength to the dynamic pressure and the third term is a simple ratio of target and projectile densities.

Equation 7.5 allows for the scaling of impacts and covers most aspects with respect to strength or gravitational regimes. However, for the purpose of this work, it was necessary to reduce Equation 7.5 down to the term which constitutes only the strength dominated regime: the second term.

$$\pi_3 = \frac{\rho V}{m} = \bar{f}\left[\frac{Y}{\rho U^2}\right] \qquad \text{Equation (7.6)}$$

The strength dominated cratering efficiency from equation 7.6 shows that the crater volume increases linearly with projectile volume and for cases where impact velocity U is constant, it will increase linearly with energy. However the Young's modulus term in Equation 7.6 uses material strength with respect to temperature and no work has been concluded on the effect of temperature related strain rates for the samples used in this work. The closest work was concluded by Ranjith et al. (2012).

This project used the two terms π_v and π_3 to ascertain whether any effect from the sample temperature could be seen.
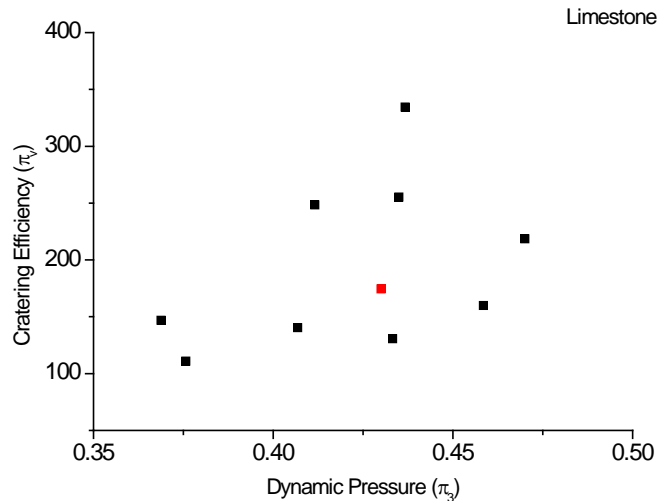
Figure 7.9: Cratering efficiency vs dynamic pressure for impacts into limestone.

An example of results is shown in Figure 7.9. The red coordinate shown gives the average cratering efficiency of the rock sample concerned (in this case limestone). The position of the red datum point is where the remaining points were expected to be located, but considerable data spread is shown and therefore concludes that temperature has an effect on crater formation and efficiency.

7.5 The KDM Method

Many research projects have looked at craters and their respective profiles, but the choice of which cross-sectional profile has depended on individual crater morphologies, and the crater characteristic which appeared most interesting to the researcher involved. Although this approach has worked well for a long time, the nature of this new work required a method to show the overall change of crater morphology with respect to the variance of internal temperature. It was decided that a robust statistical method was needed to profile the whole crater in terms of 360° profiling, with options to show average crater profiles in terms of median height throughout the whole profile and include the standard deviations with maxima and minima profiles.

The Kinnear-Deller-Morris or KDM method was worked on by the author of this work and two collaborators Timothy Kinnear and Jakob Deller. The KDM method utilises the raw DEM data obtained from the MeX profile as an exported text file.

The data is fed into the KDM method Python language programme (added in Annex D) and compiled to form a point source data map of the three-dimensional data with generated statistics of all data points (minima/maxima/mean/median/total depth(max-min); this, in effect, recreates the DEM but as a graphical representation with statistical information.

The programme was written to perform a statistical centroid which uses a median averaging of singular datum points, around the centre of the crater to 'home in' on the lowest points of the crater, thereby determining the centre at that position. In order to facilitate this centring method, the centre nearby position is located by a horizontal slice taken through data at some depth based on 1/3 of max depth of crater; the mean location in each dimension is then taken to obtain the first guess of a centralised location. This method works well when the centralised region of a crater is relatively simple, but the method would have problems for very complex structures such as peaks or broken/weathered peaks.

Sometimes a gradient correction was required due to the DEMs having offset surfaces, so making the assumption that axial tilt was in one dimension only, and that the crater did not intersect the edge of the image at the extremes of that axis being plotted against, the mean profile positions were taken at each of the two opposing edges to get two datapoints with a linear gradient. The opposite to that gradient was then applied to the entire dataset to force it to a `flat' reference plane, thereby levelling the offset.

For every one of the 11×11 positions, the measure of sum(std/sqrt(radius)) is calculated. This is to ensure that greater radii data do not dominate simply by virtue of more grid points. The best of these locations is then selected as the new centroid, about which is the degree of greatest symmetry as categorised by the selected metric. That selection is then used to give the radial profile in the same binned fashion, along with ± the standard deviation for each bin, which then forms a two dimensional plot.

The main advantage of the KDM method is that the concept of crater profiling can now have a statistical assuredness, instead of a personalised view. However, the main

disadvantage to this method is the statistical averaging of the crater profiles. The crater profile becomes 'washed-out' from the averaging done and therefore does not show the fine detailing of crater morphology, such as terracing and grabens, when compared to taking single simple crater profiles.
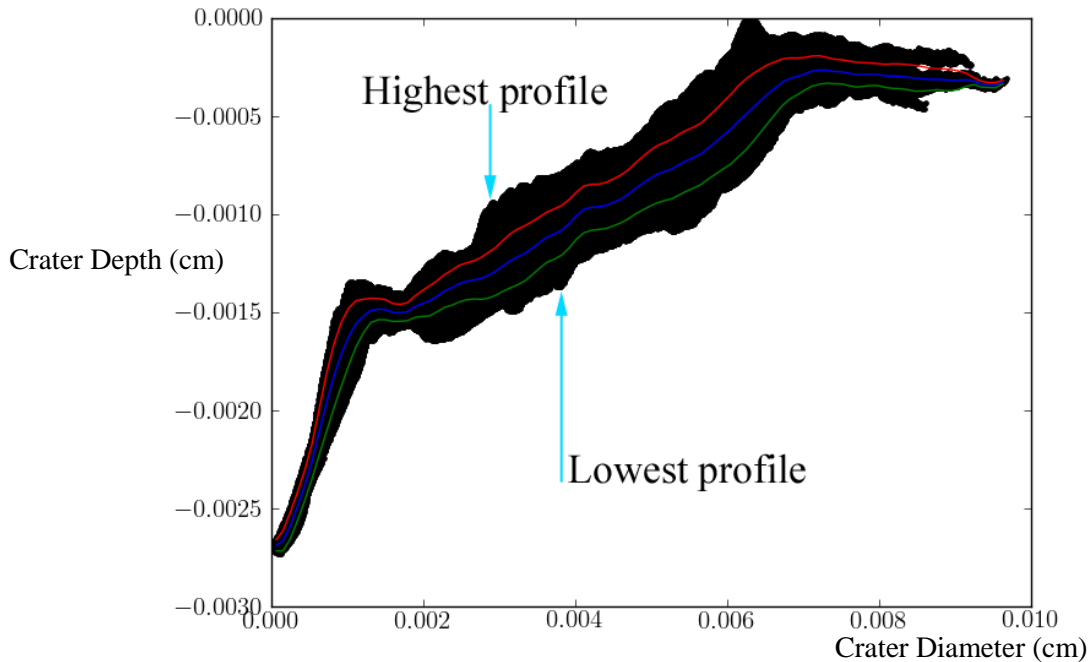

Figure 7.10: A complete KDM method data set from the 793 K sandstone impact. The black shape shows all crater profiles obtained via KDM and the blue line shows the median average for all of the profiles with ± standard deviations as red and green.

From Figure 7.10, the whole data set for a single impact is shown. The axes are depth on the y-axis and crater radius on the x-axis. The black profile gives all profiles obtained from the crater in the positions from the lowest point at the bottom left position of the plot, to the edges of the crater at the top right position.

The arrow labelled lowest profile gives the lowest recorded data profile from the crater, whereas the upper limit to the profiles is shown from the highest profile. The thickness of the black section shows each individual crater profile from the lowest to the highest, so craters which show greater amounts of variance in morphology will show a wider black data section to those with very little change in morphology.

The blue central line through the black data set shows the average of the crater profile. This line gives the overall shape of the crater as an average position with respect to

every profile made from the code. As can be seen, the blue line gives only a general shape but little information on the individualised morphologies contained in the crater.

The other two lines; the red and green lines give information on the statistical averaging of the maxima and minima positions respectively. The red and green lines take only the data profiles which correspond to the highest and lowest profiles.
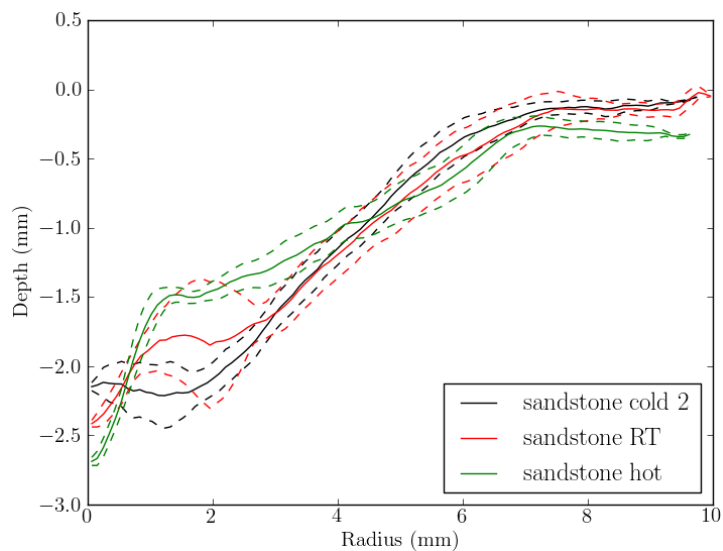

Figure 7.11: Crater comparisons are made by taking the average profile data and error for each full data set, as in Figure 7.10 and compiling the trends with respect to temperature.

The KDM method allows comparisons to be made by removing all the profile raw data (the black section) from the plots and including the statistical profile data to be plotted together (Figure 7.11).

Each line corresponds to a certain profile data set and each line has the standard deviation of each line shown by the dashed lines accompanying the solid profile lines. This makes overall crater profiling easy to ascertain changes in morphology with respect to external influences such as varying temperature.

7.6 MeX

The precision of the direct measurements of the crater characteristics were limited due to the positioning of the callipers and level of system accuracy of the measuring devices themselves. The level of tactile contact between the crater and the measuring devices was undesirable due to the fragile nature of the specimens.

A new method to measure the crater dimensions was found by utilising the MeX measurement and modelling software. The MeX software proposed by the Alicona Company, is a surface analysis tool, commonly used in making measurements with SEMs but for the purposes of this project, was used with a Leica microscope in the laboratory.

A stereo image first had to be compiled of the sample crater; this was done using the lowest magnification (multiplication factor ×0.71) in order to take pictures with the whole crater in the view, as both the Leica image capture programme and the MeX software respectively, have boundaries in which the image must fit into.

The sample was rotated around the y-axis (the optical axis) in order to establish a stereo pair of images, but in a tilt range of 6° to 10° to give the best results for the stereo image. Both images were then imported into the MeX programme with the measured parameters of:

- Sample to lens distance in mm
- Lens to focal point in mm
- Tilt angle in degrees
- Pixel size in μm

As stated in Chapter V – Impact Target Holders, a MeX stereomount was designed to hold the rock samples and to tilt them through a series of angles used by the MeX computer program. For more information, please refer to Chapter V.

The sample-to-lens distance was found using vernier callipers. It is the distance from the surface of the crater, to the mid-section of the focal compensating lens of the microscope.

The lens-to-focal point distance was measured to be 306.69 mm, and was the distance from the mid-point of the focal lens to the CCD region of the Leica camera positioned at the top of the microscope in the optical axis. This value is fixed.

The tilt of the sample was registered from the MeX stereomount and was usually designated as 3° left and right to give a total angular sweep of 6°.

The pixel size was determined by Equation 7.7 and the use of a micrometer screw gauge and vernier callipers with 1 mm separation in-between the measuring faces. The two 1 mm distances were focused in the field of view of the Leica microscope and both instruments were used to ensure accuracy. Once the photograph for the 1 mm separations was obtained, the distance in pixels between two successive x-axis points corresponding to the edges of the separations were recorded. Repeating this measurement across the two faces produced the statistics needed to reduce error.

$$Pixel\ Size = \frac{0.001\ m}{pixel\ count}$$ Equation 7.7

The typical value for the pixel size came to 6.524 μm.

Image alignment was then completed through either, a manual rectification by overlapping the two images on the bottom black-and-white image window, or by choosing the automatic rectification function of the software.

Rotation of the sample around the y-axis was needed to be as accurate as possible, to limit errors, One problem, which is the result of incorrect eucentric tilting of the specimen, is in the rectification of the images. Sometimes the MeX software was able to correct for this, but on most occasions the rectification process could not be completed and therefore rectification was done manually.

Calibration of the MeX software took around one month to complete for the highest accuracy in the measurements possible. A sample crater was placed into the MeX stereomount and an inclination meter was placed onto the mount in order to measure tilt axis with an accuracy of ±0.005°. Using the stereomount eliminated eucentric tilting issues and images of the test crater were taken and used with the programme.

The calibrations were checked using direct measurements on a sample such as crater diameter, depth and volume. The accuracy obtained through MeX was found to be within the range of 95 to 99% accuracy.

7.6 a Measuring Crater Diameter with MeX

Using the central portion of the crater as the measurement focus, lines of distance rotating around the central point were used to obtain the diameter of the crater, with

the level of crater variance from the calculated standard deviation as seen in Figure 7.12
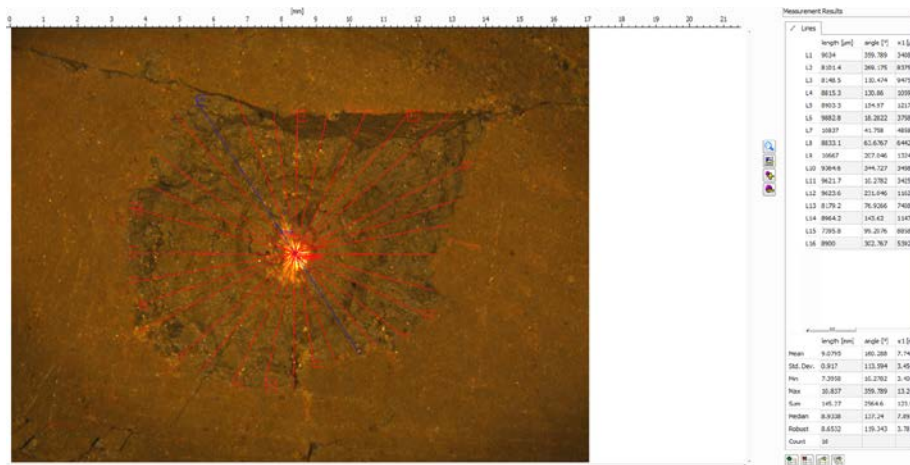

Figure 7.12: A 'screen-grab' from the MeX software; the measurement of crater diameter was very accurate due to the ability of picture zooming.

7.6 b Calculation of the Crater Depth and Profile

The MeX programme uses the premeasured distances, pixel size and tilt angle to formulate three-dimensional positions for each pixel from the stereo-pair images. The tilt allows the program to ascertain the levels of height for each pixel in terms of incident light striking the surface and the amount of shadow.

From this data, the programme constructs a three-dimensional Digital Elevation Map or DEM (see Figure 7.13) which can be used to obtain the crater depth and profile in any given direction.
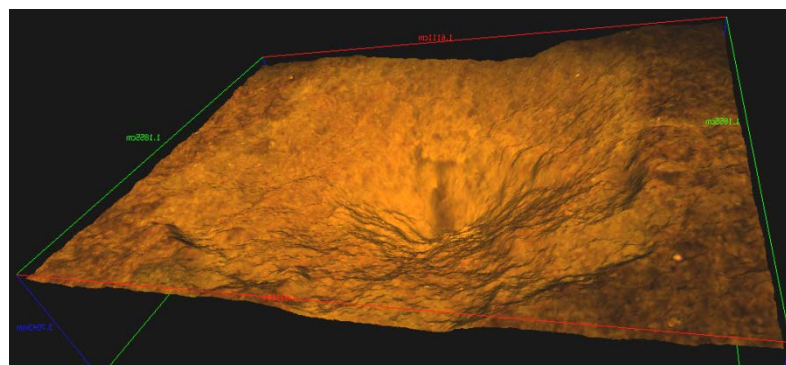

Figure 7.13: Constructing DEMs of the craters allowed easy selection of crater profiles. This DEM shows a sandstone crater.
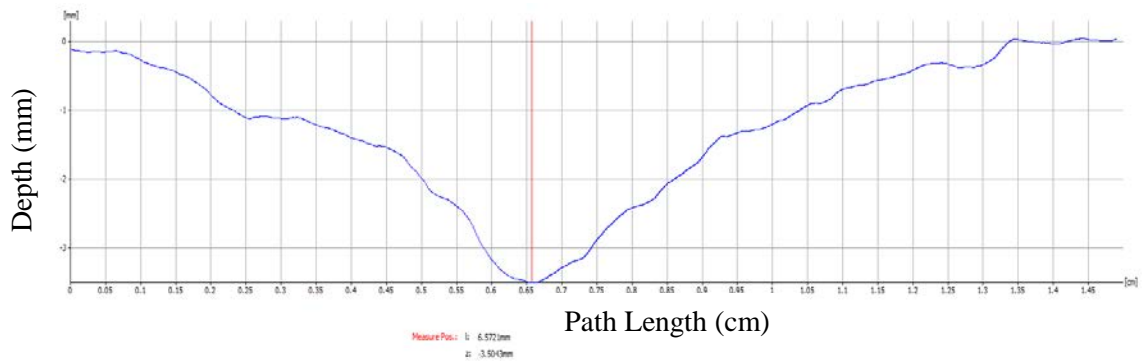
Figure 7.14: The profile of the sandstone crater shown in Figure 7.13, changes in morphology are shown along a chosen profile slice.

From a constructed DEM, the program has a useful application which slices the DEM along a selected direction chosen by the operator. The slice becomes a profile of the crater which can then be analysed or exported depending on what is needed (see Figure 7.14).

7.6c Crater Volumes with MeX

Another advantage of using this program to digitally construct the craters and thereby allowing for measurements to be obtained without touching the crater was to measure the crater volumes.

From the three-dimensional DEMs, the programme uses four types of volume calculation method such as "Soap Film" and "Cutting Plane", with the latter being the calculation method of choice for this work. Each method uses the same base method of algorithmically 'filling' the crater void with geometrically shaped tessellations, normally triangles.

The Cutting Plane method used a volume plane which could be manually manipulated in free space to provide the filling algorithm a position to fill up to. The plane was only ever altered in the z-direction to include the crater void which corresponded to the surface of the target and not the crater rim (Figure 7.15).
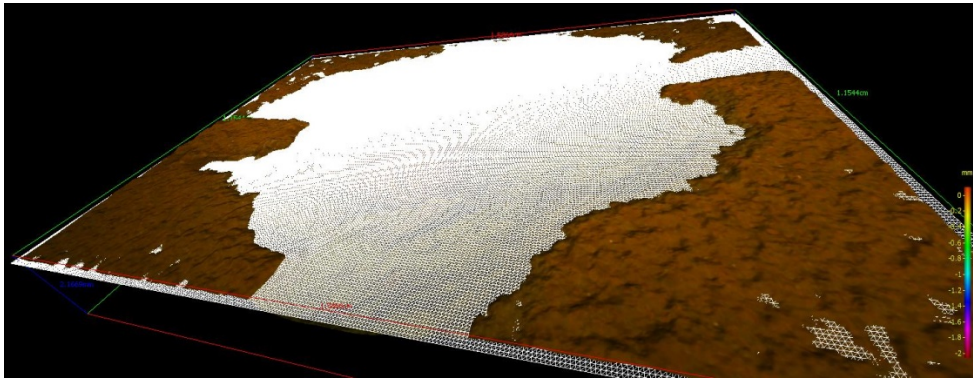
Figure 7.15: The "cutting plane" crater volume method used a planar reference position as a maximum position for in-filling of the crater void. Because the tessellation packing fraction is known along with the triangle volume, the crater volume was calculated.

7.7   Variable Temperature Impact Results
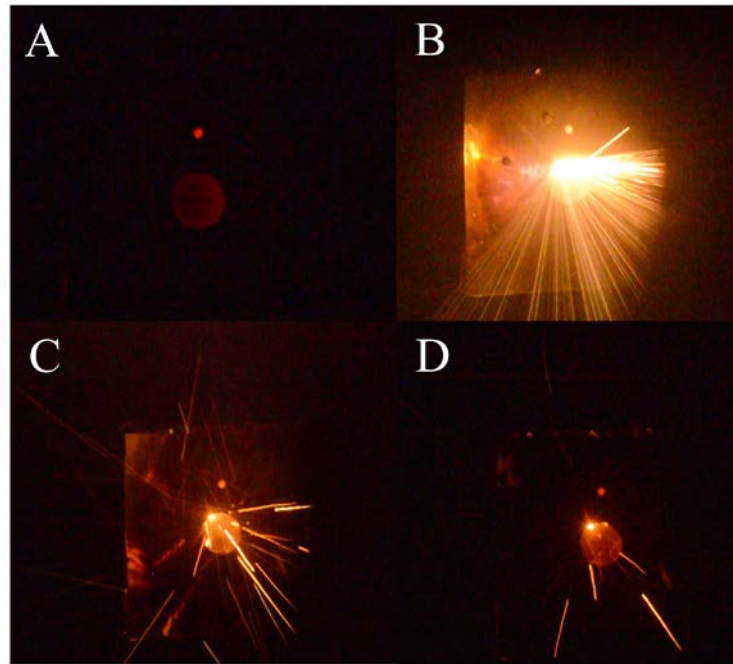
Figure 7.16: A sandstone target heated up to 1003 K being impacted by an stainless steel 420 0.8 mm projectile at 5 kms^{-1}. The image is a collection of video stills. The glowing sample (A) is impacted and releases a large amount of highly energetic ejecta (B and C) with the original impact site glowing brightly afterwards (D).

Common measurement from cratering experimentation are crater depth, diameter and the ratio between the two. This work covers the physical dimensions and also includes (where possible), the MeX DEMs, video footage stills showing the impact process as shown in Figure 7.16 and the new 360° crater profiles from the KDM method as previously described.

7.7 a Video Capture Analysis

Figure 7.16 shows the impact process for a heated sandstone shot (1003K impacted with 0.8 mm stainless steel 420 projectile at 5 kms^{-1}). Picture A reveals the glow from the target at the end of the heating cycle, just prior to impact. B is the first ejection of thermal energy and vaporising target material within the first milliseconds of the impact. This impact was slightly higher than it should have been impacting at the upper edge of the target. This explains the slightly truncated projection of the ejecta.

C and D show the relative settling stages of the impact with the final energetic ejections of target fragments and the afterglow of the impact site.

The impact glow from a hypervelocity impact can help in further scientific information regarding any increase in the level of temperature at the impact site. Using the images complied in Figure 7.16, an approximation of the impact temperature can be obtained, but it must be stated that the colours obtained from Figure 7.16 are not true but approximated due to the nature of the footage concerned.

The colour of the flash and afterglow is approximated to the higher yellow-white region of yellow and therefore assigned a peak wavelength of 570 nm.

Wien's Displacement Law is given by:

$$\lambda_{max} = \frac{b}{T} \hspace{2cm} \text{(Equation I)}$$

Where λ_{max} is the peak or maximum wavelength in m, b is the Wien's displacement constant 2.9×10^3 m K and T is the thermal heat in K.

Using equation I we find:

$$\lambda_{max} = \frac{b}{T}$$

$$T = \frac{b}{\lambda_{max}}$$

$$T = \frac{2.9 \times 10^3}{570 \times 10^{-9}} = 5087.72 \ K$$

To ascertain whether this is correct using specific heat capacity of sandstone and the kinetic energy supplied during impact, will determine if the amount of mass ejected from the impact is comparable to this level of impact.

Specific Heat Capacity is given by:

$$Q = mc\Delta\theta \qquad \text{(Equation II)}$$

Where Q is the energy supplied in J, m is the mass in kg, c is the specific heat capacity in J kg^{-1} K and $\Delta\theta$ is the change in temperature in K.

Kinetic Energy is given by:

$$E_{kin} = \frac{1}{2}mv^2 \qquad \text{(Equation III)}$$

Where E_{kin} is kinetic energy in J, m is mass in kg and v is velocity in ms^{-1}.

In order to calculate the mass of the projectile to use in Equation III density and spherical volume are used:

$$\rho = \frac{m}{v} \qquad \text{(Equation IV)}$$

$$V_{sphere} = \frac{4}{3}\pi r^3 \qquad \text{(Equation V)}$$

Where ρ is density in kg m^{-3}, m is mass in kg and v is volume in m^3 and V_{sphere} is spherical volume in m^3 and r is radius in m.

In order to calculate the mass of the projectile, Equation V is needed to ascertain the volume of the projectile:

$$V_{sphere} = \frac{4}{3}\pi r^3$$

$$V_{sphere} = \frac{4}{3}.\pi.(0.0004)^3 = 3 \times 10^{-10} m$$

The mass of the projectile is found by using Equation IV and the result from Equation V:

420 Stainless Steel density is 7740 kg m^{-3} (AK Steel 2007)

$$\rho = \frac{m}{v}$$

$$\therefore m = \rho \, v = 7740 \times 3 \times 10^{-10} = 2.3 \times 10^{-6} \, kg$$

Using Equation III, the projectile impact energy is:

$$E_{kin} = \frac{1}{2} m v^2$$

$$E_{kin} = \frac{1}{2} . 2.3 \times 10^{-6} . (5000)^2 = 28.75 \, J$$

Finally in order to check the calculation from Equation I, Equation II must be used to find whether the amount of mass associated, with such an increase in temperature from the kinetic energy in Equation III, is comparable to the mass of the projectile. If the amount of mass required to display approximately 4000 K temperature increase greatly exceeds the masses associated with the projectile's kinetic energy, then the approximations of wavelengths would be incorrect.

Therefore, using Equation II to check Equation I:

Specific heat capacity for sandstone = 0.93×10^3 J kg^{-1} K (Robertson 1988).

$$Q = mc\Delta\theta$$

$$\therefore m = \frac{Q}{c\Delta\theta} = \frac{28.75}{0.93x10^3 \times 4084.72} = 7.6 \times 10^{-6} \, kg$$

This concludes that the mass required for this level of temperature increase is comparable to the mass of the projectile with an approximate 30% further mass being ejected.

The three frames compiled in Figure 7.16 concludes 0.00625 seconds of impact (from the recorded frame-rate of 480 fps).

7.7 b Impact Data

Table 7.0: Shot data corresponding to cold limestone impact.

Shot Number	30513.2			
	Celsius	Kelvin		
Temperature	-96.7	176.3		
Rock Type	Limestone			
Impact Speed (km s^{-1})	5.17			
Projectile (mm)	0.8			
Depth (mm)		3.0348		
Cutting Plane Volume (mm^3)		122.11		
Mean Diameter (mm)		15.89	σ	0.84

An example of the data collected is shown in Table 7.0 with the shot number included to aid with identification and displays the date and shot number after the decimal point; this case the date was 030513 i.e. 3rd May 2013 and the shot number was No. 2. The next point of information details the temperature of the shot in both Celsius and Kelvin. Rock type, Impact speed and projectile information follows. The final section of the data sheet gives the information on the physical crater characteristics with depth, cutting plane volume from analysing the DEMs, the mean diameter and standard deviation.

7.7 c Crater Profiles
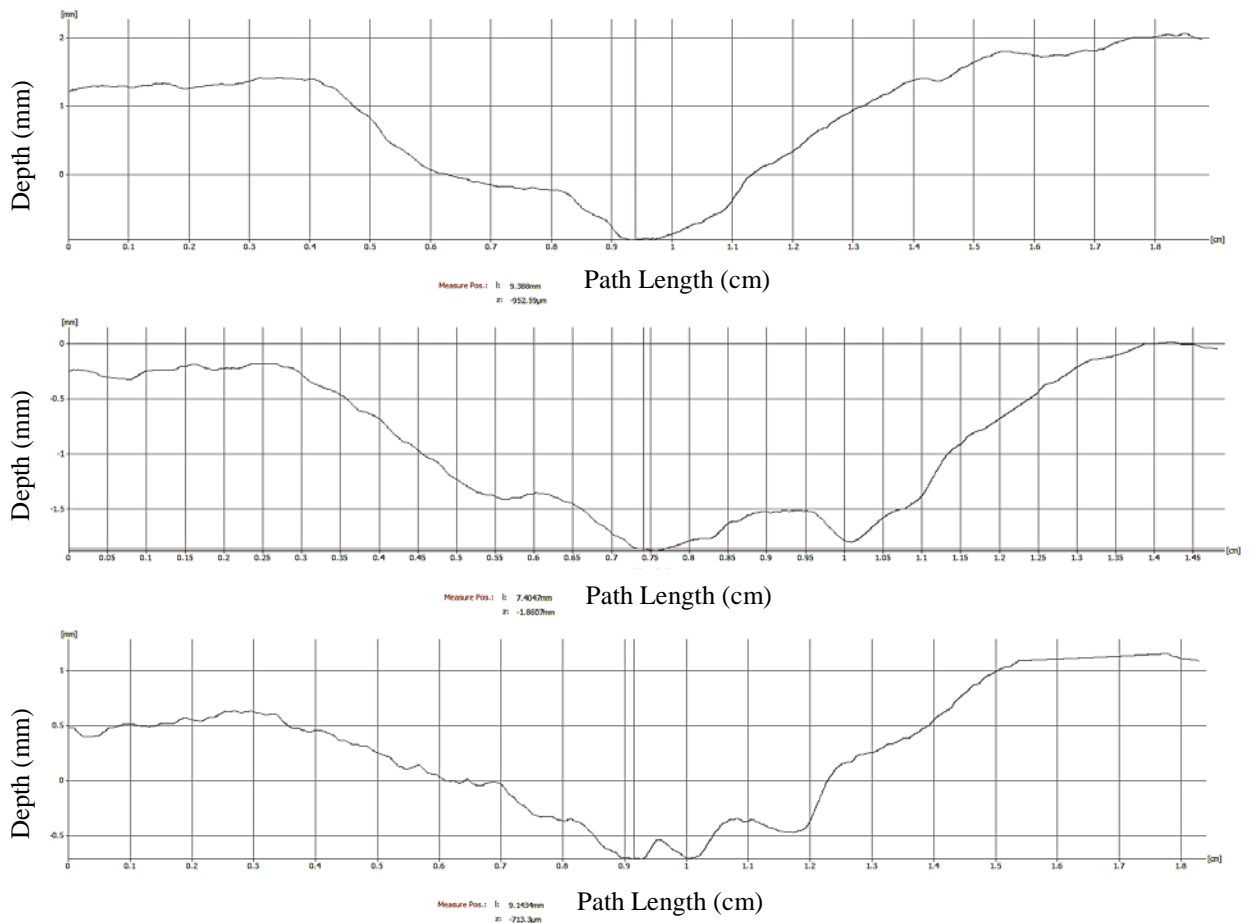
Figure 7.17: Three profiles obtained from MeX showing differences in crater floors for cold (top), room temperature (middle) and hot (bottom) basalt impacts (outlined later in this Section).

As covered earlier, the MeX surface analysis tool is capable of displaying crater profiles along a predetermined orientation chosen by the operator of the programme. In Figure 7.17 three profiles for basalt impacts are shown with the lowest temperature profile at the top, room temperature profile in the middle and the hottest impact profile at the bottom. Viewing crater profiles in this fashion allows for comparisons to be made, such as the crater floor broadening seen in Figure 7.17.

7.7 d The KDM Method

This new technique was covered earlier (Section 7.5) so will not be overly covered in this section, but, as shown in Figure 7.18 the median profiles for the total crater profiles detail averaged whole crater shapes and are plotted together to show the level of change with respect to the internal target temperature.
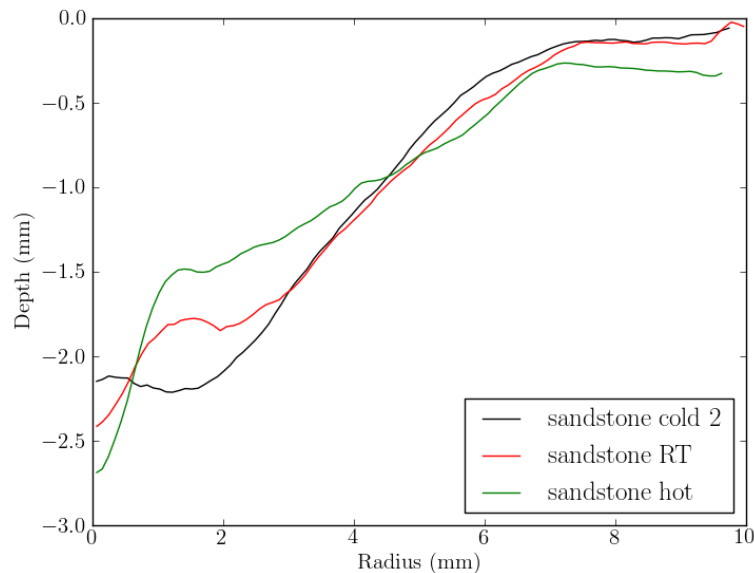

Figure 7.18: Median profiles for three different temperature impacts are shown using the KDM method. This is a version of Figure 7.11, modified for clarity by removing the error curves.

7.7 e Treatment of Errors

To ascertain the errors in the measurements of depth, diameter and volume etc. repeat measurements were taken on the same craters both manually and using MeX analyses.

Manual repeated measurements were conducted with the same piece of apparatus such as the depth microscope, or vernier callipers, on the same crater sample. When dealing with the computational repeats, six separate DEMs were produced of the same crater. Each DEM was used to obtain the MeX values of depth, diameter and volume.

Depth

Table 7.1: Microscope Depth Test for Errors	
Depth Number	Depth (mm)
1	2.555
2	2.490
3	2.384
4	2.475
5	2.631
6	2.598
7	2.379
8	2.522

The level of variance in the manual depth measurements are shown in Table 7.1. It can be seen that the variance in the above dataset shows that the method using the depth probe microscope to find the level of uncertainty as represented by the standard mean deviation $\sigma = 0.071$ mm for this case, the mean average is 2.504 mm.

Volume

As data for volumes came from the MeX surface analysis programme and manually from crater in-filling, it was decided that multiple measurements were needed for both methods and the mean of both standard deviations would represent the error for the volumes.

Table 7.2: Microscope Depth Test for Errors		
	Test Type	Volume (mm^3)
Sandstone	MeX	82.849
	MeX	100.58
	MeX	98.255
	MeX	107.12
	MeX	110.46
	MeX	101.85
Basalt	Manual	249.75
	Manual	249.75
	Manual	235.88

Two different impact samples were used for the volume error tests, sandstone and basalt (Table 7.2). The sandstone sample was specifically chosen for the MeX DEM generations due to its small crater diameter. The basalt sample chosen for the crater

in-filling manual method, because of the smooth surface of the basalt allowed the 75-90 μm glass beads to be easily collected from the sample. The same samples were used. The standard deviation for the MeX method was 9.60 mm^3 and for the manual in-filling was 8.00 mm^3. The average from the two standard deviations came to 8.80 mm^3.

Diameter

The diameter was treated in the same way as for the volume with a mixture of both computational and manual methods.

Table 7.3: Microscope Diameter Test for Errors

| Test Type	Diameter (mm)
MeX	12.64
MeX	13.16
MeX	12.29
Manual	12.49
Manual	13.25
Manual	12.42

The values included in Table 7.3 are the mean values from at least six diameter measurements per value for both methods. The standard mean deviation for these values was calculated to be 0.33 mm.

## 7.8 Basalt Results

A
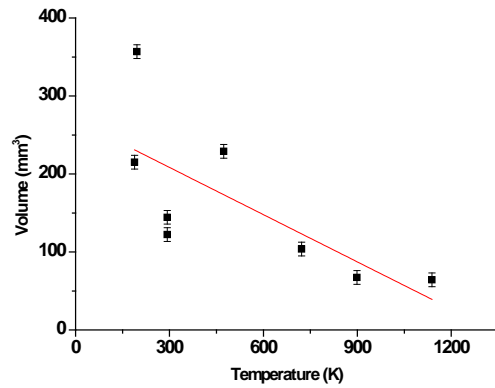
B
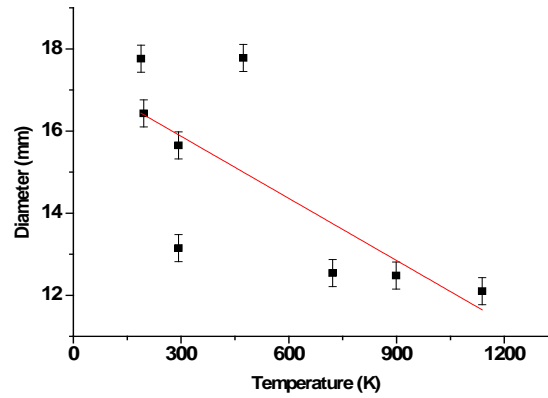
C
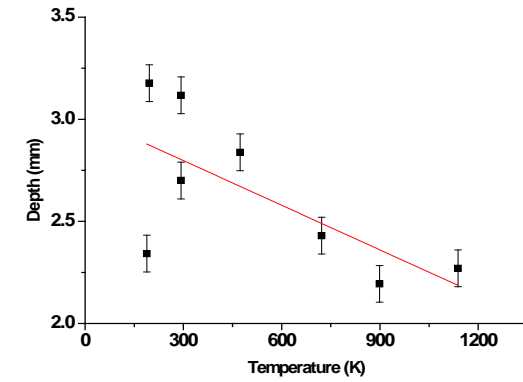
D
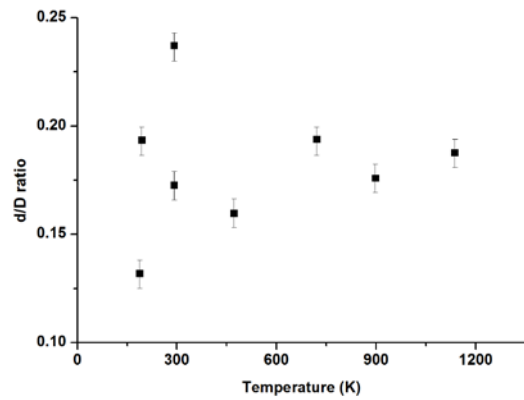
E
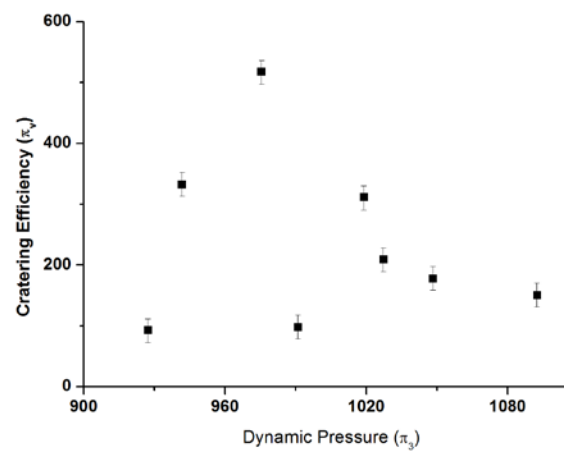
Figures 7.19 A, B, C, D and E: Series of graphs showing volume, diameter, depth, d/D ratio and cratering efficiency with respect to temperature Basalt impacts.

7.8.1   Basalt Discussion

The general trend for the basalt data shows that as the temperature increases, the smaller the basalt craters become. However, it must be stated at this point, that the regression coefficients (r) from the data fitting are very low with values 0.67, 0.68 and 0.61 for volume, diameter and depth respectively.

The volume data shows a large spread at the lowest temperatures with a value of approximately 150 mm^3. The same two data points show the largest spread in the crater depth plot. Because the sample of basalt used for this project was the same throughout the whole shot programme, the explanation for this was due to the coldness of the basalt making the basalt increasingly brittle at these temperatures.

This brittle nature continues up to the room temperature regime with the spallation photos showing large chips of the craters having been removed in addition to the excavated craters.

The data did show that as temperatures increased, the crater characteristics reduced in size thereby showing that the craters became smaller at hotter temperatures. Experiments performed by Scarfe, showed that as basaltic temperatures increase so does the viscosity of the basalt (Scarfe 1997). The experiment used basaltic (olivine and andesite) glass fibres under load at different temperatures (close to the temperatures involved in this experiment). At the lower temperatures, the basalt did not stretch as much as the hotter temperatures, which helps to explain the reasons behind the basalt craters being smaller at the hotter temperatures than the colder.

During the excavation stage of crater formation, the heated basalt acted much more in the plastic phase (due to the temperatures generated during the compression stage) which in turn meant that plastic deformation (applied pressure causing shear or bending without failure) kept the craters smaller. The associated solidus and liquidus temperatures of basalt are given as 1273 K and 1473 K respectively. Although the basalt temperatures were not as high as the associated liquidus temperature for basalt, during the projectile-target interaction during the compression stage, these temperatures would be obtained. With the impacts reaching the liquidus temperatures of the basalt targets, the excavation and modification stages of crater formation meant that the craters were smaller.

7.9 Limestone Results
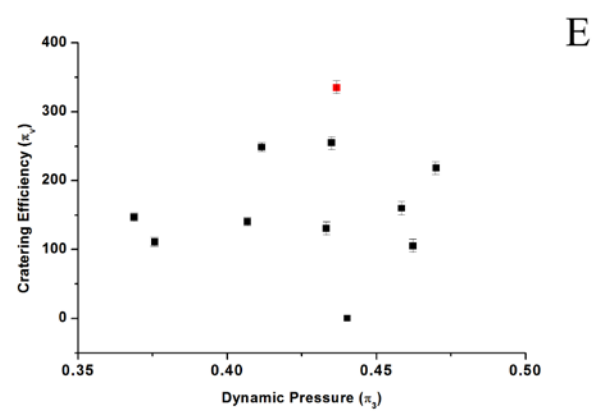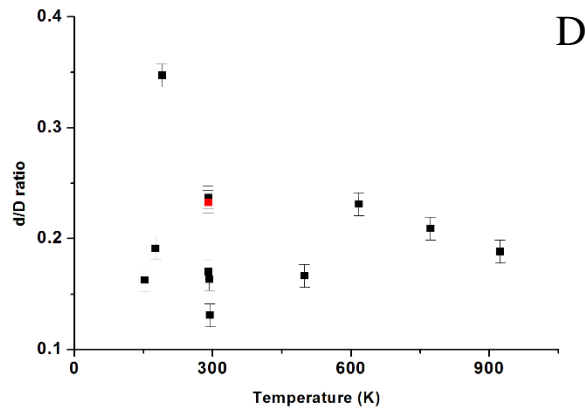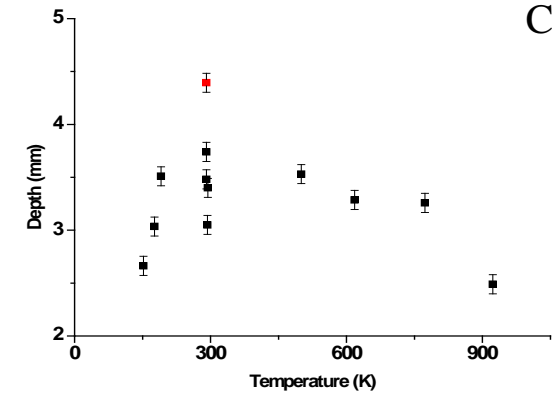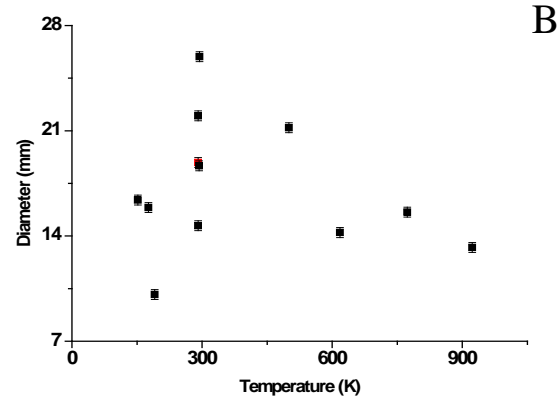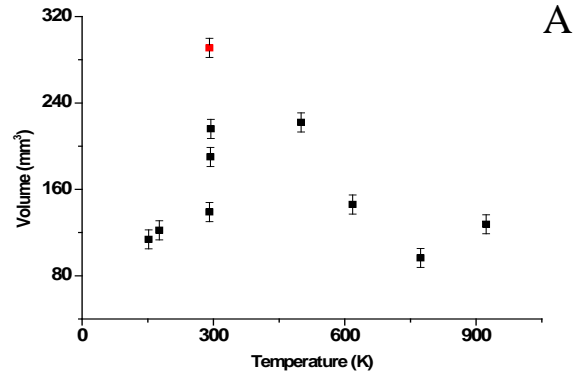
Figures 7.20 A, B, C, D and E: Series of graphs showing volume, diameter, depth, d/D ratio and cratering efficiency with respect to temperature respectively for Limestone impacts. The red datum was associated with an impact affected by the presence of another crater.

7.9.1 Limestone Discussion

From each plot given in this Section, it can be seen that the data ranges at the lower temperatures (room temperature and below) show a large scatter in the data. For example, the room temperature shots have a spread which shows that no trend can be assigned to the data sets; this is reflected through the r^2 coefficients.

The red datum present in all Figures 7.20, was associated with an impact too close to another crater made in the same target. Previously the size of this particular target was large enough to accommodate multiple impacts, but the shot was off-axis and impacted too close to the previous shot. This meant that the datum would have had some influence from the damage underneath from the previous shot and could not be included. It has however been left in for completeness.

Upon inspection of the plots, it was decided to isolate the Ancaster Hard White limestone data from the 'stock' limestone used in the previous phase of the variable temperature impact project and will be covered shortly.

7.10 Sandstone Results
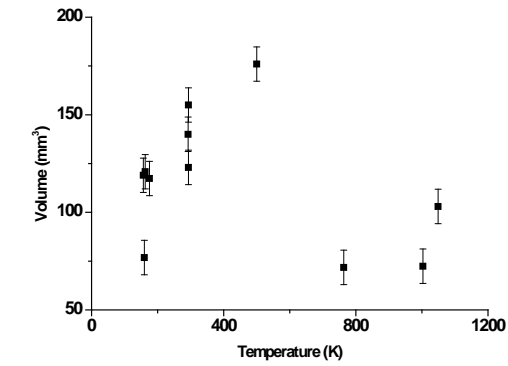
A
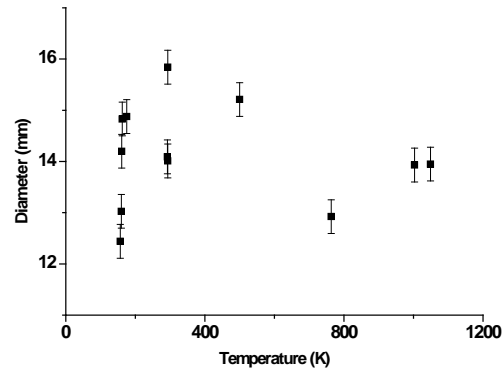
B
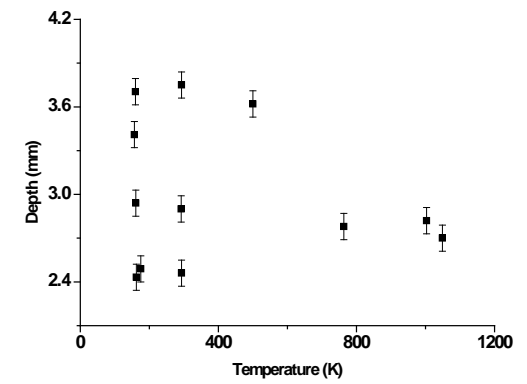
C
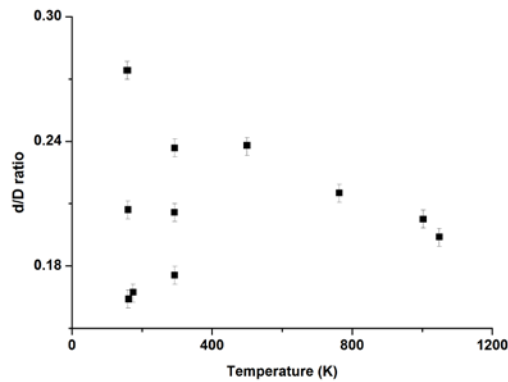
D
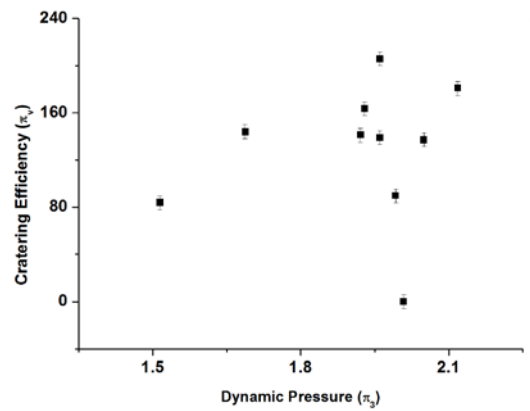
E

Figures 7.21 A, B, C, D and E: Series of graphs showing volume, diameter, depth, d/D ratio and cratering efficiency with respect to temperature for sandstone impacts.

7.10.1 Sandstone Discussion

Once again the inclusion of the unknown 'stock' sandstone samples has produced a large amount of data spread which is most notable in the depth plot. The Beestone Red sandstone plots were isolated, as with the Ancaster case, and re-plotted following the Ancaster Hard White limestone discussion.

7.11 Ancaster Hard White Data
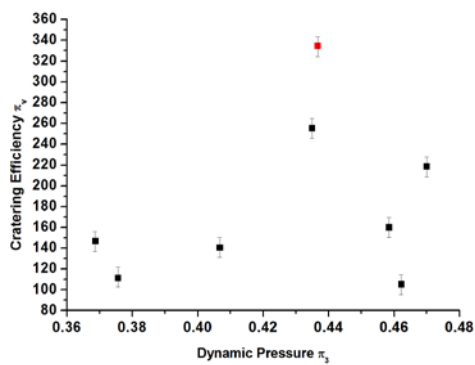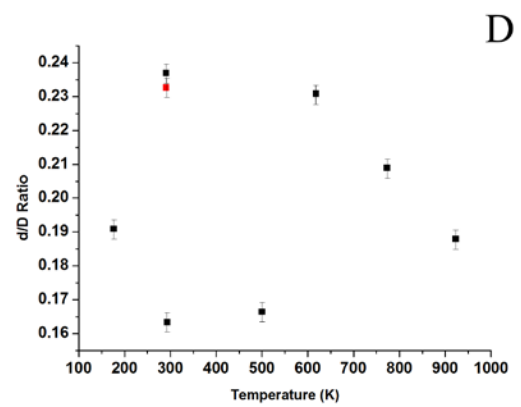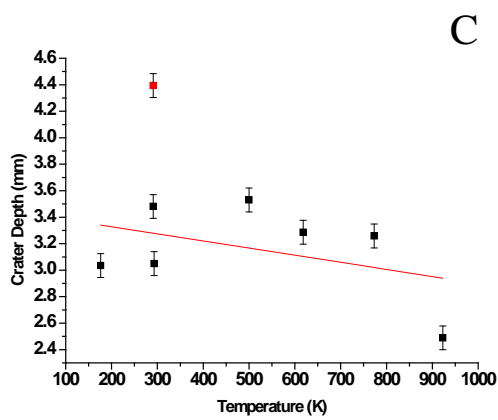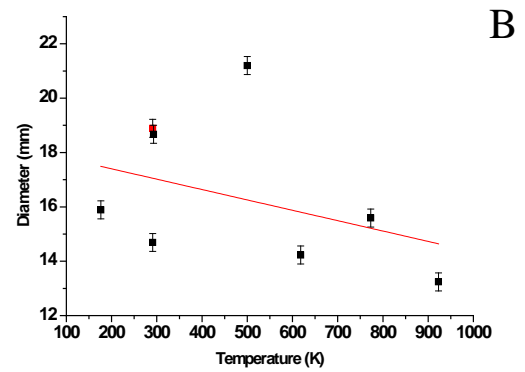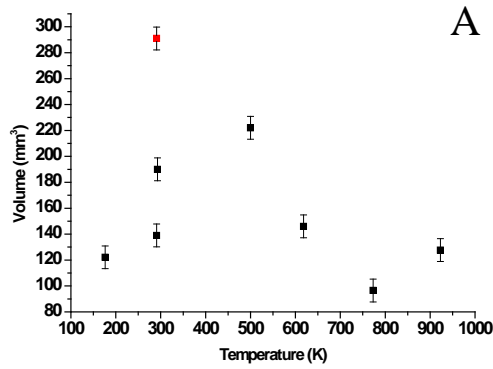
Figures 7.22 A, B, C, D and E: Series of graphs showing volume, diameter, depth, d/D ratio and cratering efficiency with respect to temperature for Ancaster Hard White limestone impacts.

7.11.1 Ancaster Hard White

The Ancaster Hard White limestone data shows little trend with respect to the previous all-inclusive limestone data set. One datum point (red in colour) was flagged. This crater shows unusual level of spallation in the crater volume and a large depth. The impact may have occurred at the sight of a natural flaw which caused larger amounts of spallation.

The volume graph shows the largest volume created was at approximately 500 K with the smallest crater volume being made at 750 K. The plots show no real correlation between the cratering of Ancaster Hard White limestone and temperature.

Table 7.4 shows the statistics associated with the physical characterisitcs obtained from the Ancaster Hard White crater measurements.

Table 7.4 :Ancaster Hard White Limestone Statistics

	Mean	Standard Deviation	Min	Median	Max
Vol (mm^3)	149.05	42.92	96.52	139	222
Diameter (mm)	16.22	2.78	13.24	15.59	21.2
Depth (mm)	3.16	0.35	2.49	3.26	3.53
d/D Ratio	0.20	0.03	0.16	0.19	0.24
π_v	162.35	55.41	105	146.78	255.19
π_3	0.43	0.04	0.37	0.43	0.47

7.12 Beestone Red Sandstone Data
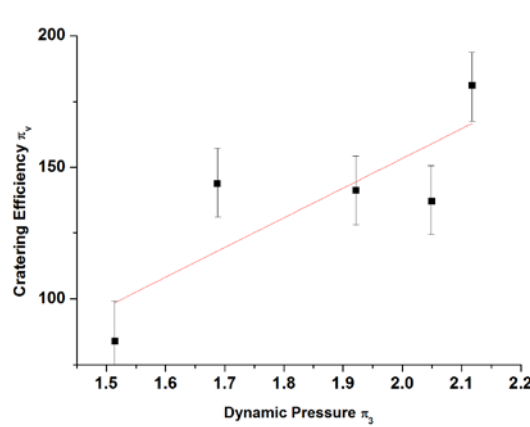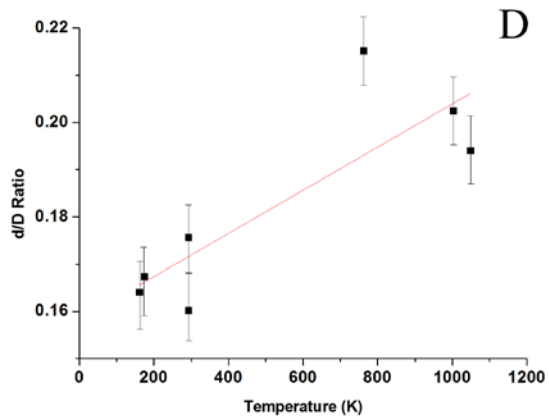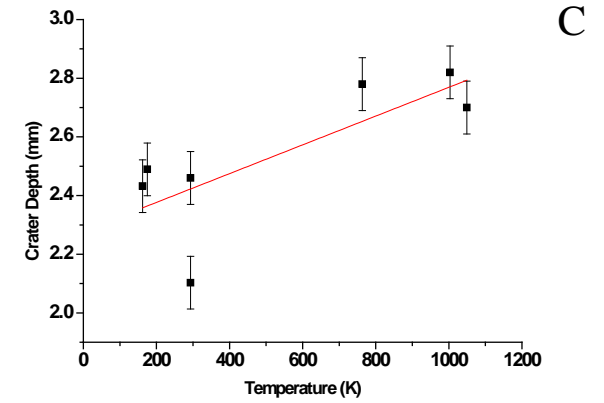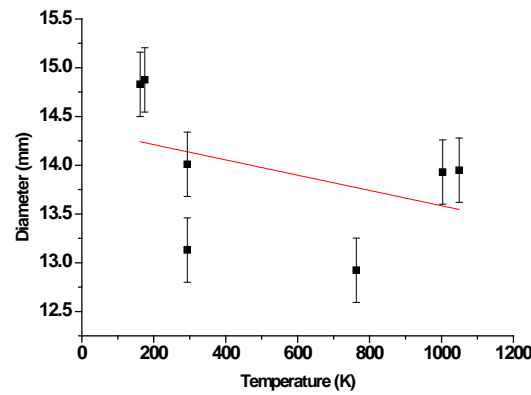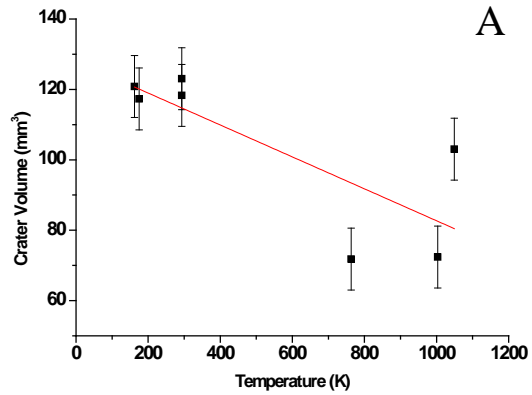
Figures 7.23 A, B, C, D and E: Series of graphs showing volume, diameter, depth, d/D ratio and cratering efficiency with respect to temperature respectively for Beestone Red sandstone impacts.

7.12.1 Beestone Red Sandstone Discussion

The exclusion of the unknown sandstone data has allowed the Beestone Red sandstone data to be fitted to look for trends. However, once again, the Beestone data showed a low regression coefficient, therefore requiring more data to be obtained at a later time.

The volume plot (Figure 7.12 A) shows two distinct groupings of data at the lower and higher regions of temperature; the mid regions of temperature were from the original stock sandstone. The data show that the hotter the sandstone, the smaller the volume of crater produced. The hot data points show considerably more spread than the colder ones.

The diameter plot shows the worst fit in the Beestone Red data set. The amount of data spread at the room temperature points, and the singular datum point situated at 763 K, affected the residue calculations for the fit, thereby severely reducing the regression coefficient. The 763 K datum point was produced with the fastest impactor speed at 5.7 kms^{-1} and was shown to be the second deepest crater of the Beestone Red data set. Crater photos show no adverse spallation from this particular crater. Due to the spread in the data, there is very little, or no effect, of temperature on crater diameter.

Crater depth in the Beestone Red data shows the craters get deeper as temperature increases. This effect, when combined with the volume data displays that the craters are becoming more conical in shape at higher temperatures. Therefore, as temperature increases, it is easier for an impactor to excavate the Beestone Red sandstone due to the possibility of being closer to the plastic phases of the rock.

The Beestone Red d/D ratios are the only data which indicate the possibility of a clear trend. The colder the Beestone Red sandstone, the lower the d/D ratio with ratios approximately close to 0.17, whereas the hotter ratios tend towards the 0.20 value found (Melosh 1989). Also the cratering efficiency graph shows a slight trend to the fit but this is due to the limited number of data points on the graph.

	Mean	Standard Deviation	Min	Median	Max
Vol (mm^3)	103.82	22.60	71.79	117.32	123.04
Diameter (mm)	13.95	0.75	12.92	13.95	14.88
Depth (mm)	2.54	0.25	2.10	2.49	2.82
d/D Ratio	0.18	0.02	0.16	0.18	0.22
π_v	137.41	34.75	83.89	141.18	181.12
π_3	1.83	0.24	1.51	1.80	2.12

7.13   Spall Zones

Figures 7.24 to 7.33 are photographs taken of each impact crater associated with the variable temperature impacts project. It is important in aiding the understanding of the processes involved with this work, to know how each crater has formed during the excavation and modification stages of formation.

Cold Limestone
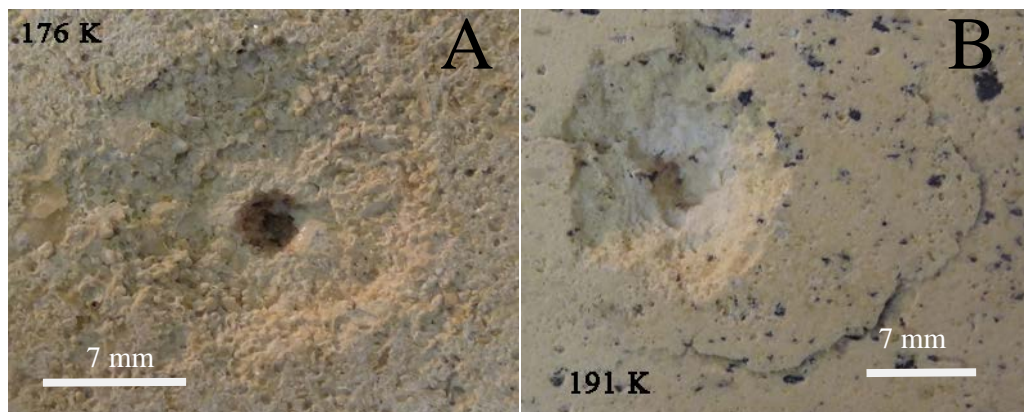
Figure 7.24 A and B: The coldest temperature impacts for limestone. Photo A shows a cold target impact from the Ancaster Hard White limestone whereas photo B shows the older unknown stock limestone.

The two photos in Figure 7.24 show craters into cold limestone. The left picture is the Ancaster Hard White sample and shows an almost circular crater rim but with an extended amount of spall in the top left region of the crater. The right hand photo shows the stock limestone sample displaying an irregular crater with a very large impact petal to the right of the crater. As will be seen in other pictures, this type of limestone was prone to forming petals during the excavation stage.

7.13.1 Limestone Room Temperature

The craters concerned with the room temperature impacts were made at approximately 19 °C (292 K). Figure 7.25 show three impact craters made in the main limestone Ancaster Hard White (A, B and C) and three craters impacted into the older stock limestone found in the impact lab (D, E and F).

(Craters D and E were omitted from the data analysis due to the impacts being very close to each other. They have been included in this section for completeness.)
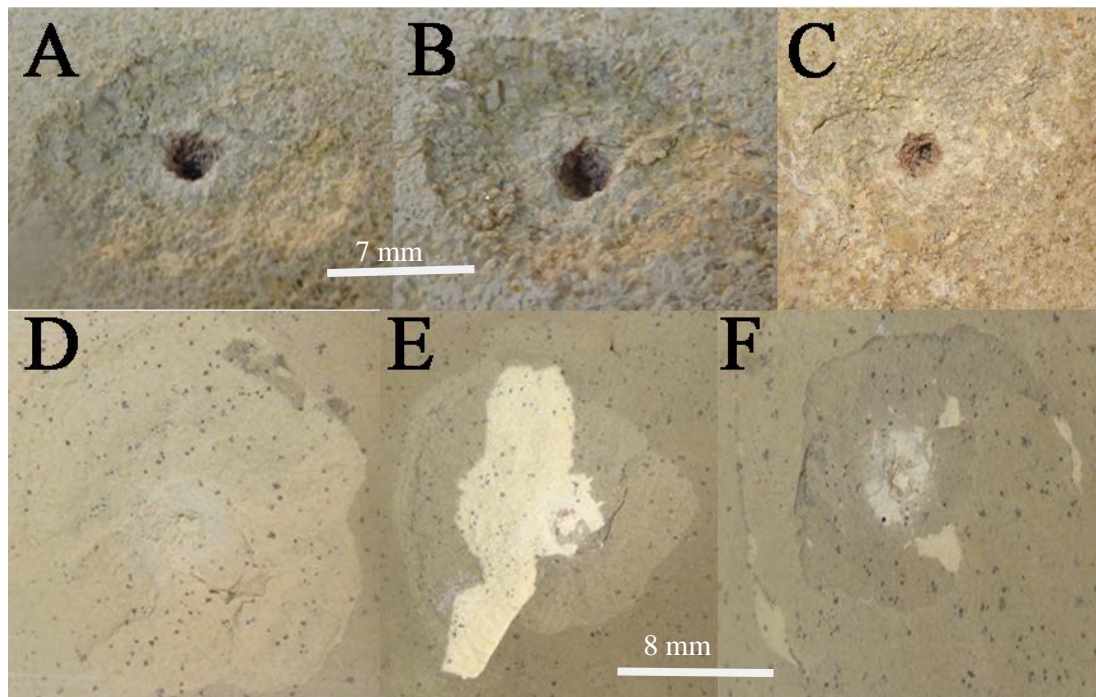

Figure 7.25 A, B, C, D, E and F: Photos A, B and C are room temperature impacts into the known Ancaster Hard White Limestone and D, E and F represent spallation zones associated with old stock limestone.

As can be seen with all of the photos, the impact craters into the old stock limestone are more circular than the craters produced in the Ancaster samples. However the floor from the older limestone samples could be considered different due to the central pit surrounding the initial excavation cone being raised with respect to the level of the crater floors. Also noted in D and E are scarp cracks appearing very close to the initial excavation zones.

Each Ancaster sample shows the initial excavation cone with a red hue in the cone itself, this is due to oxidisation of iron present in the limestone or, possibly, iron from the stainless steel ball bearing interacting with the limestone.

Spallation features from the Ancaster samples show terracing around the crater edges whilst the old stock limestone appears smooth. The older stock sample is very smooth and could possibly be reconstituted limestone which would account for the smoothness, whereas, the Ancaster sample is a pure limestone with easily recognised grains.

One other spallation property seen in D, E and F are large areas of the surrounding environment having been damaged enough to lift petals away from the Limestone surface, this once again would be due to the properties associated with the reconstituted limestone.

7.13.2 Hot Limestone
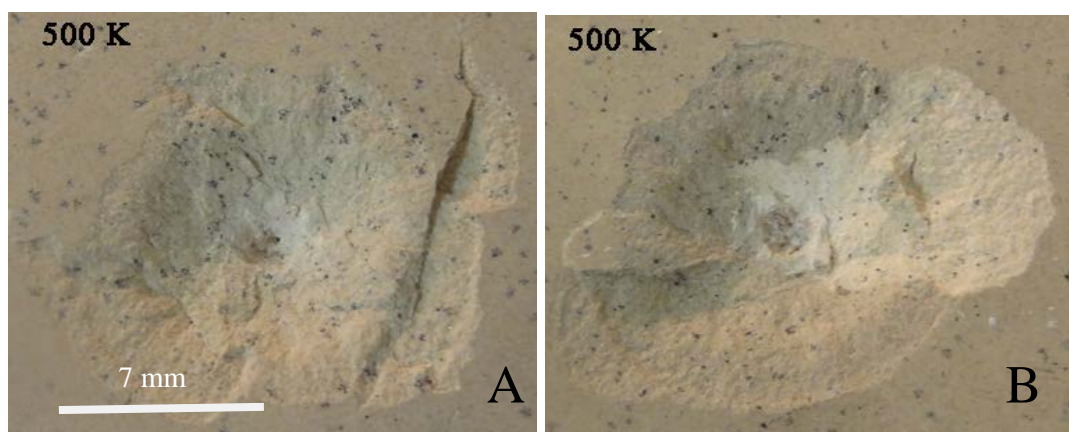
Figure 7.26 A and B: Both Figures A and B are from the older stock limestone. A shows a large extra spallation area to the right of the original crater. Photo B shows received further damage from handling where a spallation 'petal' disconnected from the crater.

Figure 7.26 in this section are old stock limestone samples, cratered at 500K during the initial stages of the variable impact project. As stated in the previous example, the right hand crater shows post impact damage from a large petal (the lighter segment of the crater) having fallen off. Once again with this form of limestone, the central impact cone has elevated lip surrounding the cone. The right hand crater also shows the crater rim intersecting the petal which would have made the crater resulted in a slightly extended circular crater rim.

The left hand photo shows once again extended spallation at the top and bottom left corner of the crater rim but with a large excavated region to the right of the crater. The straight edge indicates that the crater was made in a region with an inherent flaw which broke away with the motion of the shockwave.

7.13.3 Very Hot Limestone
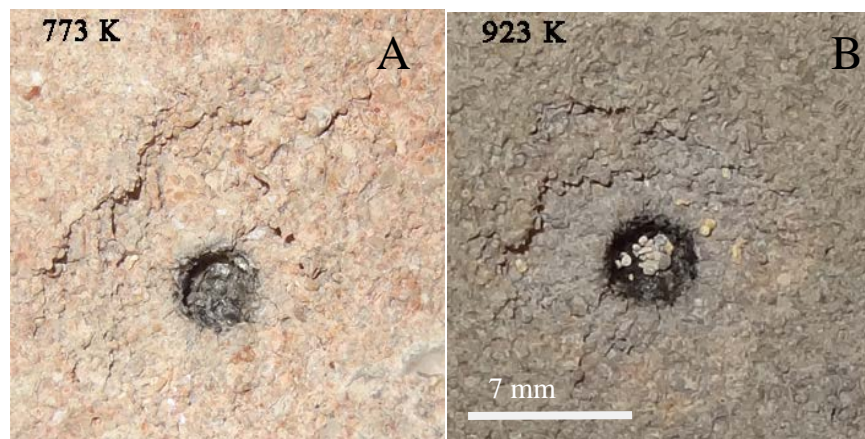
Figure 7.27 A and B: The two photos show the hottest Ancaster Limestone impacts where A and B are 773 and 923 K respectively.

The limestone samples used for the high temperature impacts only used the Ancaster Hard White samples. The immediate result which can be seen from the pictures above are the discolouration of the limestone samples from the heating processes. The slightly cooler limestone sample on the left displays a pink hue whereas the hotter sample on the right shows a darkened surface. Both craters from Figure 7.27 show incomplete spallation of the crater with varying levels of terracing in the crater walls. Both samples also show similar bowl-like initial excavation zones instead of the more common cone-like form.

7.13.4 Very Cold Sandstone
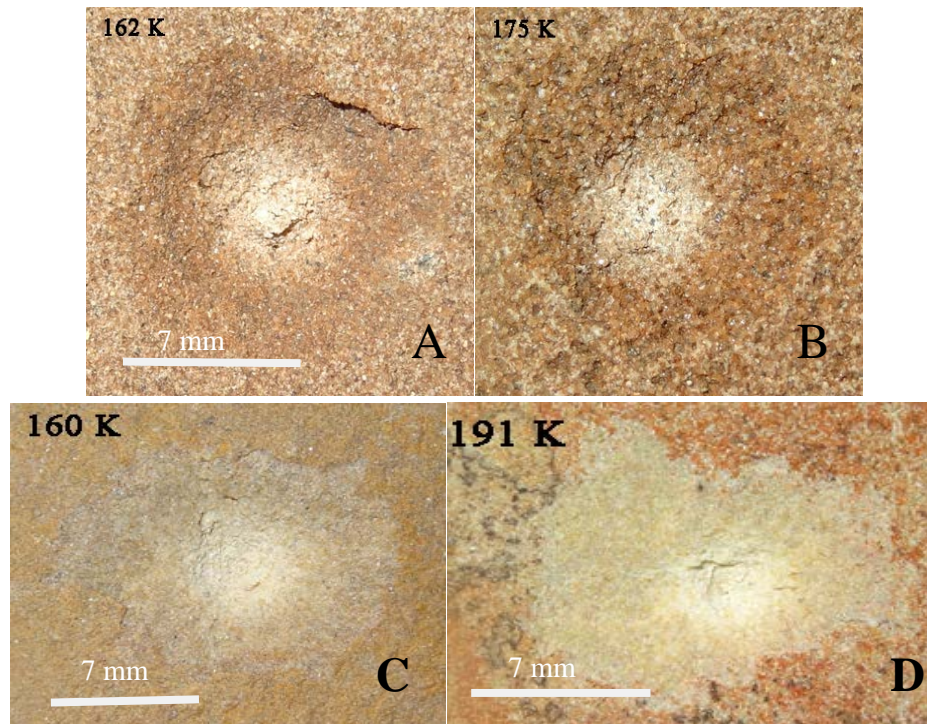
Figure 7.28 A, B, C and D: Photos A and B show Beestone Red sandstone and photos C and D are craters from the stock sandstone. All craters were impacted in the cold region.

The crater records for the cold sandstone impacts show the four temperatures of 162, 175, 160 and 191 K respectively. The top two craters shown in Figure 7.28 A and B are from the newly sourced Beestone Red samples, whereas, the lower two craters (C and D) were produced from impacting the old sandstone stock from the laboratory.

Both pairs of craters show similar morphologies to each other, but very different morphologies between the pairs. The Beestone craters show circular crater circumferences whereas the unknown sandstone craters were elongated via extra spallation. Another similar feature in each crater is a complex formation crater floor; each crater shows a peak in the crater floor being formed during modification. The 162 K crater (top left) shows a crater wall lip leading to a scarp line traversing the opposite wall.

7.13.5 Room Temperature Sandstone
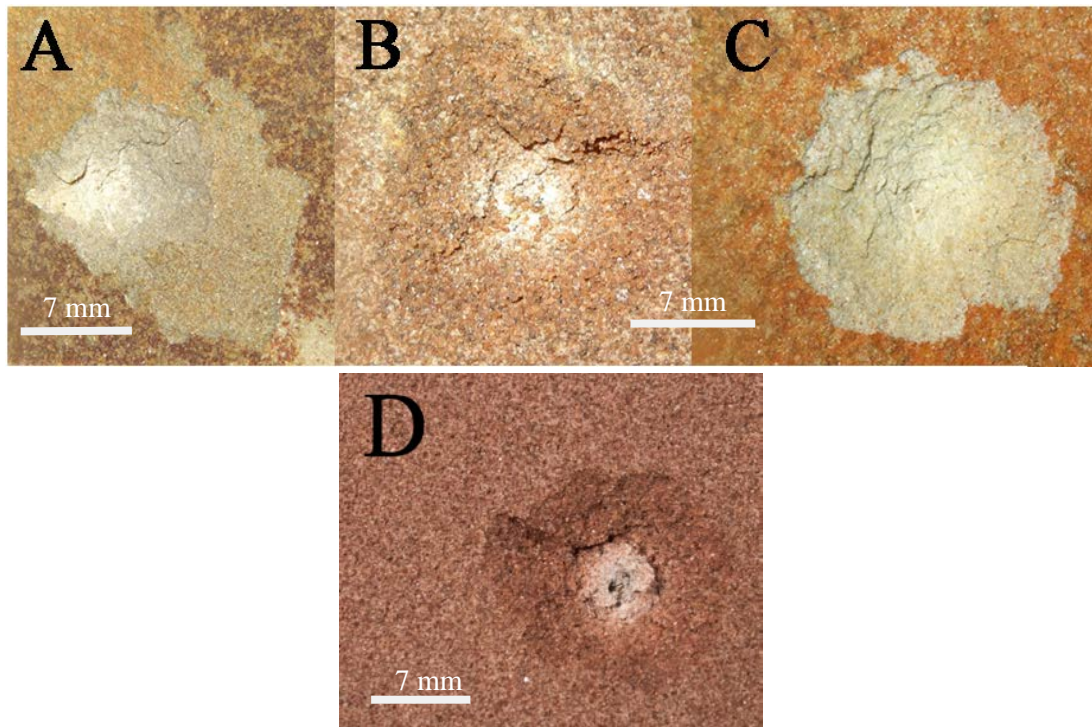
Figure 7.29 A, B, C and D: Photos A, B and C show room temperature stock sandstone and photo D shows a crater from the Beestone Red sandstone.

The room temperature sandstone impact craters were made with the ambient target chamber temperature of approximately 292 K. The sandstone room temperature targets show differing levels of spallation with respect to the two types of sandstone used. Pictures A and C are the 'stock' sandstone samples which were found in the laboratory during the first phase of the variable temperature impact project. Picture A shows a large amount of extra spallation emanating from the crater which has been altered from a surface feature of the rock. Pictures B and D are the Beestone Red sandstone which both craters show peaked floors and slight extra spallation from the impact with vertical crater wall scarps.

7.13.6 Hot Sandstone
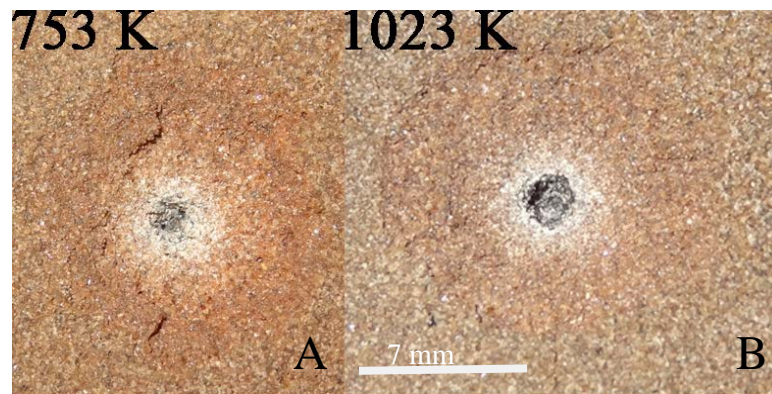
Figure 7.30 A and B show hot impacts into Beestone Red sandstone at the hottest regions during the impact tests.

The two photos for the hot sandstone impact craters (Figure 7.30) show both craters having a crater shape close to circular. The hotter of the two craters shows a simple crater with very little change in morphological form throughout the whole crater.

The colder impact of the two, shows impact morphology similar to the sandstone impacts; 162 K and room temperature. In the crater wall the damage from the excavation into modification stages has left the crater wall lipped with a visible scarp in the crater. Whereas the previous two examples have only shown one lip and then the scarp line, the 753 K crater shows the scarp line attached to two lips.

7.13.7 Very Cold Basalt
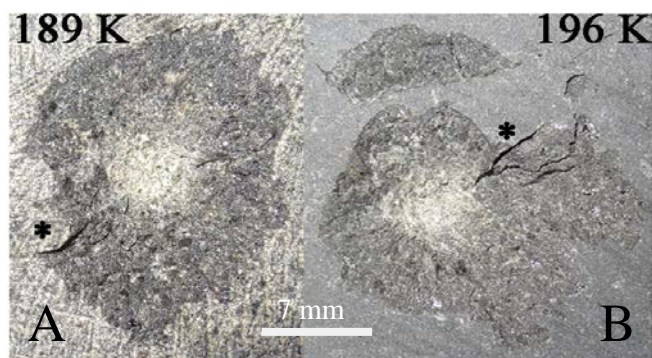
Figure 7.31 A and B: These photos detail very cold impacts into basalt. The asterisks denote sheer faces interrupting the crater walls from incomplete spallation.

The result of reducing the ambient rock temperature to very low values such as 175 K increases the brittle nature of the rock as the craters show extensive spallation surrounding what would be expected for a circular crater (Figure 7.32 A and B). Both craters display incomplete or interrupted spallation, where the crater wall has had the resilience to withstand the shockwave interaction and thereby producing sheer faces in the crater wall (indicated by *).

The 196 K crater displays the same type of extended fracturing resulting from target material properties as in the 500 K limestone case. At the top of the picture, the shockwave was strong enough during the surface boundary interaction to remove further spall not attached to the crater itself. The straight edge in this section would suggest material dislocation, or possible a boundary which directed the damage.

Also associated with the 196 K crater is the extended spallation below the region marked with the "*", which resulted in spreading the crater size properties much further than expected. The extension of the damage is shown with a further spall damaged chip resting on a crack emanating from the spall. The shot characteristics, such as dynamic pressure and cratering efficiency for both of these craters show the weaker impact being assigned to the 196 K crater, but the damage resulted in the large volume due to the extensive spallation.

7.13.8 Room Temperature Basalt
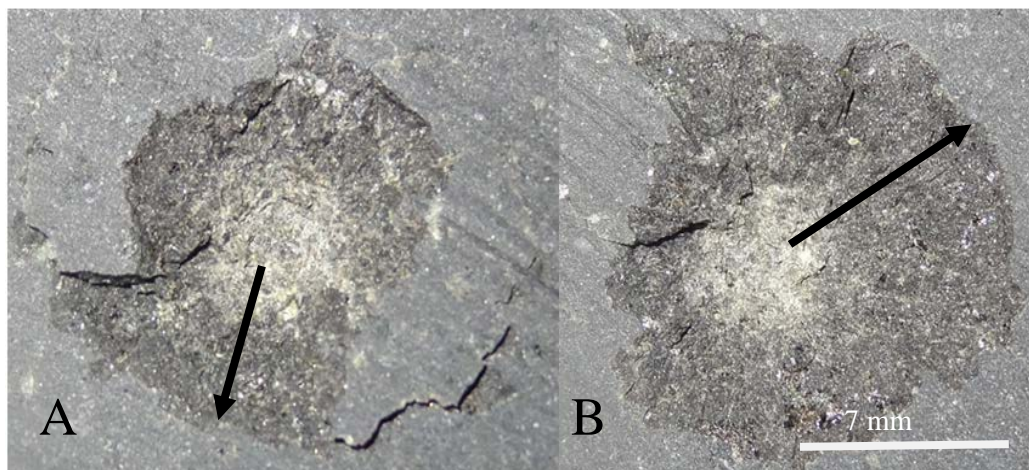
Figure 7.32 A and B Room temperature basalt impacts with interrupted spallation as mark by the arrows in both cases.

The room temperature craters displayed the interrupted spallation as is seen in each basalt crater, but again, extended levels of spallation (indicated by the arrows)

increasing the crater dimensions as with the 196 K crater case. The left hand side crater shows the development of a spall petal which would designate similar surface shockwave properties to the reconstituted limestone discussed earlier.

7.13.9 Hot Basalt
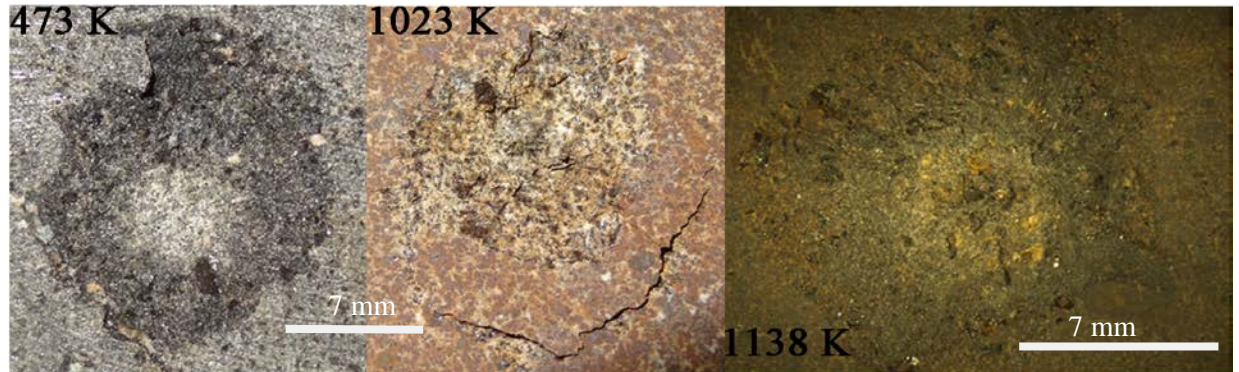
Figure 7.33 Three impacts are shown in this Figure with form part of the hot basalt impacts. Note the colour change as the temperature increased from 473 to 1138 K.

The heated basalt craters (Figure 7.33) ranged from 473 to 1138 K, which is the largest range obtained in this project. The crater walls show interrupted spallation being most pronounced at the coldest impacts and least at the hottest temperature crater. The middle temperature crater showed a strange form of crater, with no discernible central crater zone as opposed to the lighter crater floors present in all basalt craters. Once again the presence of a spall petal is shown with the 1023 K crater. As with the heated limestone cases, it is easy to see discolouration from the heating of the stone samples as they get hotter.

7.14   MeX Crater Profiles (Single Form)

This section is concerned with the diameter profiles obtained from the Ancaster Limestone, Beestone Sandstone and Basalt rock samples. Analysis of craters often use profiles which are taken in one or two planes of reference (Buhl et al. 2014) in order to ascertain morphological processes during cratering and to assign any trends to impact properties. Although this project details many forms of profile such as 360º full or orthogonally averaged, the following are single plane profiles in order to

preserve the greatest amount of morphological information possible from the MeX surface analysis program.

The profiles are obtained via selecting a single plane reference from the top left corner of the MeX picture window to the bottom right corner, this allowed for the choice of the plane of reference to be the same every time per profile taken and included the largest amount of data.

-77°C Basalt
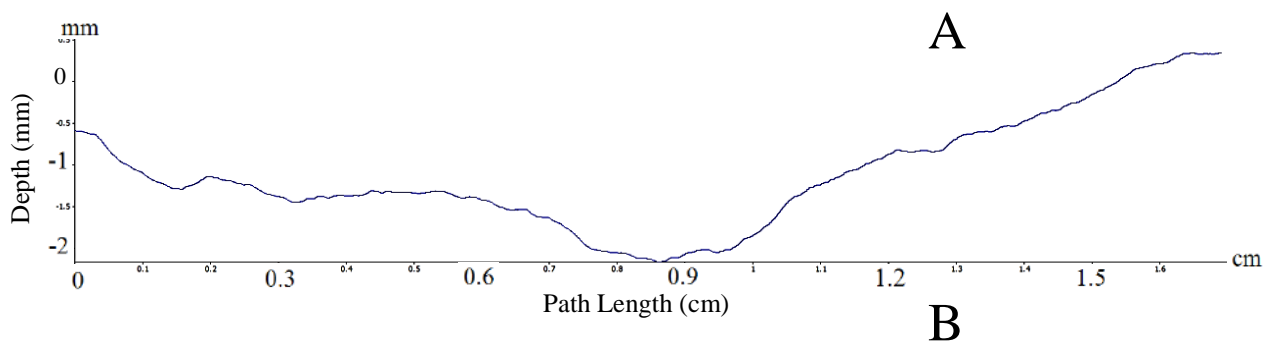
RT Basalt 1
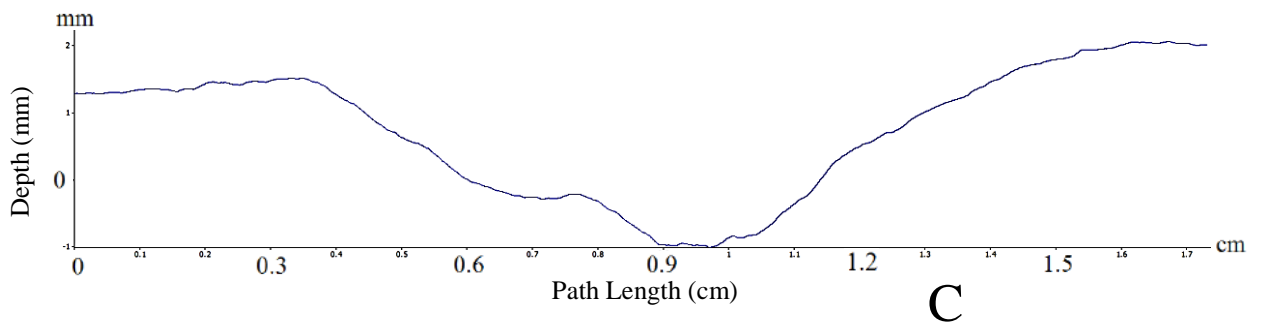
RT Basalt 2
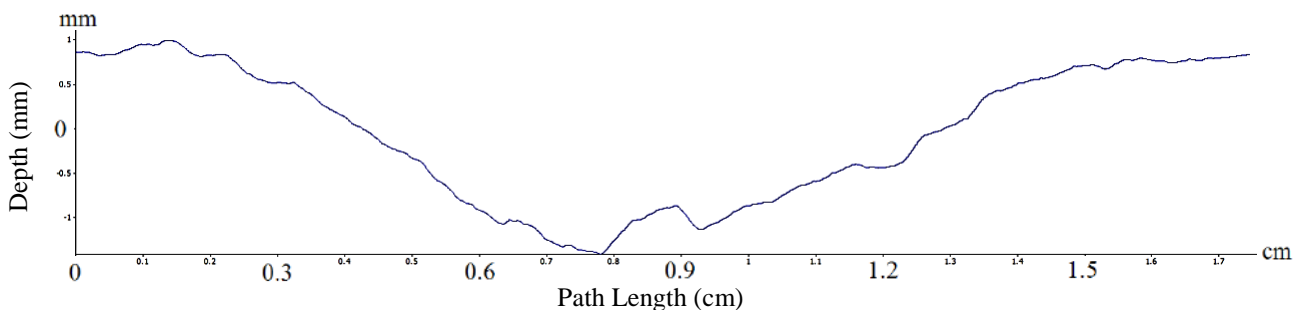
Figures 7.34 A to C: The craters shown in these MeX generated profiles showing a direct non-averaged profiles for Basalt through the temperature range. The profiles were always taken along the same axis.

500°C Basalt
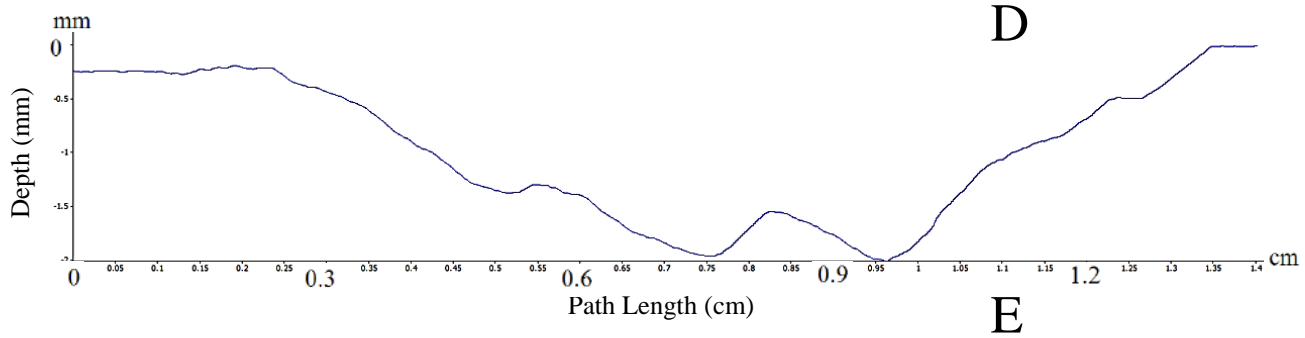
750°C Basalt
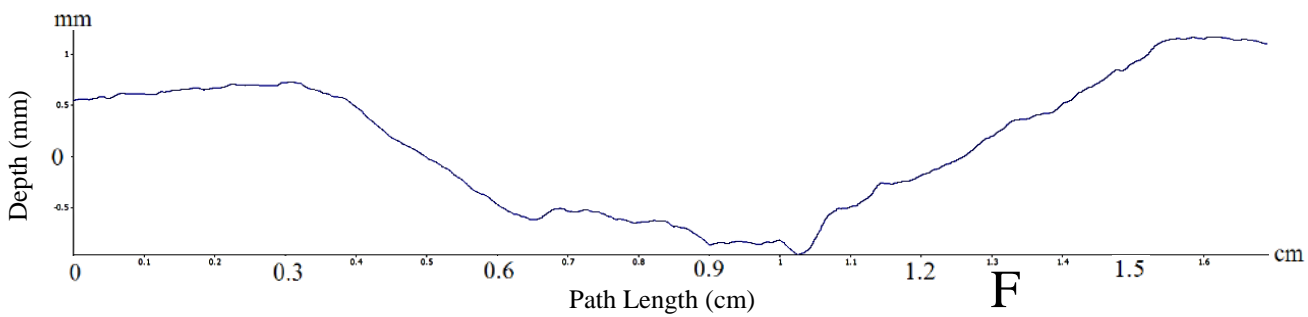
865°C Basalt
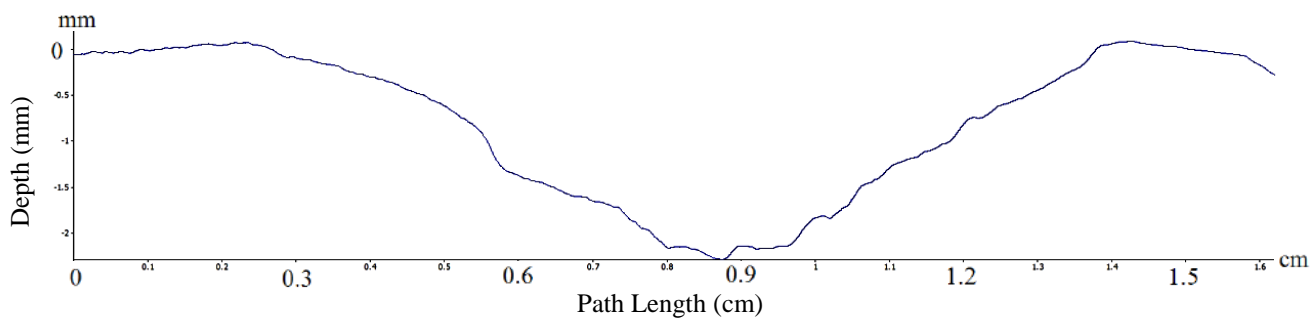
Figures 7.34 D to F: The craters shown in these MeX generated profiles showing a direct non-averaged profile form for Basalt changing through the temperature range. The profiles were always taken along the same axis.

7.14.1 Basalt Discussion

Figures 7.34 show the level of crater change with respect to the increase of target temperature. The profiles were generated from MeX profiling and were not averaged, thereby resulting in profiles in one direction only. At the colder regions of the temperature ranges included in this dataset, the crater floors are relatively bowl-like in

appearance. However, as temperature increases to the maximum, the floors widen and produce crater floors with raised regions.

Ancaster Hard White Limestone

-121°C Limestone
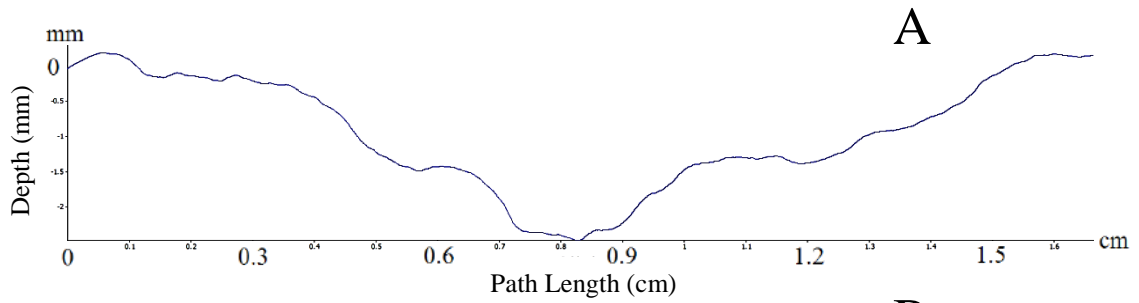
-97°C Limestone
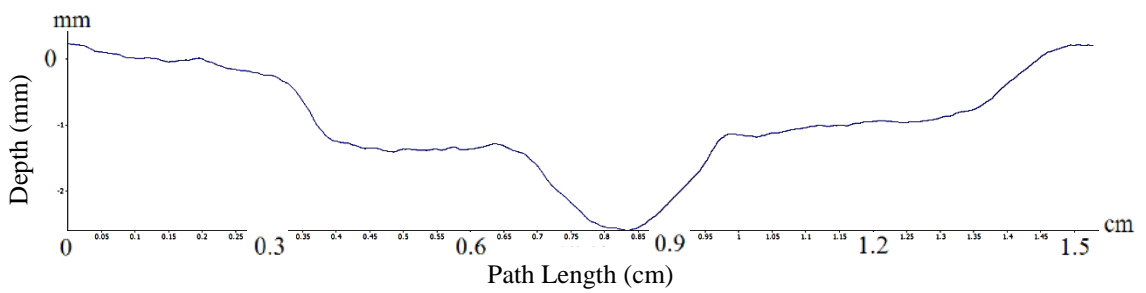
500°C Limestone
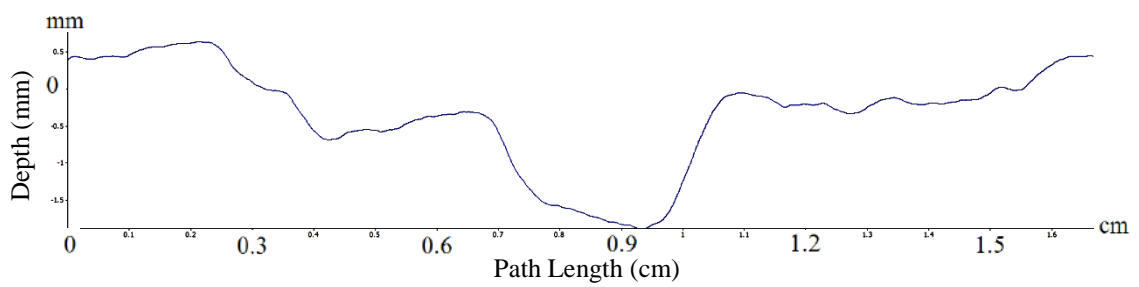
650°C Limestone
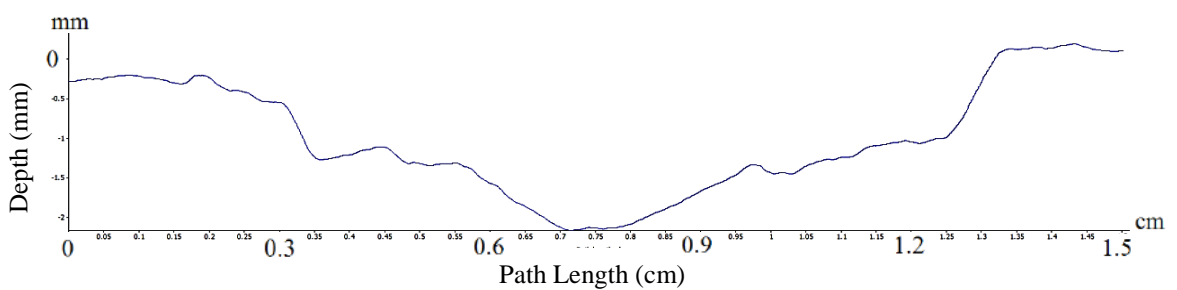
Figures 7.35 A to D: MeX profiles of the limestone impacts. A change was noted with the broadening of the initial excavatin zone for each crater as temperature increased to the decomposition limit.

7.14.2 Limestone Discussion

Although the effects of wall terracing and deviation varies throughout the profiles for limestone (Figure 7.35 A to D), the most notable change which can be seen is the affect on the initial crater excavation zones. The coldest temperature almost shows a simple crater produced from the impact but as the temperature increases, the initial excavation zones increase in depth but more so in width. The hottest temperature shows the existence of the initial excavation zone but it is very wide and the craters display simple crater morphology.

Beestone Red Sandstone

-111ºC Sandstone
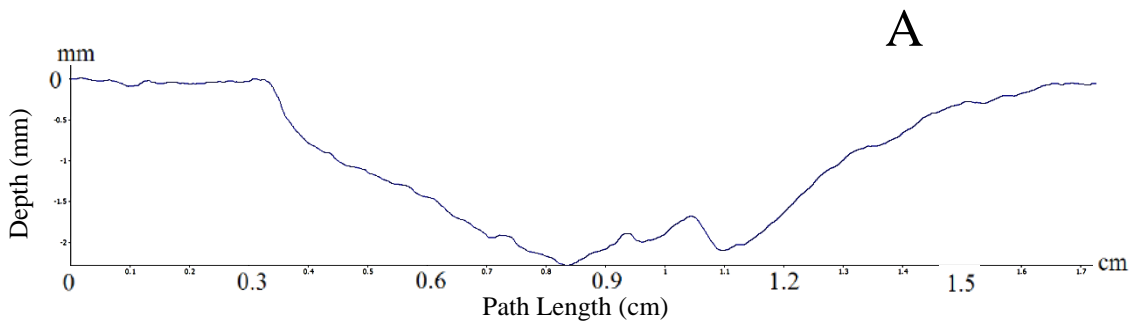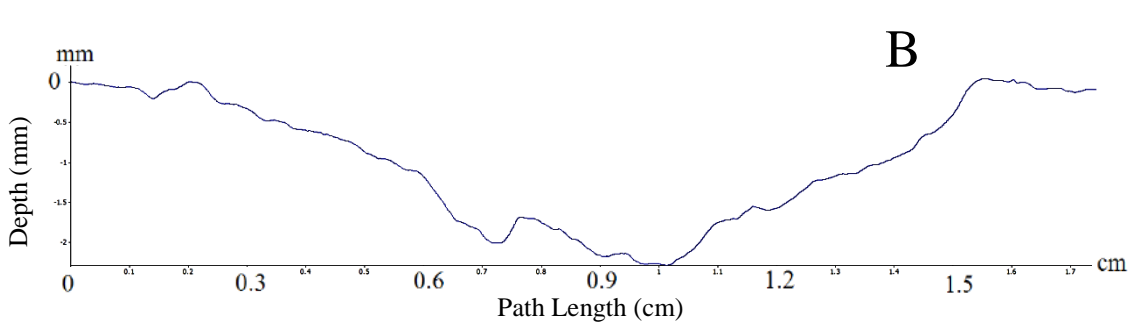
-98ºC Sandstone

RT Sandstone
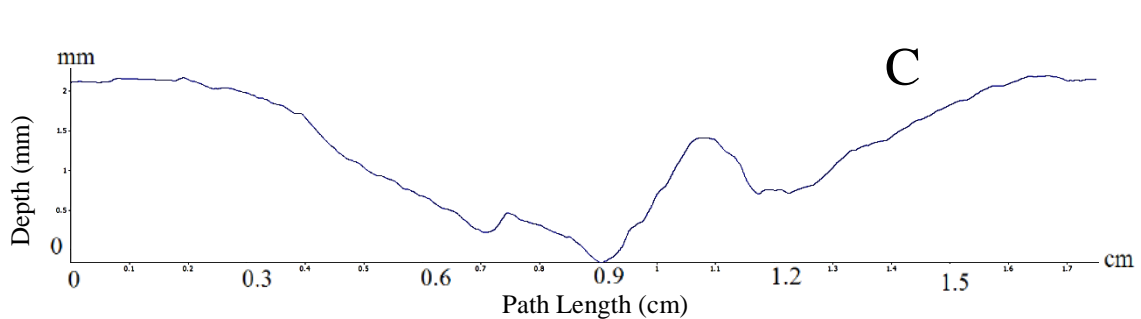
Figure 7.36 A to C: Single profiles generated from MeX of the sandstone craters.

500°C Sandstone

D

730°C Sandstone

E

750°C Sandstone

F

776°C Sandstone

G
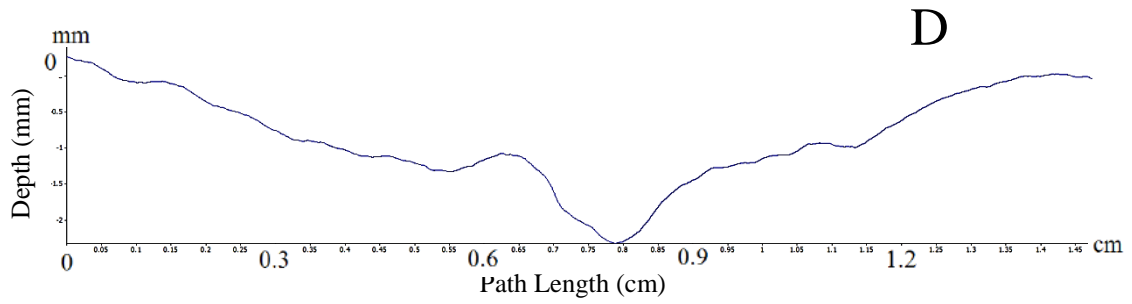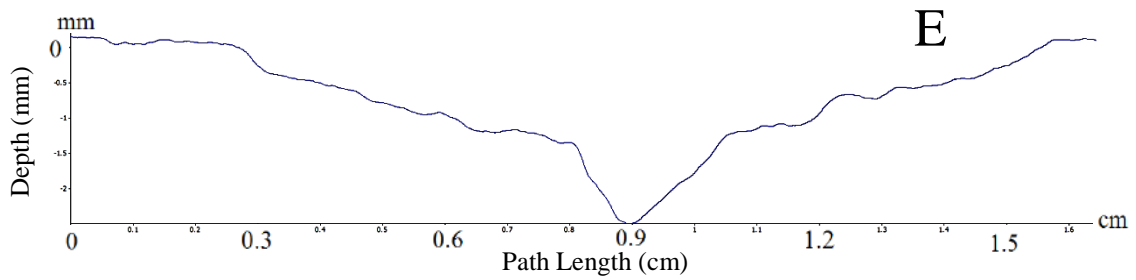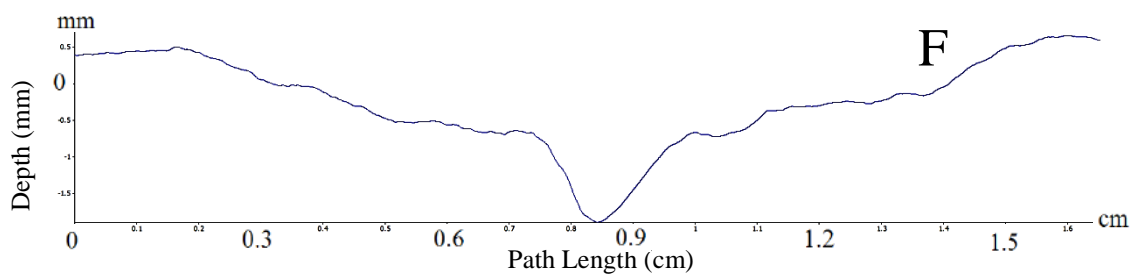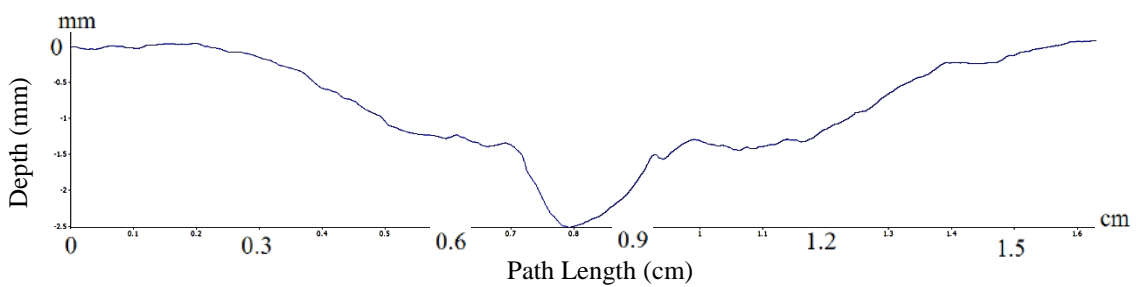
Figure 7.36 D to G: Single profiles generated from MeX of the sandstone craters.

7.14.3 Sandstone Discussion

The crater floors in the sandstone samples (Figure 7.36 A to G) show a morphological change with respect to temperature increasing. At the coldest temperatures, and up to the room temperature region, the crater floors show crater floor peaks to be present.

However as temperature is increased the crater floors in the sandstone samples show conical initial excavation zones.

7.15   Orthogonal Profiles

In order to help preserve a level of crater profile morphology whilst incorporating an element of statistical averaging, orthogonal profile plots were made using the MeX DEM data. Profiles chosen from two diagonal positions in each crater were averaged with respect to profile height and the resultant plotted. The data can be seen in Annex C but the discussions follow.

7.15.1 Sandstone Orthogonal Profiles

The profiles obtained show the craters from 162 to 1023 K. The coldest profile shows a complex broadened crater floor and the averaged trends show the broadened nature of the crater floor to reduce in width as temperature increases, thereby producing a steep-walled initial excavation cone.

7.15.2 Basalt Orthogonal Profiles

The basalt orthogonal profile included in this Section show only three averaged trends because the colder impacts produced basalt craters which were too large for successful MeX profiling.

The basalt data shows the evolution of the crater profiles as temperature increases. The profiles show the room temperature crater profile in blue with an initial excavation cone present, but as temperature increases, the crater floors broadens with increasing ridges of the crater floor. The room temperature profile indicates a level of terracing within the crater walls whereas the crater walls expand with spallation zones increasing slightly with width.

7.15.3 Limestone Orthogonal Profiles

One major property which can be seen from the data is the level of wall terracing. The coldest profiles show a deep broad initial excavation cone which peaks in width close to room temperature. Also the coldest profiles outline the spallation of the

limestone craters to be relatively flat surrounding the initial excavation cones and then to extend to the crater walls.

A definite reduction in initial excavation cone size is apparent for the hotter impacts which results in the craters displaying simple bowl formations with a degree of complexity either from terracing or scarps.

7.16   KDM Method Results

The plots obtained from the KDM method are shown in Annex E by their respective stone type and temperatures. Included here to aid the reader are the KDM data for Basalt 195.8 K.

Basalt 195.8 K
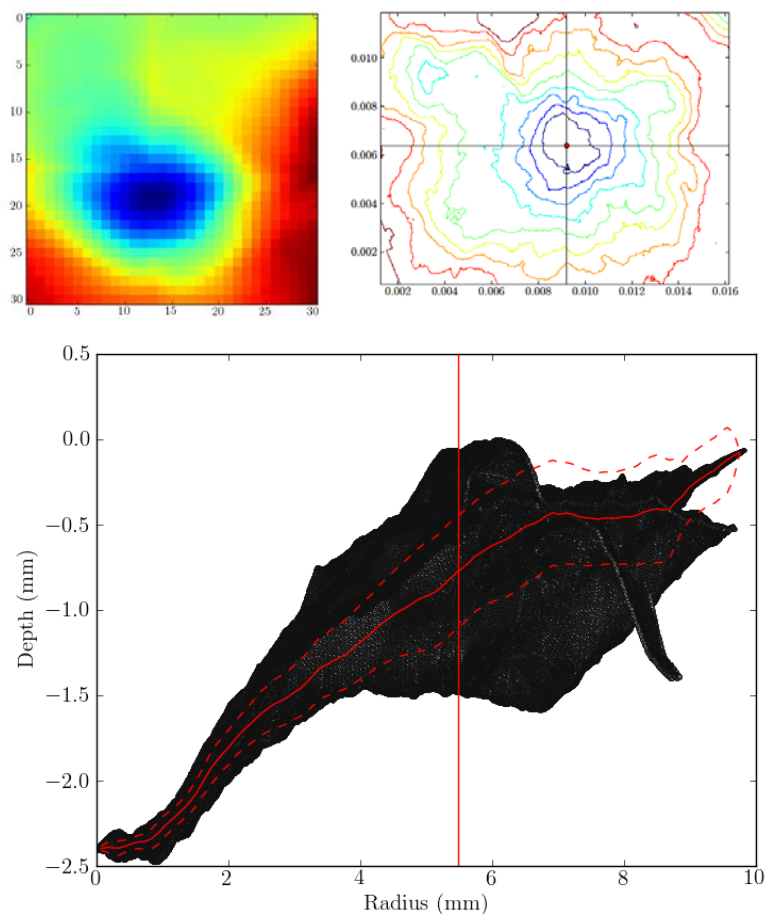
Figure 7.37: KDM method positioning and profile plots. Through depth iterations, the method locates a centroid for the crater on a 'best-guess' basis (upper left Figure) and then finalises the positioning of the centroid with respect to median averaging (upper right), afterwards the method generates the median average 360º crater profile (lower Figure).

The upper right diagram in Figure 7.37 shows the averaged contour positions used by centroid on a 'best-guess' basis. The method assigns weight to contours in the crater at half depth. The colours in the plot are associated with varying levels of height in the crater with red being the highest and the darkest blue being the lowest positions.

The top left diagram (Figure 7.37) shows the contours found from the KDM method during the centralisation of the centroid after the 'best-guess' stage as mentioned before. Once the 'best-guess' stage has found the area corresponding to the lowest position, the centroid will then be placed at the lowest section which provides the method with the best level of symmetry from the mean values of height from the lowest points. Once the lowest point is found, the KDM programme then sweeps the whole internal section of the crater and averaging the heights through a median approach, which is shown in the lower diagram.

The lowest position found from the centroid is displayed at the lowest left section of the whole data diagram. The black section to the plot gives the total cross-sections from the crater thereby producing a highest and lowest profile distribution with all corresponding cross-sections from the crater in between.

The vertical red line in Figure 7.37 details the radius at which the data is completely 100% enclosed by the MeX window. It is important to display this as some craters were elongated from the lowest mean position and the crater was dissected by the MeX programme's photo window size. This could mean that the crater itself shows the whole crater radius except for the top for example. The red vertical line shows that the data from 0 radius up to the line is 100% crater image and the data after the line details the crater with excluded sections.

The red lines which are aligned with the full data background show the best median averaged total crater profile with dashed standard deviation markers.

Each KDM crater profile will now be discussed with the images following.

Figure 7.38: KDM method generated average crater profiles obtained from the Basalt impacts. The different colours shows the different average cater profiles obtained from each crater.

Basalt 195.8 K

In the case of the cold basalt shot at a temperature of 195.8 K, the centre position was found very accurately but the total data gives a strange outcome resulting from one of the edges of the crater being cut-off by the MeX programme.

The crater profile is thin when compared to the other profiles to begin with (at radius = 0) which shows little height variation but broadens out further into the spallation zones (radius > ~3 mm).

Basalt 293 K

This crater shows the effect from the averaging of the profiles. From the initial radius, both lower and upper crater profiles show a small incline leading to a lipped drop or a crater floor peak (radius = ~ 1mm) but the averaged median line shows only a small variation in morphology. The data then shows another increase from the first lip to a terraced wall section (radius = ~3mm) but the corresponding median line shows very little effect from the upper and lower boundaries. One other consideration which occurs after the 100% line is the appearance of further terracing resulting in the median

line showing a crater wall hummock. Because the hummock is present in the median, it means that the hummocky feature is an extensive wall terrace which covers a significant section of the crater.

Basalt 722K

The "best guess" window shows the contours from this crater to be elongated with the presence of a crater floor peak. Likewise with the previous example, the crater floor peak is shown in the initial radii of the full profile but the averaging of the profiles smoothed this out. This crater was too big for the MeX programme photo window which is shown by the positioning of the 100% line occurring approximately at 3 mm. One other aspect to notice is that this profile shows the largest range in crater heights.

Basalt 898.8 K + 1138 K

This crater shows the median average line to be steeper than the other basalt average lines with the presence of crater floor peaks. However, the lower standard deviation after the peaks and terracing shows a drop away from the median position due to the effects from the full profile.

Basalt Trends

The average trends from the basalt data given in Figure 7.38 show no real effect from temperature on the cratering morphology.
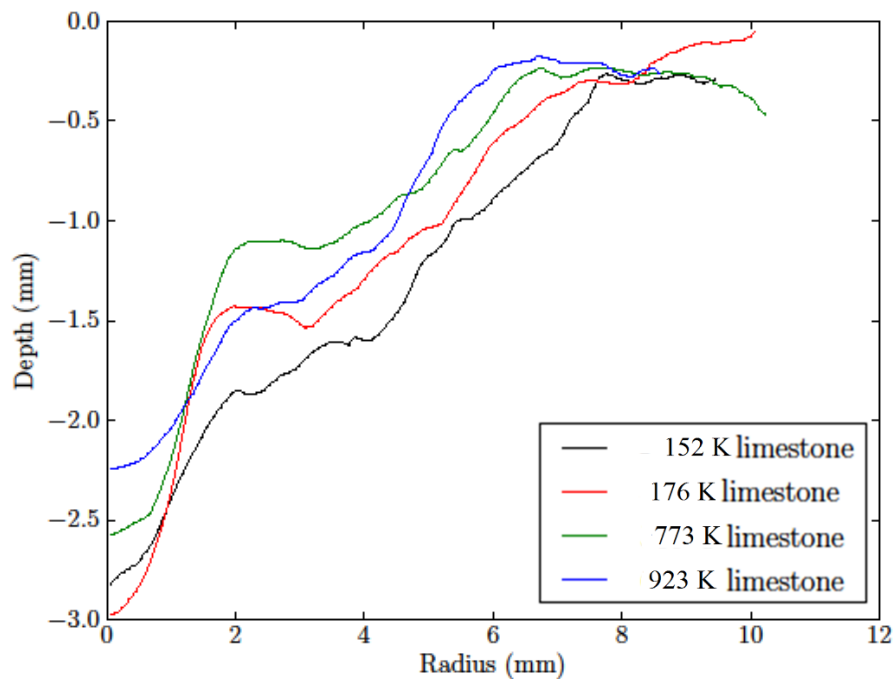
Figure 7.39: The average profiles obtained through the KDM method for limestone. Note the prominent initial excavation cones at the start of each profile.

Limestone 151.9 K

One common aspect presented from the KDM profiles for the limestone samples is the formation of the initial excavation zone. The initial trendline starts from the central position and increases quickly in gradient to the spallation zone. This effect is more prominent with the 176 and 773 K craters.

This crater is well centralised with the full profiles increasing in range at approximately 4 to 8 mm radius.

Limestone 176.3 K

The full profile data shows this crater to have the least variation of morphology but the most prominent initial excavation zone.

Limestone 773 K

Once again approximately situated near radius = 4 mm the data spreads to the largest profile range, however, at the furthest regions in the full profiles, the data splits between two branches. This is due to the MeX photo window cutting off some of the craters (apparent by the free space in between both branches). It can be assumed that one edge of the crater rim was not included (shown in the upper right best guess window) and affected the overall trend at the edge of the crater. Therefore the trend experienced more statistical weight from the lower branch of the full profile.

Limestone 923 K

This crater showed the widest range of profiles with the least initial excavation zone present.

Limestone Trends

The most prominent effect from the variance of temperature is the initial excavation zone gradients in Figure 7.39.

With the exception of the red average trendline, the general effect is that the hotter the limestone, the shallower the initial excavation zone. However due to positioning of the profiles and the increase on initial excavation depth in-between -97 and 500°C, the initial excavation zones do show a maximum in that temperature region. As is show in the limestone crater data, one possible maximum occurs around 450K.
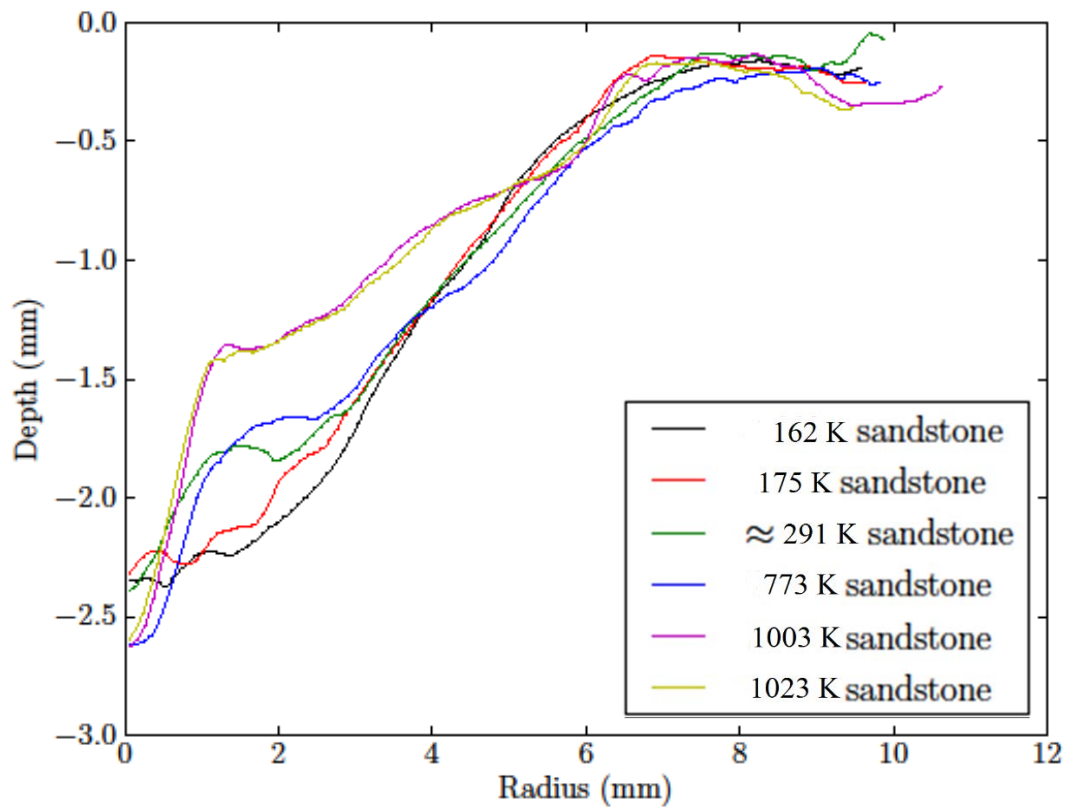
Figure 7.40: KDM method average profiles for sandstone impact crater for the temperature range tested. The two hottest impacts show very prominent initial excavation zones.

Sandstone 161 K

The crater floor peak shown in this dataset did affect the centralisation of the centroid. The lowest position for the crater occurs around ~ 1 mm from the designated position given in the bottom plot. This is common throughout the sandstone craters where crater floor peaks are prominent. This crater also shows reduced profile variance compared to the other profiles.

Sandstone 175 K

The centre of this crater was relatively complex and is shown in the variance of the full profile just after the start of the average trendline. The remainder of the profile is similar to the 161 K case.

Sandstone 292 K

This profile shows a very large crater floor peak with respect to the depth of the crater at approximately 2 mm position. After the large peak, the full profile pinches and then expands to a wider range of height levels.

Sandstone 793 K and Sandstone 1003 K

Both craters were included in the explanation because of the shared appearance of the initial excavation zone. In both cases, the initial excavation zones show properties very close to the limestone cases with prominent gradients leading to the spallation zones afterwards.

Sandstone Trends

The prominent feature of the average crater profile (Figure 7.40) comparison for the sandstone samples is the increasing depth and gradient of the initial crater excavation zones as temperature increases.

7.17   Summary

The first set of variable temperature rock related impacts ($< 500^{\circ}$C), helped to outline the experimental processes needed to develop this phase of the research project. The use of the laboratory stock rock samples helped to define the experimental processes but was found to be very different in crater properties when compared to the known source rock samples used later on.

Because of the dissimilar natures of the limestone and sandstone samples (lab stock and sourced), the limestone and sandstone graphs were recompiled in order to remove the first phase stock samples from the data sets and to concentrate purely on the sourced rock samples of Ancaster Hard White Limestone and Beestone Red sandstone.

The basalt rock samples were sourced from a colleague working at the National History Museum and was used solely for the purposes of this project.
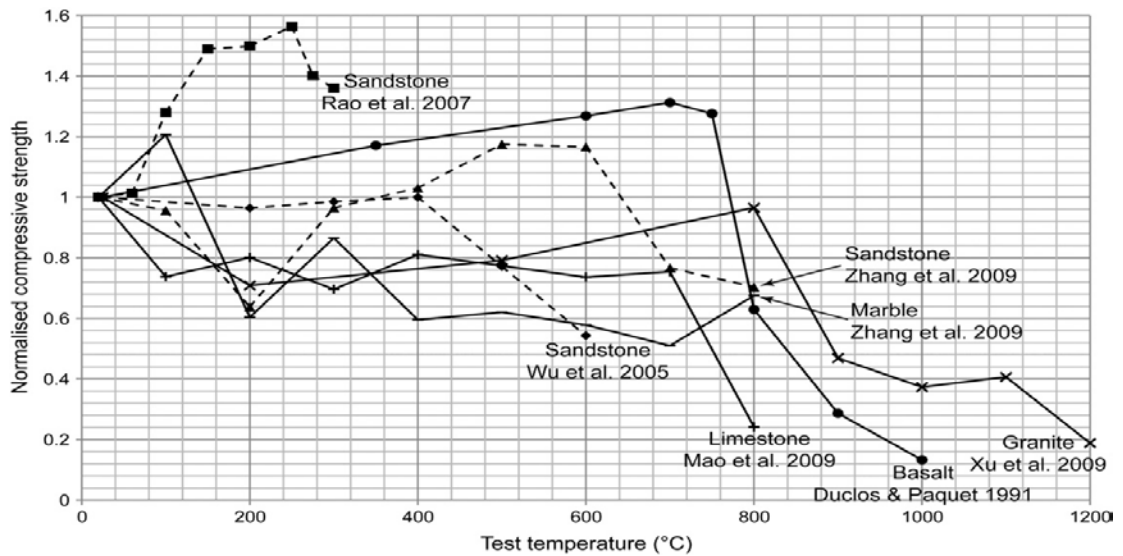
Figure: 7.41 : Strength tests of rock types with varying temperatures from Ranjith et al. (2012). The level of scatter in strength shows the variable nature of the rocks under test. Even a single material (e.g. sandstone) shows a wide range of behaviour depending on the source used.

The second conclusion for the variable temperature rock impacts is the level of variance in the datasets for all three rock types. Although removing the older stock rock sample data points from the limestone and sandstone plots has helped to remove unknown factors, the data still show considerable spread, most notably in the room temperature ranges for the sandstone and the limestone samples; the basalt shows large spread around the room temperature and cold ranges. One reason may lie in the irregular spallation discussed earlier, which could introduce scatter into the diameter and volume data.

However, variance in temperature related rock strength investigations has been highlighted before through the work of Ranjith et al. (2012). The normalised data shown in Figure 7.41 details large variance in the strengths of different rock types tested at different temperatures. The presence of variability in the data obtained from Ranjith et al. shows that rock strengths vary differently during heating even for a single

rock type. However, if we take a single data set in Figure 7.41, it is clear that strength does change.

Although the spread at certain temperature ranges are undesirable, the data sets do show relative trends. The values resulting from the calculations of the fitting residues, and therefore the fits themselves from the graphs, do show positive regression coefficients. Although the regression coefficients are low, it must be pointed out at this stage, that more temperature varied impacts are needed to help pinpoint the crater properties but effort is also needed to allow for irregular spallation (e.g. bigger targets with larger projectiles to give larger craters). Unfortunately this project was working towards a strict timetable for completion and also a limited supply of the basalt rock meant that more experiments on these rock types would require more time.

As the basalt environmental temperatures increased towards 1200 K, the internal energy of the rock samples meant that when the rocks were impacted, the cratering processes were closer to the plastic phase of the sample thereby resulting in the craters producing less volume and diameter; the depth was also the lowest if the range in the liquid nitrogen temperature could be ignored.

Because smaller craters were produced at the higher temperatures, this would suggest that the chemical bonds within the basalt matrix have much more energy than when compared to the colder temperatures, allowed the modification stage of cratering to be very efficient.

The d/D ratios show very large spreads in the data at the very cold and the room temperature regions, with the values tending towards 0.20 which is a common value for simple cratering.

The crater profiles produced from the singular plane and orthogonally averaged profiles show that the crater floors produced at lower temperatures are relatively simple bowl-like in appearance, but become more complex with increased levels of peaks and widened flatness.

The KDM method data shows that temperature has little effect on the cratering in basalt; however, due to the averaging nature of this new method, it does not show the level of variation described above but would need large temperature changes in order to register a definite effect from temperature.

Ancaster Hard White Limestone

The volume data shows a maximum in the fit around the 450K region, but once again the data fitting coefficients were affected from the data spread at room temperature. The removal of the red datum point (the furthest outlier) did little to stabilise the fits. The diameters show the similar increase to the 450K region but the data has such a low regression coefficient that this cannot be verified. Crater depth once again shows very little effect from the increasing temperature and therefore no trend is present.

The crater characteristics included in Table 7.4 for limestone show data variance for volume, diameter and depth being 29%, 17% and 11% standard deviations respectively. The percentages obtained from the standard deviations highlight the problems from the data spread in the room temperature region. Larger variation were found for volume with reduced variations for depth.

The d/D ratio plot shows no trend but a large spread in the data with the mean value being 0.20.

The profiles show very different outcomes with respect to the increase in temperature. The singular MeX profiles show an increase in the initial excavation zone in the crater floor at temperature increases, but at the hottest temperature, the initial excavation zone has almost reverted back to the cold limestone crater form of almost simple.

The KDM results show the dependence of temperature on the initial excavation zone and gives rise to the possibility of a maximum cratering efficiency when the limestone is near 450K.

Beestone Red Sandstone

The data obtained from the Beestone Red sandstone results show the variance which has been common throughout the variable rock impacts project.

The fits for each sandstone dimension graphs show spread in the data but a general slope to the lines of best fit. It appears that cratering in low temperature sandstone yields more crater volume and diameter but not depth.

Table 7.5 outlines the sandstone data which demonstrates the volume, diameter and depth mean averages to be 104 mm^3, 14mm and 2.5 mm respectively. However in comparison with the limestone data in Table 7.4, the difference in cratering from limestone to sandstone highlights the fact that the craters produced in the limestone impacts were considerably larger in all dimensions than the sandstone craters. Several possible explanations for this outcome could be as follows:

- Relative grain sizes between the two different types of rock. The packing of the rock grains would either introduce larger or smaller pore spaces in between each grain. Therefore larger pore spaces would require greater amounts of energy to crush them as opposed to smaller pore crushing. In turn, if more energy is being diverted into pore crushing, the shockwave will not excavate a larger crater as it would with a less pore space environment.
- The nature of the rock chemicals. Sandstone is considered to constitute quartz and/or feldspathic framework grains, whereas limestone originates from organic material through decomposition and inorganic precipitates and acts differently under high temperatures.

The sandstone KDM data reveals that the craters produced are affected by the temperature. Through the temperature range investigated, the KDM data shows that colder impacts resulted in shallow broader crater floors, whereas the hotter impacts produced much deeper and steeper initial crater excavations and broader spallation zones higher up the crater profile. These results are substantiated from the MeX singular craters profiles and the orthogonal crater profile plots.

One possible issue which could be rectified with respect to the variable temperature impacts project, is rock target grain size. In order to produce craters which were large enough to present adequate morphological results, and be small enough to reproduce an adequate image on the Leica microscope, the projectile size was limited to a maximum of 0.7 mm in diameter. Also it must be re-emphasised that the impact velocity remained constant at 5 km s^{-1}.

However, the samples such as the Ancaster white limestone and the Beestone red sandstone comprised grains which were large enough to affect the overall crater morphology. To limit this issue, the use of different rock samples with smaller grain sizes in comparison to the projectile diameter would be an advantage. Samples such

as solid chalk or fine grained limestone and marble would have been good samples for limestone. Volcanic ash and ashstone are very small grained sandstones and finally basaltic glass with no grain formations are equally appropriate samples to reduce the effect of grain size; this discussion gives rise to further investigation possibilities.

Solidus and Liquidus Temperatures of the Rock Types

Depending on the type of rock, the heating and subsequent melting of rock structure goes through different crystallisations at different temperatures. The temperature at which the rock has completely crystallised from a molten state is called the solidus temperature and is attributed to 2/3 of the liquidus temperature (explained next).

If further thermal energy is supplied to a rock in solidus form, it will enter the liquidus phase which is the state of matter where the rock is completely liquid in state. The transition between both states in not necessarily an abrupt change (dependant on rock type) but the states can exist in a semi-coexistent state called a freezing range where the rock is both liquid and solid.

The experiments detailed in this Chapter, investigated the effects of thermal energy with respect to crater morphology. At the highest obtained temperatures, the rock targets where close to their respective liquidus temperatures (Table 7.6) and any impact induced temperature increase would have exceeded such temperatures. The associated phase change temperatures for the rocks used in the experiments and the maximum temperatures are given in Table 7.6.

Table 7.6: Data concerning solidus and liquidus temperatures of the rock types used and maximum experimental temperatures obtained.

Rock Type	Temperatures (K)		
	Experimental Maximum	Solidus	Liquidus
Limestone	923	726	1100
Sandstone	1003	1038	1573
Basalt	1138	924	1400

As noted in Table 7.6, the maximum temperatures achieved in each rock type were close, or above the respective liquidus temperatures. However, each rock type was solid during and after impact with the exception of the limestone sample which started thermal decomposition shortly after impact which concludes that the rocks were not in the freezing range formation at these times. The rock samples (limestone, sandstone and basalt) were 177, 570 and 262 K less than liquidus temperatures respectively.

Nevertheless, the maximum temperatures were within the temperature boundaries in between liquidus and solidus which means that upon impact, each rock is closer to the plastic phase than crystallisation/glassy.

Chapter VIII : Conclusions

The research detailed in this work was set out to explore the validity and experimental consequences of two areas of astrophysical research; the effect of rotation on a body being impacted at hypervelocity speeds and the effect of target temperature on cratering and morphology. The Chapter will conclude the work contained in this thesis.

The first question relates to the aspects of asteroid rotation, and whether the spin experienced by many asteroids, is likely to have an effect on the overall strength of the asteroid and therefore influence the formation and distribution of asteroid families resulting from collisions.

The second question was to investigate crater production and morphology when the targets were held at different temperatures to simulate impacts on different planets within the solar system.

The results contained within these projects are original studies in the areas discussed before. The aspect of target rotation in catastrophic disruption has never been covered before, except for an unpublished centrifugal study in America by Housen and SPH simulations from Michel and Richardson very recently (in which the work covered in this project was cited by Michel and Richardson). When considering the level of rotational data for small bodies coming from sky surveys and the work on the YORP effect, the lack of rotational consideration needed to be addressed.

With respect to temperature related work and cratering, once again many studies have been concluded but without considering the two aspects together. Planetary impacts are prevalent throughout the inner solar system where the bodies are able to record and preserve the impact histories, provided there is very little, or no, geological resurfacing mechanisms present. But no questions have been asked on the aspect of temperature during cratering on rocky bodies. When considering the inner solar system, the surface temperatures of the planets and moons which form this section of the solar system, vary greatly due to solar proximity and atmospheric phenomena

Studies have looked at geological considerations on cratering on various planets as covered in Chapter 2, but the only work on temperature affecting the material

properties on planetary matter, has been strength tests on different rocks held at different temperatures. Bringing target temperature and cratering together is a vital step in the development of crater studies.

8.1 Catastrophic Disruption – Key Conclusions

The catastrophic disruption phase of the project required new equipment to be made and new experimental methodologies to be devised. In order to ascertain whether rotation of an impacted target had any influence on target disruption, stationary targets were impacted to allow for corresponding analyses between rotation and static targets to be made. A new in-situ rotating target holder was devised and manufactured to rotate the targets and for investigations to be made. The rotating target holder was fully controllable externally to the target chamber and allowed for impact positioning with respect to rotation to be determined.

The data were separated into two different sections, static for stationary target impacts for comparison with the second section of rotational target impacts. The static series of impacts progressed along trends expected as seen in previous studies (see Chapter 2 for references) into catastrophic disruption using stationary targets. However two data points were positioned below Q^* were heavily disrupted. These anomalous points would have been due to weaker material strength arising from inherent flaws in the targets. The data from the rotational target impacts show the cratering regime behaving similarly to the static case. However, the regime cross-over shows the greatest level of effect from the target rotation. Within the 'knee-joint' (transition region), the spread of data becomes very large and when considering the variables from the project, the only explanation for the spread in data is target rotation. The data towards the Q^* region for the rotating target case were taken several times, but all shots showed the same level of data spread. It was not expected that the data would be positioned exactly at Q^* with no scatter, but rather closer to Q^* than the spread showed as with the case of the static impacts. One final key observation arising from the rotational data and which has the same cause for the 'knee-joint' spread, is the reduced value in the catastrophic disruption boundary where the impact energy density Q results in 50% remnant mass (Q^*). The effect the rotation has on the target effectively reduces the target strength due to fragmentation and crack propagation being increased by the rotational motion. As the target rotates, the rotational kinetic

energy increases crack propagation and the fragments are removed from the main body due to Newton's laws of straight line motion (because the fragment mass is sufficient to inhibit the rotational sense of motion, the fragments would have crossed from rotational motion to tangential motion a lot sooner than if intact). The power law β values obtained from the mid-section of the fragment distributions, showed, larger debris pieces were thrown off from the rotation than compared with the static fragment data which helps to support this view.

The final part of the catastrophic disruption project was a theoretical section where Smoothed Particle Hydrodynamics models of the experimental targets were impacted under the same conditions as in the laboratory. The aim for the theoretical modelling was to develop an adequate material and failure model to replicate the experimental results as close as possible. It was found that a simplistic Von-Mises material model with P-α failure gave the best comparison to the experimental data. However, whilst Q* could be fairly well determined in the simulations, the fragment size distributions need more work.

Further work with respect to rotating targets could include investigations in varying the rate of target rotation to see how much the knee-joint is affected by target rotation. Targets could be impacted as a function of rotational rate with the possibility of increasing rotational rates past the recorded rates displayed by fast rotating asteroids, this in turn could experimentally establish the limits to which asteroids can rotate. Also, because of the wide range of asteroids observed from ice-fused to S type, the target material could be changed in order to further investigate collisional outcomes. Leading on from this would be investigations in target structure. The targets included in this project were monolithic but many asteroids have been found to be rubble piles (Michel et al. 2001). Also an accumulation of impact damage needs to be addressed because of the continual impacts happening throughout asteroid belts and largrangian points. This question would raise the point of accumulated values of Q on a parent body undergoing rotation, and the effect the rotation would have for each impact into the same body.

The modelling section requires further refinement on the material and failure models. The Von-Mises model was found to produce data close to the data seen from experiments, but the accuracy of the data would be improved with further refinement

of the model. This could allow for integration of larger body physics with a possibility of incorporating a gravity model to extend this work and to link experimental size regimes with astronomical.

8.2   Variable Temperature Impact Cratering – Key Conclusions

The second of the two projects, the variable temperature impact cratering project required new experimental and analyses methods. Two new target holders were needed; a heated target holder designed to heat rocks in situ was required not only to reach temperatures close to 1000 K but also to withstand the impact processes associated with the experiments. The second mount for analysis after a shot was the steromount designed for non-eucentric crater rotation about a common axis for images to be taken and then formulated into a three-dimensional digital elevation map for analysis. Also a new analysis was designed using the three-dimensional data from Alicona MeX surface analysis tool to form a statistically robust method in determining whether temperature had any effect on crater morphology. The use of MeX provided an accurate (to within 5% error measurements) modelling data analysis technique, which did not take direct measurements from the samples that could have altered the properties of the craters such as crater-floor grain crumbling from depth probes.

The final new data analysis technique devised for this work was the KDM method. The KDM method used the raw 3-dimensional data obtained through the MeX software and plotted median average 360° crater profiles in 2-dimensions. This new method gave an overall total view of the crater in terms of profiling, and allowed for a proper statistical analysis in terms of crater profiles.

The rock types used for the purposes of this project were limestone (fine-grained Jurassic type), sandstone (fine-grained with clay holes Triassic type), haematite (pre-main test) and basalt. All types were cooled down to 82 K with the aid of an LN_2 freezer or heated up to approximately 1000 K, with the exception of limestone which decomposes at temperatures of approximately 800 K.

Each rock type was impacted by a stainless steel 420 ball bearing 0.8 mm in diameter at varying temperatures impacted at 5 kms^{-1}. The data obtained from the physical characteristics such as depth, diameter and volume showed little dependence on target temperature due to scatter on the data. However, the increase in temperature did effect

the rock target's level of spallation at the higher temperatures. As the rock samples were heated, the hottest temperatures recorded from the newly designed target holder showed the rocks to be above solidus temperatures but below liquidus temperatures. Although some rocks do show a jump boundary between solidus and liquidus (and abrupt change between the two states of rock), many others including the rocks used in this work, show a quasi-existence in-between solidus and liquidus or quasi-liquidus state. Because the rock targets were maintained in the quasi-liquidus regions, the rocks displayed an increased level of plastic behaviour instead of brittle, this in turn meant, that the excavation and modification stages of crater formation resulted in less to zero spallation.

The data associated with the temperature related impacts did highlight the need for much more research. The variability in the data needs to be addressed through a project run with an adequate number of impacts to obtain statistically robust averages in crater morphology. Possible avenues for future research could include an extensive shot regime as detailed before, increasing the temperature ranges further than included in this work to investigate the liquidus phases and investigating the possibility of petrological metamorphosis through impact at the higher temperature ranges.

8.2.1 Basalt – Key Conclusions

Very common throughout the solar system (Basaltic Volcanism Study Project 1981), basalt targets were tested through the whole temperature range possible with the current experimental set up. The data for volume showed that the hotter the basalt rock was when impacted, the smaller the volume of the crater. This appeared to be the case with diameter and crater depth. The d/D ratios show no dependence on target temperature and ranged from 0.12 to 0.24.

8.2.2 Limestone – Key Conclusions

The limestone data displayed the greatest degree of scatter at room temperature for all three characteristics; volume, diameter and depth. However, it was noted that the data showed an increase in these parameters around 550 K and then reduced back down as the temperatures were increased. The d/D ratios also displayed this form of increase.

8.2.3 Sandstone – Key Conclusions

The crater volume and diameter data showed a decrease in value with increasing temperature, whereas the crater depth increased with increasing temperature. One aspect from this was that the craters were becoming more cone shaped in morphology as temperature increased. The d/D ratios also showed an increasing trend with temperature.

The new analytical method (KDM) took raw data from the model profiles explained before and statistically analysed the whole crater profile as an averaged two-dimensional profile.

For any real dependence to be noted, the level of change in morphology had to be large enough to overcome the averaging effect of the method. There was very little change in the profiles associated with the basalt samples but the limestone and sandstone samples did show morphological change with respect to temperature.

Limestone displayed a broadening of the initial excavation zone the hotter the target was when impacted. The level of crater spallation also reduced as temperature increased.

The sandstone profiles showed little difference except for the presence of crater lips around the initial excavation zones in the 161 – 292 K range, but from this point on, the craters became much deeper with prominent cones forming from the initial excavation zones.

The information obtained from this project acts as a feasibility study into the effects of temperature and shows the possibility of morphological dependence with respect to temperature. This details the need for further work to reduce the level of scatter on the data and to determine whether temperature truly has any effect on cratering.

8.3 Limitations of the work

The study has offered a viable range of experimental processes into two areas of research and preliminary results which show to answer the questions first set out in Chapter 2: Questions to be addressed. However with all projects there are associated limitations which further work will help to eliminate.

8.3.1 Catastrophic Disruption

The use of cement paste afforded a close analogue to S type asteroids with a degree of production malleability. However cement, although considered as a usable medium for the catastrophic work carried out, is not a true analogue of the taxonomic classes of asteroids.

Further limitations are associated with the theoretical modelling of the experimental impacts. The material model used an adapted pre-set concrete model from the Ansys Autodyn library. In order to truly replicate the experiments, full testing would be required to ascertain every material constant associated with cement and not concrete. This would require a completely new project in its own right and therefore was outside of the scope of this project.

Moreover, the timing constraints on this project meant that the modelled data did not show every point associated with the experimental data, but a small amount. This was due to problems with the previous model used and the size difference between impactor and target – especially problematic for the 1 mm projectiles impacting 75 mm targets.

8.3.2 Variable Temperature Impact Cratering

The biggest limitation with the variable temperature cratering project was the degree of data scatter. The total number of shots conducted was insufficient to deal with the variable nature of crater characteristics associated with the test subjects. One limitation was due to the low number of available basalt samples being much fewer than the sandstone or limestone. The basalt obtained did not come from a quarry and so could not be replenished when needed. Also the highly variable nature of spallation at this crater size scale maybe obscuring some aspect of the results.

For future work, one possible key to minimise variation in crater size in the target would be to use larger projectiles to make larger craters. This might reduce variation due to grain size, or imperfections in the targets. With the rotating target work, a range of rotational rates would help provide further insights.

8.4 Summary

The projects described within this work set out to ascertain whether rotation has any effect on an impacted body and if a range of thermal energy inside a body undergoing a hypervelocity impact could affect crater formation. This work has been successful in answering these questions with the previous caveat.

New methods were developed in order to answer the questions set by this work, and this work brings both experimental and theoretical insights into two areas of research where every contribution is vitally important, not just for the acquisition of knowledge, but also the influence of impacts and their outcomes in the solar system.

The solar system is a constantly changing environment where impacts occur every day. Most impacts are deemed fascinating but harmless and some on rare occasions are very dangerous. This work has highlighted important factors which will help with the formulation of theories concerning evolution, and interactions within the asteroid belts, to explaining why certain craters on certain solar system bodies show the morphology they do.

"If we knew what it was we were doing, it would not be called research, would it?"

Albert Einstein

References

Abed A.M., Amireh B. S. and Al Zghoul K. 2015, Some observations facing the interpretation of Waqf as Suwwan structure, SE desert of Jordan, as an impact crater, *Arabian Journal of Geosciences*, 8, 4025-4037

Abdulagatov I., Z Abdulagatova Z., Kallaev S., Bakmaev A. and Ranjith P., 2015, Thermal-diffusivity and heat-capacity measurements of sandstone at high temperatures using laser flash and DSC methods, *International journal of thermophysics*, 36, 658-691

Aittola M., Ohman T., Leitner J. J. and Raitala J. 2007, The characteristics of polygonal impact craters on Venus, Earth Moon Planet, 101, 41-53

Alfvèn H. and Arrhenius G. 1976, In evolution of the solar system 16, Washington: CR-2291 NASA

Amelin Y., Krot A. N., Hutchson I. D. and Ulyanov A. A., 2002, Lead isotopic ages of chondrules and calcium-aluminum-rich inclusions, *Science*, 297, 1678.

Arnould M., Paulus G. and Meynet G. 1997, The production of short-lived radionuclides by new non-rotating and rotating Wolf-Rayet model stars, *A and A*,321, 452.

Asphaug E., Ryan E., Zuber M., Bottke W., Cellino A., Paolicchi P., Binzel R., 2002, Asteroid interiors, Asteroids III, Univ. of Arizona Press, Tucson, pp. 463–484

Ballouz R. L., Richardson D. C., Michel P. and Schwartz S. R. 2014, Rotation-dependent catastrophic distruption of gravitational aggregates, *Astrophysical Journal*, 789, 158

Bart G.D. 2014. The quantitative relationship between small impact crater morphology and regolith depth. *Icarus* 235:130–135.

Baldwin, E.C., Milner, D.J., Burchell, M.J.. Crawford, I. A. 2007. Laboratory impacts into dry and wet sandstone with and without an overlying water layer: Implications for scaling laws and projectile survivability. Meteoritics and Planetary Science 42, 1905-1914.

Basaltic Volcanism Study Project, 1981, Basaltic volcanism on the terrestrial planets, Pergamon Press Inc, 1286

Batygin K. and Laughlin G., 2014, Jupiter's decisive role in the inner Solar System's early evolution, *PNAS*, 112, 4214-4217

Benavidez .P G., Durda D. D., Enke B. L., Bottke W. F., Nesvorný D., Richardson .D C., Asphaug E. and Merline W. 2012, A comparison between rubble-pile and monolithic targets in impact simulations: Application to asteroid satellites and family size distributions, *Icarus* 219, 57-76.

Bendjoya P., 1993, A classification of 6479 asteroids into families by means of the wavelet clustering method, *Astronomy and Astrophysics supplement series*, 102, 25-55

Bendjoya P. H. and Zappalá V.2002, Asteroid family identification, Asteroids III, 2002.

Borovicka J, Spurný P., Brown P., Wiegert P., Kalenda P., Clark D. and Shrbený L., 2013, The trajectory, structure and origin of the Chelyabinsk asteroidal impactor, *Nature* 503,235-237

Boss A. P. and Keiser S. A. 2012, Supernova-Triggered Molecular Cloud Core Collapse and the Rayleigh-Taylor Fingers that Polluted the Solar Nebula *Astrophysical Journal Letters*, 756, 6pp.

Boss A. P. and Keiser S. A. 2010, Who Pulled the Trigger: A Supernova or an AGB Star? *Astrophysical Journal Letters*, 717, L1-L5

Bottke W. F., Cellino A., Paolicchi P., Binzel R. P. 2002a An overview of the asteroids: the asteroids III perspective, Asteroids III, 3-15

Bouvier A. and Wadhwa M. 2010, The age of the solar system redefined by the oldest Pb-Pb age of a meteoritic inclusion, *Letters, Nature Geoscience*, (2010)

Buhl E., Poelchau M., Dresen G. and Kenkmann T., 2014, Scaling of sub-surface deformation in hypervelocity impact experiments on porous sandstone, *Tectonophysics*, *634*, p. 171-181.

Burr D. M. and Howard A. D. 2015, Introduction to the special issue: *Planetary geomorphology, Geomorphology*, 240, 1-7

Brandt A. M., 1998, Optimisation Methods for Material Design of Cement-Based Composites, CRC Press, 120

Burchell M. J., Brooke-Thomas W. and Leliwa-Kopystynski J. 1997, Hypervelocity impact experiments on solid CO_2 targets, *Icarus*, 131, 210-222 (1998).

Burchell M. J. et al., 1999, Hypervelocity Impact Studies Using the 2 MV Van der Graaff Dust Accelerator and Two Stage Light Gas Gun of the University of Kent at Canterbury, *Meas. Sci. Tech.* 10, 41-50, 1999.

Buffon. Comte de G-L., Les époques de la nature, Tome I De la formation des planets, 1778, translated by Marine Riesenmey.

Cameron A. G. W. and Truran J. W. 1977, The supernova trigger for the formation of the solar system *Icarus* 30, 447-461.

Carry B. 2012, Density of Asteroids, Planetary and Space Science 73, 98-118

Chapman C. R., Morrison D., and Zellner B. 1975, Surface properties of asteroids: A synthesis of polarimetry, radiometry and spectophotometry, *Icarus*, 25 issue 1, 104-130

Chapman C. R., Cohen B. A. and Grinspoon D. H. 2007, What are the real constraints on the existence and magnitude of the late heavy bombardment?, *Icarus* 189, 233 – 245

Chesley S. R., Ostro S. J., Vokrouhlický D., Čapek D., Giorgini J. D., Nolan M. C., Margot J-L., Hine A. A., Benner L. A. M. and Chamberlin A. B. 2003, Direct detection of the Yarkovsky effect by radar ranging to asteroid 6489 Golevka, Science 302 1739, (2003). D D Clayton 1977, *Icarus* 32, 255-269.

Cicero S., Garcia T., Castro J., Madrazo V. and Andres D., 2014, Analysis of notch effect on the fracture behaviour of granite and limestone: An approach from the theory of critical distances, *Engineering geology*, 177, 1-9

Cochrane C. and Ghail R. 2006, Topographic constraints on impact crater morphology on Venus from high-resolution stereo synthetic aperture radar digital elevation models, *Journal of Geophysical Research*, 111

Crozier W. D. and Hume W., 1957, High-Velocity, Light-Gas Gun, *Journal of Applied Physics,* 28, 892-894.

Cuk M., Christou A. A. and Hamilton D. P. 2015, Yarkovsky-driven spreading of the Eureka family of Mars Trojans, *Icarus*, 252, 339-346

Copernicus N., De Revolutionibus Orbitum Cœlestrium Libri VI 1543, Nicola Copernici Torinensis, Translated by Prof J. F. Dobson, Occasional Notes No.10 Vol 2, May 1947

Descartes, R., The world or Treatise on light, available from http://www.princeton.edu/~hos/mike/texts/descartes/world/worldfr.htm

Translated by Michael S. Mahoney

Durda, D. D., Greenberg R., and Jedicke R. 1998. Collisional models and scaling laws: A new interpretation of the shape of the main-belt asteroid size distribution. *Icarus* 135, 431–440

D D Durda, W F Bottke Jr, D Nesvorný, B L Enke, W J Merline, E Asphaug and D C Richardson 2006, Size-frequency distributions of fragments from SPH/N-body simulations of asteroid impacts: Comparison with observed asteroid families, *Icarus* 186, 498-516, (2007).

Durda D., Bagatin A. C., Aleman R. A., Flynn G. J., Strait M. M., Clayton A. N. and Patmore E. B., 2015, The shapes of fragments from catastrophic disruption events: Effects of target shape and impact speed, *Planetary and Space Science*, 107, 77-83

Fairhurst C., 1964, On the Validity of the 'Brazilian' Test for Brittle Materials, *International Journal of Rock Mechanics and Mining Science & Geomechanics Abstracts*, 10, 535-546

Farinella P., Vokrouhlický D. and Hartmann W. K., 1997, Meteorite delivery via Yarkovsky orbital drift, *Icarus* 132, 378 – 387

Fedo C. M., McGlynn I. O. and McSween H. Y. 2015, Grain size and hydrodynamic sorting controls on the composition of basaltic sediments: Implications for interpreting martian soils, *Earth and Planetary Science Letters*, 423, 67-77

Fernandes V. A., Fritz J., Wiess B. P., Garrick-Bethell I. and Shuster D. L., 2013, The bombardment history of the Moon as recorded by ^{40}Ar – ^{39}Ar chronology, *Meteoritics and Planetary Science* 48, 241 – 269 (2013)

Flynn G., Durda D. D., Patmore E., Clayton A., Jack S., Lipman M. and Strait M., 2015, Hypervelocity cratering and disruption of porous pumice targets: Implications for crater production, catastrophic disruption and momentum transfer on porous asteroids, *Planetary and Space Science*, 107, 64-76

French B. and Korberl C., 2010 The convincing identification of terrestrial meteorite impact structures: What works, what doesn't, and why. *Earth Science Reviews* 98 123 – 170

French L. M., Stephens R. D., Coley D., Wasserman L. H. and Sieben J., 2015, Rotation lightcurves of small jovian Trojan asteroids, *Icarus*, 254, 1-17

Ghobadi M. and Babzadeh R., 2015, Experimental studies on the effects of cyclic freezing-thawing, salt crystallisation, and thermal shock on the physical and mechanical characteristics of selected sandstones, *Rock mechanics and rock engineering*, 48, 1001-1016

Giblin I., Davis D. R. and Ryan E. V., 2002, On the collisional disruption of porous icy targets simulating Kuiper belt objects, *Icarus* 171, 487-505.

Gonzalez-Gomez W., Quintana P., May-Pat A., Aviles F., May-Crespo J. and Alvarado-Gil J., 2015, Thermal effects on physical properties of limestones from the Yucatan Peninsula, *International journal of rock mechanics and mining sciences*, 75, 182-189

Gritschneder M., Lin D. N. C., Murray S. D., Yin Q. Z. and Gong M. N. 2012, ^{26}Al – ^{26}Mg isotope systematics of the first solids in the early solar system, *Astrophysical Journal Letters,* 745, 12

Halikia I., Zoumpoulakis L., Christodoulou E. and Prattis D., 2001, Kinetic study of the thermal decomposition of calcium carbonate by isothermal methods of analysis, The European Journal of Mineral Processing and Environmental Protection, *The European Journal of Mineral Processing and Environmental Protection*, Vol.1, 89 - 102

Hamilton W. M., 2014, Dwarf planets and asteroids: Minor bodies of the solar system, Strategic Book Publishing and Rights Co., 10, 978-1-62857-728-0

Hampson P. and Moatamedi M., 2007, A review of composite structures subjected to dynamic loading, *International journal of crashworthiness*, 12, 411-428

Helm, van der E. and Jeffers S. 2012, Dynamical and collisional evolution of Halley-type comets, *Icarus*, 218, 448-458

Hirabayashi M. and Scheeres D. J., 2015, Stress and failure analysis of rapidly rotating asteroid (29075) 1950 DA, *Astrophysical Journal Letters*, 798, L8

Hirayama K., 1918, Groups of asteroids probably of common origin, *Astron. J.* 31, 185-188

Hofmeister A. and Mao H-K., 2002, Redefinition of the mode Gruneisen parameter for polyatomic substances and thermodynamic implications, *Proc Natl Acad Sci*, 99, 559-564

Holsapple K., 1993, The scaling of impact processes in planetary sciences, Annual Review of Earth and Planetary, *Science*, 21, 333–373.

Holsapple K, Giblin I., Housen K., Nakamura A. and Ryan E., 2002, Asteroid Impacts: Laboratory Experiments and Scaling Laws, Asteroids III, 443 – 462.

Hossain M. S. and Kruhl J. H. 2015, Fractal Geometry-Based Quantification of Shock-Induced Rock Fragmentation in and around an Impact Crater, *Pure and Applied Geophysics,* 172, 2009-2023

Hugoniot H., 1887, Mémoire sur la propagation des mouvements dans les corps et spécialement dans les gaz parfaits (première partie), Journal de l'Ècole Polytechnique, 57, 3-97

Jin C., Yang C., Fang D. and Xu S., 2015, Study on the failure mechanism of basalt with columnar joints in the unloading process on the basis of an experimental cavity, *Rock mechanics and rock engineering*, 48, 1275-1288

Jones B. W. 2007, Discovering the solar system, Wiley 2nd Edition, ISBN 978-0-470-01830-9

Jutzi M., Michel P., Benz W. and Richardson D. C., 2010, Fragment properties at the catastrophic disruption threshold: The effect of the parent body's internal structure, *Icarus* 207, 54-65 (2010).

Jutzi M., 2015, SPH calculations of asteroid disruptions: The role of pressure dependent failure models *Planetary and Space Science*, 107, 3-9

Jutzi M., 2015, SPH calculations of asteroid disruptions: The role of pressure dependent failure models, *Planetary and Space Science*, 107, 3-9

T Kadono, A Suzuki, K Wada, N Mitani, S Yamamoto, M Arakawa, S Sugita, J Haruyama and A Nakamura, 2015, Crater-ray formation by impact ejecta particles, *Icarus*, 250, 215-221

Kaur P., Chauhan P., Rajawat A. S. and Kiran A. S. 2015, Study of olivine-rich dark halo crater - Beaumont L in Mare Nectaris using high resolution remote sensing data, *Planetary and Space Science*, 109, 92-105

Keller H. U., Barbieri C., Koschny D., Lamy P., Rickman H., Rodrigo R., Sierks H., A'Hearn M. F., Angrilli F., Barucci M. A. , Bertaux J-L., Cremonese G., Da Deppo V., Davidsson B., De Cecco M., Debei S., Fornasier S., Fulle M., Groussin O., Gutierrez P. J., Hviid S. F., Ip W-H., Jorda L., Knollenberg J., Kramm J. R., Kührt E.,

Küppers M., Lara L-M., Lazzarin M., Lopez Moreno J., Marzari F., Michalik H., Naletto G., Sabau L., Thomas N., Wenzel K-P., Bertini I., Besse S., Ferri F., Kaasalainen M., Lowry S., Marchi S., Mottola S., Sabolo W., Schröder S. E., Spjuth S., and Vernazza P., 2010, E-type asteroid (2867) Steins as Imaged by OSIRIS on board Rosetta, *Science*, 327, 190-193

Kieffer S. and Simonds C., 1980 The role of volatiles and lithology in the impact cratering process. *Reviews of Geophysics and Space Physics* 18, 143 – 181

Kryszczýnsky A. 2013, Do Slivan states exist in the Flora family? II. Fingerprints of the Yarkovsky and YORP effects*, *A&A* 551, A102 (2013)

Laplace, Simon-Pierre Marquis de, 1796, Le Système Du Monde

Lauretta D., Bartels A., Barucci M., Bierhaus E., Binzel R., Bottke W., Campins H., Chesley S., Clark B., Clark B., Cloutis E., Connolly H., Crombie M., Delbo M., Hamilton V., Hergenrother C., Johnson C., Keller L., Michel P., Nolan M., Sandford S., Scheeres D., Simon A., Sutter B., Vokrouhlicky D. and Walsh J., 2015, The OSIRIS-Rex target asteroid (101955) Bennu: Constraints on its physical, geological and dynamical nature from astronomical observations, *Meteoritics & Planetary Science*, 50, 834-849

Lee T., Papanastassiou D. A. and Wasserburg G. J. 1976, Demonstration of ^{26}Mg excess in Allende and evidence for ^{26}Al, Geophys. *Res. Lett* 3, 41.

Leuschner A. O., 1922, Comparison of theory with observation for the minor planets 10 Hygeia and 175 Andromache with respect to perturbations by Jupiter, *Proc. N. A. S.*, 8, 170 – 173

Levison H. F., Drones L., Chapman C. R., Stern S. A., Duncan M. J. and Zahnle K., 2001, Could the lunar "late heavy bombardment" have been triggered by the formation of Uranus and Neptune?, *Icarus* 151, 286 – 306 (2001)

Lissauer J. J., 1993, Planet formation, *Annu. Rev. Astron. Astrophysics* 31 (1993), 129-174

Lowry S. C., Fitzsimmons A., Pravec P., Vokrouhlický D., Boehnhardt H., Taylor P. A., Margot J-L., Galád A., Irwin M., Irwin J. and Kusnirák P. 2007, Direct detection of the asteroidal YORP effect, *Science* 316, 272, 2007.

Lynden-Bell D. and Pringle J. E., 1974, The evolution of viscous discs and the origin of the nebular variables *Mon. Not. R. Astr. Soc.* 168, 603 – 637

Marchi S., Bottke W. F., Kring D. A. and Morbidelli A. 2012, The onset of the lunar cataclysm as recorded in its ancient crater populations, *Earth and Planetary Sci. Lett.* 325 – 326 (2012) 27 – 38

Martellato E., Cremonese G., Marzari F., Massironi M., and Capria M. T. 2007, Analysis of impact craters on Mercury's surface, *Mem. S.A.It. Suppl.* Vol. 11, 124

McCrea W. H., 1974, Origin of the solar system, Earth, Moon and Planets, 75 – 110

McCrea W. H., 1960, The origin of the solar system, *Proc. R. Soc. Lond.* 1960 256 245 – 266

Melosh J., 1989 Impact Cratering: A geological process, Oxford University Press

Michel P., Benz W., Tanga P. and Richardson D. C., 2001, Collisions and Gravitational Reaccumulation: Forming Asteroid Families and Satellites, *Science*, 294 (5547)

Michel P., Jutzi M., Richardson D. C., Goodrich C. A., Hartmann W. K. and O'Brien D. P., 2015, Selective sampling during catastrophic disruption: Mapping the location of reaccumulated fragments in the original parent body, *Planetary and Space Science*, 107, 24-28

Ming L., Xianbiao M., Aihong L., Jing T., Guanghui Z., Lianying Z., Chong L., 2014, Effect of specimen size on energy dissipation characteristics of red sandstone under high strain rate, *International journal of mining science and technology*, 24, 151-156

Morbidelli A., Petit J-M., Gladman B. and Chambers J. 2001, A plausible cause of the late heavy bombardment, *Met. & P. Sci.* 36, 371 – 380 (2001)

Morris A., et al. LPSC XLII, Abstract 1943, 2011

Morris A., Price M. and Burchell M, 2013, Is the large crater on the asteroid (2867) Steins really an impact crater?, *Astrophysical Journal Letters*, 774, L11

Nakamura A., Yamane F., Okamoto T. and Takasawa S., 2015, Size dependence of the disruption threshold: laboratory examination of millimetre-centimetre porous targets, *Planetary and Space Science*, 107, 45-52

NASAJPL, 1991 BA http://ssd.jpl.nasa.gov/sbdb.cgi?sstr=1991BA;cad=1#cad

NASA 2014 https://solarsystem.nasa.gov/news/display.cfm?News_ID=46833

Neish C. D., Barnes J. W., Sotin C., MacKenzie S., Soderblom J. M., Le Mouelic S., Kirk R. L., Stiles B. W., Malaska M. J., Le Gall A., Brown R. H., Baines K. H., Buratti B., Clark R. N. and Nicolson P. D., 2015, Spectral properties of Titan's impact craters imply chemical weathering of its surface, *Geophysical Research Letters*, 42, 3746-3754

Neukum G., Oberst J., Hoffman H., Wagner R. and Ivanov B. A. 2001, Geologic evolution and cratering history of Mercury, Planetary and Space Science, Volume 49, Issue 14-15, 1507-1521.

Newton I., Four Letters from Sir Isaac Newton to Doctor Bentley containing some arguments in proof of a Deity (London, 1756)

Nugent C. R., Margot J-L., Chesley S. R. and Vokrouhlický D., 2012, Detection of semi-major axis drifts in 54 near-Earth asteroids: new measurements of the Yarkovsky effect, arXiv:1204.5990v2 (2012).

Okamoto T., Nakamura A. and Hasegawa S., 2015, Impact experiments on highly porous targets: Cavity morphology and disruption thresholds in the strength regime, *Planetary and Space Science*, 107, 36-44

Parisi M. G. and Brunini A. 1999, Dynamical constraints to the masses of large planetesimals, *Planetary and Space Science,* 47, 607 – 617

PCA (2012) Portland Cement Association, Available from http://www.cement.org/tech/cct_floors_shrinkage.asp

Pierazzo, E., Artemieva, N., Asphaug, E., Baldwin, E.C., Cazamias, J., Coker, R., Collins, G.S., Crawford, D.A., Davison, T., Elbeshausen, D., Holsapple, K.A., Housen, K.R., Korycansky, D.G., Wuennemann, K. 2008. Validation of numerical codes for impact and explosion cratering: Impacts on strengthless and metal. Targets. Meteoritics and Planetary Science 43, 1917-1938.

Poelchau M., Kenkmann T., Thoma K., Hoerth T., Dufresne A., and Schäffer F., 2013, The MEMIN research unit: Scaling impact cratering experiments in porous sandstones, *Meteoritics & Planetary Science* 48, 8–22

Pollack J. B., Hubickyj O., Bodenheimer P. and Lassauer J. 1996, Formation of the giant planets by concurrent accretion of solids and gas, *Icarus* 124, 62 – 85.

Powers T. C., 1958, The structure and physical properties of hardened Portland cement paste, *Journal of the American Ceramics Society*, 1958.

Rafikov R. R., 2003, The growth of plantary embryos: orderly, runaway or oligarchic?, *The Astronomical Journal*, 125: 942 – 961

Ranjith P. G., Viete D. R., Chen B. J., Samintha M. and Perera A., 2011, Transformation plasticity and the effect of temperature of Hawkesbury sandstone at atmospheric pressure, *Engineering Geology,* 151 2012, 120-127.

Rankine W. J. M., 1870, On the thermodynamic theory of waves of infinite longitudinal disturbances, *Philosophical Transactions of the Royal Society of London,* 160, 277-288

Reddy V., Vokrouhlicky D., Bottke W., Pravec P., Sanchez J., Gary B., Klima R., Cloutis E., Galad A., Guan T., Hornoch K., Izawa M., Kushnirak P., Le Corre L., Mann P., Moskovitz N., Skiff B. and Vrastil J., 2015, Link between the potentially hazardous Asteroid (86039) 1999 NC43 and the Chelyabinsk meteoroid tenuous, *Icarus*, 252, 129-143

Roatsch T., Jaumann R., Stephan K. and Thomas P. C., 2009, Cartographic mapping of the icy satellites usings ISS and VIMS data, Saturn from Cassini-Huygens, 763-781, ISBN 978-1-4020-9216-9

Robertson E., 1988, Thermal properties of rocks, United States dept. of the interior geological survey, 88-441

Russell C. T., Raymond C. A., Coradini A., McSween H. Y., Zuber M. T., Nathunes A., De Sanctis M. C., Jaumann R., Konopliv A. S., Preusker F., Asmar S.W., Park R. S., Gaskell R., Keller H. U., Mottola S., Roatsch T., Scully J. E. C., Smith D. E., Tricarico P., Toplis M. J., Christensen U. R., Feldman W. C., Lawrence D. J, McCoy T. J., Prettyman T. H., Reedy R. C., Sykes M. E. and Titus T. N. 2012, Dawn at Vesta; Testing the protoplanetary paradigm, *Science* 336, 684 (2012)

Schedl A., 2015, Searching for Distal Ejecta on the Craton: The Sedimentary Effects of Meteorite Impact, *Journal of Geology*, 123, 201-232

Sevecek P., Broz M., Capek D. and Durech J., 2015, The thermal emission from boulders on (25143) Itokawa and general implications for the YORP effect, *Monthly Notices of the Royal Astronomical Society*, 450, 2104-2115

Shi J-M. and Chiang E., 2013, From dust to planetesimals: criteria for gravitational instability of small particles in gas, *The Astrophysical Journal*, 764, pp14, (2013)

Siegler M., Paige D., Williams J. P. and Bills B., 2015, Evolution of lunar polar ice stability, Icarus, 255, 78-87

Stewart G. R. and Wetherill G. W., 1989, *Icarus*, 74, 542

Stewart S. T. and Leinhardt Z. M. 2009, Velocity-dependant catastrophic disruption criteria for planetsimals, *The Astrophysical Journal* 691 L133-L137 (2009).

Steinberg E. and Sari R., 2015, Spins of large asteroids: A hint of a primordial distribution in their spin rates, *Astronomical Journal*, 4, 149

Strom R., Malhotra R., Zhi-Yong X., Ito T., Yoshida F. and Ostrach L., 2015, The inner solar system cratering record and the evolution of impactor populations, *RAA*, 15, 3, 407-434

Swedenborg E., The Principia or the First Principles of Natural Things Being New Attempts Toward a Philosophical Explanation of the Elementary World, Translated by The Rev. Augustus Clissold MA 1846

Tatischeff V., Duprat J. and de Séréville N., 2010, A runaway Wolf-Rayet star as the origin of ^{26}Al in the early solar system, *APJ* 688, 1382.

Taylor P. A., Margot J-L., Vokrouhlický D., Scheeres D. J., Pravec P., Lowry S. C., Fitzsimmons A., Nolan M. C., Ostro S. J., Benner L. A. M., Giorgini J. D. and Magri C. 2007, Spin rate of asteroid (54509) 2000 PH5 increasing due to the YORP effect, *Science* 316, 274, 2007.

Thiessen F., Besse S., Staid M. I. and Hiesinger H., 2014, Mapping lunar mare basalt units in mare imbrium as observed with the moon mineralogy mapper (M-3), *Planetary and Space Science*, 104, 244-252

Tholen D. J., 1989, Asteroid taxonomic classifications, Asteroids II, pp 1130-1150

Touboul M., Puchtel P. and Walker R., 2015, Tungsten isotopic evidence for disproportional late accretion to the Earth and Moon, *Nature*, 520, 530

Wasserburg G. J., Gallino R., Busso M., Goswansi J. and Raiteri C. M. 1995, Short-lived Nuclei in the Early Solar System: Possible AGB Sources, *APJ* 400, L101.

Weihs G. T., Leitner J. J. and Firneis M. G., 2015, Polygonal impact craters on Mercury, *Planetary and Space Science*, 111, 77-82

Williams D. R., 2005, Venus fact sheet, NASA

Williams N., Bell J., Christensen P. and Farmer J., 2015, Evidence for an explosive origin of central pit craters on Mars, *Icarus*, 252, 175-185

Woolfson M. M., 1979, Star Formation in a Galactic Cluster, *Phil. Trans, R. Soc. Lond*. A 291, 219 – 252

Woolfson M. M. FRS 1984, The evolution of rotation in the early history of the solar system, *Phil. Trans. R. Soc. Lond*. A 313, 5 – 18 (1984)

Vocadlo N. and Price G., 1993, The Gruneisen parameter – computer calculations via lattice dynamics, *Physics of the Earth and Planetary Interiors*, 82, 261-270

Vokrouhlicky D., Broz A., Bottke W., Nesvorny D., Morbidelli A., 2006, Yarkovsky/YORP chronology of asteroid families, *Icarus*, 182, 118-142

Vokrouhlicky D., Farnocchia D., Capek D., Chesley S. R., Pravec P., Scheirich P. and Mueller T. G., 2015, The Yarkovsky effect for 99942 Apophis, *Icarus*, 252, 277-283

Yang S., 2015, An experimental study on fracture coalescence characteristics of brittle sandstone specimens combined various flaws, *Geomechanics and engineering*, 8, 541-557

Yuan P., Liu H., Wang Z., 2013, An interacting crack-mechanics based model for elastoplastic damage model of rock-like materials under compression, *International journal of rock mechanics and mining sciences*, 58, 92-102

Yasui M. and Arakawa M., 2011, Impact experiments of porous gypsum-glass bead mixtures simulating parent bodies of ordinary chondrites: Implications for re-accumulation processes related to rubble-pile formation, *Icarus*, 214, 754-765

Yu Y., , Richardson D. C., Michel P., Schwartz S. R. and Ballouz R. L. 2014, Numerical predictions of surface effects during the 2029 close approach of Asteroid 99942 Apophis, *Icarus*, 242, 82-96

Zappala V., Bendjoya P., Cellino A., Farinella P. and Froeschle C., 1995, Asteroid families – search of a 12,487-asteroid sample using 2 different clustering-techniques, *Icarus*, 116, 291-314

Zellner N. E. B. and Delano J. W., 2015, Ar-40/Ar-39 ages of lunar impact glasses: Relationships among Ar diffusivity, chemical composition, shape, and size, *Geochimica et Cosmochimica Acta*, 161, 203-218

Zhang Z., Kou S., Jiang L. and Lindqvist P., 1999, Effects of loading rate on rock fracture: fracture characteristics and energy partitioning, *International journal of rock mechanics and mining sciences*, 36, 597-611

Zou C., Ngai L. and Wong Y., 2014, Experimental studies on cracking processes and failure in marble under dynamic loading, *Engineering geology*, 173, 19-31

http://www.aksteel.com/pdf/markets_products/stainless/martensitic/420_data_sheet.pdf

Rotating	Projectile	Impact Speed	Visual Inspection
190111.1	1	7.75	*
210111.1	2	5.78	*
80211.2	3	4.16	*
90211.1	3	1.916	*
90211.2	3	2.93	*
140211.1	3	0.999	*
140211.2	3	3.62	*
180211.1	3	4.07	*
250211.1	2.5	4.09	*
50411.2	1	3.07	*
80411.1	2	1.63	*
150411.2	1	1.187	*
100511.1	2	4	*
160511.1	2	4.05	*
150711.1	2	4.71	*
150711.2	2	4.62	*
220711.1	2	4.24	*
260811.1	2.5	3.46	*
200811.2	2.5	3.85	*
90911.1	2	3.46	*
90312.1	solid s	7.59	*
90312.3	2	3.86	*
220612.2	2.5	4.61	*
200712.2	3	3.81	*
240812.1	2.5	4.16	*
140912.5	2.5	4.54	*

Static	Projectile
30311.1	3
30311.2	2
140311.1	1
140311.2	2.5
210311.2	3
210311.3	3
280311.3	1
280311.4	1
290311.2	2
130511.1	2
240511.1	2
100611.1	2.5
150611.1	2
50711.1	2
90711.1	2.5
120711.1	2
300911.1	2.5
200712.1	3
200712.3	3

Impact Speed	Visual Inspection
3.81	*
4.58	*
7.5	*
3.05	*
4.36	*
1.954	*
1.124	*
3.06	*
1.731	*
3.4	*
3.87	*
3.75	*
5.03	*
4.84	*
4.57	*
4.83	*
4.44	*
3.81	*
3.79	*

Annex C – Orthogonally Averaged Crater Profiles

This section of chapter 7 data analysis is concerned with the crater profiles obtained from the MeX data. The craters were profiled using the profile analysis tool in the MeX programme but to help preserve morphological data, only two profiles were taken and then mean averaged. To aid in the level of data acquisition, the profiles were taken from corner to corner to give the largest profiles with respect to each crater (figure C1).

The crater profiles are separately selected as described above and then the data is exported into a spreadsheet. The data comprising of the two profiles lengths and depths are then mean averaged and plotted to give the orthogonal averaged single plot.

Crater profiles which are covered in this section show the ranges of temperatures able to be analysed with the MeX surface programme. The temperature ranges which include multiple impacts such as room temperature shots, are shown as one profile with each separate profile being averaged in that particular temperature range.
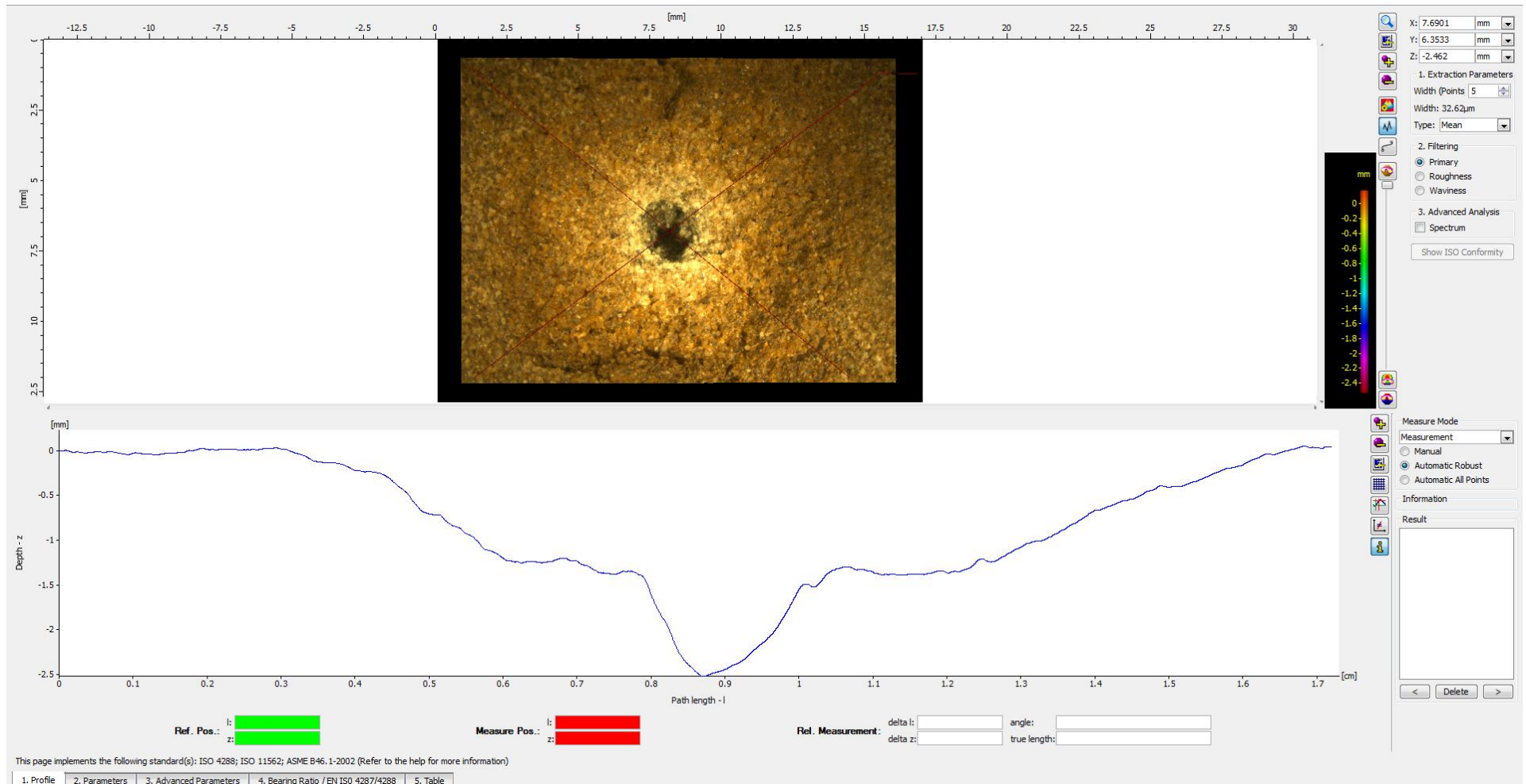
Figure C1: This screen dump shows the orthogonal profiles chosen for each crater.
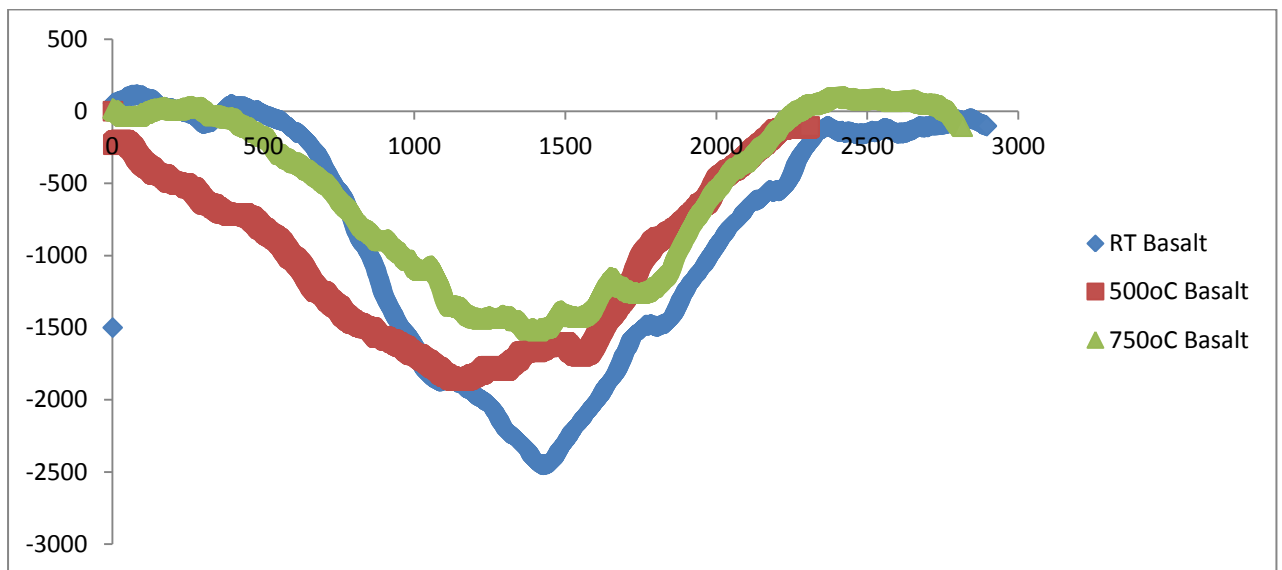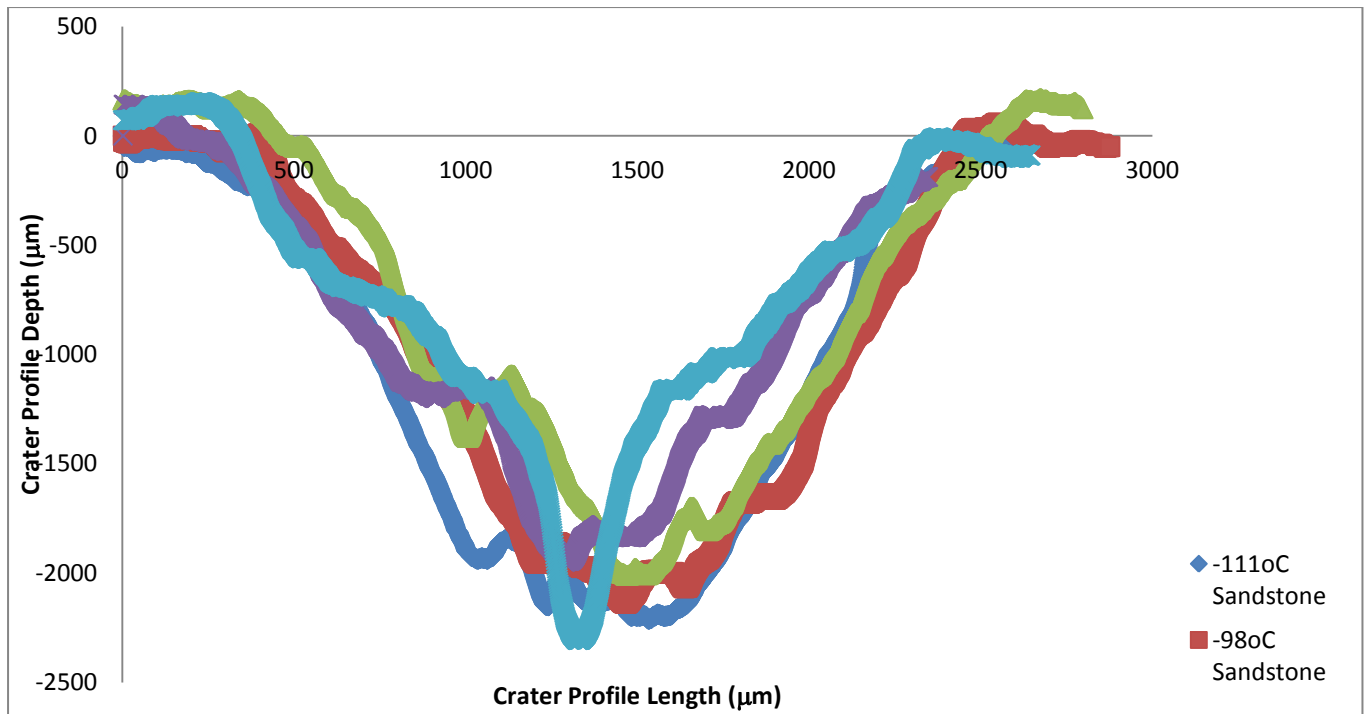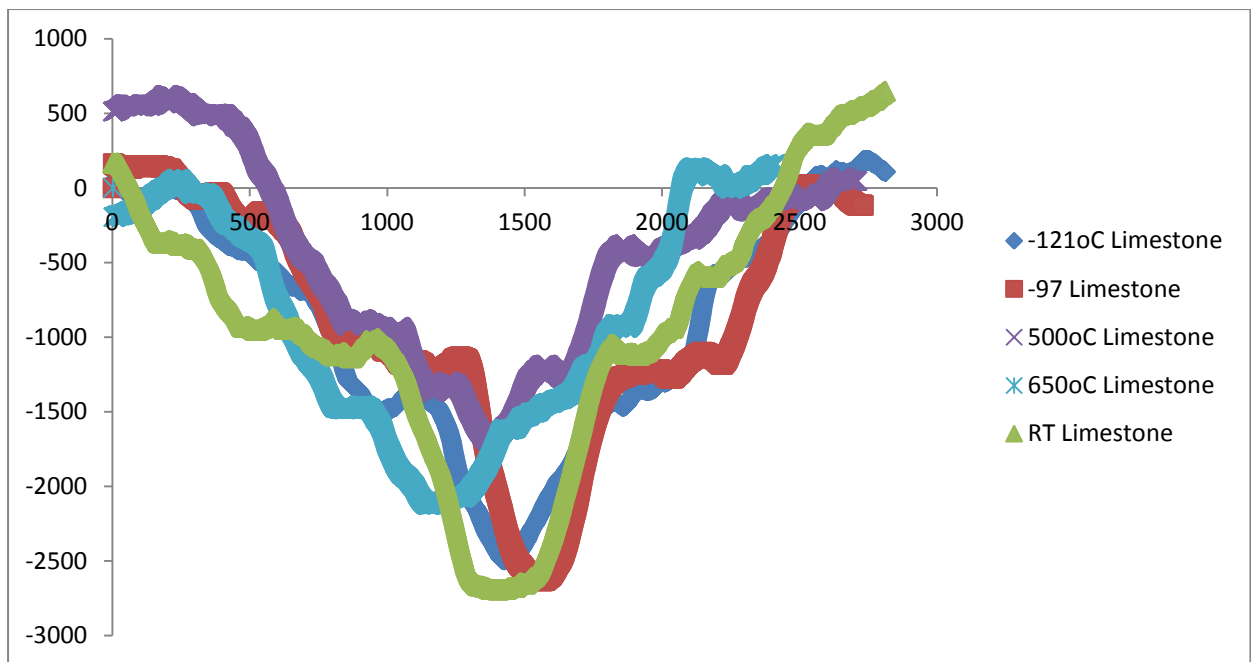
Annex　D　KDM Method Code

```python
import numpy

import pylab

import scipy

import matplotlib

import mpl_toolkits.mplot3d.axes3d as p3

import os

import sys


if (len(sys.argv) < 2):

        print 'Please supply mesh filename to process'

        sys.exit()

else:

        filename = sys.argv[1]


xs = []

ys = []

zs = []


fin = open(filename,'r')

fdata = fin.read().split('\n')
```

```python
for line in fdata:

        comp = line.split()

        if ((len(comp) >= 3) and ('{' not in line) ):

                x = float(comp[0])

                y = float(comp[1])

                z = float(comp[2])

                xs.append(x)

                ys.append(y)

                zs.append(z)


#xs, ys, zs = zip(*[ [x,y,z] for x,y,z in zip(xs,ys,zs) if z != -0.005960 ])




## make lin data into mesh


print 'Creating Mesh'


x_res = numpy.shape(numpy.unique(xs))[0]

y_res = numpy.shape(numpy.unique(ys))[0]


print 'x grid', x_res

print 'y grid', y_res

print 'total square', x_res * y_res
```

```python
print 'total square', numpy.shape(zs)


xs = numpy.reshape(xs,(y_res,x_res))

ys = numpy.reshape(ys,(y_res,x_res))

zs = numpy.reshape(zs,(y_res,x_res))



## Trim null edge data


print 'Trimming Mesh'


baseval = zs[0,0]


low_x = -1

high_x = -1

low_y = -1

high_y = -1


for i in range(len(zs[y_res/2,:])):

        value = zs[y_res/2,i]

        if (low_x == -1 and value > baseval):

                low_x = i

        if (low_x != -1 and high_x == -1 and value == baseval):
```

```
        high_x = i


for i in range(len(zs[:,x_res/2])):

        value = zs[i,x_res/2]

        if (low_y == -1 and value > baseval):

                low_y = i

        if (low_y != -1 and high_y == -1 and value == baseval):

                high_y = i


low_y += 1

high_y -= 1

low_x += 1

high_x -= 1

print 'xs, ', low_x, high_x, 'ys, ', low_y, high_y

interval = 1

xs = xs[low_y:high_y:interval,low_x:high_x:interval]

ys = ys[low_y:high_y:interval,low_x:high_x:interval]

zs = zs[low_y:high_y:interval,low_x:high_x:interval]
```

Correcting gradient

```python
print 'Slope Correction (x-axis)'

x_low_z = numpy.mean(zs[::,0])

x_high_z = numpy.mean(zs[::,-1])

z_diff_x = x_high_z - x_low_z

x_diff = xs[0,-1] - xs[0,0]

diff = z_diff_x / x_diff

zs = zs - xs * diff

zs -= numpy.max(zs)


## Stats
arg_min = numpy.unravel_index(numpy.argmin(zs), dims=numpy.shape(xs))

#print arg_min


min_z = numpy.min(zs)

max_z = numpy.max(zs)

med_z = numpy.median(zs)

depth_z = max_z-min_z

print 'min z', min_z

print 'max z', max_z

print 'median z', med_z

print 'z depth', depth_z


print 'minima position', xs[arg_min], ',', ys[arg_min]
```

```python
## Centroid

circ_height = -depth_z*0.3333

circ_width = depth_z*0.001


cxs,cys = zip(*[ [x,y] for x,y,z in zip(xs.flatten(),ys.flatten(),zs.flatten()) if abs(z-circ_height)
< circ_width ])


cx = numpy.mean([numpy.mean(cxs),xs[arg_min]])

cy = numpy.mean([numpy.mean(cys),ys[arg_min]])


pylab.plot(cxs,cys,'k.')

myax = pylab.gca()

myax.set_aspect('equal')

pylab.scatter(cx,cy)

pylab.show()

## Plot Mesh

print 'Plotting Mesh'

interval = 10

fig = pylab.figure()

ax = p3.Axes3D(fig)
```

```python
ax.plot_surface(xs[::interval,::interval],ys[::interval,::interval],zs[::interval,::interval],rstride=
2,cstride=2,cmap=matplotlib.cm.coolwarm)

ax.plot3D([cx,cx,cx],[cy,cy,cy],[0,-depth_z*0.5,-depth_z],'k',lw=5)


ax.set_xlabel('x')

ax.set_ylabel('y')


pylab.show()

cxs = numpy.mgrid[cx-0.05*numpy.max(xs):cx+0.05*numpy.max(xs):11j]

cys = numpy.mgrid[cy-0.05*numpy.max(ys):cy+0.05*numpy.max(ys):11j]

measures = numpy.zeros((11,11),dtype=float)

best_measure = 100.

for j,cxi in enumerate(cxs):

        print cxi

        for k,cyi in enumerate(cys):


#xs -= cx#0.0085#xs[arg_min]

#ys -= cy#0.006#ys[arg_min]

                rs = numpy.sqrt((xs - cxi)**2 + (ys - cyi)**2)


                zs_r = zs.flatten()

                rs_r = rs.flatten()
```

```python
res = 100

mybins = numpy.arange(0,numpy.max(rs_r),numpy.max(rs_r)/float(res))


indices = numpy.digitize(rs_r,mybins)

radii = []#mybins + 0.5 * numpy.max(rs_r)/float(res)

medians = []

stds = []


for i in sorted(numpy.unique(indices)):

        radius = numpy.mean(rs_r[indices==i])

        median = numpy.median(zs_r[indices==i])

        std = numpy.std(zs_r[indices==i])

        radii.append(radius)

        medians.append(median)

        stds.append(std)
#       print numpy.array(sorted(rs_r[indices==i]))

medians = numpy.array(medians)

stds = numpy.array(stds)

radii = numpy.array(radii)

measure = numpy.sum(stds/numpy.sqrt(radii))

measures[j,k] = measure

if (measure < best_measure):

        print cxi, cyi
```

```python
                    best_measure = measure

                    cx = cxi

                    cy = cyi

                    keep_radii = radii

                    keep_medians = medians

                    keep_stds = stds

rs = numpy.sqrt((xs - cx)**2 + (ys - cy)**2)

zs_r = zs.flatten()

rs_r = rs.flatten()

pylab.plot(rs_r, zs_r,'k.')


pylab.plot(keep_radii,keep_medians)

pylab.plot(keep_radii,keep_medians-keep_stds)

pylab.plot(keep_radii,keep_medians+keep_stds)

pylab.show()


pylab.imshow(measures)

pylab.show()


fout = open(filename.replace('.txt','.dat'),'w')

for r, m, s in zip(keep_radii,keep_medians,keep_stds):

        fout.write('%f %f %f\n'%(r,m,s))
```

```
fout.close()


#myhist,        myedges        =        numpy.histogram(particles['z'],bins=numpy.arange(-
spacial_extent,spacial_extent,spacial_extent/res))

#            myhist2,                        myedges                        =
numpy.histogram(particles['z'],weights=particles['den'],bins=numpy.arange(-
spacial_extent,spacial_extent,spacial_extent/res))

#            pylab.plot(myedges[:-
1]+spacial_extent/res,myhist2/myhist,color=dir_colours[dirindex],label=labelname)#dir_colo
urs[dirindex]
```

Annex   E   KDM Method Results

Below are a series of plots obtained from the KDM method

Basalt 195.8 K
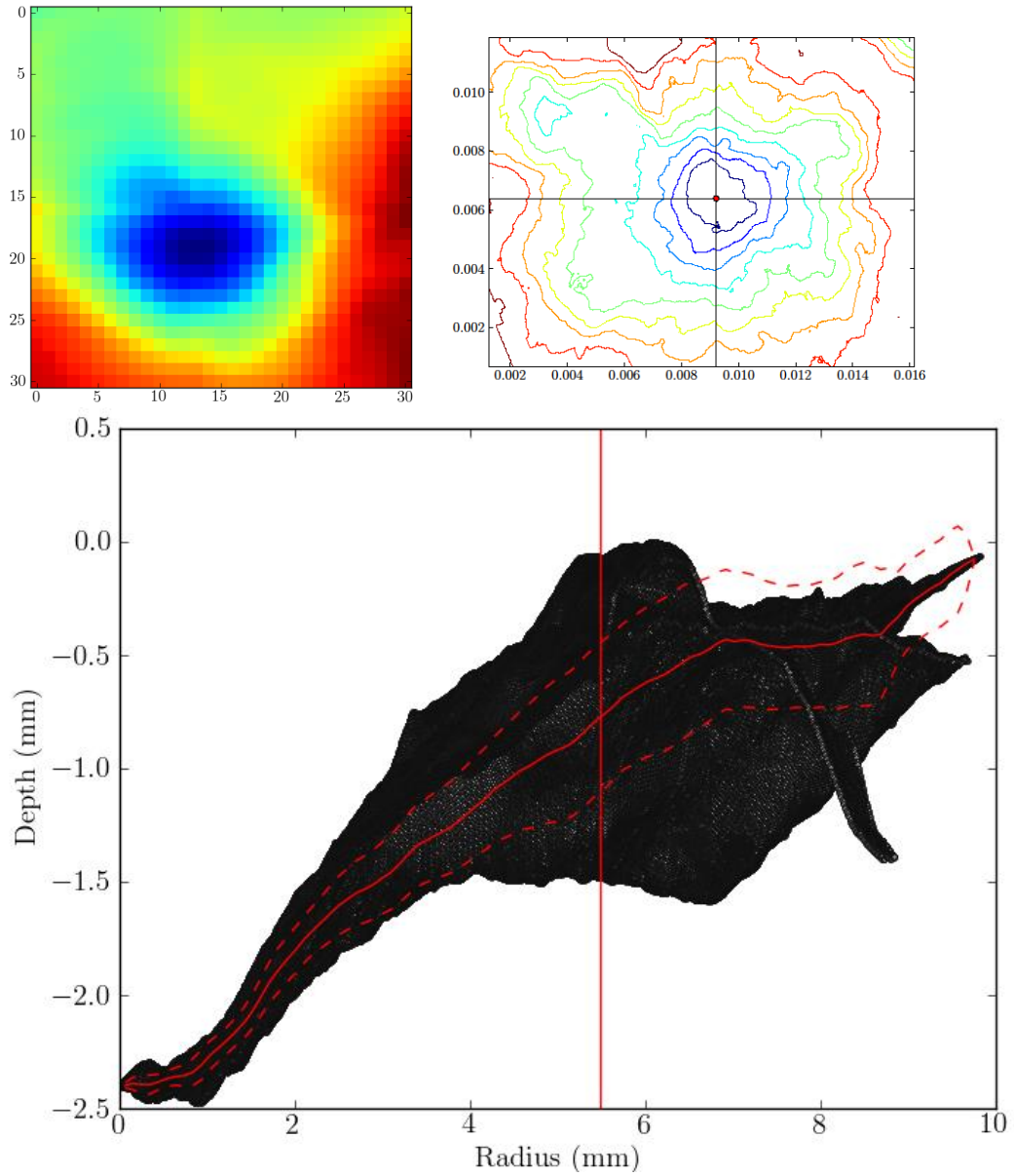
The upper right diagram shows the averaged contour positions used by centroid on a 'best-guess' basis. The method assigns weight to contours in the crater at half depth. The colours in the plot are associated with varying levels of height in the crater with red being the highest and the darkest blue being the lowest positions.

The top left diagram shows the contours found from the KDM method during the centralisation of the centroid after the 'best-guess' stage as mentioned before. Once the 'best-guess' stage has found the area it thinks is the lowest position, the centroid will then be placed at the lowest section which provides the method with the best level of symmetry from the mean values of height from the lowest points. Once the lowest point is found, the KDM programme then sweeps the whole internal section of the crater and averaging the heights through a median approach which is shown in the lower diagram.

The lowest position found from the centroid is displayed at the lowest left section of the whole data diagram. The black section to the plot gives the total cross-sections from the crater thereby producing a highest and lowest profile distribution with all corresponding cross-sections from the crater in between.

The vertical red line details the radius at which the data is completely 100% enclosed by the MeX window. It is important to display this as some craters were elongated from the lowest mean position and the crater was dissected by the MeX programme's photo window size. This could mean that the crater itself shows the whole crater radius except for the top for example. The red vertical line shows that the data from 0 radius up to the line is 100% crater image and the data after the line details the crater with excluded sections.

The red lines which are aligned with the full data background show the best median averaged total crater profile with dashed standard deviation markers.

Each KDM crater profile will now be discussed with the images following.

Basalt 195.8 K

In the case of the cold basalt held shot at a temperature of 195.8 K, the centre position was found very accurately but the total data gives a strange outcome resulting from one of the edges of the crater being cut-off by the MeX programme.

The crater profile is thin to begin with (at radius = 0) which shows little height variation but broadens out further into the spallation zones (radius > ~3 mm).

Basalt 293 K

This crater shows the effect from the averaging of the profiles. From the initial radius, both lower and upper crater profiles show a small incline leading to a lipped drop or a crater floor peak (radius = ~ 1mm) but the averaged median line shows only a small variation in morphological comparison. The data then shows another increase from the first lip to a terraced wall section (radius = ~3mm) but the corresponding median line shows very little effect from the upper and lower boundaries. One other consideration which occurs after the 100% line is the appearance further terracing resulting in the median line showing a crater wall hummock. Because the hummock is present in the median, it means that the hummocky feature is an extensive wall terrace which covers a significant section of the crater.

Basalt 722K

The best guess window shows the contours from this crater to be elongated with the presence of a crater floor peak. Likewise with the previous example, the crater floor peak is shown in the initial radii of the full profile but the averaging of the profiles smoothed this out. This crater was too big for the MeX programme photo window which is shown by the positioning of the 100% line occurring approximately at 3 mm. One other aspect to notice, is that this profile shows the largest range in crater heights.

Basalt 898.8 K

This crater shows the median average line to be steeper than the other basalt average lines with the presence once again of crater floor peaks. However, the lower standard deviation after the peaks and terracing shows a drop away from the median position due to the effects from the full profile.

Basalt 1138.16 K

The hottest KDM sample shows similar effects to the previous cases given in this section of basalt craters.

Basalt 293 K
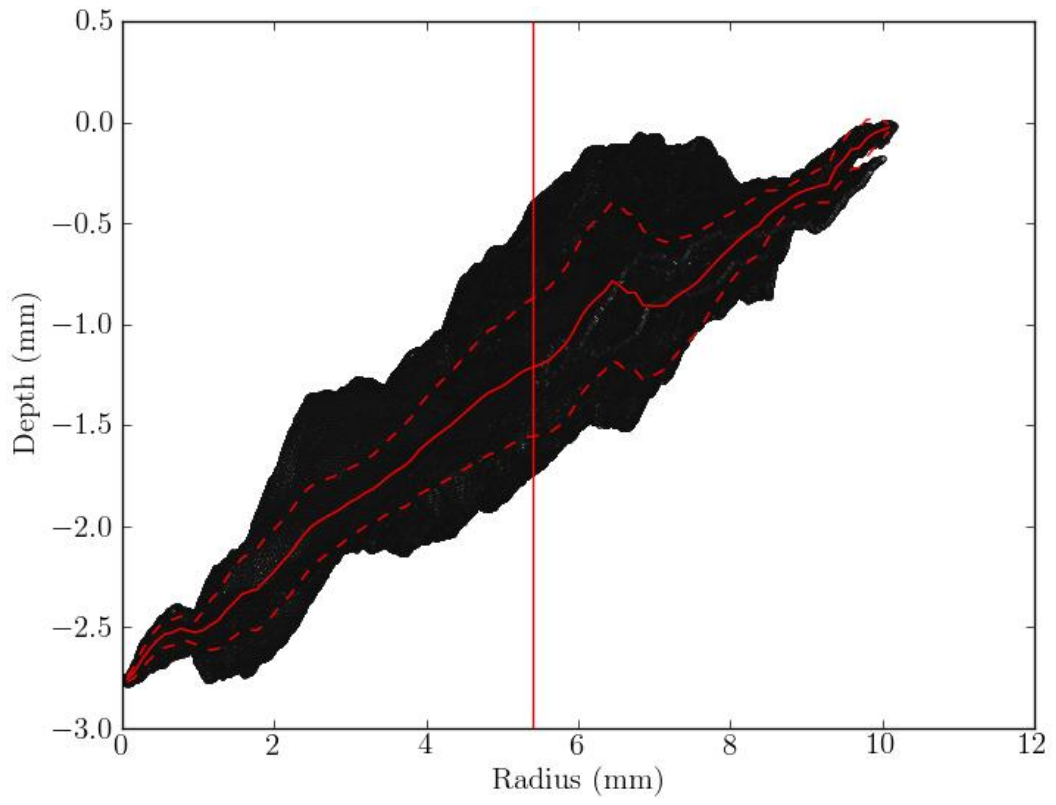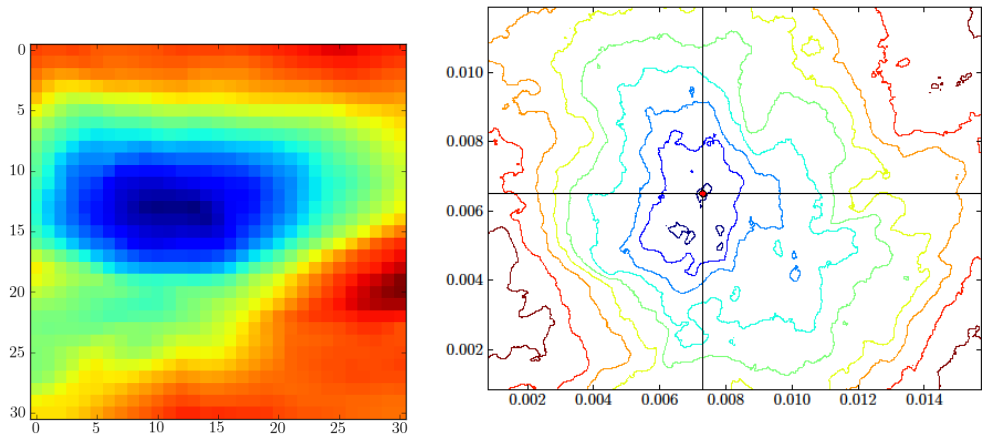
Basalt 722K
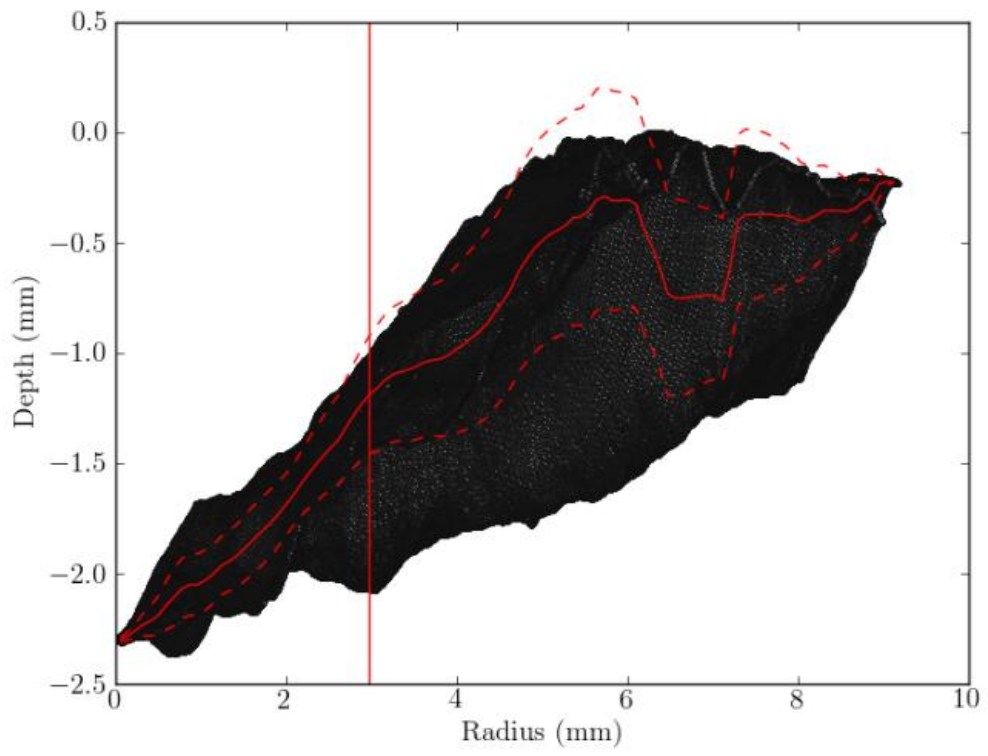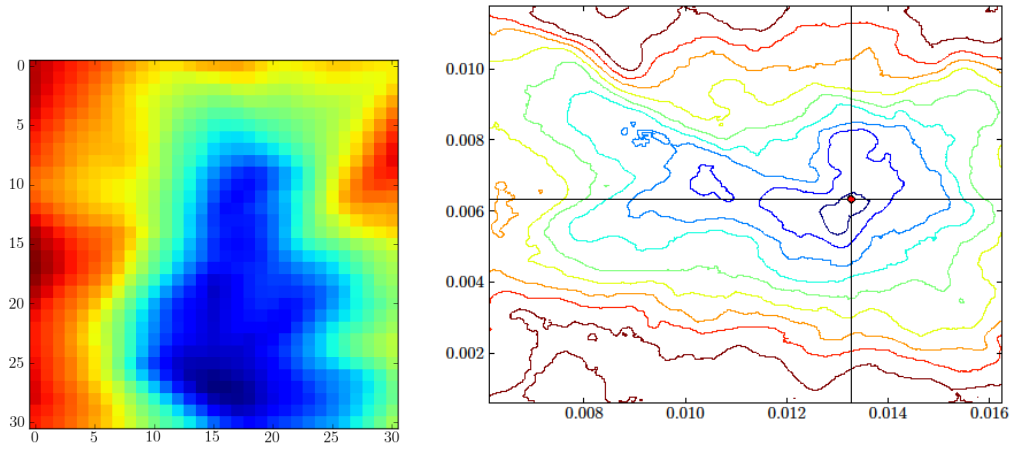
Basalt 898.8 K
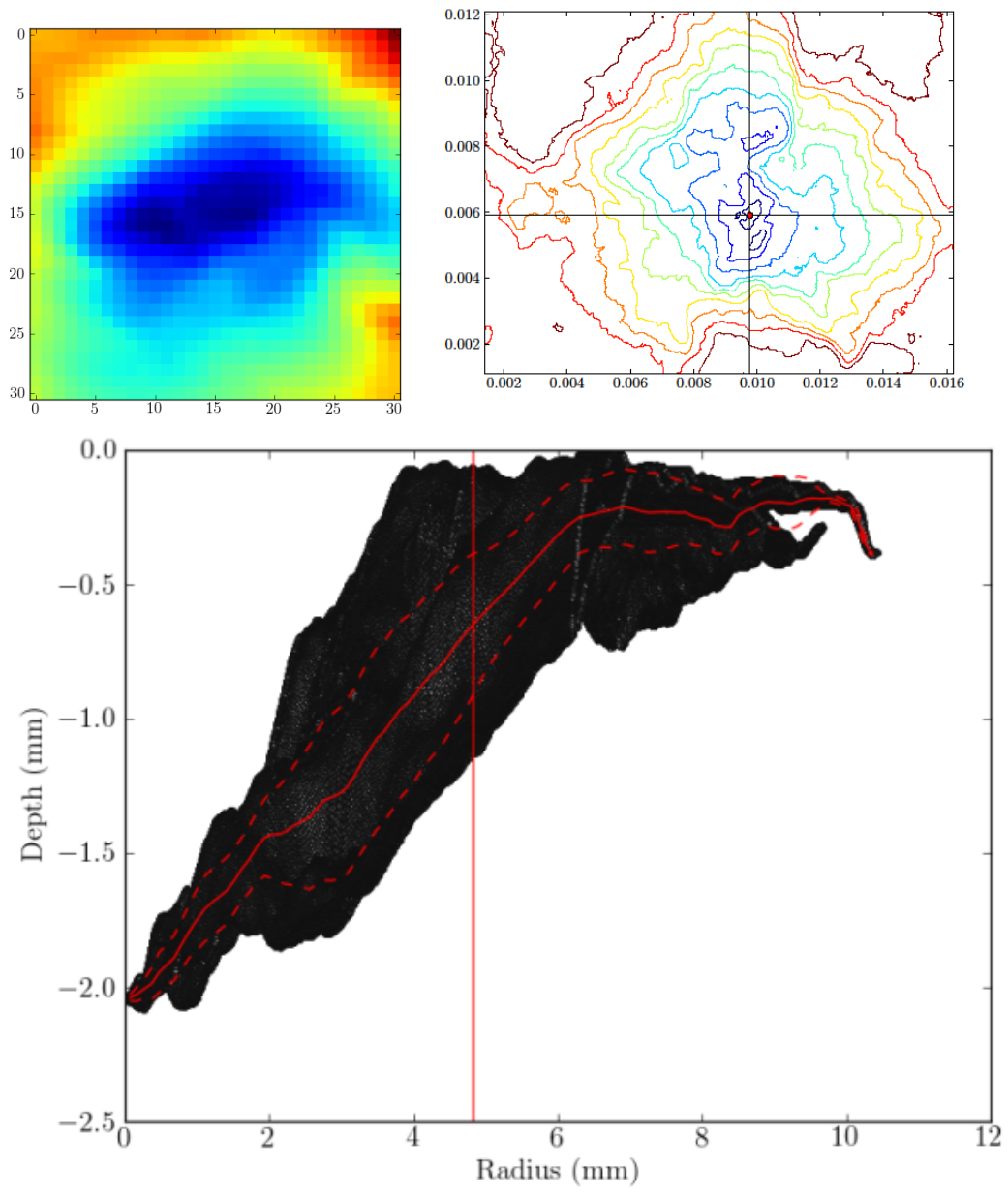
Basalt 1138.16 K
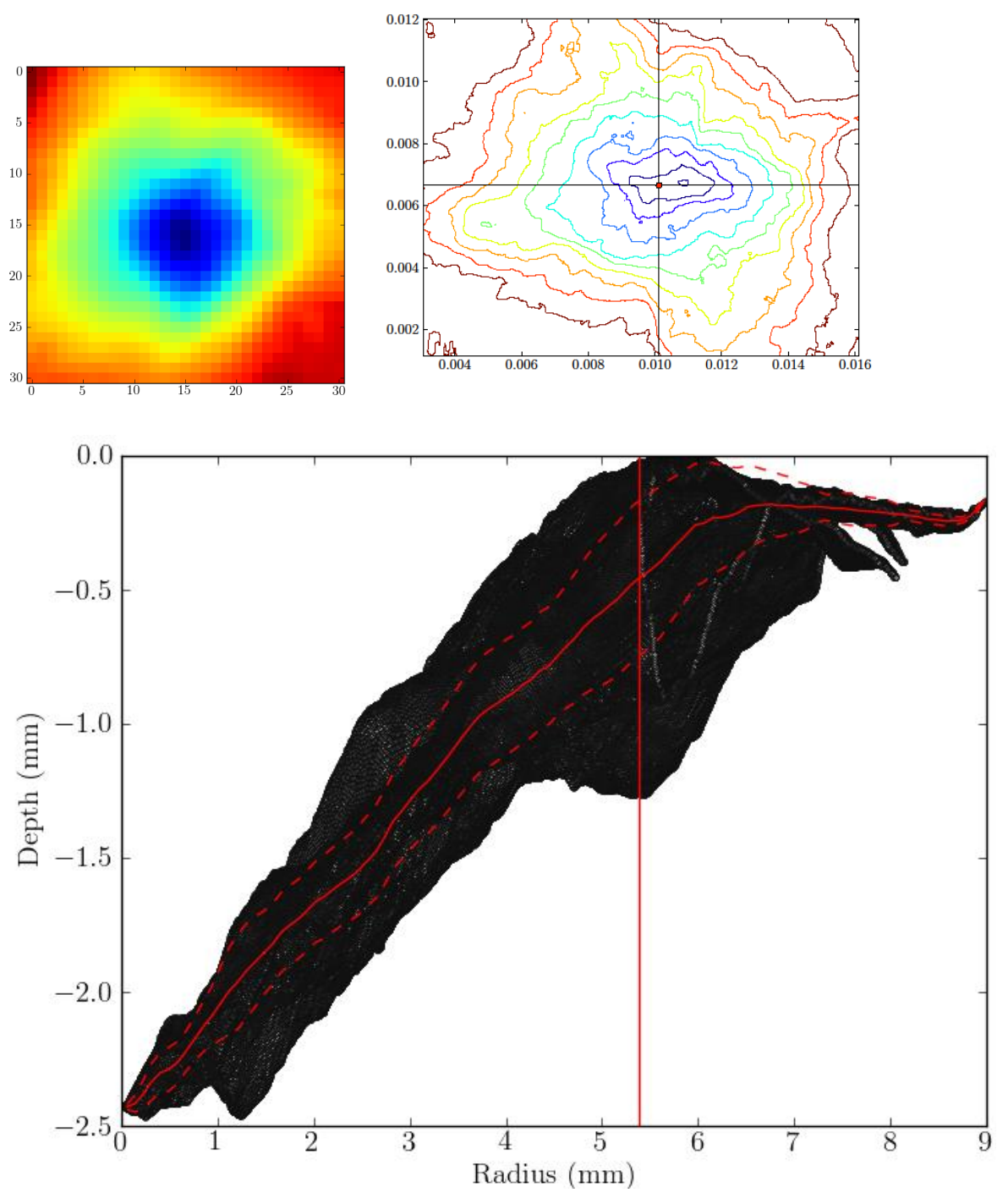
Basalt Trends
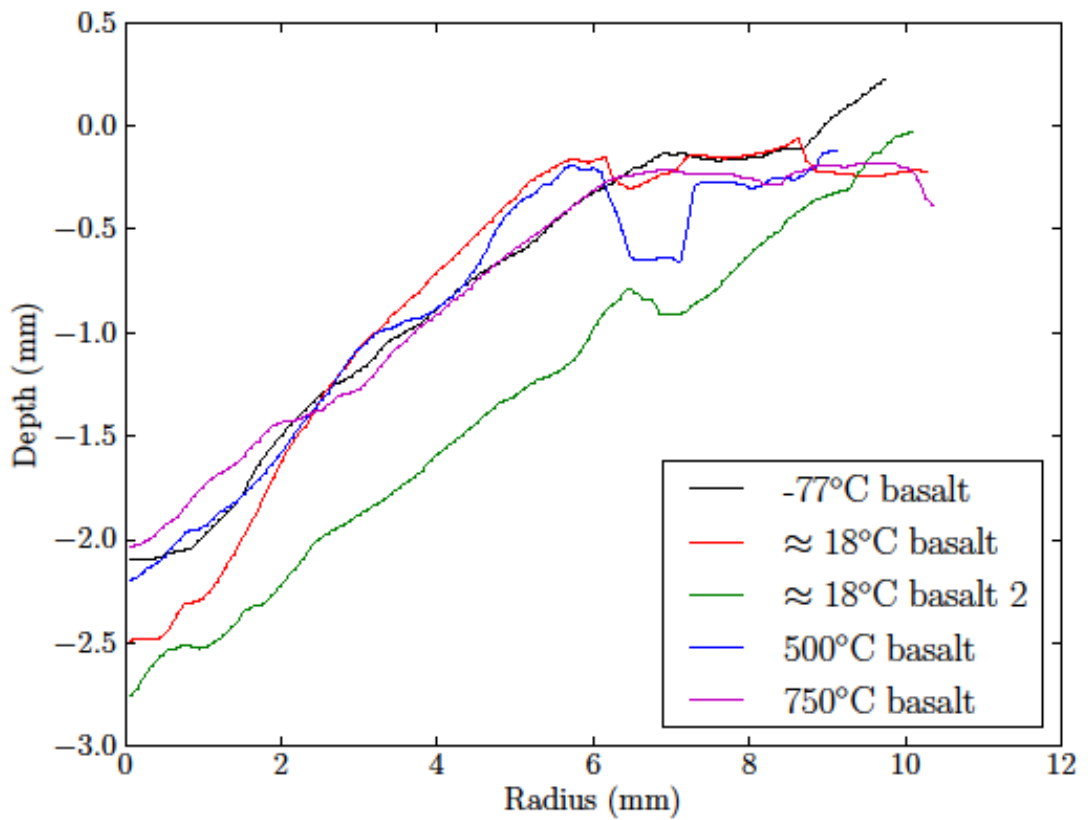
The general average trends from the basalt data given above show no real effect from temperature onto the cratering morphology of the basalt samples. However it must be stressed that the trends given are averaged therefore shows smoothed trends in relation to temperature.

Limestone 151.9 K

One common aspect presented from the KDM profiles for the limestone samples is the formation of the initial excavation zone. The initial trendline starts from the central position and increases quickly in gradient to the spallation zone. This effect is more prominent with the 176 and 773 K craters.

This crater is well centralised with the full profiles increasing in range at approximately 4 to 8 mm radius.

Limestone 176.3 K

The full profile data shows this crater to have the least amount of profile range but the most prominent initial excavation zone.

Limestone 773 K

Once again approximately situated near radius = 4 mm the data spreads to the largest profile range, however, at the furthest regions in the full profiles, the data splits between two branches. This is due to the MeX photo window cutting off some of the craters (apparent by the free space in between both branches). It can be assumed that one edge of the crater rim was not included (shown in the upper right best guess window) and affected the overall trend at the edge of the crater. Therefore the trend experience more weight from the lower branch of the full profile.

Limestone 923 K

Represented with this crater is the widest range of profiles with the least initial excavation zone present.

Limestone 151.9 K
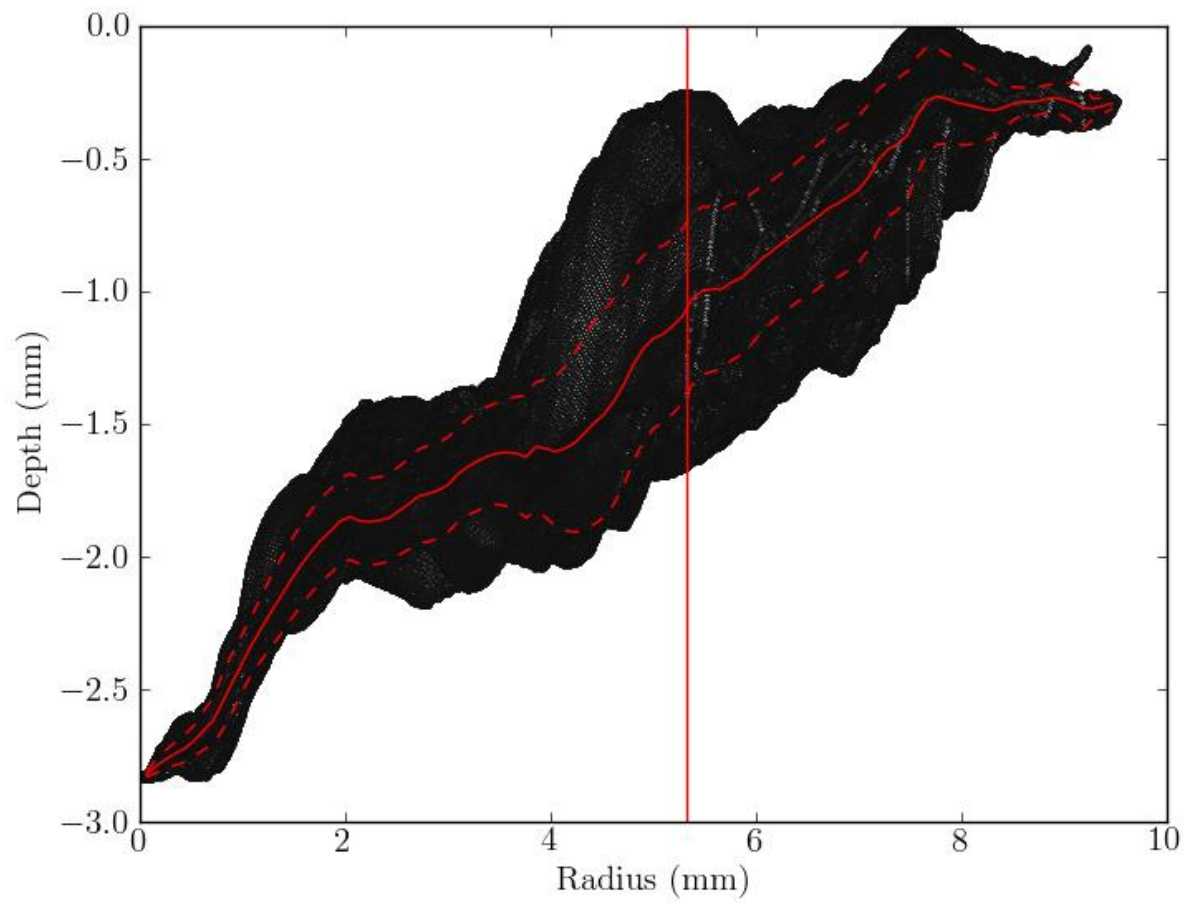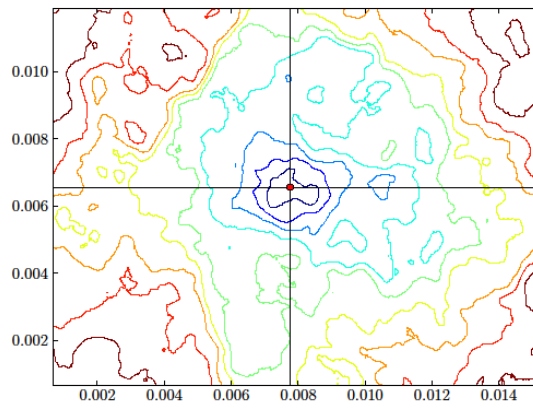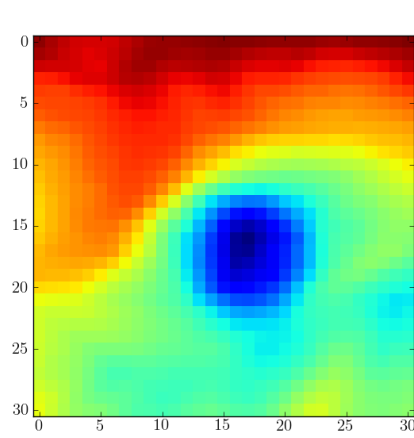
Limestone 176.3 K
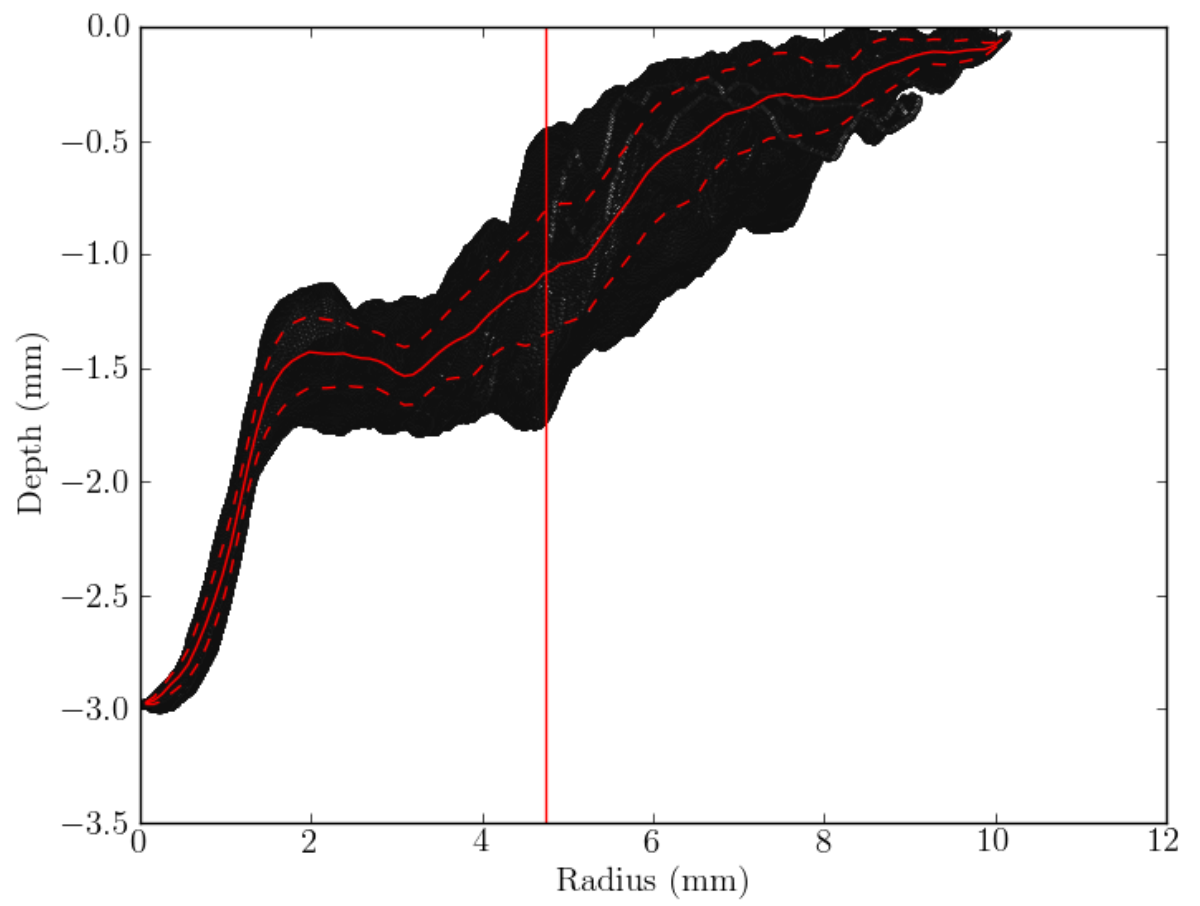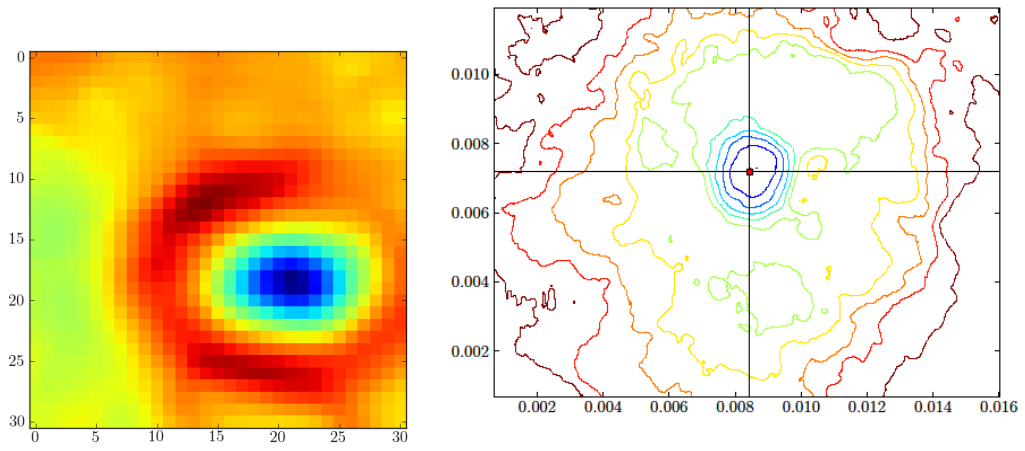
Limestone 773 K
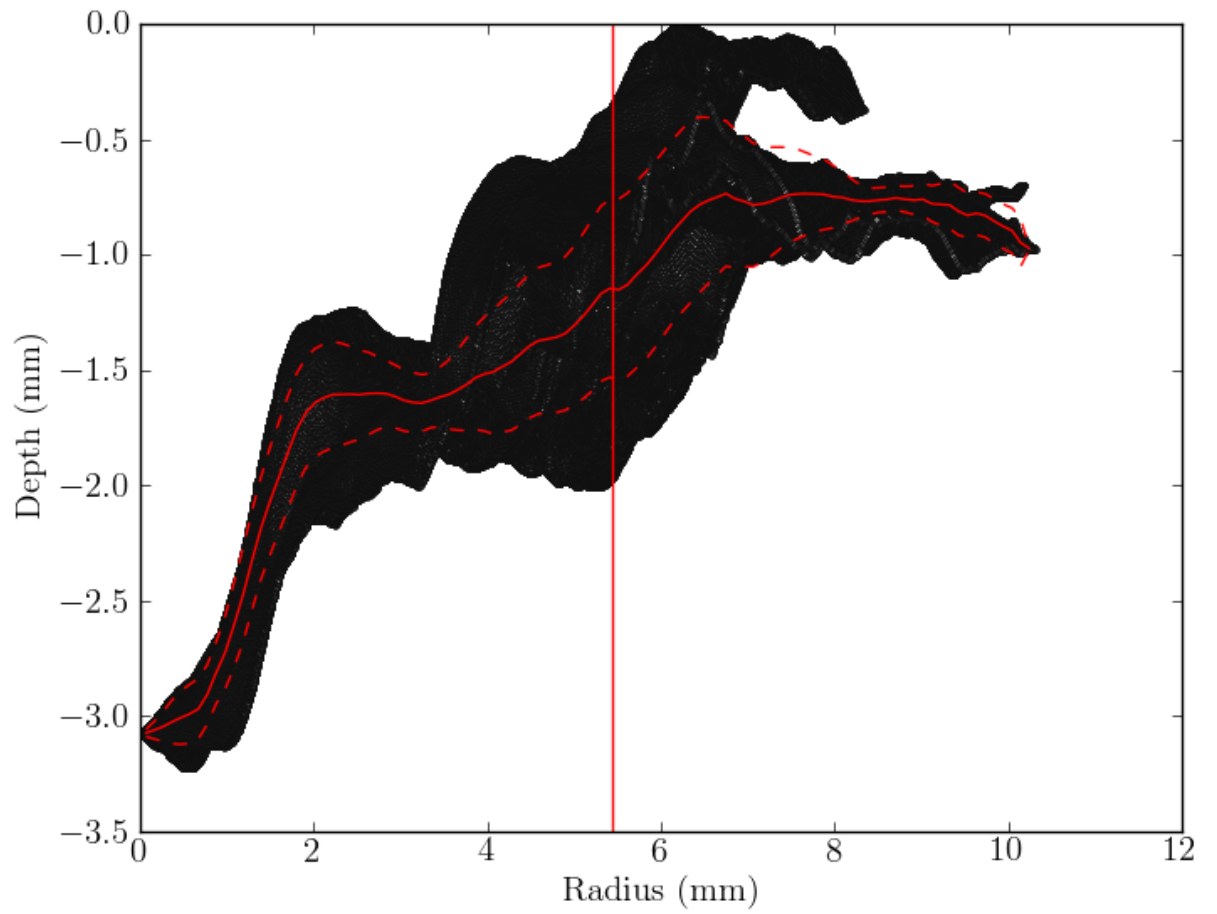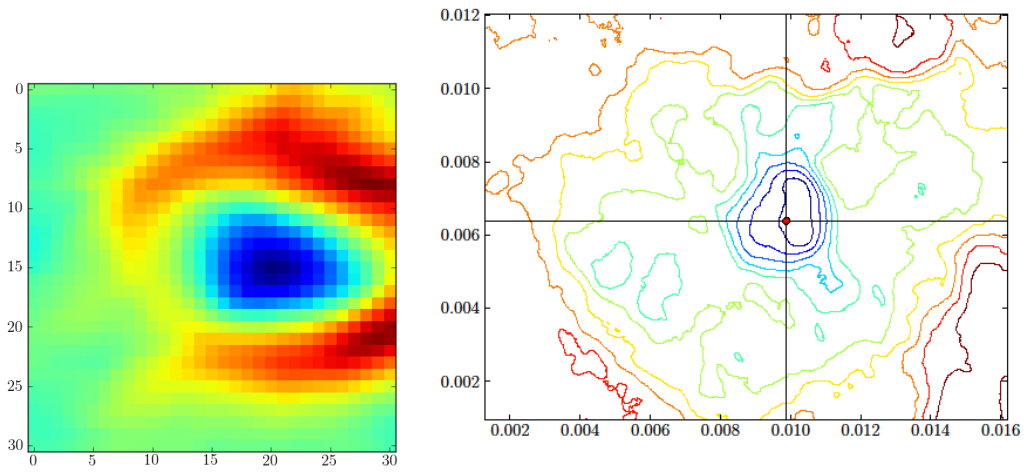
Limestone 923 K
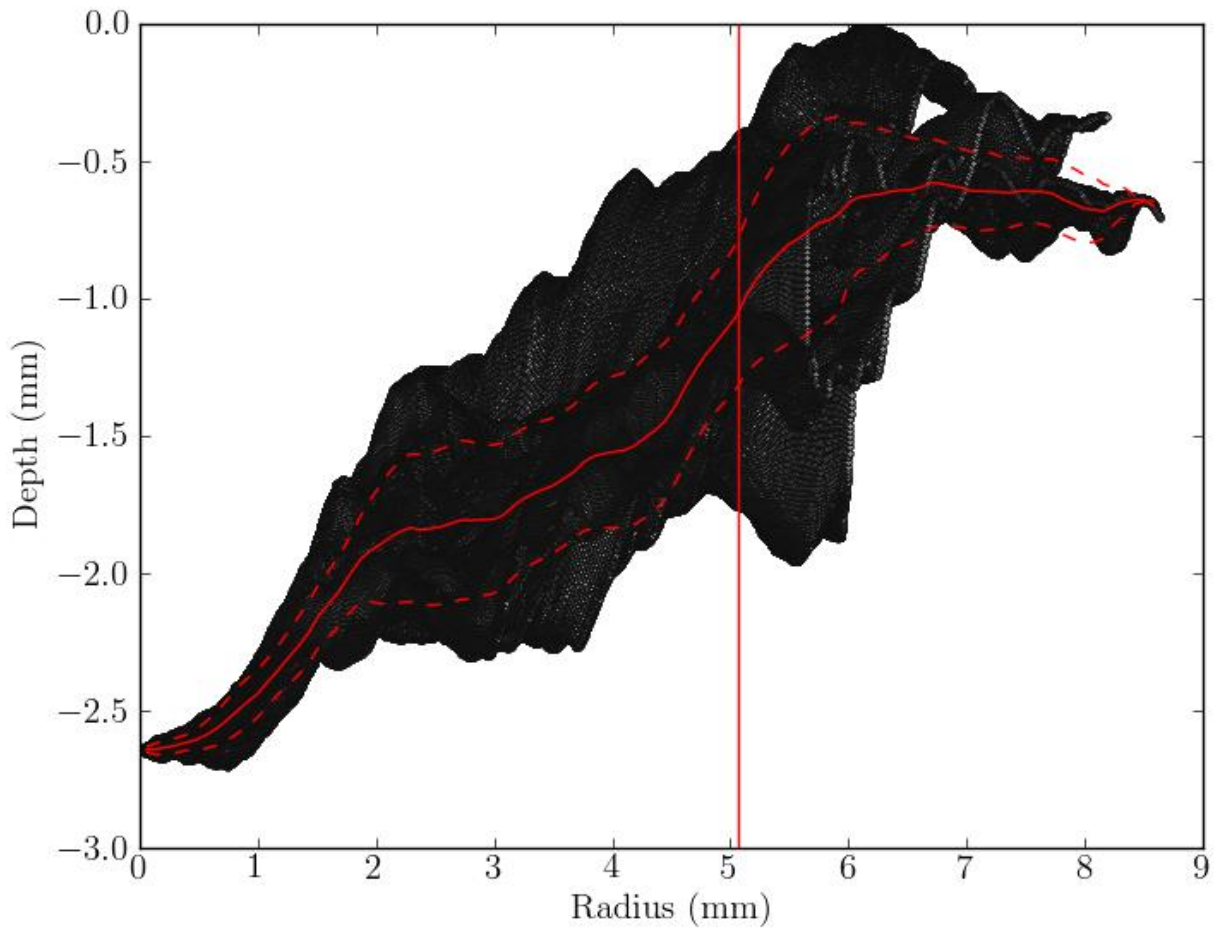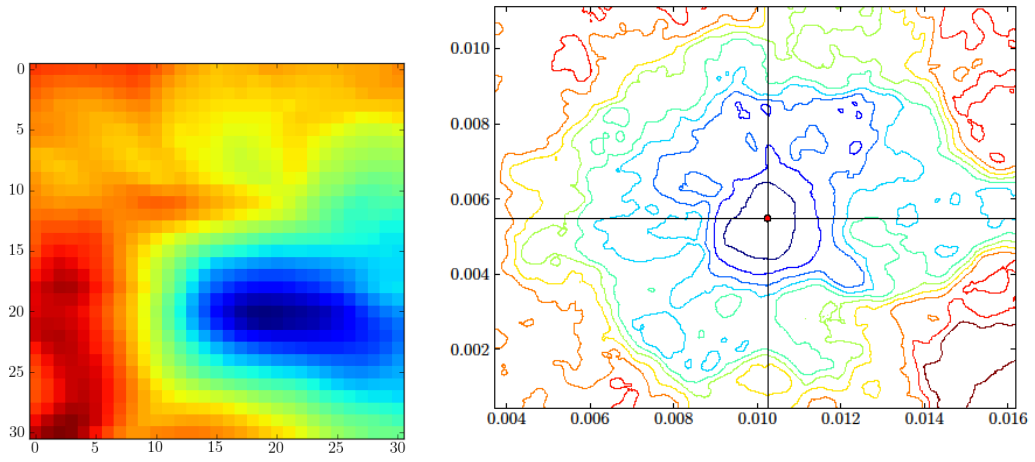
Limestone Trends
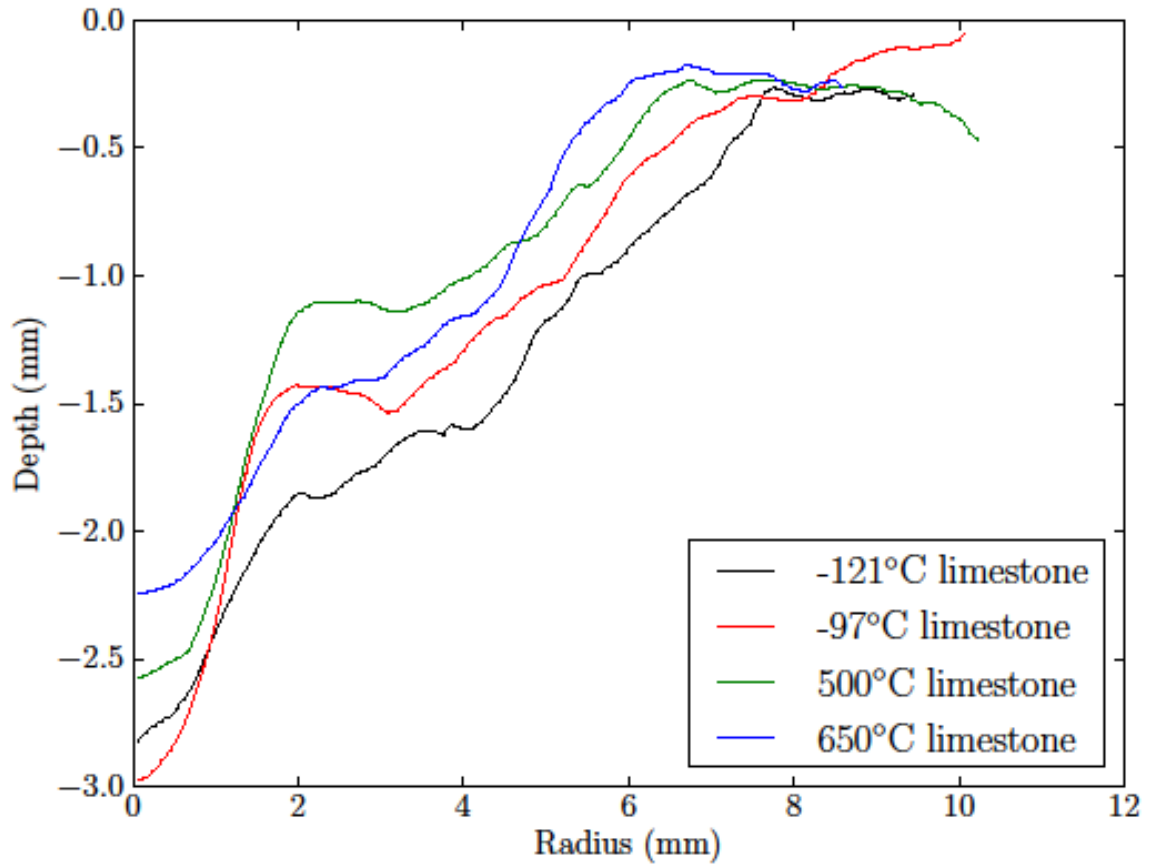
The most prominent effect from the variance of temperature with respect to the limestone samples shown above in the averaged collected data is the initial excavation zone gradients.

With the exception of the red average trendline, the general effect is that the hotter the limestone, the shallower the initial excavation zone. However due to positioning of the profiles and the increase on initial excavation depth in between -97 and 500oC, the initial excavation zones do show a maximum in that temperature region. As is show in the limestone crater data, one possible maximum occurs around 450K.

Sandstone 161 K

The crater floor peak shown in this data set did affect the centralisation of the centroid. The lowest position for the crater occurs around ~ 1mm from the designated position given in the bottom plot. This is common throughout the sandstone craters where crater floor peaks are prominent. This crater also shows a small amount in the profile variance range.

Sandstone 175.16 K

The centre of this crater was relatively complex and is shown in the variance of the full profile just after the start of the average trendline. The remainder of the profile is similar to the 161 K case.

Sandstone 292.16 K

This profile shows a very large crater floor peak at approximately 2 mm position. After the large peak, the full profile pinches and then expands to a wider range of height levels.

Sandstone 793.16 K and Sandstone 1003.16 K

Both craters were included in the explanation because of the shared appearance of the initial excavation zone. In both cases, the initial excavation zones show properties very close to the limestone cases with prominent gradients leading to the spallation zones afterwards.

Sandstone 161 K
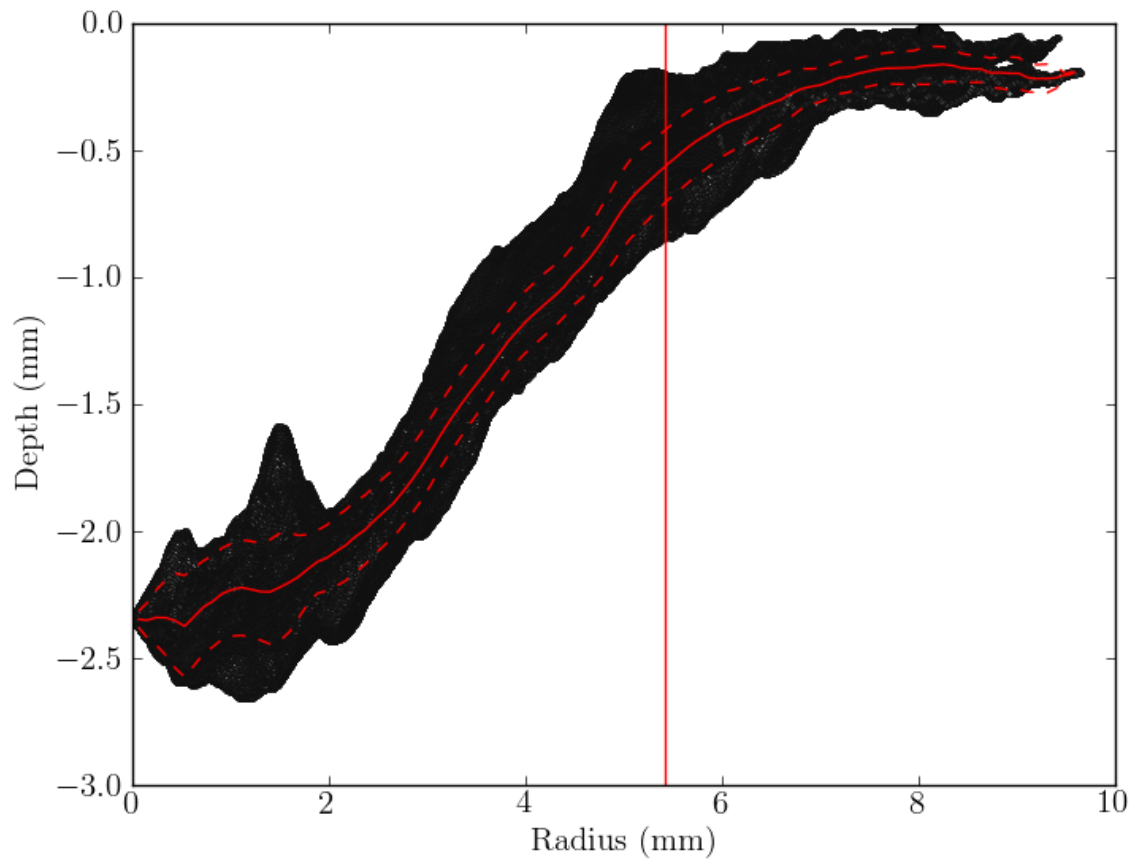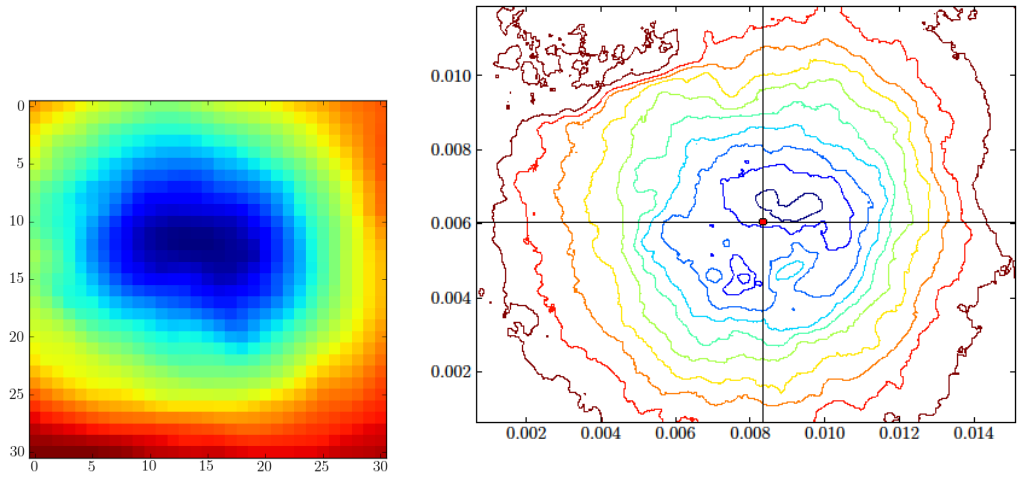
Sandstone 175.16 K
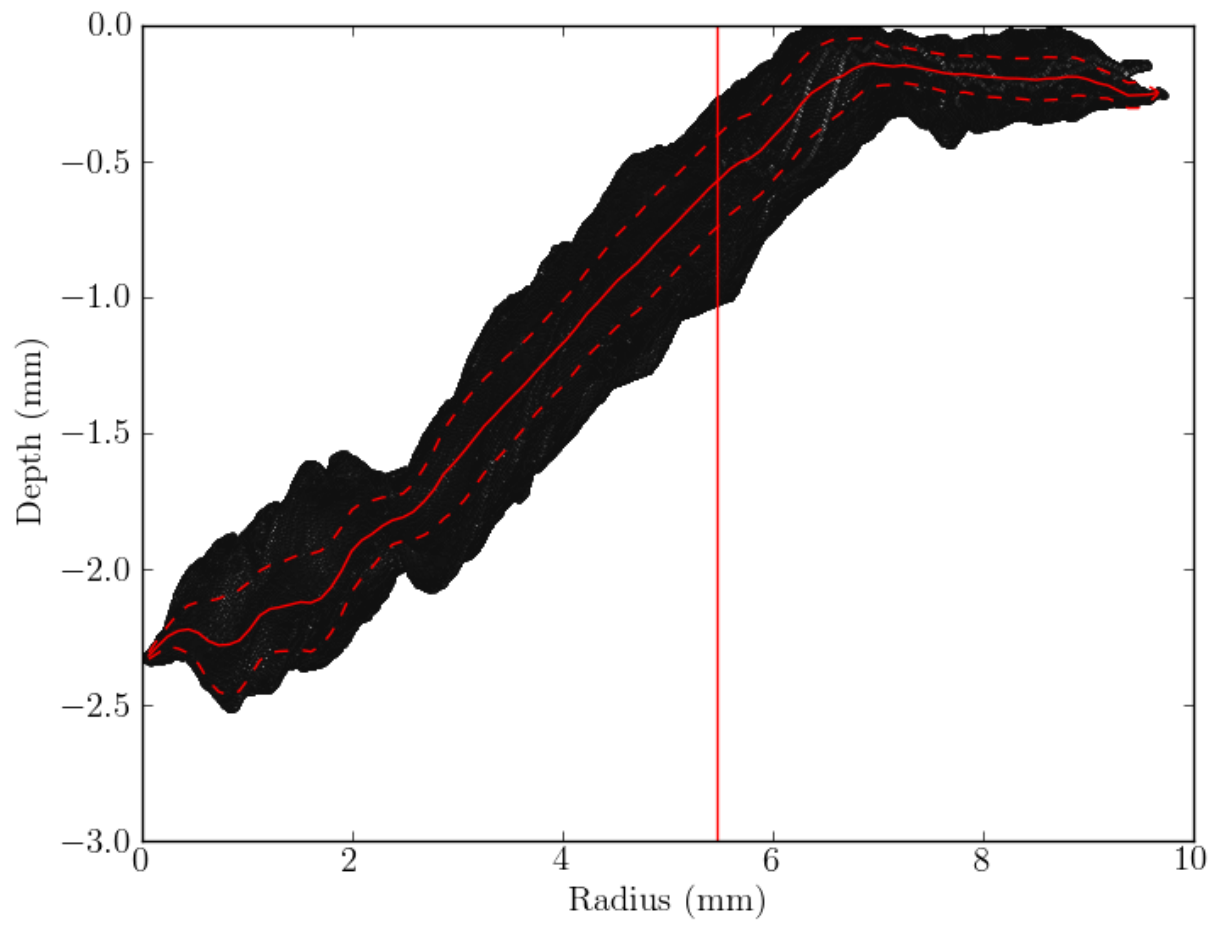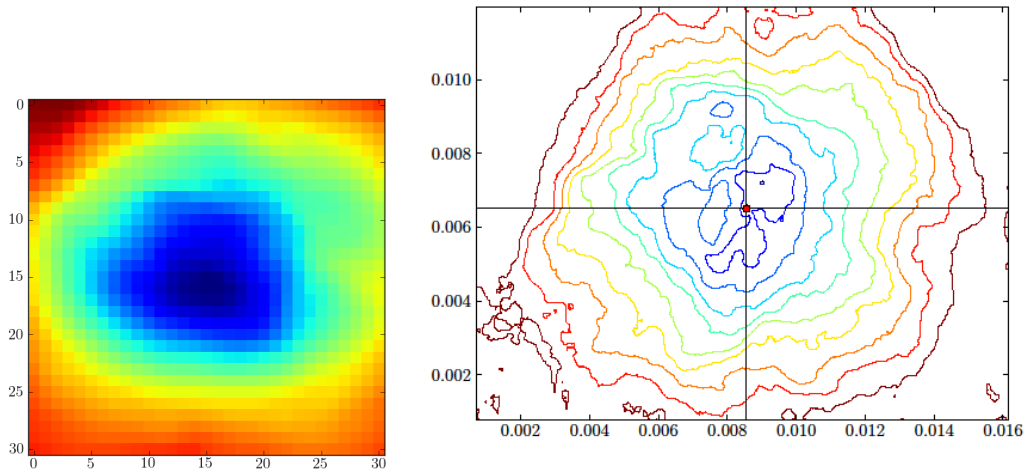
Sandstone 292.16 K
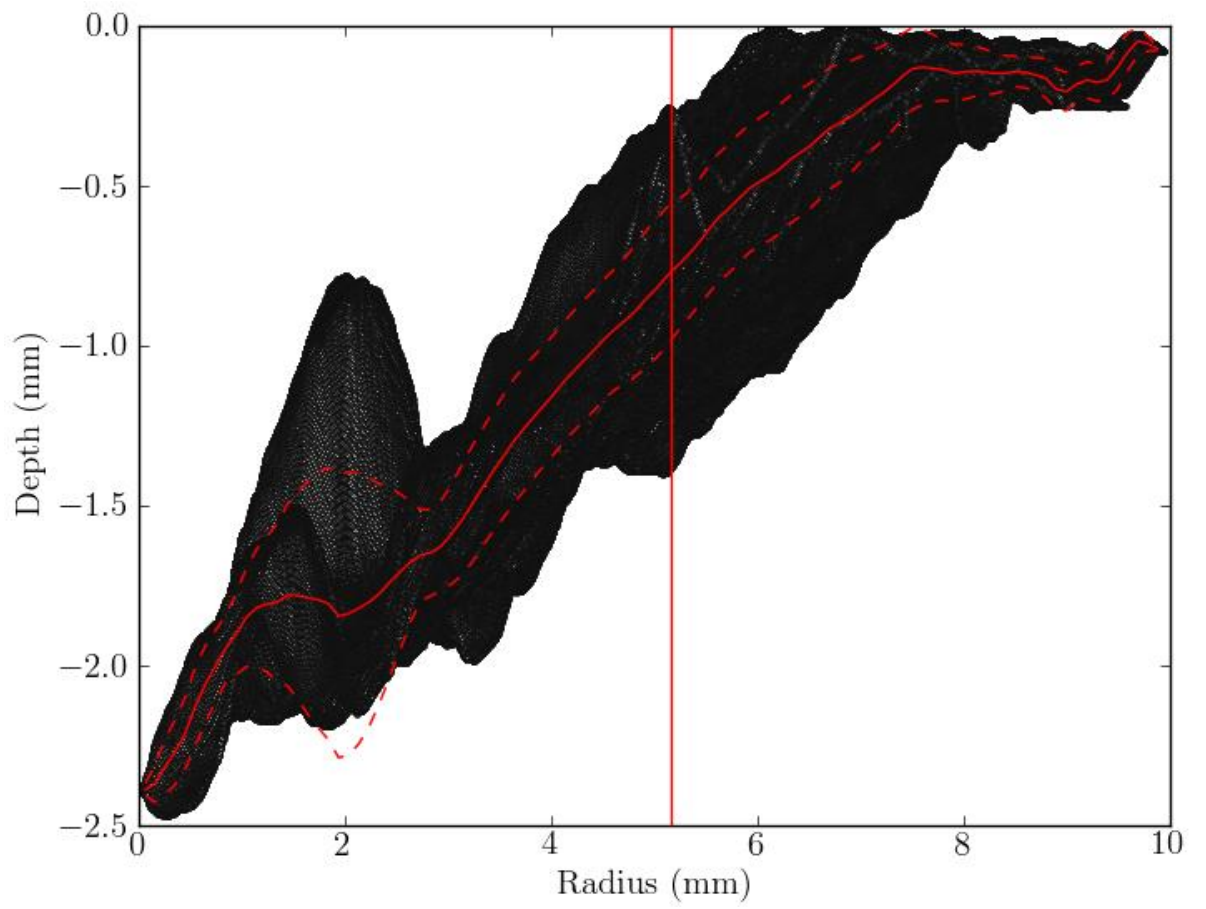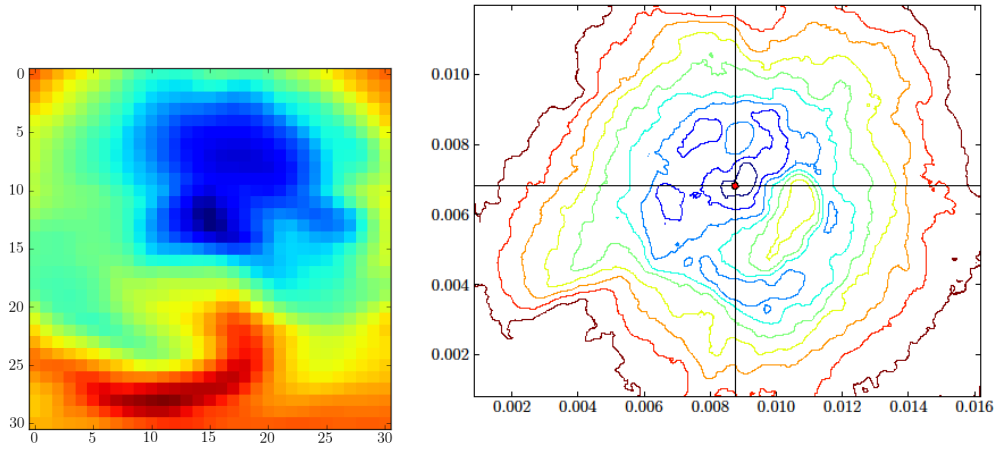
Sandstone 793.16 K
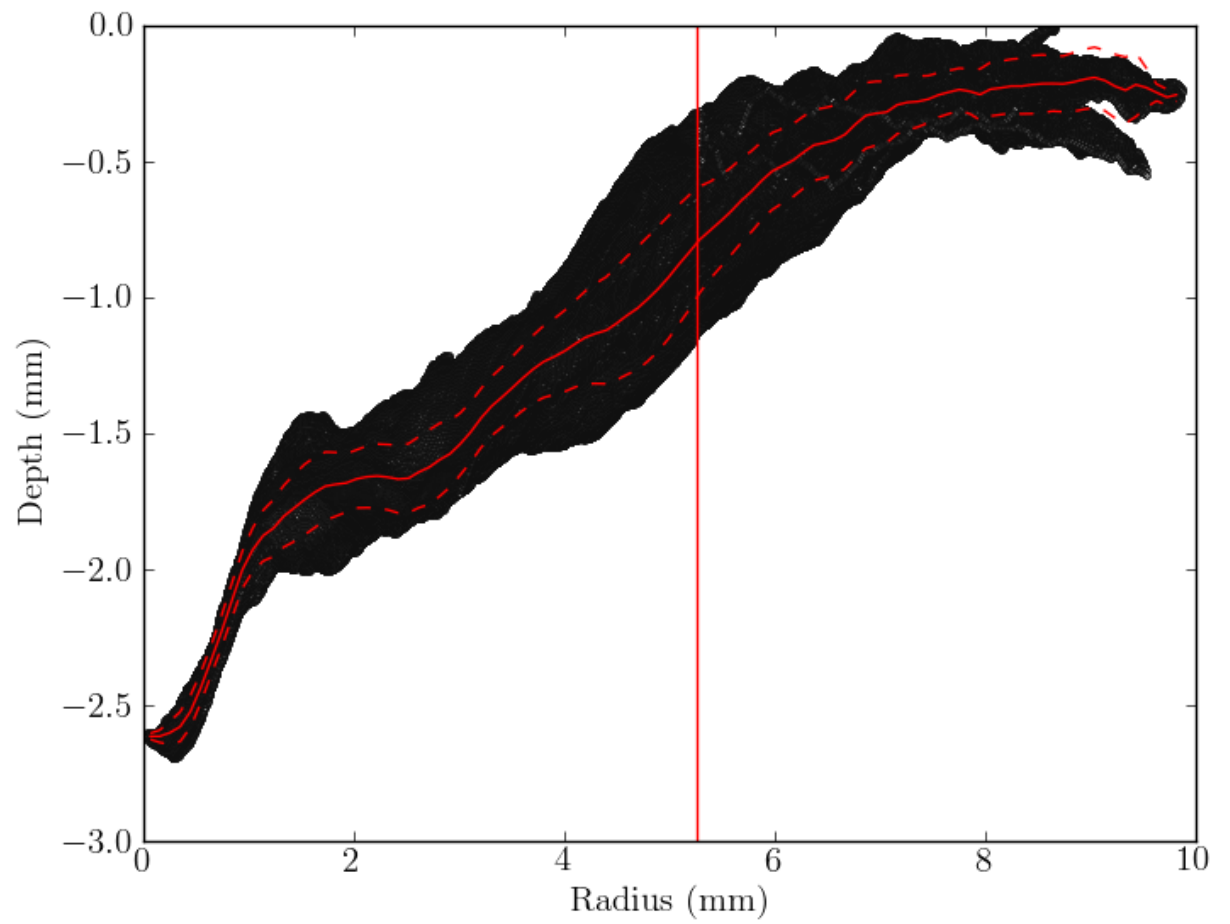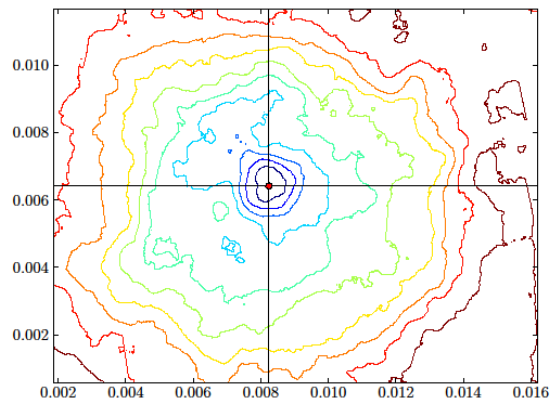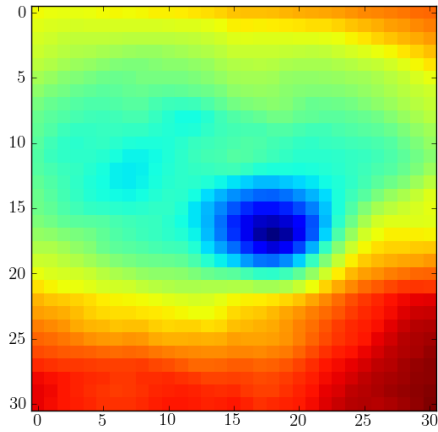
Sandstone 1003.16 K
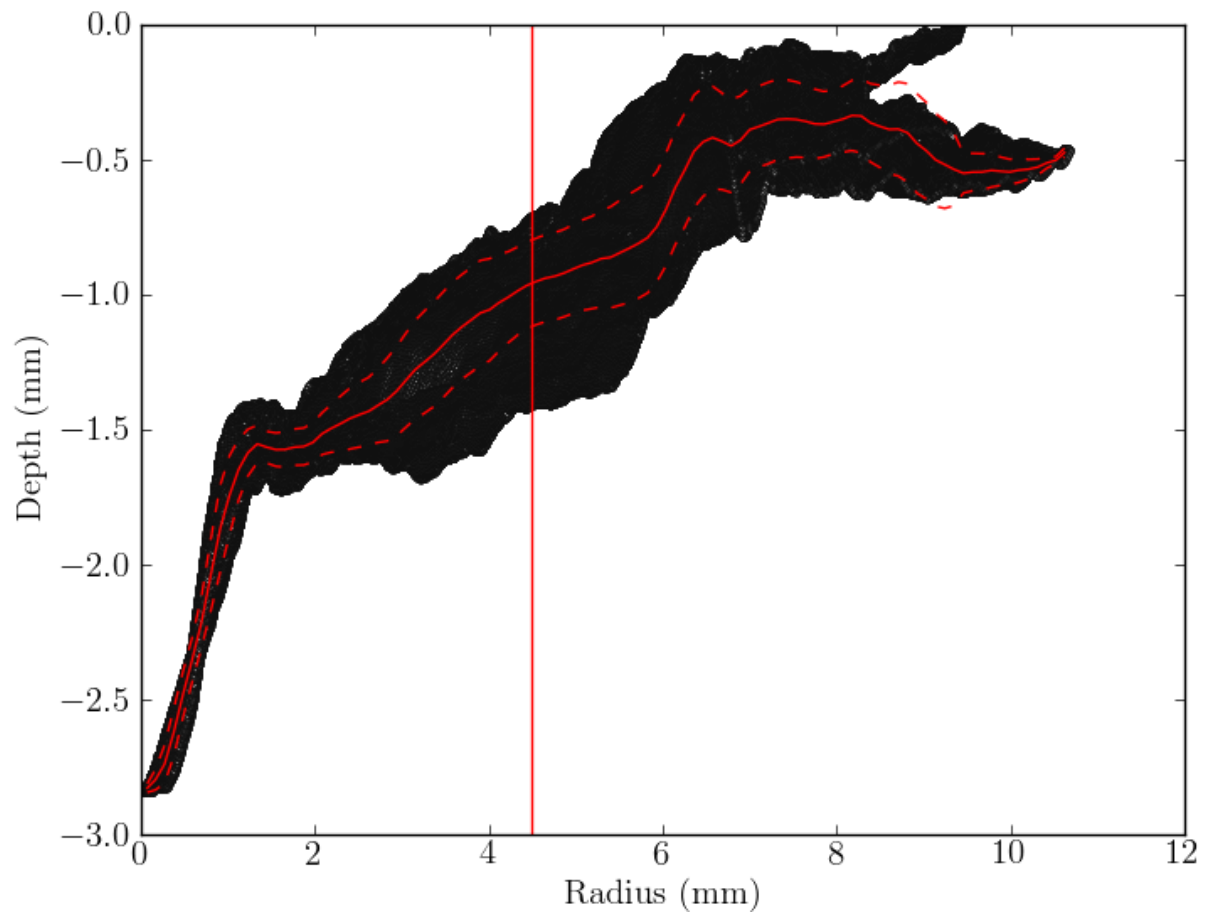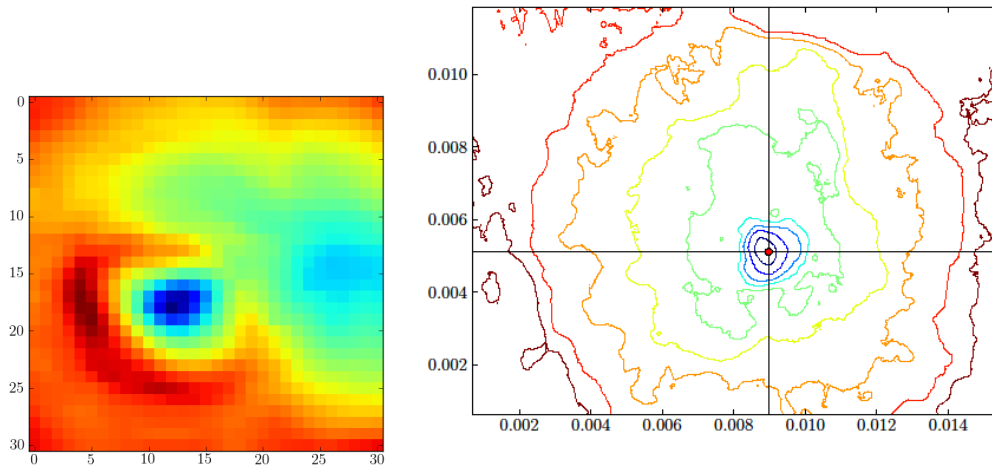
Sandstone Trends
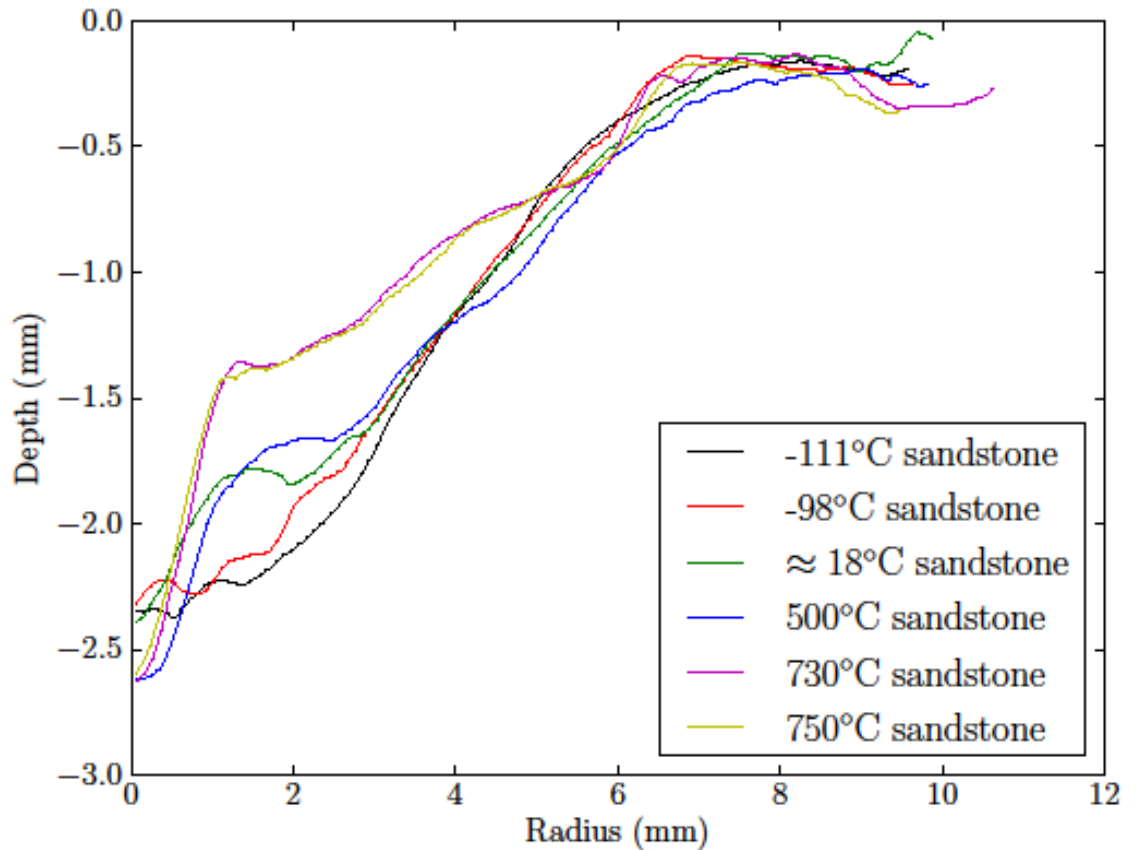
The prominent feature of the average crater profile comparison for the sandstone samples is the increasing depth and gradient of the initial crater excavation zones as temperature increases.